

2020-03-31

Remote Sensing For An Improved Geospatial Flash Flood Susceptibility Modeling Over An Arid Environment

Khadra, Mohamed Shawky Mohamed Ali

Khadra, K. S. M. A. (2020). Remote Sensing For An Improved Geospatial Flash Flood Susceptibility Modeling Over An Arid Environment (Doctoral thesis, University of Calgary, Calgary, Canada). Retrieved from <https://prism.ucalgary.ca>.

<http://hdl.handle.net/1880/111773>

Downloaded from PRISM Repository, University of Calgary

UNIVERSITY OF CALGARY

Remote Sensing For An Improved Geospatial Flash Flood Susceptibility Modeling Over An Arid
Environment

by

Mohamed Shawky Mohamed Ali Khadra

A THESIS

SUBMITTED TO THE FACULTY OF GRADUATE STUDIES
IN PARTIAL FULFILMENT OF THE REQUIREMENTS FOR THE
DEGREE OF DOCTOR OF PHILOSOPHY

GRADUATE PROGRAM IN GEOMATICS ENGINEERING

CALGARY, ALBERTA

MARCH, 2020

© Mohamed Shawky Mohamed Ali Khadra 2020

Abstract

Flash floods are the foremost cause of irretrievable environmental damage in the arid Arabian Peninsula, particularly over the Sultanate of Oman. The rapidly changing climate has led to year-by-year increases in the frequency and severity of flooding. The better understanding of the geomorphologic, topographic, climatic, and hydrologic characteristics of a selected watershed, and determining their geospatial relationships with respect to the flood extent are the core steps for mitigating and minimizing negative impacts of flooding. Therefore, the overall aim of the current study was to employ different remote sensing datasets in predicting prone areas to future flash floods in the ‘wilayats’ (i.e., cities) of El Hamra, Bahla, and Nizwa, Ad Dakhiliyah Governate, the Sultanate of Oman. In this respect, three specific objectives were studied to achieve the main goal.

First, precipitation is a crucial variable for studying various climate-related research such as flash flood monitoring and prediction. However, given the fact that in-situ rainfall gauge measurements are usually limited in this arid area. The performance of five global satellite precipitation estimates (GSPEs) (i.e., Global Precipitation Mission-Integrated Multi-satellitE Retrievals for the GPM (GPM-IMERG), and Global Satellite Mapping of Precipitation (GSMaP)) was evaluated using the available sub-daily and daily ground rainfall records. While GSPEs can provide wide coverage with high spatio-temporal resolutions, assessing related accuracies is a compulsory step before researchers can include them in flood susceptibility modeling. Generally, the five sub-daily and daily GSPEs showed good performance compared to the in-situ measurements. Moreover, statistical error models were employed to quantify the uncertainties in the daily GSPEs.

Second, accurate digital terrain model (DTM) and channel network/orders with fine spatial details are mandatory for flood extent modeling. The DTM has been applied successfully in multiple studies to extract various topographic (e.g., altitude, aspect, and convergence index) and hydrologic (e.g., flow direction, length, and accumulation) attributes. Furthermore, channel networks have been used effectively by different researchers in deriving various geomorphometric measures (e.g., stream order, frequency, and density), as well as topographic and hydrologic features (e.g., height above nearest drainage network (HAND), valley depth (VD), and topographic wetness index (TWI)).

Therefore, a new pixel-based method was developed to quantify the horizontal accuracy of channel networks/orders-based three global digital elevation models (DEMs) (i.e., Advanced Land Observing Satellite (ALOS) Phased Array type L-band Synthetic Aperture Radar (PALSAR), Shuttle Radar Topography Mission (SRTM), and ALOS Panchromatic Remote-sensing Instrument for Stereo Mapping (PRISM)) using those extracted from light detection and ranging (LiDAR) datasets as references. The vertical accuracy of global DEMs were also evaluated utilizing reference LiDAR elevation datasets. Based on the achieved results, the PALSAR DTM (12.5 m) and its derived channel network/orders were found to be the optimal candidates to derive various geospatial layers required for flood susceptibility modeling.

Last, integrated statistical based-improved flood-susceptibility models were developed to define the likelihood of future flash flooding—the extent of which depends on the intrinsic characteristics of the selected study area, including rainfall, soil, HAND, VD, TWI, among others. The spatial relationships between different flood triggering factors (i.e., climatic, geomorphic, topographic, and hydrologic attributes) and flood inventory map were quantified. Random spatially distributed flood and non-flood locations were used for the purpose of training and testing the introduced models. The findings showed that the integrated bivariate and multivariate statistical methods-based flood susceptibility models provided precise maps to predict future flood-prone areas under a close rainfall intensity to that which prevailed during the past flood event, at both high- and low- lands. In addition, the outcomes of the validation of different releases of recent GSPEs can help to have continuous rainfall records that, even in the absence of permanent in-situ rain gauges' measurements, can significantly contribute to future flash flood studies. The developed flood susceptibility models can contribute to mitigating the negative impacts of flash floods by providing accurate information to both the administrators and local settlers about future flash flooding extent at a fine spatial resolution (12.5 m).

Acknowledgement

I would like to express my great appreciation to my supervisors. Prof. Dr. Naser El-Sheimy kept providing continuous guidance, suggestions, valuable remarks, draft reviewing, and motivation on the way towards my Ph. D. thesis. Prof. Dr. Quazi K. Hassan helped me in discussing different concepts, reviewing my drafts, and providing solutions, advices, and comments to enhance my Ph. D. research.

I would like to express my great gratitude to my supervisory committee members. Dr. Xin Wang introduced valuable comments and discussions. Dr. Omar Charif kept introducing valued suggestions, comments, and solutions for some scientific problems challenged me during my Ph. D. research.

I would like to introduce my deep thanks and appreciation to some professional scientists from different global organizations and institutions for their help, advice, information, and materials. Mr. Wenli Yang (Principal Scientist at NASA/GSFC) for providing help and advice on how to read GPM-IMERG data. Dr. Reuben Hansman (Department of Geological Sciences, Stockholm University) for providing geologic maps of the Sultanate of Oman. Mr. Dawood Al-Ghatrifi (my neighbor in the Family Housing, University of Calgary, Canada and one of the local citizens of Nizwa city, Oman) for the valuable discussions about flood aspects in his city.

I would like to introduce my great thanks and gratitude to the global organizations and institutions that introduced valued help, information, data, and materials for my Ph. D. research. I do acknowledge National Aeronautics and Space Administration (NASA), United States of America (USA) and Japan Aerospace Exploration Agency (JAXA), and European Space Agency (ESA) for providing multiple satellite products free of charge. I highly appreciate that the United States Geological Survey (USGS), USA allowed me to download Landsat 8 surface reflectance products for my study area free of charge. I do thank the ESA and the European Union's Copernicus programme for allowing me to use Sentinel-1A in my scientific research free of charge. I do acknowledge to Alaska Satellite Facility Distributed

Active Archive Center (ASF DAAC) for modifying ALOS PALSAR RTC scenes, which were created by JAXA/Ministry of Economy, Trade, and Industry, Japan (METI), and for allowing me to access Sentinel1A images. I am so grateful for OpenTopography web domain for allowing me to download the LiDAR point cloud data that were acquired and processed for the Pacific Gas and Electric Company (PG&E) by Watershed Sciences, Inc. (WSI) across the DCPD San Simeon survey area from 29 January 2013 to 25 February 2013. I am so grateful, and I do highly appreciate the help of the above-mentioned organizations to my research and to the scientific community.

I am so grateful, and I do highly appreciate the help introduced by the National Survey Authority (NSA) Ministry of Defence, the Sultanate of Oman for providing topographic maps for my study area. I would like to express my sincere gratitude and appreciation for Ministry of Regional Municipalities and Water Resources (MRMWR), the Sultanate of Oman for providing rain gauge data. I highly appreciate and acknowledge the administrators of Sabalet Oman forum for allowing me to cite the materials available in their weather webpages. I am so grateful for the above-mentioned organizations, institutions, companies, and experts, and I do appreciate their contributions and support to the scientific community.

Finally, I would like to introduce my special and deep thanks to the Cultural Affairs and Missions Sector, Ministry of Higher Education and Scientific Research of Egypt for granted me a four-years Ph. D. scholarship that supported me during my Ph. D. study.

Dedication

Dedication:

My late mother: I would like to dedicate my Ph. D. thesis to my late mother. She is still the constant source of inspiration to my life. I would not be the person I am today if it was not for her. She taught me to face the challenges with faith and true confidence. I always feel her presence that strives me to achieve my goals.

My father: thank you for your support, caring, and Doaa.

My wife and kids: thank you for your support and for introducing continuous motivations during study times.

My sisters and nieces: thank you for your support.

Table of Contents

Abstract.	ii
Acknowledgement.	iv
Dedication.	vi
Table of Contents.	vii
List of Tables.	xii
List of Figures.	xv
List of Abbreviations.	xviii
Chapter One: Introduction	1
1.1. Introduction and Background.....	2
1.2. Problem Statement.....	9
1.3. Research Objectives.....	15
1.4. Research Challenge.....	16
1.5. Thesis Structure.....	17
Reference.....	19
Chapter Two.	35
Abstract.	36
Chapter Two (A): Performance Assessment of Different Sub-daily and Daily Precipitation Estimates Derived from GPM and GSMaP Products Over An Arid. Environment.	38
2A.1. Introduction and Background.	38
2A.2. Study Area and Datasets.	42
2A.2.1. Study Area.	42
2A.2.2. Rainfall Datasets.	44
2A.2.2.1. GPM-IMERG Products.	44
2A.2.2.2. GSMaP Estimates.	45
2A.2.2.3. Rain Gauge Data.	45
2A.3. Methods.	46
2A.3.1. Data Preparation.	47

2A.3.2. Statistical Comparison Procedures.	49
2A.3.2.1. Continuous Statistical Metrics.	50
2A.3.2.2. Categorical Indices.	50
2A.4. Results.	51
2A.4.1. Daily Analysis Utilizing Traditional Statistical Metrics per Entire Ground Rain Gauges.	51
2A.4.2. Sub-daily Analysis Utilizing Traditional Statistical Metrics per Entire Ground Gauges.	54
2A.4.3. Daily Analysis Utilizing Categorical Metrics per Entire Ground Gauge.	59
2A.4.4. Sub-daily Analysis Utilizing Categorical Metrics per Entire Ground Gauges.	60
2A.5. Discussion.	63
2A.6. Conclusions.	66
Author Contributions.	70
Acknowledgments.	70
Conflicts of Interests.	70
Chapter Two (B): Quantifying Uncertainties associated With Different Global Satellite Precipitation Using Statistical Error Models.	71
2B.1. Introduction and Background.	71
2B.2. Methods.	74
2B.3. Results.	76
2B.4. Discussion.	78
2B.5. Conclusions.	79
References.	80
Chapter Three: Pixel-Based Geometric Assessment of Channel Networks/Orders Derived from Global Spaceborne Digital Elevation Models.	92
Abstract.	93
3.1. Introduction.	94
3.2. Materials.	98
3.2.1. Study Area.	98
3.2.2. Data Requirements.	100

3.3. Methods.	101
3.3.1. Data Preparation.	102
3.3.2. Evaluating the Vertical Elevation Accuracy of Global DEMs Based on LiDAR DTM/DSM.	103
3.3.3. Extraction of the Channel Networks/Orders.	104
3.3.4. Developing ArcGIS Python Toolbox for Geometric Assessment of Channel Networks.	107
3.3.5. Categorical Performance Measures for Assessing the Horizontal Accuracy of Channel Networks/Orders.	112
3.4. Results.	115
3.4.1. Traditional Statistical Indices for Evaluating the Vertical Height Accuracy of Global DEMs.	115
3.4.2. Horizontal Evaluation of the Channel Networks.	118
3.4.3. Performance Evaluation Metrics of the Geometric Assessment of Channel Orders.	123
3.4.4. Effect of Global DEM Spatial Resolution on the Evaluation of Channel Networks/Orders.	126
3.4.5. Characterizing the Horizontal Offset Between the Extracted Channel Networks.	129
3.5. Discussion.	132
3.5.1. Vertical Accuracy of Global DEM.	132
3.5.2. Horizontal Accuracy of Channel Networks.	134
3.5.3. Similarity Between the Findings of the Vertical Assessment of Global DEMs and the Horizontal Evaluation of Their Derived Channel Networks/Orders.	135
3.5.4. Potential Applications of the Introduced Method.	137
3.6. Conclusions.	137
Author Contributions.	140
Acknowledgments.	140
Conflicts of Interest.	140
References.	141

Chapter Four: Remote Sensing-based An Enhanced Flash Flood Susceptibility Mapping Using Integrated Bivariate and Multivariate Statistical Models.	157
Abstract.	158
4.1. Introduction.	159
4.2. Materials.	169
4.2.1. Study Area.	169
4.2.2. Data Requirements.	171
4.2.2.1. Sentinel-1A.	171
4.2.2.2. DEM Dataset.	172
4.2.2.3. GSMap-G.	173
4.3. Methods.	174
4.3.1. Flash Flood Inventory Map.	174
4.3.2. Flood-Affecting Independent Factors.	180
4.3.3. Multicollinearity Assessment of the Flood Causative Variables.	187
4.3.4. Bivariate and Multivariate Statistical Models.	187
4.3.4.1. Relative Frequency Ratio (FR).	188
4.3.4.2. Statistical Index (SI).	189
4.3.4.3. Logistic Regression (LR).	189
4.3.5. Models' Performance Validation.	190
4.4. Results.	194
4.4.1. Multicollinearity Assessment.	194
4.4.2. FR Model-based Flood Susceptibility.	194
4.4.3. SI-based Flood Susceptibility Model.	200
4.4.4. Integrated Bivariate and Multivariate Statistical Approaches-Derived Flood Susceptibility Models.	202
4.5.5. Evaluation of the Flash Flood Susceptibility Models.	204
4.5.6. Comparing Five Classes' Percentages Derived from Four Flood susceptibility Models.	209
4.6. Discussion and Conclusions.	211
References.	215

Chapter Five: Conclusions and Recommendations.	240
5.1. Concluding Remarks.	241
5.2. Research Outcomes (Contributions).	244
5.3. Recommendations for Future Work.	247
References.	249
Appendices.	250
Appendix A:	251
Appendix B:	264
Appendix C: Copyright Related Information.	266
Published Work.	271

List of Tables

Table 2A.1. The continuous difference statistical metrics used for evaluating the performance of different GSPEs. Note: Variables: i: sample size “single rainfall event for a single satellite grid point”; N: number of pixels “observed days”; S: satellite precipitation estimates (centers of grids); O: observed point ground rain data.	49
Table 2A.2. Contingency table to determine the possible conditions (combination) for detecting rainfall from the GSPEs and ground measurements.	49
Table 2A.3. The categorical statistical indicators utilized for evaluating the performance of the GSPEs.	50
Table 2A.4. Statistical metrics of daily rainfall events per different intensities (mid-March 2014 to October 2016). NoE refers to the number of recorded rainfall events.	53
Table 2A.5. Statistical metrics of sub-daily rainfall events of total intensity (mid-March 2014 to October 2016). NoE refers to the number of recorded rainfall events.	55
Table 2A.6. Statistical metrics of sub-daily rainfall events at a rainfall intensity of less than 2.5 mm (mid-March 2014 to October 2016). NoE refers to the number of recorded rainfall events.	56
Table 2A.7. Statistical metrics of sub-daily rainfall events at intensity 2.5–10 mm (mid-March 2014 to October 2016). NoE refers to the number of recorded rainfall events.	57
Table 2A.8. Statistical metrics of sub-daily rainfall events at intensity 10–50 mm (mid-March 2014 to October 2016). NoE refers to the number of recorded rainfall events.	58
Table 3.1. Descriptions of the three global Digital Elevation Models (DEMs). SRTM, Shuttle Radar Topography Mission; ALOS, Advanced Land Observing Satellite; PALSAR, Phased Array type L-band Synthetic Aperture Radar; DSM, Digital Surface Model; ASF DAAC, Alaska Satellite Facility Distributed Active Archive Data Center; JAXA, Japan Aerospace Exploration Agency.	100

Table 3.2. Outcomes of classification matrix resulting from comparing a LiDAR DTM/DSM-derived channel network (reference class) and a global DEM-based network (test class); where Net denotes network.111

Table 3.3. Outputs of multiclass error matrix resulting from comparing a LiDAR DTM/DSM (reference data)-derived channel orders and a global DEM (test data)-based orders with a channel having a higher order of n; where Ord denotes channel order and B0 refers to the background of 0 value.111

Table 3.4. Statistical vertical differences between global DEMs and LiDAR DTMs/DSMs expressed in terms of RMSE and MD in m.118

Table 3.5. Performance accuracy metrics computed based on a comparison between whole channel networks/orders extracted from the LiDAR DTM/DSM 28.5 m and the ALOS DSM 28.5 m at different ATs expressed in the corresponding number of pixels and PBTv in pixels.121

Table 3.6. Performance accuracy metrics computed based on a comparison between whole channel networks/orders extracted from the LiDAR DTM/DSM 28.5 m and the SRTM DEM 28.5 m at different ATs expressed in the corresponding number of pixels and PBTv in pixels.123

Table 3.7. Performance accuracy metrics computed based on a comparison between whole networks/orders extracted from the LiDAR DTM/DSM 28.5 m and the PALSAR DEM 28.5 m at different ATs expressed in the corresponding number of pixels and PBTv in pixels.126

Table 3.8. Performance accuracy metrics computed based on the comparison between whole networks/orders extracted from the LiDAR DTM/DSM 12.5 m and the PALSAR DEM 12.5 m at different ATs expressed in the corresponding number of pixels and PBTvs in pixels.127

Table 3.9. Performance metrics computed based on the comparison between networks/orders extracted from LiDAR DTMs and global DEMs at different ATs expressed

in the corresponding number of pixels, PBTv in pixels, and spatial resolution in m.
.....129

Table 4.1. Classification matrix’s outcomes of the comparison between actual flood inundation and predicted flood extent datasets. F and NF denote flood and non-flood, respectively.191

Table 4.2. The metrics for measuring the predictive performance of the flood susceptibility models.192

Table 4.3. The spatial relationships between flood occurrence and each class of the flood causative factors based on estimating FR and SI.196-199

Table 4.4. The results of fitting the FR-LR and SI-LR models on the flash flood datasets. The parameters utilized in both models, their estimated weights and p-values are shown below.203

Table 4.5. Evaluation metrics for quantifying the predictive performance of the four flood susceptibility models.205

List of Figures

Figure 1.1. A schematic diagram shows the thesis outlines.	18
Figure 2A.1. The study area is enclosed in the red polygon (as shown in the upper panel), and the 38 meteorological ground rainfall gauges are shown in black dots shown in the bottom panel. Note the elevation irregularities (color in m) were derived from ALOS PALSAR DEM with a spatial resolution of 12.5 m. The source of the satellite imagery (top part) is ESRI [32].	43
Figure 2A.2. The flow chart for comparing the Global Satellite-based Precipitation Estimates (GSPEs) against the in-situ rain gauges' measurements over an arid area (Ad Dakhiliyah, the Sultanate of Oman).	46
Figure 2A.3. Categorical statistical indices of daily rainfall events at different initialization thresholds: (a) 0.00 mm/day, (b) 2.5 mm/day, and (c) 10 mm/day.	60
Figure 2A.4. Categorical statistical indices of sub-daily rainfall events using the total rainfall intensity per three temporal resolutions: (a) 6 h, (b) 12 h, and (c) 18 h.	61
Figure 2A.5. Categorical statistical indices of sub-daily rainfall events at an intensity less than 2.5 mm and three-time scales: (a) 6 h, (b) 12 h, (c) 18 h, and (d) 24 h.	63
Figure 2B.1. Evaluating performance of the additive and multiplicative error models in quantifying the uncertainties in the GSPEs at different rainfall intensity classes.....	77
Figure 3.1. The study area in San Luis Obispo County, the western part of the central coast of California, USA. (1 to 4) refer to Cambria, Harmony, Cayucos, and Whale Reservoir, respectively. The source of the satellite imagery (top left) is ESRI, 2018 [78].	99
Figure 3.2. Methodology flow chart for the per-pixel geometric evaluation of channel networks/Strahler orders.	102
Figure 3.3. Sketch for comparing pixels of channel networks/orders using error matrices: (a) reference datasets, (b) test datasets, (c) two-class confusion matrix outcomes resulting from matching between the whole networks in a and b (regardless of the channels' of the	

channels' orders), and (d) multiclass error matrix outcomes resulting from matching between channels that have the same order in a and b. TP, true positive; FP, false positive; FN, false negative; and TN, true negative.109

Figure 3.4. Concept of the pixel buffer tolerance values (PBTVs).110

Figure 3.5. Elevation surface differences between: (a) LiDAR DTM and PALSAR DEM 28.5 m, (b) LiDAR DSM and PALSAR DEM 28.5 m, (c) LiDAR DTM and PALSAR DEM 12.5 m, (d) LiDAR DSM and PALSAR DEM 12.5 m, (e) LiDAR DTM and SRTM DEM 28.5 m, (f) LiDAR DSM and SRTM DEM 28.116-117

Figure 3.6. Confusion matrix outcomes resulting from comparing channel networks extracted from: (a,b) LiDAR DTM and PALSAR DEM 12.5 m at an area threshold (AT) corresponding to 25 pixels and pixel buffer tolerance value (PBTV) of 0 and 3 pixels, respectively, (c,d) LiDAR DSM and PALSAR DEM 12.5 m using an AT corresponding to 25 pixels and PBTV of 0 and 3 pixels, respectively, (e,f) LiDAR DTM and PALSAR DEM 28.5 m using an AT corresponding to 100 pixels and PBTV of 0 and 3 pixels, respectively, and (g,h) LiDAR DSM and PALSAR DEM 28.5 m using an AT corresponding to 100 pixels and PBTV of 0 and 3 pixels, respectively.119-120

Figure 3.7. Deviations of channels' pixels in in both $\pm X$ and $\pm Y$ directions at different ATs and PBTVs in a comparison between the networks extracted from both: (a) LiDAR DTM and SRTM 28.5 m, (b) LiDAR DSM and SRTM 28.5 m, (c) LiDAR DTM and ALOS DSM 28.5 m, (d) LiDAR DSM and ALOS DSM 28.5 m, (e) LiDAR DTM and PALSAR DEM 28.5 m, (f) LiDAR DSM and PALSAR DEM 28.5 m, (g) LiDAR DTM and PALSAR DEM 12.5 m, and h. LiDAR DSM and PALSAR DEM 12.5 m.131-132

Figure 4.1. The area of the study shows the selected watershed extends among the wilayats of El Hamra, Bahla, and Nizwa at the Dakhiliyah Governate, the Sultanate of Oman. The source of the satellite imagery is ESRI, 2018 [84]. The upper map of the Sultanate of Oman is not an authority on international borders.170

Figure 4.2. Methodology flow chart for the improved flood susceptibility models.175

Figure 4.3. (a) the flood inventory map, (b) and (c) training and testing datasets, respectively.	179
Figure 4.4. Reclassified flash flood triggering factor in the selected area of study: (a) geology, (b) soil, (c) altitude (m), (d) height above nearest drainage network (HAND) (m), (e) Melton ruggedness number (MRN), (f) drainage line density (DLD) (km/km ²), (g) topographic position index (TPI), (h) Aspect (°), (i) valley depth (VD), (j) topographic wetness index (TWI), (k) convergence index (CI), (l) flow length in the downstream direction (FL_DS), and (m) Global Satellite Mapping of Precipitation-Gauge calibrated (GSMaP-G).	183-186
Figure 4.5. Multicollinearity assessment of the flood triggering factors.	194
Figure 4.6. Flash flood susceptibility maps generated using: (a) FR, (b) SI, (c) FR-LR, and (d) SI-LR models.	201
Figure 4.7. The success (a) and prediction (b) rate curves for the four statistical models-based flash flood susceptibility maps.	208
Figure 4.8. The area percentage of the flash flood zones located within the five classes of the developed susceptibility maps.	210

List of Abbreviations

Abbreviation	Definition
AHP	Analytic Hierarchy Process
ALOS	Advanced Land Observing Satellite
ANFIS	Adaptive Network-based Fuzzy Inference System
ANN	Artificial Neural Network
arcsec	Arc-Second
ASCII	American Standard Code for Information Interchange
ASF DAAC	Alaska Satellite Facility Distributed Active Archive Data Center
ASI	Italian Space Agency
ASTER	Advanced Spaceborne Thermal Emission and Reflection Radiometer
AT	Flow Accumulation Area Threshold
AVHRR	Advanced Very High Resolution Radiometer
BT	Brightness Temperature
CAT	Comparable Area Threshold
CGDPA	China Gauge-Based Daily Precipitation Analysis
CHIRPS	Climate Hazards Group InfraRed Precipitation with Stations
CI	Convergence Index
CMA	China Meteorological Administration
CMOPRH	Climate Prediction Center Morphing Data
CPC	Climate Prediction Center Unified Daily Gauge Dataset
CREST V2.1	Coupled Routing and Excess Storage Model
CSI	Critical Success Index
CSV	Comma-separated Values File
DEM	Digital Elevation Model
DEMs	Digital Elevation Models
DLD	Drainage Line Density

Abbreviation	Definition
DLR	German Aerospace Center
DN	Digital Number
DPR	Dual-frequency Precipitation Radar
DSM	Digital Surface Model
DT	Decision Tree
DTM	Digital Terrain Model
ECMWF	European Centre for Medium-Range Weather Forecasts
EGM	Earth Gravitational Model
El Niño	El Niño Southern Oscillation
EORC	Earth Observation Research Center
ESA	European Space Agency
ESA-Copernicus	European Space Agency-Commission's Earth Observation Programme
ESRI	Environmental Systems Research Institute
ETM+	Landsat Enhanced Thematic Mapper Plus
F	False (Contingency Table)
F	F-Score
FAO	United Nations Food and Agriculture Organization
FAR	False Alarm Ratio
FBD	Fine Beam Mode
FBI	Frequency Bias Index
FIS	Fuzzy Interface System
FL_DS	Flow Length in the Downstream Direction
FN	False Negative (Confusion Matrix)
FP	False Positive (Confusion Matrix)
GCA	Gauge Calibration Algorithm
FR	Frequency Ratio
GCS	Geographic Coordinate System

Abbreviation	Definition
GEO-IR	Geosynchronous Infrared-based sensors
GeoTIFF	Geostationary Earth Orbit Tagged Image File Format
GES DISC	Goddard Earth Sciences Data and Information Services Center
GIS	Geographic Information System
GMI	GPM Microwave Imager
GMT	Greenwich Mean Time
GOES	Geostationary Environmental Satellite
GPCP-1DD	Global Precipitation Climatology Project-1°, Daily
GPM	Global Precipitation Measurements
GPROF	Goddard Profiling Algorithm
GPS	Global Positioning System,
GRASS	Geographic Resources Analysis Support System
GRDH	Ground Range Detected High Resolution
GRIB	GRIdded Binary or General Regularly-distributed Information in Binary Form
GSMaP	Global Satellite Mapping of Precipitation
GSMaP-G	Gauge-Calibrated Global Satellite Mapping of Precipitation
GSMaP-S	Standard Global Satellite Mapping of Precipitation
GSOD	US National Climate Data Center Global Summary of Days
GSPPs	Global Satellite-based Precipitation Products
h	Hour
H	Hit (Contingency Table)
HAND	Height Above Nearest Drainage Network
HDF	Hierarchical Data Format
HH	SAR Polarization-Horizontal-Horizontal
HMS	Watershed-oriented Hydrological Modeling System
HRD	High-Resolution DEM
HRIT	High Rate Information Transmission

Abbreviation	Definition
HRV	High Resolution Visible band
IDW	Inverse Distance Weighting
IMD	Indian Meteorological Department
IMERG	Integrated Multi-satellitE Retrievals for the GPM
IMERG-E	Early Integrated Multi-satellitE Retrievals for the GPM
IMERG-F	Final Integrated Multi-satellitE Retrievals for the GPM
IMERG-L	Late Integrated Multi-satellitE Retrievals for the GPM
IMO	Iranian Meteorological Organization
InSAR	Interferometric Synthetic Aperture Radar
IPCC	Intergovernmental Panel on Climate Change
IR	Infrared
ITCZ	Inter-Tropical Convergence Zone
JAXA	Japan Aerospace Exploration Agency
JPL	Jet Propulsion Laboratory
KI	Kappa Index
km	Kilometer
KML	keyhole markup language
LAS	LIDAR Data Exchange File.
LEO-PMW	Low Earth Orbit-Passive Microwave-based sensors
LiDAR	Light Detection and Ranging
LP DAAC	Land Processes Distributed Active Archive Center
LR	Logistic Regression model
LRD	Low-Resolution DEM
LULC	Land Use and Land Cover
m	Meter
M	Miss (Contingency Table)
MAD	Mean Absolute Difference

Abbreviation	Definition
MAF	Ministry of Agriculture and Fisheries, The Sultanate of Oman
MD	Mean Difference
MESMA	Multiple Endmembers Spectral Mixture Analysis
METI	Ministry of Economy, Trade, and Industry of Japan
MIR	MID InfraRed band
MLC	Maximum Likelihood Classification
MLP	Multi-Layer Perceptron
MNDWI	Modified Normalized Difference Water Index
MODIS	Moderate-resolution Imaging Spectroradiometer
MRN	Melton Ruggedness Number
MSG	Meteosat Second Generation
MWI	The Ministry of Water and Irrigation of Jordan
NADV 83	North American Datum 1983
NADV 88	North American Vertical Datum of 1988
NASA	National Aeronautics and Space Administration Agency
NCAR	National Centers for Environmental Prediction/National Center for Atmospheric Research
NCEP	National Centers for Environmental Prediction
NDWI	Normalized difference Water Index
NED	the National Elevation Dataset
Net	Drainage Network
NGA	National Geospatial-Intelligence Agency
NIR	Near Infrared
NOAA	National Oceanic and Atmospheric Administration
NRLP	Naval Research Laboratory's Blended Product
NRT	Near-real time
NVE	Neighborhood Valley-Emphasis
NWP	Numerical Weather Prediction

Abbreviation	Definition
OA	Overall Accuracy
OLS	Ordinary Least Squares
OpenTopography	High-Resolution Topography Data and Tools Website
Ord	Drainage Order
PA	Producer Accuracy
PALSAR	Phased Array type L-band Synthetic Aperture Radar
PBTv	Pixel Buffer Tolerance Values
PERSIANN-CDR	Remotely Sensed Information using Artificial Neural Networks-Climate Data Record
PM	Passive Microwave
POD	Probability of Detection
PR	Precipitation Radar
PRISM	Panchromatic Remote-sensing Instrument for Stereo Mapping
QA	Quality Assurance
QAT	Original Area threshold based on which the channel network/orders were extracted
QC	Quality Control
QMPF	Wadi Mean Peak Flow
R²	Coefficient of Determination
Radar	Radio Detection and Ranging
RFE	African Rainfall Estimation Algorithm
rKFDA	Regularized Kernel Fisher's Discriminant Analysis
RMSE	Root Mean Square Error
ROC	Receiving Operating Characteristic
RTC	Radiometric Terrain Correction
SAGA	System for Automated Geoscientific Analyses
SAR	Synthetic Aperture Radar
SAR HH	Single Co-Polarization SAR type, Horizontal transmit/Horizontal receive

Abbreviation	Definition
SAR HV	Single Co-Polarization SAR type, Horizontal transmit/Vertical receive
SAR VH	Single Co-Polarization SAR type, Vertical transmit/Horizontal receive
SAR VV	Single Co-Polarization SAR type, Vertical transmit/Vertical receive
SCS-CN	Soil Conservation Service-Curve Number Method
SDS	Science Data Sets
SEVIRI	Spinning Enhanced Visible and Infrared Imager
SI	Statistical Index
SNAP	Sentinel Application Platform Software
SP	Specificity
SPOT	Satellite Pour l'Observation de la Terre
SQL	Structured Query Language
SRTM	Shuttle Radar Topography Mission
SSM/I	Special Sensor Microwave/Imager
SVMs	Support Vector Machines
SWIR	ShortWave InfraRed Band
TIRS	Thermal InfraRed Sensor
TM	Landsat Thematic Mapper
TMI	TRMM Microwave Imager
TMPA	TRMM Multi-satellite Precipitation Analysis
TMPA V6	Multi-satellite Precipitation Analysis Version 6
TMPA V7	Multi-satellite Precipitation Analysis Version 7
TN	True Negative (Confusion Matrix)
TOL	Tolerance
TP	True Positive (Confusion Matrix)
TPI	Topographic Position Index
TRRM	Tropical Rainfall Measuring Mission
TWI	Topographic Wetness Index

Abbreviation	Definition
UA	User Accuracy
UB	Unconditional Bias
UNDP	UN Development Programme
UNISDR	The United Nations Office for Disaster Risk Reduction
USGS	United States Geological Survey
UTC	Coordinated Universal Time
UTM	Universal Transverse Mercator
VD	Valley Depth
VGI	Volunteered geographic information
VIF	Variance Inflation Factor
VIS	Visible Band
WGS	World Geodetic System
WMO	World Meteorological Association
WoE	Weights-of-Evidence
X	Null (Contingency Table)

CHAPTER ONE

INTRODUCTION

1.1. Introduction and Background

Natural disasters are deemed to be the principal cause of irrecoverable damages to the environment, on a global scale [1], with flash flooding being one of the most extreme [2]. Flash floods can cause severe casualties, destroy infrastructures, increase land erosion, pollution, and place serious constraints on the development of the affected areas [3]. Furthermore, the potential negative impacts of flash floods in the arid Arabian Peninsula are heightened due to a lack of effective responses at their rapid onset, which is usually less than six hours after rainfall events [4]. Flash floods can be generated instantly, during, or shortly after rainfall events, especially when rain falls on steep mountain slopes with exposed rocks and lack of vegetation [5], [6]. They occur whenever a drainage system receives more water than it can handle [7]. In particular, the negative effects of flooding are exacerbated when extreme rainfall invades areas of impervious and/or hard ground surfaces that significantly reduce the infiltration rate of surface runoff. The latter may take the form of water sheets [8].

Flash flood is a linked hydro-meteorological system [9] where hydrologic, climatic, geomorphic, and topographic characteristics of the watersheds under considerations control it. Rainfall is the primary hydrological input that initiates the flash flood [6]. Though for many decades, flash floods have been considered as an environmental hazard, the exact processes triggering its initiation and spreading remain uncertain and/or are insufficiently documented [10]. Therefore, the first step in mapping the flash flood-prone areas is to determine the spatial and temporal rainfall distribution that initially controls the generation of rapid runoff in the catchment area under investigation.

Predictive global climate change models indicate that changing precipitation patterns and the increasing number of extreme rainfall events will raise the magnitude and frequency of future flood events [11]. Over the last decade, severe and unstable global climatic changes induced flash floods that were more violent, extensive, and frequent [8]. Flash flooding is often associated with convective thunderstorms, monsoons, and tropical cyclones, which can be intensified during complex weather patterns such as ice melting [8]. Nowadays, climatic changes are more pronounced and, thereby, profoundly affect global weather leading to

intensive rainfall and associated severe flash floods [12]. For instance, in recent years, most of the arid and semi-arid countries were invaded by intense flash floods that reached more than one meter in height (e.g., flooding events in the Sultanate of Oman, Arab Republic of Egypt, Hashemite Kingdom of Jordan, Kingdom of Saudi Arabia, Yemen, Qatar, and Iraq).

The destructive effects of such tremendous flash flooding were recorded over the Arabian Peninsula, particularly the Sultanate of Oman. In the last few years, a series of successive flood events were frequently reported in Oman. For example, on November 15, 2013, a major flash flood hit Oman and other Gulf countries following an unexpected and intense rainfall event and resulted in the death of one person [13]. Five months later, at the Niyabat of Lima of Khasabon, Northern Oman, an extreme rainfall event of 415 mm that resulted in the death of six people, that had been, essentially, washed away by the fast runoff and sediment load [14]. Northern Oman is continuing to face flash flood hazards. In 2015, for four days (October 14 to 17), the areas of Nizwa, Ras Al Hadd, and Bahla received severe flash floods. On October 16, according to the report of Oman's Ministry of Regional Municipalities and Water Resources [15], the city of Ibra received rainfall with an intensity of 104 mm, while three other locations endured a cumulative rainfall intensity of around 40 mm. These extreme flood events caused the death of seven people, while fifty others were rescued. Similarly, on Friday, September 04, of that same year, four people died, and one was declared missing as a result of flooding associated with thundershowers in northeastern Oman, with Amerat and Rustaq, respectively, experiencing a maximum intensity of 59.8 and 17.4 mm [16]. Moreover, during the period from December 16 to 19, 2017, another devastating flood event occurred over northern Oman, whereby, the affected areas received around 20 mm of rainfall [17]. Three persons died, while dozen were injured due to severely damaged homes and road accidents.

The combination of the flood event itself (i.e., source), pathways (i.e., surface overflow and inundation), receptors (i.e., people, property, and environment), and consequences (i.e., lives loss and infrastructure damage) can quantify the magnitude of the flood risk [18], [19]. Many infrastructures, such as towns and roads, are inadequately located and unprotected from flood hazards to mitigate the potential damage of future flood events

[20]. It is mandatory to analyze past flash floods' events thoroughly [5]. However, less attention has been given to historic flash floods in the aforementioned arid areas due to various long intervals between flood events. This lack of awareness makes the local populations have a false sense of security to the catastrophic flash floods.

Furthermore, newcomers to flood-prone areas usually settle and develop the land without consideration of the expected hazards [10]. Accurate prediction of the vulnerable areas to flash floods would help in designing measures to protect such zones from future damage and assist in preparing new developments such as roads and housing [10]. The hydrological response of the flood-prone basin to rainfall is governed intrinsically by its geomorphometric, topographic, and hydrologic characteristics. As it stands, the drainage basin is very sensitive to the size, intensity, and location of the rainstorm, which can affect response [20]. Although flash flooding is one of the main hazards in the arid regions, it is also considered a vital natural recharge source of groundwater [21].

Flood management can be achieved through four significant steps: prediction, preparation, prevention, and damage assessment [22]. Flood extent mapping allows emergency responders to handle extreme flood events while directing their limited resources to the highest-priority areas [23]. Flash floods are very challenging to predict as they characterize by rapid and intense run-off generation leading to a rapid rise in water levels and high-peak discharge over a short duration proceeding the onset of the generating storm [24].

Earth observation satellites and GIS techniques introduce valuable datasets and methods to study flash floods (e.g., [24]–[29]) since they (i) provide essential tools for observing and investigating the spatial dynamics of floods, (ii) have relatively low or no acquisition and mapping costs, (iii) allow mapping over large, and sometimes inaccessible, regions, in a time repetitive manner, (iv) grant a compelling set of tools for analyzing and extracting spatial information to support decision making reliably and consistently, and (v) introduce new methods to process big digital data volumes since the repeated acquisitions

offer a wealth of archival data to enable the detection of flash floods changes over space and time.

Determining future flash floods' extents (i.e., flood susceptibility assessments) based on the current and past prevailing physical factors is the central concept used in most available flood research. Flood susceptibility (i.e., potential) map can be defined as the likelihood of future flooding extent depending on the intrinsic properties of a given area such as rainfall, lithologic units, soil type, topographic wetness index, and more [30]. Such models were developed using either statistical or machine learning or integration between both techniques [31]. It is imperative to have a spatial association in each input factor to gain accurate results [32]. Flood susceptibility maps can assess the past spatial extents of flood events [33] and classify the hazard degree in prone areas [34]. It can also help policymakers and authorities to prepare necessary emergency plans and implement mitigation measures to reduce the loss of life and property damage.

Precipitation is one of the key components of the water cycle that is crucial to study flood modeling, water resources management, as well as critical social and climatological issues [35]. However, quantifying precipitation is complicated because it is highly variable over space and time, even on a small scale [35], [36], particularly in the arid areas. The unknown future precipitation still constitutes the largest source of uncertainty in flash flood mapping [37]. Many global satellite precipitation estimates (GSPEs) are currently available to introduce real contributions to the scientific community [38]–[40]. Earth observation-based precipitation products have proved to be the world's most cost-effective and continuous method to locate the spatial and temporal variability of rainfall, particularly over extensive ungauged regions [41]–[43]. The main hurdles associated with GSPEs are the high uncertainties associated with rainfall estimates. Therefore, evaluating the performance of GSPEs against a less biased in-situ rain gauge measurements in the areas under investigation is a mandatory step before researchers can incorporate them into further flash flood modeling.

Traditional point rain gauges cannot capture the areal representation and variation of rainfall, especially in regions where the in-situ rain gauges are limited in number and coverage [44]. Even if rain gauge network measurements are interpolated, they yield a uniform rainfall field that does not represent the real spatial and temporal rainfall variability [45]. Furthermore, the operation of rain gauges is costly, and in most cases, they are sparsely distributed or unavailable in remote areas due to accessibility challenges and limitations with respect to installation and maintenance [24]. The latter case has been escalated among the arid Gulf countries.

The shortcomings of the previously mentioned ground-based methods to measure precipitation highlighted the need for enhanced global coverage by the Earth observation satellites [46]. GSPEs are usually used to identify the spatial magnitude of rainfall events at fine spatial and temporal resolutions [47]. The respective advantages were outlined by Gebregiorgis and Hossain [48], such as (i) overcoming the problem of geopolitical boundaries, (ii) covering continents and oceans, (iii) producing consecutive records at day and night, (iv) introducing a cost-effective way comparing to in-situ networks, and (v) delivering the data in a near-real-time, which would be critical to some applications such as monitoring and forecasting of flash flooding events.

GSPEs are usually unable to provide estimates that are entirely similar to the gauge measurements in both temporal and spatial scales [49]. The uncertainties (i.e., non-negligible errors) associated with GSPEs introduce a significant challenge for the end-users to apply these data in practical meteorological and hydrological applications [50]. Therefore, the nature and magnitude of these errors must be thoroughly evaluated and determined to take better advantage of GSPEs' products. Quantifying the level of uncertainty in different GSPEs can be helpful for data producers to improve their algorithms and for the end-users to verify the accuracy of these products before utilizing them in a specific application [48].

Moreover, GSPEs involve indirect precipitation estimates from visible-, infrared (IR)-, and/or passive microwave (PMW)-based cloud properties information. As such, they include inherent errors [51]. GSPEs are not always reliable, and a consensus has been

reached that they require the quantification of the associated uncertainties using statistical error models. The in-situ rain gauges' measurements represented the reference data [52] to assess the reliability and accuracy of GSPEs. Tian et al. [53] assumed that the ground rain gauge records are error-free, insofar as the associated biases were considered much smaller than those in the GSPEs. Furthermore, it is simple to take these errors into account if they are available [54].

Current advances in remote sensing techniques are essential in producing high-quality Digital Elevation Models (DEMs). In general, a DEM is an umbrella term for any electronically accessible elevation datasets, such as digital terrain models (DTMs) and digital surface models (DSMs). It comprises elevation measures of the Earth's terrain, in addition to natural- and human-based objects above a specific vertical datum [55]. DEMs have been used extensively for a wide range of applications, particularly for various hydrological and geomorphological models. The outcomes of these models depend mainly on the accuracy and quality of the utilized DEMs [56]–[61].

Extracting channel networks from DEMs is mandatory in various hydrological [62] and geomorphological [63] studies. A drainage system's evolution over time is profoundly affected by different variables, such as geomorphology, geologic units, soil, tectonics, landscape topography, and land cover [64]. Furthermore, it was used to explicate the hydrological behavior of drainage basins and to quantify surface water potentialities [65].

Most of the available global DEM datasets can be considered as compromises between DTM and DSM [66], [67], [68]. DTMs are more applicable to different hydrological-related research than DSMs. The DTMs have been applied successfully to determine the spatial distributions of many topographic (e.g., aspect, slope, surface curvature, and gully morphology) [69]–[72] and hydrologic (e.g., flow direction, length, and accumulation) attributes [73]. Furthermore, many hydrologists have used DTMs to extract channel networks accurately [69], [74], [75]. Different geomorphometric measures (e.g., stream order, frequency, density) can be estimated utilizing channel networks. These topographic, hydrologic, and geomorphometric parameters contribute as the primary inputs

to various physical and conceptual hydrological models that address the link between hydrological and geomorphic processes operating on the Earth's surface [70], [76].

Recently, airborne light detection and ranging (LiDAR)-based DTMs have been broadly used for various hydrological modeling studies [74], [77], [78], as well as channel network delineation [79], [80]. Note that airborne LiDAR-based DEMs are only available over a small percentage of the Earth's landmass, due to their high cost. Therefore, for many studies—particularly for flood monitoring and flood hazard zoning over the arid regions—researchers have used the freely available remote sensing-based DEMs with global coverage (e.g., [81]–[88]). However, most of these researchers did not investigate the nature of the DEM used (i.e., either a DSM or a DTM) and errors that could profoundly affect their developed models. In addition, most of these studies did not evaluate the horizontal accuracy of the channel networks extracted from different global DEMs to select the optimum channel network for their environmental research.

One efficient method to reduce the risk of flash floods lies in the implementation of an adequate monitoring system and predictions of probable floods' extents [4]. Prediction of flooding extent requires a good understanding of climatic, hydrological, topographical, and geomorphological behaviors for the particular areas in question.

1.2. Problem Statement

Flash flooding is the foremost cause of irretrievable environmental damage in the arid Arabian Peninsula, particularly over the Sultanate of Oman. Currently, climatic changes such as global changing patterns of temperature and precipitation, are noticeable and represent a challenging problem for all scientists [89], [90]. The unstable global climatic changes can cause many negative consequences, such as tremendous increases in temperature and generation of heavy precipitation—the precursor of deadly flash floods, especially in the aforementioned arid area. The frequency and severity of flooding immensely increase year-by-year, particularly with the rapid change in the global climate. Moreover, the frequency of intense precipitation events increases during warming periods [91].

The Sultanate of Oman, along with other countries located in the arid zone, is frequently affected by flooding hazards. To the best of my knowledge, detecting spatial variabilities of flash floods' extents in 'wilayats' (i.e., cities) of El Hamra, Bahla, and Nizwa, Ad Dakhiliyah Governate, the Sultanate of Oman, has not, to date, been carried out. The better understanding of the geomorphologic, topographic, climatic, and hydrologic characteristics of the selected catchment is the core step for mitigating and minimizing negative flooding impacts. Therefore, developing models to identify potential flood-prone areas is mandatory to predict future flash floods and subsequent mitigation measures. Flash flood management is becoming more significant as a program to reduce both accelerating losses of life and infrastructure damage. Developing flood risk maps to detect the flood-prone areas and predict inundation at similar future topographic and climatic conditions is a compulsory process to educate administrators and local settlers [92]. The availability of such flooding risk maps is the key requirement for any future sustainable development of areas under investigation.

In natural hazards research, massive databases are often needed [93]. These data are not easy to collect, and in some cases, the lack of thereof can impede such research [94]. The majority of studies related to flash flooding in arid and semi-arid areas were performed in

the absence of real- and near-real-time rainfall data (e.g., [25], [95]–[98]). Systems of field-based monitoring that are required to record detailed rainfall and runoff datasets are limited (or absent) [99], especially in many countries in the Arabian Peninsula. To date, it is questionable that such field monitoring systems will be installed anytime soon on account of the enormous efforts and resources entailed to create and maintain such systems. This situation makes it difficult to characterize and monitor the floods' extents. Furthermore, field-based mapping of flooded zones is limited in terms of the spatial and temporal extents and can be labor-intensive and costly [100]. Current advances in remote sensing and GIS methods have introduced valuable contributions in flood modeling and prediction and have held the promise to address the previously mentioned inadequacies.

In the case of extreme flash floods, understanding what might happen in the future is necessary to set requisite adaptation policies and develop preparatory guidelines and mechanisms for climatic changes [101]. Flash floods are a linked hydro-meteorological system [9], with rainfall being the primary hydrological input, for the most part, initiates the flash flood [6], as well as inherent watershed characteristics (e.g., drainage line density (DLD), valley depth (VD), flow length in the downstream direction FL_DS) controlling the flood spreading [92].

Lack of accurate and continuous hydro-meteorological data increases the uncertainties associated with flash flooding events [4]. The primary cause of flash floods in the arid regions is precipitation. However, the in-situ rainfall gauges are usually limited or absent in the arid regions of the world, particularly in the Arabian Peninsula. Additionally, the point rain measurements cannot represent the spatial rainfall field. GSPEs, with relatively fine spatio-temporal resolutions, introduce alternative means for estimating the precipitation intensity over the selected area of study. Therefore, the first step to maintain a reliable model for predicting future flash flood inundation scenarios is to detect the intensity of rainfall required to initiate the flooding process.

Validating GSPEs to acquire the spatiotemporal variation of rainfall introduces an optimistic alternative to the in-situ rain gauges. However, very few studies attempted to

validate the satellite precipitation in arid areas, especially over sub-daily and daily time scales at local watershed spatial details. The restriction of these studies was due to a lack of rain gauge measurements covering these areas, and the uncertainties associated with the space-borne precipitation estimates, particularly light ones. Moreover, these studies were mainly validated monthly, seasonally, and annually. GSPEs have to be investigated against reliable ground gauges' measurements for quantifying the uncertainties, followed by updating the developers by the drawbacks of their algorithms in order to improve rainfall estimations in these arid locations [102], [103]. Ground truth data from rain gauges and/or radar measurements are necessary to validate the GSPEs, but the majority of the Earth's land is ungauged or has limited in-situ measurements. This situation is worsening since the in-situ observation networks continue to decrease worldwide [103].

GSPEs are not always reliable, and consensus has been reached that they require the quantification of the deviation of the GSPEs from the reference datasets. The in-situ rain gauges' measurements are considered to be the primary reference data [52] to assess the reliability and accuracy of GSPEs. Tian et al. [53] assumed that the ground rain gauge records are error-free, where the associated biases considered much smaller than those in the GSPEs. Although there were many studies aimed at evaluating GSSEs, they were limited to specific regions, and quantifying the uncertainties in the GSPEs using statistical error models in the arid Arabian Peninsula has not been systematically investigated enough to date. The different performance of GSPEs makes it mandatory to determine whether a product is suitable for a specific environment or region.

The accuracy of a DEM in representing the land surface mainly depends on its source data's spatial resolution [104]. The more accurate the information, the higher the spatial resolution the DEM can have. A DEM's spatial resolution has been shown to affect the outcomes of many hydrological parameters [105]–[109]. Extracting channel networks from DEMs is mandatory in various hydrological [62] and geomorphological [63] studies. The DTMs have been applied successfully to extract different topographic, hydrologic, and geomorphometric parameters that contribute as the primary inputs to flood susceptibility modeling [110], [34]. Each DEM source has intrinsic errors due to data acquisition

technology and processing methodology with respect to specific terrains and land cover types [111]. Therefore, it was mandatory to evaluate the vertical accuracy of DEMs and the horizontal variability of its derived channel network/orders before involving them and their derivatives in the flood susceptibility models.

The regionalization techniques have been successful in transferring parameters from a calibrated catchment to a similar ungauged basin (i.e., has similar climatic, topographic, geologic, and land cover features to the ungauged basin). It used to transfer rainfall, runoff, and recharge data over the arid areas lacking adequate coverage of in-situ measurements [99], [112]–[114]. Precise LiDAR DTM datasets are still limited in most areas of the world due to the required extensive cost and labor work to collect them. Additionally, the catchment under study in the current research has a vast area (i.e., around 5000 km²). Therefore, the concept of regionalization was adopted as a mean to transfer evaluation results of the global DEMs between two similar catchments. Accurate LiDAR datasets were acquired from an area in the United States of America (USA) of similar topographic characteristics to my current study area, were selected to act as reference dataset to evaluate global DEMs and their derived drainage networks/orders.

Flood susceptibility mapping shows the inundation's likelihood of vulnerable areas depending on the intrinsic climatic, geomorphic, topographic, and hydrologic properties of a given area [30]. The local residents in the arid flood dangerous zones commonly tend to have a misinformed sense of being safe as a consequence of the long periods of time among flash flood events. In this respect, flood predictive susceptibility modeling can evaluate the past, current, and upcoming spatial flood dynamics [33] and quantify the hazard level of the susceptible regions [34]. There were some limitations to the previously defined flood susceptibility modeling. It is extremely challenging to obtain a reasonable flood inundation map from most of the countries in the Arabian Peninsula in order to validate predictive flood models. Conventional methods for generating flood inventory maps such as field work and topographic maps were not effective enough. It was only possible to collect a few points of representation of flood locations that were mostly located along the main valleys due to complex topography and the required extensive cost and effort [34], [96]. Additionally, the

previous researchers located non-flood points on the upstream areas of the complex topography, which did not represent the real spatial distribution of non-flood locations through the entire study areas. The use of an innovative approach to detect the flood extent was obligatory during the current study. The synthetic aperture Radar (SAR) sensors that can provide their illumination source, record data at both day and night, and penetrate cloud cover [115]–[117]. The current advances in these satellite sensors provide optimum means to monitor the extent of floods. Furthermore, volunteered geographic information (VGI) is a quickly growing data source for natural hazards research [118]. A vast amount of real-time ground data has become available as a result of rapid advancement in technology. Some authors used volunteered data in their studies about such hazardous events, particularly to estimate the extent of flood inundation [119]–[125]. The integration of these data with conventional ones introduces valuable information for mapping the extents of flash floods.

Many studies have been carried out on flash floods in the arid regions, but daily rainfall data were usually not considered in the different developed models [21], [95], [96], [126]. In addition, most of the previous authors collected flood locations from multiple past flood events. Sometimes, these authors used average yearly rainfall data that was not matched with a certain flood extent. With the rapidly changing global climate, it was critical to develop susceptibility models using a corresponding daily rainfall and related flood event to predict a future flood extent under a similar rainfall intensity to that prevailed during a past flood event. Even at low rainfall intensity (i.e., from less than 1 mm to 5 mm), it is possible to have multiple flood events in arid catchments [4]. The annual average precipitation data could not capture the dynamicity of the flash floods.

There is no agreement about the optimum number of conditioning factors required to generate an efficient flood susceptibility map [110], [127]. However, different studies recommend using more than six factors to avoid misidentifying flood-prone areas that could be affected by a single weight of a specific class and subsequent over-rating of the probability of certain contributing variables [128]. Selecting and testing non-collinear flood triggering factors needed a thorough understanding of the hydrogeomorphical characteristics, detailed

literature survey, and previous field experience in regions similar to the current study area in topography and climate.

Earth observation satellites and GIS techniques introduce valuable datasets and methods to detect susceptible areas to flash floods. Reliable and precise dynamic flood susceptibility maps can efficiently help the decision-makers and planners to develop their plans to reduce the costs, infrastructure damage, and human life threat associated with future flash floods. The current study overcame the limitations mentioned above, whereby it introduced an improved flood susceptibility modeling that included both spatial and temporal details. It employed corresponding flood inventory mapping and satellite-based rainfall data that contributed to the selected flood event. The achieved enhancement resulted in developing more accurate maps that can mimic the susceptible areas to future flood hazards over space and time at a similar rainfall intensity. The predictive flood maps can assist the planners and government authorities to deploy emergency plans to mitigate the negative impacts associated with potential flooding.

1.3. Research Objectives

The main goal of this research is to develop a model to detect and predict areas prone to flash floods at the local watershed scale of 12.5 m in the arid area of Ad Dakhiliyah Governate, the Sultanate of Oman. This overall objective was achieved through the integration of different geomorphological, hydrological, topographical, and climatological geospatial datasets derived from remote sensing sources. The specific objectives were to:

- 1) evaluate the performance of five daily and sub-daily ground satellite precipitation estimates (GSPEs) (i.e., Global Precipitation Mission-Integrated Multi-satellite Retrievals for the GPM (GPM-IMERG), and Global Satellite Mapping of Precipitation (GSMaP)), per different rainfall intensity classes, utilizing the in-situ rain gauge measurements over the selected watershed at the Sultanate of Oman. Next, to model the errors in these five daily GSPEs using statistical approaches.
- 2) develop a new pixel-based geometric assessment method of the spatial horizontal variability in the channel networks/orders derived from global spaceborne digital elevation models (DEMs) (i.e., Advanced Land Observing Satellite (ALOS) Phased Array type L-band SAR (PALSAR), Shuttle Radar Topography Mission (SRTM), and ALOS Panchromatic Remote-sensing Instrument for Stereo Mapping (PRISM)) at different area thresholds (ATs) and pixel buffer tolerance values (PBTVs). This objective also included: (i) pixel-based vertical evaluation of the elevation accuracies of satellite DEMs, (ii) determining which global DEM dataset would be closer in performance to the airborne LiDAR DTM or LiDAR DSM, and (iii) developing a new Python toolbox for ArcGIS to automate the previously-mentioned approaches.
- 3) develop improved flood susceptibility models using integrated bivariate and multivariate statistical methods to predict and classify the degree of hazard underlying the future flood-prone areas.

1.4. Research Challenges

There is insufficient availability of rain gauge datasets. In-situ rain gauge records are usually limited or absent in the Arid Arabian Peninsula. There is a poor coverage of the rain gauge networks over the desert and rugged mountainous areas occupy most of the Arabian Peninsula. Installing and maintenance of such rain gauge are costly and labor extensive.

There is a limited understanding of the responses of different wadis to flood inundation. Proper selection of the flood triggering factors and detecting their spatial association with flood inundation are the key steps in the geospatial flood predictive models.

Flow measurements are usually absent as a consequence of the devastating power of flash floods. In general, limited flow gauges are often located in the valleys' outlets across paths of different flash flood events, which cause the gauges to be ruined. As a consequence, many studies in the Arabian Peninsula have been carried out without flow measurements.

The remoteness, severe climate, and damaged roads inside wadis make it complicated and unsafe to measure and collect field data related to flood and non-flood locations. Field-based monitoring of flooded areas requires much time and effort, as well as it requires high degrees of safety and multiple precautions. In most of the cases, researchers can only monitor flood traces after the complete retreat of the flood water.

In natural hazards research, massive databases are often needed [93]. These data are not easy to collect, and in some cases, the lack of thereof can impede such research [94].

1.5. Thesis Structure

Figure 1.1 demonstrates the current Ph. D. thesis outlines. It comprises five chapters; each chapter has its detailed literature review included within the section of introduction and background.

In general, Chapter 1 introduces background information about flash floods occurrences, trigger factors, and negative consequences in the selected arid area for the current study. It also includes: (i) the problem statement outlined the past flood studies over the selected watershed, respective limitations, and the introduced solutions for addressing these concerns in the current research, (ii) overall and specific objectives, (iii) research challenges, and (iv) thesis outlines.

Chapter 2 shows information about the statistical evaluation of the performance of the five sub-daily and daily GSPEs. Additionally, it involves modeling the errors in these five GSPEs using statistical approaches.

Chapter 3 presents the development of a new pixel-based methodology to evaluate the horizontal accuracies of the channel networks/orders derived from three global DEMs based on LiDAR datasets. It also incorporates the assessment of the vertical accuracies of these global DEMs and the development of a new Python toolbox for ArcGIS to automate the introduced methods. This chapter helped select the DEM with the highest accuracy to be applied for deriving different spatial layers used in developing flood susceptibility models.

Chapter 4 introduces integrated bivariate and multivariate statistical approaches-based improved flood susceptibility models to predict future flood-prone areas at similar climatic and topographic conditions to those which dominated during the current models. It also includes the generation of flood inventory accuracy from SAR scenes and deriving flood conditioning factors from PALSAR DEM (12.5 m), as well as preparing soil and geologic maps.

Chapter 5 summarizes the concluding remarks of each objective, research contributions, and future work recommendations.

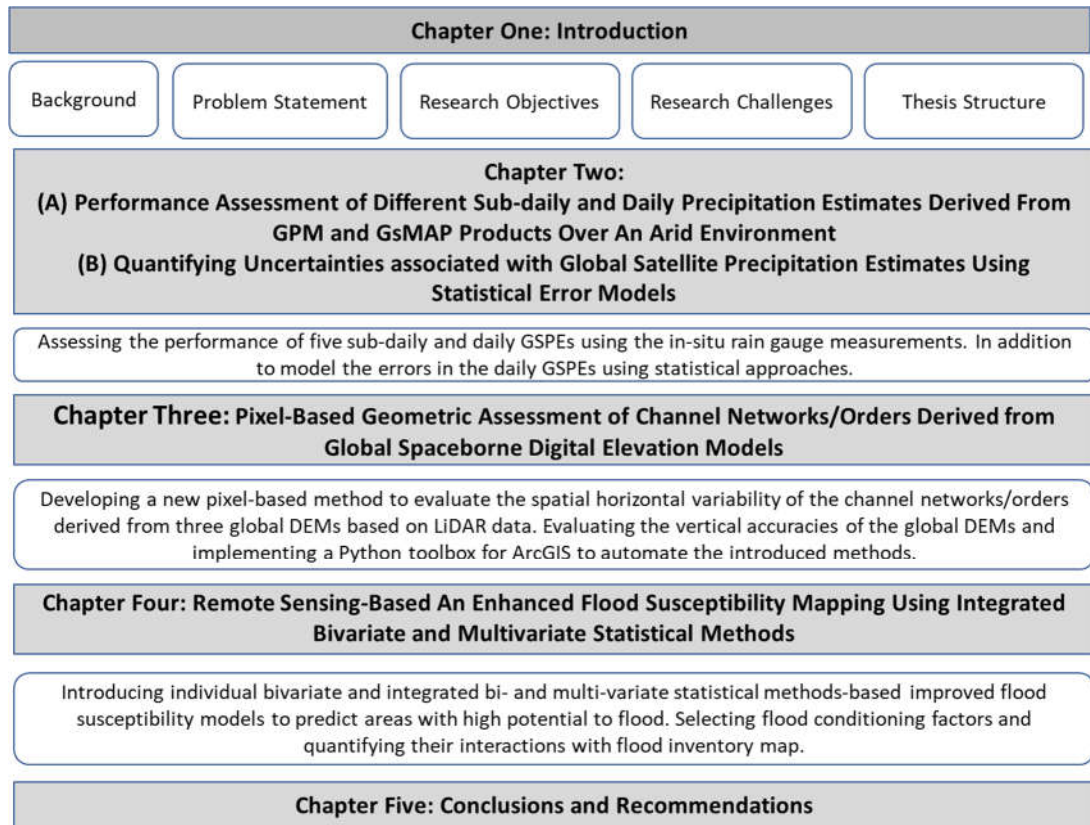


Figure 1.1. A schematic diagram shows the thesis outlines.

References

- [1] S. Vorogushyn, K. E. Lindenschmidt, H. Kreibich, H. Apel, and B. Merz, “Analysis of a detention basin impact on dike failure probabilities and flood risk for a channel-dike-floodplain system along the river Elbe, Germany,” *J. Hydrol.*, vol. 436–437, pp. 120–131, May 2012.
- [2] H. a P. Hapuarachchi, Q. J. Wang, and T. C. Pagano, “A review of advances in flash flood forecasting,” *Hydrol. Process.*, vol. 2784, no. 18, pp. 2771–2784, Aug. 2011.
- [3] M. S. El-sammany, “Forecasting of Flash Floods over Wadi Watier – Sinai Peninsula Using the Weather Research and Forecasting (WRF) Model,” *Int. J. Geol. Environ. Eng.*, vol. 4, no. 10, pp. 996–1000, 2010.
- [4] J. Cools *et al.*, “An early warning system for flash floods in hyper-arid Egypt,” *Nat. Hazards Earth Syst. Sci.*, vol. 12, no. 2, pp. 443–457, Feb. 2012.
- [5] X. Lin, “Flash floods in arid and semi-arid zones,” Paris, 1999.
- [6] H. Wheater, “Modeling Hydrological Processes in Arid and Semi Arid Areas,” in *Proceedings of the G-WADI International Modeling Workshop, Roorkee, India, p 39*, 2005, pp. 1689–1699.
- [7] A. Abdelkhalek, “Development of an early warning system for flash floods in wadi Watir – Sinai desert,” PhD thesis at Vrije Universiteit Brussel (VUB), Brussels, Belgium, 2011.
- [8] WMO, “Manual on flood forecasting and warning,” Geneva, 2011.
- [9] M. Borga, E. N. Anagnostou, G. Bloschl, and J. D. Creutin, “Flash flood forecasting, warning and risk management: The HYDRATE project,” *Environ. Sci. Policy*, vol. 14, no. 7, pp. 834–844, Nov. 2011.

- [10] A. P. Schick, T. Grodek, and J. Lekach, "Sediment management and flood protection of desert towns: effects of small catchments," *Hum. impact Eros. sedimentation. Proc. Int. Symp. Rabat, Morocco, 1997*, vol. 245, pp. 183–189, Jan. 1997.
- [11] R. Khatami and G. Mountrakis, "Implications of classification of methodological decisions in flooding analysis from Hurricane Katrina," *Remote Sens.*, vol. 4, no. 12, pp. 3877–3891, Dec. 2012.
- [12] K. E. Trenberth, "Changes in precipitation with climate change," *Clim. Res.*, vol. 47, no. 1–2, pp. 123–138, Dec. 2011.
- [13] FloodList, "Floods Across the Gulf Region – FloodList," 2013. [Online]. Available: <http://floodlist.com/asia/floods-across-the-gulf-region>. [Accessed: 19-Jan-2018].
- [14] FloodList, "6 Dead in Oman Floods – FloodList," 2014. [Online]. Available: <http://floodlist.com/asia/6-dead-flooding-oman>. [Accessed: 19-Jan-2018].
- [15] FloodList, "Floods Kill 7 People in Northern Oman – FloodList," 2015. [Online]. Available: <http://floodlist.com/asia/floods-kill-7-people-in-northern-oman>. [Accessed: 19-Jan-2018].
- [16] FloodList, "4 Killed in Flash Floods in Northern Oman – FloodList," 2015. [Online]. Available: <http://floodlist.com/asia/4-killed-in-flash-floods-in-northern-oman>. [Accessed: 19-Jan-2018].
- [17] FloodList, "Oman and UAE – Deadly Floods Hit After Torrential Rain – FloodList," 2017. [Online]. Available: <http://floodlist.com/asia/oman-uae-floods-december-2017>. [Accessed: 10-Jan-2018].
- [18] B. Merz, J. Hall, M. Disse, and A. Schumann, "Fluvial flood risk management in a changing world," *Nat. Hazards Earth Syst. Sci.*, vol. 10, no. 3, pp. 509–527, Mar. 2010.

- [19] Floodsite, “Floodsite: Frequently Asked Questions,” 2020. [Online]. Available: <http://www.floodsite.net/html/faq2.htm>. [Accessed: 30-May-2017].
- [20] E. Ghoneim and G. M. Foody, “Assessing flash flood hazard in an arid mountainous region,” *Arab. J. Geosci.*, vol. 6, no. 4, pp. 1191–1202, Sep. 2011.
- [21] A. H. A. Taha, E. H. Ibrahim, A. S. Shalaby, and M. Shawky, “Evaluation of geological hazards for landuse planning in Nabq protectorate, southeastern Sinai using GIS techniques,” *Int. J. Geosci.*, vol. 04, no. 04, pp. 816–836, Jul. 2013.
- [22] D. D. Konadu and C. Fosu, “Digital elevation models and GIS for watershed modelling and flood prediction – a case study of Accra Ghana,” in *Yanful E.K. (eds) Appropriate Technologies for Environmental Protection in the Developing World*, Springer, Dordrecht, 2009, pp. 325–332.
- [23] D. C. Mason, L. Giustarini, J. Garcia-Pintado, and H. L. Cloke, “Detection of flooded urban areas in high resolution Synthetic Aperture Radar images using double scattering,” *Int. J. Appl. Earth Obs. Geoinf.*, vol. 28, pp. 150–159, May 2014.
- [24] T. Bangira, B. H. P. Maathuis, T. Dube, and T. W. Gara, “Investigating flash floods potential areas using ASCAT and TRMM satellites in the Western Cape Province, South Africa,” *Geocarto Int.*, vol. 6049, no. 7, pp. 1–18, Aug. 2015.
- [25] J. Mashaly and E. Ghoneim, “Flash Flood Hazard Using Optical, Radar, and Stereo-Pair Derived DEM: Eastern Desert, Egypt,” *Remote Sens.*, vol. 10, no. 8, p. 1204, Aug. 2018.
- [26] S. M. Abuzied and B. M. H. Mansour, “Geospatial hazard modeling for the delineation of flash flood-prone zones in Wadi Dahab basin, Egypt,” *J. Hydroinformatics*, vol. 21, no. 1, pp. 180–206, Feb. 2019.
- [27] M. Abdulrazzak *et al.*, “Flash flood risk assessment in urban arid environment: case study of Taibah and Islamic universities’ campuses, Medina, Kingdom of Saudi

- Arabia,” *Geomatics, Nat. Hazards Risk*, vol. 10, no. 1, pp. 780–796, Jan. 2019.
- [28] E. Opolot, “Application of remote sensing and geographical information systems in flood management : a review,” *Res. J. Appl. Sci. Eng. Technol.*, vol. 6, no. 10, pp. 1884–1894, May 2013.
- [29] S. S. Durduran, “Coastline change assessment on water reservoirs located in the Konya Basin Area, Turkey, using multitemporal landsat imagery,” *Environ. Monit. Assess.*, vol. 164, no. 1–4, pp. 453–461, May 2010.
- [30] USGS, “What is a landslide hazard map?” [Online]. Available: https://www.usgs.gov/faqs/what-a-landslide-hazard-map?qt-news_science_products=0#qt-news_science_products. [Accessed: 07-Nov-2019].
- [31] V. Meyer, S. Scheuer, and D. Haase, “A multicriteria approach for flood risk mapping exemplified at the Mulde river, Germany,” *Nat. Hazards*, vol. 48, no. 1, pp. 17–39, May 2009.
- [32] J. Sanayl and X. Lu, “Application of remote sensing in flood management with special reference to Monsoon Asia: a review,” *Nat. Hazards*, vol. 33, no. 2, pp. 283–301, Oct. 2004.
- [33] M. Rahman *et al.*, “Flood susceptibility assessment in Bangladesh using machine learning and multi-criteria decision analysis,” *Earth Syst. Environ.*, vol. 3, no. 3, pp. 1–17, Oct. 2019.
- [34] D. Tien Bui *et al.*, “Flood spatial modeling in Northern Iran using remote sensing and GIS: a comparison between evidential belief functions and its ensemble with a multivariate logistic regression model,” *Remote Sens.*, vol. 11, no. 13, p. 1589, Jul. 2019.
- [35] L. A. Blacutt, D. L. Herdies, L. G. G. de Gonçalves, D. A. Vila, and M. Andrade, “Precipitation comparison for the CFSR, MERRA, TRMM3B42 and Combined

- Scheme datasets in Bolivia,” *Atmos. Res.*, vol. 163, pp. 117–131, Sep. 2015.
- [36] G. J. Huffman *et al.*, “The TRMM Multisatellite Precipitation Analysis (TMPA): Quasi-Global, Multiyear, Combined-Sensor Precipitation Estimates at Fine Scales,” *J. Hydrometeorol.*, vol. 8, no. 1, pp. 38–55, Feb. 2007.
- [37] T. Wagener, H. Gupta, S. Yatheendradas, D. Goodrich, C. Unkrich, and M. Schaffner, “Understanding sources of uncertainty in flash-flood forecasting for semi-arid regions,” in *IAHS-AISH Publication- International Symposium: Quantification and Reduction of Predictive Uncertainty for Sustainable Water Resources Management - 24th General Assembly of the International Union of Geodesy and Geophysics (IUGG)*, 2007, vol. 313, pp. 204–212.
- [38] H. Wu, R. F. Adler, Y. Tian, G. J. Huffman, H. Li, and J. Wang, “Real-time global flood estimation using satellite-based precipitation and a coupled land surface and routing model,” *Water Resour. Res.*, vol. 50, no. 3, pp. 2693–2717, Mar. 2014.
- [39] H. Wu, R. F. Adler, Y. Hong, Y. Tian, and F. Policelli, “Evaluation of Global Flood Detection Using Satellite-Based Rainfall and a Hydrologic Model,” *J. Hydrometeorol.*, vol. 13, no. 4, pp. 1268–1284, Aug. 2012.
- [40] Y. Li, X. Zhu, Y. Pan, J. Gu, A. Zhao, and X. Liu, “A comparison of model-assisted estimators to infer land cover/use class area using satellite imagery,” *Remote Sens.*, vol. 6, no. 9, pp. 8904–8922, Sep. 2014.
- [41] C. Kidd, D. R. Kniveton, M. C. Todd, and T. J. Bellerby, “Satellite Rainfall Estimation Using Combined Passive Microwave and Infrared Algorithms,” *J. Hydrometeorol.*, vol. 4, no. 6, pp. 1088–1104, Dec. 2003.
- [42] S. Sorooshian, K. L. Hsu, X. Gao, H. V. Gupta, B. Imam, and D. Braithwaite, “Evaluation of PERSIANN system satellite-based estimates of tropical rainfall,” *Bull. Am. Meteorol. Soc.*, vol. 81, no. 9, pp. 2035–2046, Sep. 2000.

- [43] J. G. Huffman *et al.*, “Global precipitation at one-degree daily resolution from multisatellite observations,” *J. Hydrometeorol.*, vol. 2, pp. 36–50, 1997.
- [44] B. Alhammoud, C. Claud, B. Funatsu, K. Béranger, and J.-P. Chaboureau, “Patterns of Precipitation and Convection Occurrence over the Mediterranean Basin Derived from a Decade of Microwave Satellite Observations,” *Atmosphere (Basel)*, vol. 5, no. 2, pp. 370–398, May 2014.
- [45] E. De Coning and E. Poolman, “South African Weather Service operational satellite based precipitation estimation technique: Applications and improvements,” *Hydrol. Earth Syst. Sci.*, vol. 15, no. 4, pp. 1131–1145, Apr. 2011.
- [46] A. Y. Hou *et al.*, “The Global Precipitation Measurement Mission,” *Bull. Am. Meteorol. Soc.*, vol. 95, no. 5, pp. 701–722, May 2014.
- [47] K. O. Asante, R. D. Macuacua, G. A. Artan, R. W. Lietzow, and J. P. Verdin, “Developing a flood monitoring system from remotely sensed data for the Limpopo basin,” *IEEE Trans. Geosci. Remote Sens.*, vol. 45, no. 6, pp. 1709–1714, Jun. 2007.
- [48] A. S. Gebregiorgis and F. Hossain, “How well can we estimate error variance of satellite precipitation data around the world?,” *Atmos. Res.*, vol. 154, pp. 39–59, Mar. 2015.
- [49] T. Cohen Liechti, J. P. Matos, J. L. Boillat, and A. J. Schleiss, “Comparison and evaluation of satellite derived precipitation products for hydrological modeling of the Zambezi River Basin,” *Hydrol. Earth Syst. Sci.*, vol. 16, no. 2, pp. 489–500, Feb. 2012.
- [50] M. Pan, H. Li, and E. Wood, “Assessing the skill of satellite-based precipitation estimates in hydrologic applications,” *Water Resour. Res.*, vol. 46, no. 9, p. W09535, Sep. 2010.
- [51] W. Gumindoga, T. H. M. Rientjes, A. T. Haile, H. Makurira, and P. Reggiani, “Bias

- correction schemes for CMORPH satellite rainfall estimates in the Zambezi River Basin,” *Hydrol. Earth Syst. Sci. Discuss.*, vol. 23, no. 7, pp. 1–36, Jul. 2016.
- [52] H. A. Bhatti, T. Rientjes, A. T. Haile, E. Habib, and W. Verhoef, “Evaluation of bias correction method for satellite-based rainfall data,” *Sensors*, vol. 16, no. 6, Jun. 2016.
- [53] Y. Tian *et al.*, “Modeling errors in daily precipitation measurements: Additive or multiplicative?,” *Geophys. Res. Lett.*, vol. 40, no. 1–6, pp. 2060–2065, Mar. 2013.
- [54] W. F. Krajewski, G. J. Ciach, J. R. McCollum, and C. Bacotiu, “Initial Validation of the Global Precipitation Climatology Project Monthly Rainfall over the United States,” *J. Appl. Meteorol.*, vol. 39, no. 7, pp. 1071–1086, Jul. 2000.
- [55] D. F. (David F. Maune and American Society for Photogrammetry and Remote Sensing., *Digital elevation model technologies and applications : the DEM users manual*. 2001.
- [56] T. H. Tarekegn, A. T. Haile, T. Rientjes, P. Reggiani, and D. Alkema, “Assessment of an ASTER-generated DEM for 2D hydrodynamic flood modeling,” *Int. J. Appl. Earth Obs. Geoinf.*, vol. 12, no. 6, pp. 457–465, Jun. 2010.
- [57] A. Casas, G. Benito, V. R. Thorndycraft, and M. Rico, “The topographic data source of digital terrain models as a key element in the accuracy of hydraulic flood modelling,” *Earth Surf. Process. Landforms*, vol. 31, no. 4, pp. 444–456, Apr. 2006.
- [58] J. Li and D. W. S. Wong, “Effects of DEM sources on hydrologic applications,” *Comput. Environ. Urban Syst.*, vol. 34, no. 3, pp. 251–261, May 2010.
- [59] A. A. Jarihani, J. N. Callow, T. R. McVicar, T. G. Van Niel, and J. R. Larsen, “Satellite-derived Digital Elevation Model (DEM) selection, preparation and correction for hydrodynamic modelling in large, low-gradient and data-sparse catchments,” *J. Hydrol.*, vol. 524, pp. 489–506, May 2015.

- [60] A. R. Ghumman, I. S. Al-Salamah, S. S. AlSaleem, and H. Haider, "Evaluating the impact of lower resolutions of digital elevation model on rainfall-runoff modeling for ungauged catchments," *Environ. Monit. Assess.*, vol. 189, no. 2, p. 54, Feb. 2017.
- [61] B. Purinton and B. Bookhagen, "Validation of digital elevation models (DEMs) and comparison of geomorphic metrics on the southern Central Andean Plateau," *Earth Surf. Dyn.*, vol. 5, no. 2, pp. 211–237, Apr. 2017.
- [62] W. Yang, K. Hou, F. Yu, Z. Liu, and T. Sun, "A novel algorithm with heuristic information for extracting drainage networks from raster DEMs," *Hydrol. Earth Syst. Sci. Discuss.*, vol. 7, no. 1, pp. 441–459, Jan. 2010.
- [63] J. F. O'Callaghan and D. M. Mark, "The extraction of drainage networks from digital elevation data," *Comput. Vision, Graph. Image Process.*, vol. 28, no. 3, p. 247, Dec. 1984.
- [64] A. Omran, S. Dietrich, A. Abouelmagd, and M. Michael, "New ArcGIS tools developed for stream network extraction and basin delineations using Python and java script," *Comput. Geosci.*, vol. 94, pp. 140–149, Sep. 2016.
- [65] M. Y. E. Angillieri, "Morphometric characterization of the Carrizal basin applied to the evaluation of flash floods hazard, San Juan, Argentina," *Quat. Int.*, vol. 253, pp. 74–79, Mar. 2012.
- [66] W. S. Walker, J. M. Kellndorfer, and L. E. Pierce, "Quality assessment of SRTM C- and X-band interferometric data: Implications for the retrieval of vegetation canopy height," *Remote Sens. Environ.*, vol. 106, no. 4, pp. 428–448, Feb. 2007.
- [67] C. A. Baugh, P. D. Bates, G. Schumann, and M. A. Trigg, "SRTM vegetation removal and hydrodynamic modeling accuracy," *Water Resour. Res.*, vol. 49, no. 9, pp. 5276–5289, Sep. 2013.
- [68] G. Kocak, G. Buyuksalih, and K. Jacobsen, "Analysis of digital elevation models

- determined by high resolution space images,” *Int. Arch. Photogramm. Remote Sens.*, vol. 35 (B4), p. 636–641, 2004.
- [69] A. Vianello, M. Cavalli, and P. Tarolli, “LiDAR-derived slopes for headwater channel network analysis,” *Catena*, vol. 76, no. 2, pp. 97–106, Jan. 2009.
- [70] N. Thommeret, J. S. Bailly, and C. Puech, “Extraction of thalweg networks from DTMs: Application to badlands,” *Hydrol. Earth Syst. Sci.*, vol. 14, no. 8, pp. 1527–1536, Aug. 2010.
- [71] D. Godone and G. Garnero, “The role of morphometric parameters in Digital Terrain Models interpolation accuracy: A case study,” *Eur. J. Remote Sens.*, vol. 46, no. 1, pp. 198–214, Jan. 2013.
- [72] B. Höfle, L. Griesbaum, and M. Forbriger, “GIS-Based detection of gullies in terrestrial lidar data of the cerro llamoca peatland (peru),” *Remote Sens.*, vol. 5, no. 11, pp. 5851–5870, Nov. 2013.
- [73] W.-T. T. Lin, W.-C. C. Chou, C.-Y. Y. Lin, P.-H. H. Huang, and J.-S. S. Tsai, “Automated suitable drainage network extraction from digital elevation models in Taiwan’s upstream watersheds,” *Hydrol. Process.*, vol. 20, no. 2, pp. 289–306, Feb. 2006.
- [74] M. Cavalli, S. Trevisani, B. Goldin, E. Mion, S. Crema, and R. Valentinotti, “Semi-automatic derivation of channel network from a high-resolution DTM: The example of an italian alpine region,” *Eur. J. Remote Sens.*, vol. 46, no. 1, pp. 152–174, Feb. 2013.
- [75] P. Passalacqua, T. Do Trung, E. Foufoula-Georgiou, G. Sapiro, and W. E. Dietrich, “A geometric framework for channel network extraction from lidar: Nonlinear diffusion and geodesic paths,” *J. Geophys. Res.*, vol. 115, no. F1, p. F01002, Mar. 2010.

- [76] J. P. Wilson and J. C. Gallant, *Terrain analysis : principles and applications*. Wiley, 2000.
- [77] J. F. Parrot and C. Ramírez Núñez, “Artefactos y correcciones a los modelos digitales de Terreno provenientes del LiDAR,” *Investig. Geogr.*, vol. 2016, no. 90, pp. 28–39, Oct. 2016.
- [78] P. Yang *et al.*, “What is the effect of LiDAR-derived DEM resolution on large-scale watershed model results?,” *Environ. Model. Softw.*, vol. 58, pp. 48–57, Aug. 2014.
- [79] J. Roelens, I. Rosier, S. Dondeyne, J. Van Orshoven, and J. Diels, “Extracting drainage networks and their connectivity using LiDAR data,” *Hydrol. Process.*, vol. 32, no. 8, pp. 1026–1037, Apr. 2018.
- [80] F. Cazorzi, G. D. Fontana, A. De Luca, G. Sofia, and P. Tarolli, “Drainage network detection and assessment of network storage capacity in agrarian landscape,” *Hydrol. Process.*, vol. 27, no. 4, pp. 541–553, Feb. 2013.
- [81] F. Altaf, G. Meraj, and S. A. Romshoo, “Morphometric analysis to infer hydrological behavior of Lidder watershed, western Himalaya, India,” *Geogr. J.*, vol. 2013, p. 14, Apr. 2013.
- [82] S. Bhatt and S. A. Ahmed, “Morphometric analysis to determine floods in the Upper Krishna basin using Cartosat DEM,” *Geocarto Int.*, vol. 29, no. 8, pp. 878–894, 2014.
- [83] M. M. El Osta and M. H. Masoud, “Implementation of a hydrologic model and GIS for estimating Wadi runoff in Dernah area, Al Jabal Al Akhadar, NE Libya,” *J. African Earth Sci.*, vol. 107, pp. 36–56, Jul. 2015.
- [84] S. Abuzied, M. Yuan, S. Ibrahim, M. Kaiser, and T. Saleem, “Geospatial risk assessment of flash floods in Nuweiba area, Egypt,” *J. Arid Environ.*, vol. 133, pp. 54–72, Oct. 2016.

- [85] R. Kannan, S. Venkateswaran, M. Vijay Prabhu, and K. Sankar, "Drainage morphometric analysis of the Nagavathi watershed, Cauvery river basin in Dharmapuri district, Tamil Nadu, India using SRTM data and GIS," *Data Br.*, vol. 19, pp. 2420–2426, Aug. 2018.
- [86] N. Hassan Syed, A. Adbul Rehman, D. Hussain, S. Ishaq, and A. Ahmed Khan, "Morphometric analysis to prioritize sub-watershed for flood risk assessment in Central Karakoram National Park using GIS / RS approach," in *ISPRS Annals of the Photogrammetry, Remote Sensing and Spatial Information Sciences, Volume IV-4/W4*, 2017, vol. IV, pp. 14–15.
- [87] C. S. Jahan, M. F. Rahaman, R. Arefin, S. Ali, and Q. H. Mazumder, "Morphometric analysis and hydrological inference for water resource management in Atrai-Sib river basin, NW Bangladesh using remote sensing and GIS technique," *J. Geol. Soc. India*, vol. 91, no. 5, pp. 613–620, May 2018.
- [88] P. Kumar, R. Rajeev, S. Chandel, V. Narayan, and M. Prafull, "Hydrological inferences through morphometric analysis of lower Kosi river basin of India for water resource management based on remote sensing data," *Appl. Water Sci.*, vol. 8, no. 1, pp. 1–16, Mar. 2018.
- [89] P. Lin, Z. He, J. Du, L. Chen, X. Zhu, and J. Li, "Recent changes in daily climate extremes in an arid mountain region, a case study in northwestern China's Qilian Mountains," *Sci. Rep.*, vol. 7, no. 1, May 2017.
- [90] M. H. I. Dore, "Climate change and changes in global precipitation patterns: What do we know?," *Environ. Int.*, vol. 31, no. 8, pp. 1167–1181, Oct. 2005.
- [91] R. P. Allan and B. J. Soden, "Atmospheric Warming and the Amplification of Precipitation Extremes," *Science*, vol. 321, no. 5895, pp. 1481–1484, Jul. 2008.
- [92] Z. Şen *et al.*, "Flash flood inundation map preparation for wadis in arid regions,"

Arab. J. Geosci., vol. 6, no. 9, pp. 3563–3572, Jul. 2012.

- [93] A. D. Regmi, K. Yoshida, M. R. Dhital, and B. Pradhan, “Weathering and mineralogical variation in gneissic rocks and their effect in Sangrumba landslide, East Nepal,” *Environ. Earth Sci.*, vol. 71, no. 6, pp. 2711–2727, 2014.
- [94] Y. B. Liu and F. De Smedt, “Flood modeling for complex terrain using GIS and remote sensed information,” *Water Resour. Manag.*, vol. 19, no. 5, pp. 605–624, Oct. 2005.
- [95] S. H. Mahmoud and A. A. Alazba, “Towards a sustainable capital city: an approach for flood management and artificial recharge in naturally water-scarce regions, Central Region of Saudi Arabia,” *Arab. J. Geosci.*, vol. 9, no. 2, p. 92, Jul. 2016.
- [96] A. M. Youssef, B. Pradhan, and S. A. Sefry, “Flash flood susceptibility assessment in Jeddah city (Kingdom of Saudi Arabia) using bivariate and multivariate statistical models,” *Environ. Earth Sci.*, vol. 75, no. 1, p. 12, Dec. 2016.
- [97] A. M. Youssef, S. a. Sefry, B. Pradhan, and E. A. Alfadail, “Analysis on causes of flash flood in Jeddah city (Kingdom of Saudi Arabia) of 2009 and 2011 using multi-sensor remote sensing data and GIS,” *Geomatics, Nat. Hazards Risk*, vol. 5705, no. 3, pp. 1–25, May 2015.
- [98] M. El Maghraby, M. Masoud, and B. Niyazi, “Assessment of surface runoff in arid, data scarce regions; an approach applied in Wadi Al Hamd, Al Madinah Al Munawarah, Saudi Arabia,” *Life Sci. J.*, vol. 11, no. 4, pp. 271–289, Jan. 2014.
- [99] A. Milewski *et al.*, “A remote sensing solution for estimating runoff and recharge in arid environments,” *J. Hydrol.*, vol. 373, no. 1–2, pp. 1–14, Jun. 2009.
- [100] J. D. Giraldo Osorio and S. Gabriela García galiano, “Development of a sub-pixel analysis method applied to dynamic monitoring of floods,” *Int. J. Remote Sens.*, vol. 33, no. 7, pp. 2277–2295, Dec. 2012.

- [101] J. Roman, R. Knuteson, S. Ackerman, and H. Revercomb, "Predicted Changes in the Frequency of Extreme Precipitable Water Vapor Events," *J. Clim.*, vol. 28, no. 18, pp. 1753–1754, Sep. 2015.
- [102] M. Tan, A. Ibrahim, Z. Duan, A. Cracknell, and V. Chaplot, "Evaluation of Six High-Resolution Satellite and Ground-Based Precipitation Products over Malaysia," *Remote Sens.*, vol. 7, no. 2, pp. 1504–1528, Jan. 2015.
- [103] T. Dinku, P. Ceccato, E. Grover-Kopec, M. Lemma, S. J. Connor, and C. F. Ropelewski, "Validation of satellite rainfall products over East Africa's complex topography," *Int. J. Remote Sens.*, vol. 28, no. 7, pp. 1503–1526, Apr. 2008.
- [104] W. Shi, B. Wang, and Y. Tian, "Accuracy analysis of digital elevation model relating to spatial resolution and terrain slope by bilinear interpolation," *Math. Geosci.*, vol. 46, no. 4, pp. 445–481, Jan. 2014.
- [105] K. Lin, Q. Zhang, and X. Chen, "An evaluation of impacts of DEM resolution and parameter correlation on TOPMODEL modeling uncertainty," *J. Hydrol.*, vol. 394, no. 3–4, pp. 370–383, Nov. 2010.
- [106] S. Lin *et al.*, "Effect of DEM resolution on SWAT outputs of runoff, sediment and nutrients," *Hydrol. Earth Syst. Sci. Discuss.*, vol. 7, no. 4, pp. 4411–4435, Jul. 2010.
- [107] B. F. Sanders, "Evaluation of on-line DEMs for flood inundation modeling," *Adv. Water Resour.*, vol. 30, no. 8, pp. 1831–1843, Aug. 2007.
- [108] S. Sarachi, K. Hsu, and S. Sorooshian, "A statistical model for the uncertainty analysis of satellite precipitation products," *J. Hydrometeorol.*, vol. 16, no. 5, pp. 2101–2117, Aug. 2015.
- [109] S. Saksena and V. Merwade, "Incorporating the effect of DEM resolution and accuracy for improved flood inundation mapping," *J. Hydrol.*, vol. 530, pp. 180–194, Apr. 2015.

- [110] M. Shafapour Tehrany, L. Kumar, M. Neamah Jebur, and F. Shabani, “Evaluating the application of the statistical index method in flood susceptibility mapping and its comparison with frequency ratio and logistic regression methods,” *Geomatics, Nat. Hazards Risk*, vol. 10, no. 1, pp. 79–101, Jan. 2019.
- [111] S. Mukherjee, P. K. Joshi, S. Mukherjee, A. Ghosh, R. D. Garg, and A. Mukhopadhyay, “Evaluation of vertical accuracy of open source digital elevation model (DEM),” *Int. J. Appl. Earth Obs. Geoinf.*, vol. 21, pp. 205–217, Apr. 2012.
- [112] X. Yang, J. Magnusson, and C. Y. Xu, “Transferability of regionalization methods under changing climate,” *J. Hydrol.*, vol. 568, pp. 67–81, Jan. 2019.
- [113] G. Krebs, T. Kokkonen, H. Setälä, and H. Koivusalo, “Parameterization of a Hydrological Model for a Large, Ungauged Urban Catchment,” *Water*, vol. 8, no. 10, p. 443, Oct. 2016.
- [114] J.-H. Song, Y. Her, K. Suh, M.-S. Kang, and H. Kim, “Regionalization of a Rainfall-Runoff Model: Limitations and Potentials,” *Water*, vol. 11, no. 11, p. 2257, Oct. 2019.
- [115] B. Pradhan, U. Hagemann, M. Shafapour Tehrany, and N. Prechtel, “An easy to use ArcMap based texture analysis program for extraction of flooded areas from TerraSAR-X satellite image,” *Comput. Geosci.*, vol. 63, pp. 34–43, Feb. 2014.
- [116] K. Auynirundronkool, N. Chen, C. Peng, C. Yang, J. Gong, and C. Silapathong, “Flood detection and mapping of the Thailand Central plain using RADARSAT and MODIS under a sensor web environment,” *Int. J. Appl. Earth Obs. Geoinf.*, vol. 14, no. 1, pp. 245–255, Feb. 2012.
- [117] L. Giustarini *et al.*, “Assimilating SAR-derived water level data into a hydraulic model: A case study,” *Hydrol. Earth Syst. Sci.*, vol. 15, no. 7, pp. 2349–2365, Jul. 2011.
- [118] M. F. Goodchild, “Citizens as sensors: the world of volunteered geography,”

GeoJournal, vol. 69, no. 4, pp. 211–221, Nov. 2007.

- [119] J. P. Albuquerque, B. Herfort, A. Brenning, and A. Zipf, “A geographic approach for combining social media and authoritative data towards identifying useful information for disaster management,” *Int. J. Geogr. Inf. Sci.*, vol. 29, no. 4, pp. 1–23, Apr. 2015.
- [120] F. E. A. Horita, J. P. de Albuquerque, L. C. Degrossi, E. M. Mendiondo, and J. Ueyama, “Development of a spatial decision support system for flood risk management in Brazil that combines volunteered geographic information with wireless sensor networks,” *Comput. Geosci.*, vol. 80, pp. 84–94, Jul. 2015.
- [121] M. H. Faizal, Z. A. Latiff, and M. A. M. Iskandar, “A study of volunteered geographic information (VGI) assessment methods for flood hazard mapping: a review,” *J. Teknol.*, vol. 75, no. 10, pp. 127–134, Aug. 2015.
- [122] E. Schnebele and G. Cervone, “Improving remote sensing flood assessment using volunteered geographical data,” *Nat. Hazards Earth Syst. Sci.*, vol. 13, no. 3, pp. 669–677, Mar. 2013.
- [123] E. Schnebele, G. Cervone, S. Kumar, and N. Waters, “Real time estimation of the calgary floods using limited remote sensing data,” *Water*, vol. 6, no. 2, pp. 381–398, Mar. 2014.
- [124] M. Erskine and D. G. Gregg, “Utilizing volunteered geographic information to develop a real-time disaster mapping tool : A prototype and research framework,” in *International Conference on Information Resources Management*, 2012, pp. 1–14.
- [125] K. McDougall, “Using volunteered information to map the Queensland floods,” in *Proceedings of the Surveying and Spatial Sciences Conference*, 2011, no. November, pp. 13–23.
- [126] H. Alhasanat, “Flash Flood Assessment for Wadi Mousa City-Jordan,” *Procedia Econ. Financ.*, vol. 18, pp. 675–683, Dec. 2014.

- [127] K. Khosravi, H. R. Pourghasemi, K. Chapi, and M. Bahri, "Flash flood susceptibility analysis and its mapping using different bivariate models in Iran: a comparison between Shannon's entropy, statistical index, and weighting factor models," *Environ. Monit. Assess.*, vol. 188, no. 12, p. 656, Dec. 2016.
- [128] S. H. Mahmoud and T. Y. Gan, "Multi-criteria approach to develop flood susceptibility maps in arid regions of Middle East," *J. Clean. Prod.*, vol. 196, pp. 216–229, Jun. 2018.

CHAPTER TWO

(2A) PERFORMANCE ASSESSMENT OF SUB-DAILY AND DAILY GPM AND GSMaP PRODUCTS OVER AN ARID ENVIRONMENT

(2B) QUANTIFYING UNCERTAINTIES ASSOCIATED WITH DIFFERENT GLOBAL SATELLITE PRECIPITATION ESTIMATES USING STATISTICAL ERROR MODELS

The validation part can be found in:

M. Shawky, A. Moussa, Q. K. Hassan, and N. El-Sheimy, "Performance assessment of sub-daily and daily precipitation estimates derived from GPM and GSMaP products over an arid environment," *Remote Sens.*, vol. 11, no. 23, 2019.

Abstract

Precipitation is a critical variable for comprehending various climate-related research, such as water resources management, flash flood monitoring and forecasting, climatic analyses, and hydrogeological studies, etc. Here, the current objective was to evaluate the rainfall estimates obtained from Global Precipitation Mission (GPM), and Global Satellite Mapping of Precipitation (GSMaP) constellation over an arid environment like the Sultanate of Oman that is characterized by complex topography and extremely variable rainfall patterns. Global Satellite-based Precipitation Estimates (GSPEs) can provide wide coverage and high spatial and temporal resolutions, but evaluating their accuracy is a mandatory step before involving them in different hydrological applications. In this paper, the reliability of the Integrated Multi-satellitE Retrievals for the GPM (IMERG) V04 and GSMaP V06 products were evaluated using the reference in-situ rain gauges at sub-daily (e.g., 6, 12, and 18 h) and daily time scales during the period of March 2014–December 2016. A set of continuous difference statistical indices (e.g., mean absolute difference, root mean square error, mean difference, and unconditional bias), and categorical metrics (e.g., probability of detection, critical success index, false alarm ratio, and frequency bias index) were used to evaluate recorded precipitation occurrences. The results showed that the five GSPEs could generally delineate the spatial and temporal patterns of rainfall while they might have over- and under-estimations of in-situ gauge measurements. The overall quality of the GSMaP runs was superior to the IMERG products; however, it also encountered an exaggeration in case of light rain and an underestimation for heavy rain. The effects of the gauge calibration algorithm (GCA) used in the final IMERG (IMERG-F) were investigated by comparison with early and late runs. The IMERG-F V04 product did not show a significant improvement over the early (i.e., after 4 h of rainfall observations) and late (i.e., after 12 h of rainfall observations) products. The results indicated that GCA could not reduce the missed precipitation records considerably. The statistical additive and multiplicative schemes mostly succeed in modeling the errors in the daily GSPEs. However, the additive approach was more effective than multiplicative one in quantifying the uncertainties associated with GSPEs at different classified rainfall intensities. GSMaP

products behaved better than the IMERG run based on using the error models. IMERG-F showed better performance than other IMERG estimates.

(2A) PERFORMANCE ASSESSMENT OF SUN-DAILY AND DAILY GPM AND GSMaP PRODUCTS OVER AN ARID ENVIRONMENT

2A.1. Introduction and Background

Precipitation is one of the key components of the water cycle that is crucial to study the hydrological balance, water resources management, drought monitoring, flood forecasting, as well as critical social and climatological issues [1]. However, quantifying precipitation is complicated because it has a high variability, even at a small scale [1], [2]. In general, direct surface rain observations from in-situ gauges and indirect measurements through optical and microwave satellites or weather Radars are the currently available data sources to estimate the precipitation rates. The ground rainfall gauges are used to measure rainfall flux directly and determine its rate in a small area [3]. They can capture continuous measurements at high temporal frequencies. However, traditional point rain gauges cannot capture the areal representation and variation of rainfall, especially in regions where the in-situ rain gauges are limited in number and coverage [3]. Even if rain gauge network measurements are interpolated, they yield a uniform rainfall field that does not represent the real spatial and temporal rainfall variability [4]. Furthermore, the operation of rain gauges is costly, and in most cases, they are sparsely distributed or unavailable in remote areas due to difficulties of access for installation and maintenance [5]. The latter case has been escalated over the arid Gulf countries. Ground weather Radars can gain information about the internal structure of storms and provide real-time high-resolution monitoring of precipitation over vast areas [6]. However, they are also unavailable or not dense enough over most regions of the world.

The shortcomings of the previously-mentioned ground-based methods to measure precipitation highlighted the need for the global coverage of the Earth observation satellites [7]. Over the last few decades, different Global Satellite-based Precipitation Estimates (GSPEs) were made available from multiple international organizations allowing high-quality rainfall monitoring at fine spatial and temporal resolutions. Nowadays, a new

generation of GSPEs is being made available to ensure frequent and continuous rainfall monitoring.

The GSPEs are usually used to identify the spatial extent and magnitude of the rainfall events, especially the extreme ones [8]. Their advantages were outlined by Gebregiorgis and Hossain [9], such as: (i) overcoming the problem of geopolitical boundaries, (ii) covering continents and oceans, (iii) producing consecutive records at day and night, (iv) introducing a cost-effective way comparing to in-situ networks, and (v) delivering the data in a near-real-time, which would be critical to some applications such as monitoring and forecasting of flash flooding events.

GSPEs involve indirect blended precipitation estimates from Geosynchronous Infrared (GEO-IR)- and Low Earth Orbit-Passive Microwave (LEO-PMW)-based sensors [10]. The GEO-IR satellite data identifies the cloud-top characteristics that have an indirect relationship with the rainfall rate. Additionally, they cannot record rainfall from warm clouds. The LEO-PMW estimates can be profoundly affected by the ice particles or droplets associated with rainfall. They are less frequent than GEO-IR estimates and have poor spatial resolutions. Furthermore, they encounter significant sampling errors, particularly when comparing to the short-term rainfall measurements. Therefore, blending the LEO-PMW and GEO-IR satellite data to generate the new versions of GSPEs helped to gain improved rainfall estimates.

Weather satellites, despite uncertainties in their estimates, can monitor the rainfall at effective spatial and temporal resolutions. Their effective spatial and temporal coverage allows satellite sensors to generate information at regular intervals [3], [11]–[13]. GSPEs are usually unable to provide estimates that are entirely similar to the gauge measurements in both temporal and spatial scales [14]. The uncertainties (i.e., non-negligible errors) associated with GSPEs introduce a significant challenge for the end-users to apply these data in practical meteorological and hydrological applications [15]. Therefore, the nature and magnitude of these errors must be thoroughly evaluated and determined to take better advantage of GSPEs' products. Quantifying the level of uncertainty in different GSPEs can

be helpful for data producers to improve their algorithms and for the end-users to verify the accuracy of these products before utilizing them in a specific application [9].

Dedicated efforts have been made by different researchers to evaluate the performance of various GSPEs. Many authors have studied different runs of Global Precipitation Mission-based Integrated Multi-satellite Retrievals (GPM-IMERG) over different climatic zones in many parts of the world. The annual and seasonal average precipitation of daily re-sampled Global Satellite Mapping of Precipitation, i.e., GSMaP V06 ($0.25^\circ \times 0.25^\circ$) product, capture a more accurate spatial rainfall pattern than the IMERG-Final, i.e., IMERG-F V03 and V04 for most regions of China [16]. Despite the GSMaP-Gauge, i.e., GSMaP-G V07 overestimated light rainfall and underestimated heavy rain, its overall quality still slightly outperformed the IMERG V04 and V05 over east and south China [17]. Besides, the performance of the calibrated IMERG V05 did not have a significant improvement over that of IMERG V04 [17].

Milewski et al. [18] assessed the GPM predecessor, i.e., Tropical Rainfall Measuring Mission (TRMM) Multi-satellite Precipitation Analysis (TMPA products) using a rain gauge network in northern Morocco. They found that TMPA 3B42 V7 was the most spatially consistent with the rain gauge measurements. Additionally, all four products showed overestimations across this arid environment. Monthly GSMaP Moving Vector with Kalman filter, i.e., GSMaP-MVK V06 had slightly superior performance to V06 datasets over Pakistan [19]. At daily and monthly timescales, the IMERG V04 was considered as the most suitable IMERG version to detect precipitation estimates over the extreme arid region in Pakistan. Furthermore, the daily GSMaP-G V06 had superior performance with respect to IMERG V05 and TMPA V06 in all areas and all precipitation thresholds in Brazil [20]. Mahmoud et al. [21] evaluated the daily performance of the early, late, and final GPM-IMERG over entire Saudi Arabia using 1455 measurements from in the Sultanate of Oman. They evaluated the 189 in-situ rain gauges from October 2015 to April 2016. The early and late IMERG (i.e., IMERG-E and IMERG-L) products performed well in some parts of Saudi Arabia, but the IMERG-F run had better performance than both. Moreover, Mahmoud et al. [22] evaluated the spatiotemporal performance of three daily GPM-IMERG runs over the

entire area of the United Arab Emirates (UAE) (i.e., 83,600 km²) using 1610 rainy events from January 2015 to December 2017. They interpolated rainy measurements when at least 30 in-situ rain gauge stations had records across the entire UAE on the same day. They mentioned that IMERG-F had the highest agreement with the ground measurements. Utilizing observations from 53 ground gauges from 2003–2010 over the entire UAE, Wehbe et al. [23] stated that the daily TMPA 3B42 V06 (0.25°) had a higher agreement with gauge measurements than daily Climate Prediction Center MORPHing technique (CMORPH) product (0.25°).

In the Sultanate of Oman (i.e., the selected study area), water resources are scarce [24]. The primary source of surface and sub-surface water is the rainfall, and complex mountains (400 m–3000 m above sea level [25]) act as water towers [26]. The spatiotemporal performance of GPM and GSMaP estimates has not been studied over arid areas performance of 5 quasi-global GSPEs over an arid environment using in-situ rain gauge measurements as benchmarks. The current paper introduces the first detailed daily and sub-daily assessment of GSPEs over the Arabian Peninsula. With an emphasis on the latency time aspect of these GSPEs, the ultimate objective of this research was to assess their performance per entire ground stations in relationship to different rainfall intensity classes. Because GSPEs have mostly global or quasi-global orientations, the performance of these products is expected to vary from one location to the other. Therefore, it is mandatory to assess the performances of GSPEs using the local in-situ rain gauge datasets before they can be utilized with high confidence in different environmental applications over a specific study area. Such evaluation and inter-comparison can also help to determine the most accurate and appropriate GSPEs among various alternatives.

2A.2. Study Area and Datasets

2A.2.1. Study Area

The Sultanate of Oman is located along the south-eastern coast of the Arabian Peninsula in western Asia. It covers an area of approximately 309,814 km² [27]. It can be divided geographically into three distinct parts: desert (75%), mountainous area (15%), and coastal zone and alluvial plains (5%). The current study was carried out at the foothill of the Al-Jabal Al-Akhdar chain at Ad Dakhiliyah Governorate, the Sultanate of Oman (Figure 2A.1). It is characterized by the arid climate with little precipitation over the whole year. It is highly variable and fluctuated with an average annual rainfall of more than 300 mm in the northern Oman mountains [28]. In fact, there are four main mechanisms that help generate rainfall in Oman [24], [28]–[30], i.e., (i) convective rainstorms that often occur during the summer and may reoccur at any time of the year, (ii) cold frontal troughs that originate over the Atlantic Ocean or the Mediterranean Sea and prevail throughout winter and early spring, (iii) onshore monsoon currents that induce a complex regional circulation from June to September and usually come in the form of drizzle over the southern Oman (Dhofar), and (iv) tropical cyclones that move from the Arabian Sea-side to generate extreme rainfall and can reoccur once in every five years in Dhofar and about once in every ten years over Muscat coastal regions. Figure 2A.1 showed the selected area of study, where the source of the top image is ESRI xc and the lower image contains Advanced Land Observing Satellite-Phased Array type L-band Synthetic Aperture Radar (ALOS PALSAR) [31] digital elevation model (DEM) with a spatial resolution of 12.5 m.

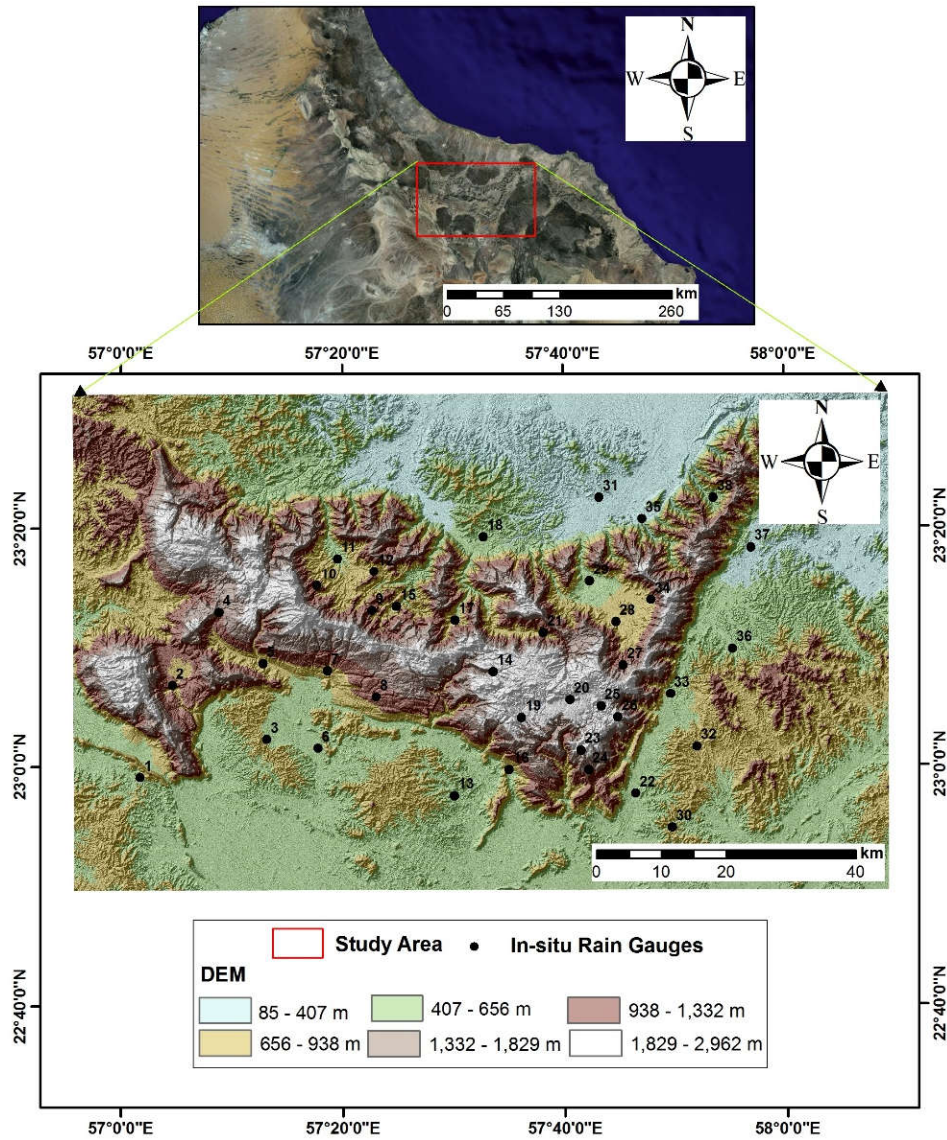


Figure 2A.1. The study area is enclosed in the red polygon (as shown in the upper panel), and the 38 meteorological ground rainfall gauges are shown in black dots shown in the bottom panel. The elevation irregularities (color in m) were derived from ALOS PALSAR DEM with a spatial resolution of 12.5 m. The source of the satellite imagery (top part) is ESRI [32].

2A.2.2. Rainfall Datasets

In this study, three different precipitation-related datasets were used: (i) GPM-IMERG, (ii) GSMaP, and (iii) in-situ gauge data. These datasets are briefly described in the following sub-sections.

2A.2.2.1. GPM-IMERG Products

The GPM is a constellation of satellite platforms operated by the National Aeronautics and Space Administration (NASA) and the Japan Aerospace Exploration Agency (JAXA) in cooperation with other international space agencies [33]. This system provides precipitation measurements in near-real time (NRT) within 3 hours of observation to enhance the understanding of Earth's energy and the water cycle. It consists of two integrated instruments, i.e., the GPM Microwave Imager (GMI) captures precipitation intensities and horizontal patterns, and the Dual-frequency Precipitation Radar (DPR) to produce a 3D structure of precipitating particles. It generates Integrated Multi-satellite Retrievals for GPM (IMERG) products by merging and interpolating of: (i) all satellite passive microwave precipitation estimates in the GPM constellation, (ii) microwave calibrated IR satellite measurements, (iii) rainfall gauge records, and (iv) other precipitation products of different sensors at fine spatial and temporal resolutions [33]. The involved methods for developing these IMERG products can be summarized in the following steps as described in [33]: (i) creating a linear interpolation between the LEO-PMW estimates and the GEO-IR-based feature motion, (ii) applying Kalman filter to process the GEO-IR precipitation when the LEO-PMW are too scattered, (iii) implementing satellite sounding-based algorithms at the high latitudes to overcome the shortcomings of the usual PMW imager channels, and (iv) utilizing the precipitation gauge networks to correct the bias of the satellite measurements and produce reliable regionalization. The system runs several times for every observation time to generate products of 0.1° and 30 minutes of spatial and temporal resolution, respectively. There are three IMERG products [34], [35]: (i) the NRT IMERG-E run provides quick estimates after 4 h of observations, (ii) the IMERG-L run yields better estimates as more data arrives after 12 h of observations, and (iii) the IMERG-F research-grade that used the monthly in-situ gauge estimates for validation purposes, and

has latency time of 3.5 months. The IMERG V04 algorithms use the Goddard Profiling Algorithm (GPROF 2014) to measure the precipitation estimates from all PMW sensors onboard GPM satellites, which represents an improvement compared with GPROF 2010 of the TRMM-TMPA products [33].

2A.2.2.2. GSMaP Estimates

GSMaP is a blended Microwave-IR product and has been developed in Japan for the GPM mission. Processing and distributing global rainfall data on an NRT basis by merging multi-satellite data. It is an hourly product at a $0.1^\circ \times 0.1^\circ$ latitude/longitude grid. The prototype version has been in operation in JAXA since 2006 data, and the GPM-GSMaP products were released in September 2014. A new version of GSMaP (V06) was released on 17 January 2017. Based on launching the GPM mission, the GSMaP project developed a corresponding GPM-era precipitation retrieval algorithm (GPM-GSMaP version 06) by adding information from GPM Core GMI. The GSMaP algorithm generates precipitation estimates according to following steps as described in [36]–[38]: (i) calculating the rainfall rate from PMW sensors, (ii) then propagating rainfall affected area using forward and backward morphing technique, and (iii) finally, refining the estimated data based on infrared brightness temperature using Kalman filter approach. The GSMaP-G is an error-corrected GSMaP product, which is based on GSMaP-MVK (i.e., a pure satellite-based GSMaP product without gauge correction) and adjusted by the CPC unified gauge-based analysis of global daily precipitation data analysis. In this study, I used “GSMaP-G” to stand for GSMaP-Gauge adjusted data, and “GSMaP-S” to denote GSMaP-MVK. More details about GSMaP algorithms, validation, and products can be obtained from [36]–[38].

2A.2.2.3. Rain Gauge Data

In total, the rain measurements from 38 in-situ gauges were collected by the Ministry of Regional Municipalities and Water Resources, the Sultanate of Oman, over the period from March 2014 to October 2016. These in-situ rain gauge data were converted to a spatial vector data structure and georeferenced to the projection system of the GSPEs. Besides, the GSPEs were adjusted to match with the Omani day, which starts 4 h ahead of Coordinated

Universal Time/Greenwich Mean Time (UTC/GMT) (i.e., UTC/GMT + 4 h). To compare the GSPEs with the corresponding ground rain records at daily and sub-daily temporal scales, the five products of half-hourly, i.e., HH IMERG and hourly GSMaP were aggregated into daily and sub-daily datasets every 6 h ranging from 00.00 UTC to 24.00 UTC and details can be found in [39].

2A.3. Methods

Figure 2A.2 demonstrates the proposed method in the form of a schematic diagram. It consists of two distinct components: (i) data preparation, and (ii) statistical comparison processes (i.e., continuous and categorical metrics) for daily and sub-daily GSPEs based on the entire in-situ rain gauges' measurements at different rainfall intensities and thresholds.

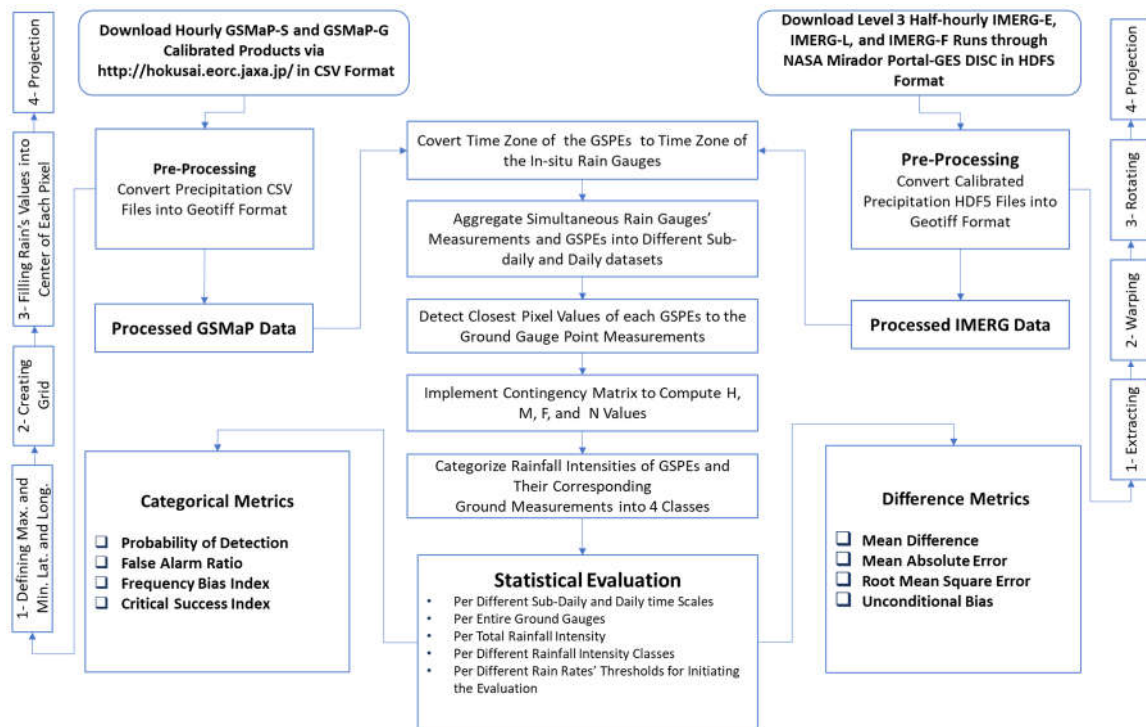


Figure 2A.2. The flow chart for comparing the Global Satellite-based Precipitation Estimates (GSPEs) against the in-situ rain gauges' measurements over an arid area (Ad Dakhilyah, the Sultanate of Oman).

2A.3.1. Data Preparation

Llasat [40] stated that there was no generic schema for classifying the rainfall intensity into different categories as they could significantly vary from one country to another. The analysis of in-situ rainfall measurements for the period from 1997 to 2003 over Al-Jabal Al Akhdar toward Ad Dakhiliyah Governorate (Nizwa, Bahla, and Al Hamra cities), Sultanate of Oman revealed that the intensity of rainfall less than 10 mm/day constituted 66-95% of the total rainfall amount, while rainfall of at least 50 mm/day was erratic [24]. Therefore, I selected certain accumulated rainfall intervals (i.e., 0.0–2.5 mm, 2.5–10 mm, 10–50 mm, greater than 50 mm that can represent light, moderate, heavy, and very heavy rainfall in the selected arid study area) to evaluate the GSPEs, per different sub-daily and daily temporal resolutions, using the in-situ rain gauges' measurements. The three runs of the HH IMERG datasets were originally stored in a native complex Hierarchical Data Format (HDF5). The HDF5 is a unique open-source, cross-platform technology for data storage of scientific and descriptive metadata in an organized hierarchy. The IMERG V04 runs were downloaded from the Mirador web tool of NASA Goddard Earth Sciences Data and Information Services Center (GES DISC) for the period from March 2014 to October 2016. The downloaded data were converted to the GeoTIFF data format with subsequent extraction of the calibrated precipitation datasets. The IMERG products were projected to the Geographic Coordinate System (GCS), WGS 1984. The next step was to correct the orientation of the grids by rotating the images through a 90° counter-clockwise, then the corrected georeferenced longitude and latitude values were defined. The point rain gauges were transferred into the same projected coordinate system of the IMERG data. The daily precipitation estimates were calculated by summing the 48 HH precipitation estimates for each day and dividing them by two. The HH IMERG data were divided by two to convert the unit of measurements into mm/hour. The precipitation estimates in successive two HH periods ($X_{n_{mm/hh}}$, $X_{n+1_{mm/hh}}$) were converted into hourly precipitation estimates ($X_{mm/h}$) based on the following mathematical relationship:

$$X_{mm/h} = [X_{n_{mm/hh}} + (X_{n+1_{mm/hh}})]/2 \quad (2A.1)$$

The GSMaP datasets were available in a CSV file format that contained latitudes, longitudes, and rainfall values. To convert these data into GeoTIFF format, the maximum and minimum values of the longitudes and latitudes were defined. Then, based on determining the full spatial extent of the GSMaP data, the grids were generated, and the pixels were filled iteratively by the precipitation values. The images were then converted to GeoTIFF format and projected to the GCS, WGS 1984.

In order to perform the comparison between the five GSPEs and in-situ gauge measurements, the IMERG and GSMaP raster datasets were converted to vector points that represented the centroid of each pixel. The gauge points were overlaid the IMERG grids, and the nearest neighbor pixel value to each ground station were extracted into matrix of the points' values (i.e., as columns) (e.g., [20]) using the nearest neighbor approach (i.e., the closest center of the correspondent GSPEs' grid points were selected). The nearest neighbor could be used to search for k nearest neighbors, or neighbors within some distance (or both). The maximum distance between the center of the GSPEs' grids and the in-situ gauges was approximately five km (i.e., below the spatial resolution of the GSPEs). This approach is used frequently in evaluating the performance of the GSPEs to ensure using the original retrievals of each satellite estimate [20], [41]. The corresponding rainfall event from GSMaP and IMERG grids, and in-situ point measurements were extracted to compute the statistical comparison measures. Ground stations' records were spatially joined with the closest centroid of the GSPEs' grids. The results from these spatial joins were used to identify hits and misses.

The in-situ rain measurements and the corresponding GSPEs were aggregated into sub-daily and daily products every 6 h from 00.00 UTC to 24.00 UTC (i.e., from 00.00 to 06.00 UTC, 06.00 to 12.00 UTC, 12.00 to 18.00 UTC, and 18.00 to 24.00 UTC) per all involved gauges in the evaluation. These accumulated products were initially compared per the total rainfall intensity per all in-situ gauges. In addition, in order to gain in-depth information about the performance of GSPEs, I also evaluated them using in-situ rain gauges measurements at different rain intensity intervals (i.e., 0.00–2.5 mm, 2.5–10 mm, 10–50 mm,

greater than 50 mm), and at different rainfall initiation thresholds (0.00 mm, 2.5 mm, and 10 mm).

2A.3.2. Statistical Comparison Procedures

In general, statistical evaluation of the performance of GSPEs could be carried out based on the continuous difference (Table 2A.1) and categorical methods (Tables 2A.2 and 2A.3). In this case, sub-daily and daily cumulative precipitation estimates were used. These assessments were carried out based on different rainfall intensities, as well as different thresholds to differentiate rain and no rain events.

Table 2A.1. The continuous difference statistical metrics used for evaluating the performance of different GSPEs. Note: Variables: i : sample size “single rainfall event for a single satellite grid point”; N : number of pixels “observed days”; S : satellite precipitation estimates (centers of grids); O : observed point ground rain data.

Metrics	Mathematical Formula	Range	Ideal Value	Units
MD	$\frac{1}{N} \sum_{i=1}^N (S_i - O_i)$	$-\infty$ to $+\infty$	0	mm/n h
MAD	$\frac{1}{N} \sum_{i=1}^N S_i - O_i $	0 to $+\infty$	0	mm/n h
RMSE	$\sqrt{\frac{1}{N} \sum_{i=1}^N (S_i - O_i)^2}$	0 to $+\infty$	0	mm/n h
UB	$\frac{\sum_{i=1}^N (S_i)}{\sum_{i=1}^N (O_i)}$	0 to $+\infty$	1	-

Table 2A.2. Contingency table to determine the possible conditions (combination) for detecting rainfall from the GSPEs and ground measurements.

Possible Combinations of Rain Detection	Satellite Product	Gauge Data
Hit (H)	Yes	Yes
False (F)	Yes	No
Miss (M)	No	Yes
Null (X)	No	No

Table 2A.3. The categorical statistical indicators utilized for evaluating the performance of the GSPEs.

Indicators	Mathematical Formula	Range	Ideal Value
POD	$\frac{H}{H + M}$	0 to 1	1
CSI	$\frac{H}{H + M + F}$	0 to 1	1
FAR	$\frac{F}{H + F}$	0 to 1	0
FBI	$\frac{H + F}{H + M}$	0 to $+\infty$	1

2A.3.2.1. Continuous Statistical Metrics

The continuous difference methods (see Table 2A.1) were mainly directed toward measuring the difference between GSPEs and the corresponding in-situ rain gauges. Numerous statistical difference methods have been reported by various researchers (e.g., [1], [16], [17], [20], [42]) to evaluate the performance of different GSPEs. Both root mean square error (RMSE) and mean absolute difference (MAD) measure the average error magnitude, but RMSE provides greater weights to the more substantial errors than the MAD. MD also determines the difference between two products. In the case of using observation data (i.e., reference in-situ gauges' measurements) are utilized for assessing the performance of the GSPEs, MD is corresponding to the bias. The unconditional bias (UB) is the ratio between the GSPE and in-situ rainfall measurements. Perfect satellite precipitation estimation results in a UB of unity. Overestimation leads to values higher than unity, while underestimation causes values less than unity.

2A.3.2.2. Categorical Indices

The categorical indicators were determined using a 2 by 2 contingency table (Table 2A.2). Precipitation is collected as discrete observable estimates, so there are four possible combinations (Table 2A.3), where 'H' is hit (i.e., number of pixels that both of satellite and gauge data simultaneously detected the rainfall at the same location), 'F' stands for false alarm (i.e., number of pixels that are recorded by satellite product as rainfall but not by the in-situ gauge), 'M' is missed (i.e., number of pixels that are reported as rainfall by the ground

gauge but not by the satellite sensor), and ‘X’ refers to ‘null’ or correct negatives (i.e., the number of pixels that are not recognized as rainfall for both satellite data and ground gauge). The possible forms of the categorical statistics [43] are the probability of detection (POD), critical success index (CSI), false alarm ratio (FAR), and frequency bias (FBI) (Table 2A.3). The POD is defined as how often the satellite product successfully estimates the rainfall. If the POD is equal to 1, this means that the satellite product correctly detects all the rainy pixels compared to the in-situ gauge data. CSI defines the fraction of rain events correctly captured by the satellite sensor. The FAR specifies how often the satellite data detects rainfall when rain does not actually fall to the ground. The FBI explains the ratio of total satellite rainfall alarms to gauges’ fall alarms. FBI is the ratio between predicted and observed rain events [44]. An ideal FBI value is 1, and it can occur if the frequencies of false alarms and missed rainfall events are equal [45], [46]. More details about the categorical classification for GSPEs could be found in [41].

2A.4. Results

In this section, the results were computed based on comparing sub-daily and daily gauge measurements with the corresponding GSPEs, at different rainfall intensity classes (except greater than 50 mm) and thresholds, using traditional continuous and categorical statistical metrics. The rationale of excluding the ‘greater than 50 mm’ intensity class was due to the fact that such events were not commonly occurred (i.e., only 14 events) within the study period of interest.

2A.4.1. Daily Analysis Utilizing Traditional Statistical Metrics per Entire Ground Rain Gauges

The evaluation of the daily 5 GSPEs against 38 ground rain gauges has been carried out based on days with only observed rainfall values (Table 2A.4). The number of events captured by both GSMaP products was higher than those recorded by the different GPM-IMERG runs. The MD and UB metrics indicated if the GSPEs under- or over-valued the in-situ rain gauge measurements. At the daily accumulated rainfall intensity, the IMERG-L showed the lowest underestimation rate with MD of -0.43 mm/day and UB closed to unity,

i.e., 0.92 (Table 2A.4). The 5 GSPEs slightly overestimated the light rainfall of intensity of less than 2.5 mm. The IMERG-F reported the lowest overestimation and followed by GSMaP-G and GSMaP-S. The UB and MD metrics were consistent in the case of IMERG-F, GSMaP-G, and GSMaP-S with values of 1.75, 1.84, and 2.08 and 0.64 mm/day, 0.71 mm/day, and 0.92 mm/day, respectively (Table 2A.4). The IMERG-L and IMERG-E, respectively, had the best performance with reporting the lowest underrated values of moderate to heavy ground rainfall observations. They slightly, moderately, and massively undervalued in-situ measurements at rainfall intensity classes of 2.5–10 mm/day, 10–50 mm/day, and greater than 50 mm/day, respectively (Table 2A.4).

Also, the GSMaP-G, GSMaP-S, and IMERG-F yielded the best (i.e., lowest) values of RMSE and MAE at the accumulated rainfall intensity per day (Table 2A.4). At the first three rainfall intensity classes in ascending order, the GSMaP-G kept providing lower values of RMSE and MAE than other GSPEs (Table 2A.4). There were some exceptions where the IMERG-F and IMERG-E ranked first at rainfall intensity classes of 10–50 mm and greater than 50 mm, respectively.

Table 2A.4. Statistical metrics of daily rainfall events per different intensities (mid-March 2014 to October 2016). NoE refers to the number of recorded rainfall events.

Intensity	Metrics	GSMaP-S	GSMaP-G	IMERG-E	IMERG-L	IMERG-F
Total Rainfall (mm/day)	NoE	2499	2499	2471	2471	2468
	MD	-1.92	-2.96	-1.08	-0.43	-2.85
	MAD	4.98	4.69	6.22	6.38	4.77
	RMSE	10.12	9.23	14.09	15.29	9.32
	UB	0.66	0.47	0.81	0.92	0.49
0.0–2.5 (mm/day)	NoE	1395	1395	1370	1370	1367
	MD	0.92	0.71	1.55	2.00	0.64
	MAD	1.82	1.61	2.56	2.91	1.59
	RMSE	3.93	2.87	8.47	10.16	3.40
	UB	2.08	1.84	2.82	3.33	1.75
2.5–10 (mm/day)	NoE	674	674	673	673	673
	MD	-2.36	-2.90	-1.37	-0.50	-3.11
	MAD	4.71	4.18	6.22	6.54	4.62
	RMSE	5.93	4.90	13.42	15.59	5.75
	UB	0.57	0.47	0.75	0.91	0.43
10–50 (mm/day)	NoE	418	418	416	416	416
	MD	-9.27	-13.61	-8.27	-7.26	-12.30
	MAD	14.59	14.14	16.97	16.22	13.93
	RMSE	18.44	16.24	22.09	22.18	15.89
	UB	0.52	0.29	0.57	0.62	0.36
> 50 (mm/day)	NoE	14	14	14	14	14
	MD	-44.16	-55.03	-33.25	-31.30	-50.74
	MAD	46.37	55.03	44.25	45.97	50.81
	RMSE	70.02	73.28	69.68	69.92	71.38
	UB	0.37	0.22	0.53	0.56	0.28

2A.4.2. Sub-daily Analysis Utilizing Traditional Statistical Metrics per Entire Ground Gauges

In terms of MD and UB metrics, it was found that the GSMaP-G, IMERG-E, and GSMaP-S tended to underestimate the ground rain measurements in ascending order at the accumulated total rainfall intensity per 6 h (Table 2A.5). The computed MD and UB values were close to each other among 5 GSPEs with difference ranges of 0.58 mm/6 h and 0.24, respectively. Using the same metrics per 12 h, the 5 GSPEs kept underestimating the in-situ rain records, where IMERG-L yielded the best MD and UB scores, i.e., -1.59 mm/12 h and 0.58, and followed by GSMaP-S and IMERG-E. Moving toward the accumulated rain per 18 h, it was found that IMERG-L, IMERG-E, and GSMaP-S outperformed the other two GSPEs by reporting the lowest MD values and the closest UB values to the unity (Table 2A.5).

The MAD and RMSE values increased with the rise of accumulated hours from 6 to 18 h (Table 2A.5). The GSMaP-G showed the best performance with reporting lowest RMSE and MAD values of 4.38 mm/6 h, 7.55 mm/12 h, and 8.87 mm/h and 1.88 mm/6 h, 3.3 mm/12 h, and 4.55 mm/18 h, respectively. The IMERG-F showed similar performance to GSMaP-G at 12 and 18 h. GSMaP-S had the lowest performance per 6 h, while IMERG-L outperformed by other GSPEs per 12 and 18 h (Table 2A.5).

Table 2A.5. Statistical metrics of sub-daily rainfall events of total intensity (mid-March 2014 to October 2016).

NoE refers to the number of recorded rainfall events.

Time	Metrics	GSMaP-S	GSMaP-G	IMERG-E	IMERG-L	IMERG-F
6 h	NoE	406	406	404	404	404
	MD	-1.30	-1.19	-1.20	-1.34	-1.77
	MAD	2.56	1.88	2.39	2.25	2.16
	RMSE	5.74	4.38	5.35	5.20	5.34
	UB	0.44	0.48	0.48	0.42	0.24
12 h	NoE	1409	1409	1397	1397	1394
	MD	-1.89	-2.35	-2.25	-1.59	-2.68
	MAD	3.75	3.30	3.94	4.03	3.47
	RMSE	8.27	7.55	9.43	9.66	7.94
	UB	0.50	0.38	0.41	0.58	0.30
18 h	NoE	2339	2339	2315	2315	2312
	MD	-1.68	-2.88	-1.33	-0.64	-2.71
	MAD	4.77	4.45	5.73	5.93	4.42
	RMSE	9.90	8.87	13.71	15.05	8.91
	UB	0.67	0.44	0.74	0.88	0.48

Table 2A.6 shows that the 5 GSPEs inclined to overestimate the sub-daily ground rain measurements at a rain intensity of 0.0–2.5 mm. The MD and UB values ranged from 0.00–0.32 mm and 0.24–0.48, respectively, for the accumulated rain per 6 h, where 5 GSPEs tended to overestimate the in-situ rain measurements except for the IMERG-F slightly. GSMaP-G showed the highest performance per 6 h, and IMERG-F ranked first per 12 and 18 h with reporting best MD and UB scores. For the other GSPEs, the IMERG-E, GSMaP-S, and IMERG-L ranked in *descending* order with MD and UB values of 0.21 mm/12 h, 0.51 mm/12 h, and 0.59 mm/12 h and 1.28, 1.69, and 1.79, respectively (Table 2A.6). The same rank was achieved at a temporal resolution of 18 h, except that the GSMaP-G outperformed the IMERG-E. The scores of RMSE and MAD were close to each other at different sub-daily time scales except for the extreme RMSE reported at a temporal resolution of 18 h by the IMERG-L, i.e., 10.01 mm/18 h and IMERG-F, i.e., 8.32 mm/18 h (Table 2A.6). The

GSMaP-G and IMERG-F alternately had the best performance at different sub-daily time scales.

Table 2A.6. Statistical metrics of sub-daily rainfall events at a rainfall intensity of less than 2.5 mm (mid-March 2014 to October 2016). NoE refers to the number of recorded rainfall events.

Time	Metrics	GSMaP-S	GSMaP-G	IMERG-E	IMERG-L	IMERG-F
6 h	NoE	331	331	328	328	328
	MD	0.26	0.00	0.32	0.22	-0.11
	MAD	0.96	0.65	0.95	0.82	0.52
	RMSE	2.17	1.10	1.97	1.56	0.86
	UB	1.50	1.00	1.62	1.42	0.79
12 h	NoE	899	899	888	888	885
	MD	0.51	0.19	0.21	0.59	0.00
	MAD	1.45	1.08	1.28	1.52	0.97
	RMSE	3.53	1.71	3.49	4.28	2.02
	UB	1.69	1.26	1.28	1.79	1.00
18 h	NoE	1339	1339	1317	1317	1314
	MD	0.89	0.60	1.35	1.80	0.50
	MAD	1.78	1.54	2.34	2.71	1.46
	RMSE	3.86	2.68	8.23	10.01	3.20
	UB	2.05	1.71	2.59	3.12	1.59

Within accumulated rainfall intensity ranged from 2.5–10 mm, the GSMaP-G was found to be the best depending among different intervals of computations (Table 2A.7). GSMaP-G was the best performer for 8 out of 12 times, i.e., (i) -2.54 mm, 3.74 mm, 4.38 mm, and 0.54 for MD, MAD, RMSE, and UB, respectively, per 6 h; and (ii) approximately 4.16 mm, 4.86 mm for MAD and RMSE, respectively, per 12 and 18 h. In terms of MD and UB metrics, the 5 GSPEs tended to underestimate moderately the in-situ rain measurements (Table 2A.7). The IMERG-L demonstrated the closest matching with in-situ rainfall measurements with reporting lowest MD values, i.e., -2.65 mm and -0.57 mm, and UB scores, i.e., 0.52 and 0.89 per 12 and 18 h, respectively.

Table 2A.7. Statistical metrics of sub-daily rainfall events at intensity 2.5–10 mm (mid-March 2014 to October 2016). NoE refers to the number of recorded rainfall events.

Time	Metrics	GSMaP-S	GSMaP-G	IMERG-E	IMERG-L	IMERG-F
6 h	NoE	52	52	52	52	52
	MD	-3.26	-2.54	-3.36	-3.66	-4.39
	MAD	5.36	3.74	4.54	4.25	4.73
	RMSE	6.22	4.38	5.57	5.05	5.36
	UB	0.41	0.54	0.39	0.34	0.21
12 h	NoE	363	363	362	362	362
	MD	-2.98	-3.64	-3.77	-2.65	-4.04
	MAD	4.95	4.16	5.02	5.17	4.55
	RMSE	6.05	4.86	6.70	7.83	5.19
	UB	0.46	0.33	0.31	0.52	0.26
18 h	NoE	627	627	626	626	626
	MD	-2.29	-2.94	-1.55	-0.57	-3.11
	MAD	4.64	4.16	5.96	6.36	4.50
	RMSE	5.86	4.89	13.48	15.84	5.67
	UB	0.57	0.45	0.71	0.89	0.42

In terms of MAD and RMSE, the GSMaP-G and IMERG-F had the highest performance and followed by the GSMaP-S, IMERG-E, and IMERG-L at the three temporal resolutions. There was an exception at a temporal resolution of 6 h where IMERG-L and GSMaP-S were ranked second and fifth in the performance order, respectively.

Within a rainfall intensity between 10 mm and 50 mm (Table 2A.8), the computed MD and UB values were much larger than those estimated at a rainfall intensity of 2.5–10 mm (Table 2A.7). These values can be interpreted by the possible occurrence of heavy rainfall events that were captured by the in-situ gauges while heavily undervalued by the GSPEs. The GSMaP-G reported the minimum MD values, i.e., -14.74 and -3.64 mm at temporal resolutions of 6 and 12 h, and the IMERG-L, i.e., -8.42 mm when evaluating the accumulated rainfall per 18 h (Table 2A.8). The UB and MD values were consistent, where

the UB scores also proved that IMERG-F heavily underestimated the ground rain measurements at temporal resolutions of 6 and 12 h, and GSMaP-G at a time interval of 18 h (Table 2A.8).

Table 2A.8. Statistical metrics of sub-daily rainfall events at intensity 10–50 mm (mid-March 2014 to October 2016). NoE refers to the number of recorded rainfall events.

Time	Metrics	GSMaP-S	GSMaP-G	IMERG-E	IMERG-L	IMERG-F
6 h	NoE	24	24	24	24	24
	MD	-18.57	-14.74	-17.35	-17.57	-18.90
	MAD	18.57	14.74	17.35	17.57	18.90
	RMSE	20.24	16.35	19.03	19.16	20.20
	UB	0.06	0.26	0.13	0.12	0.05
12 h	NoE	147	147	147	147	147
	MD	-12.67	-13.51	-12.12	-10.95	-14.21
	MAD	13.58	13.57	16.10	15.15	14.61
	RMSE	15.66	15.08	20.44	19.52	16.24
	UB	0.25	0.20	0.28	0.35	0.16
18 h	NoE	368	368	367	367	367
	MD	-8.95	-14.13	-9.55	-8.42	-12.41
	MAD	14.72	14.24	16.34	15.62	13.80
	RMSE	18.60	16.20	21.62	21.81	15.77
	UB	0.52	0.25	0.49	0.55	0.34

The computed MAD and RMSE values at a rainfall intensity of 10–50 mm (Table 2A.8) were approximately three times more than those estimated at rainfall intensity of 2.5–10 mm (Table 2A.7). The reported MAD and RMSE values at a temporal resolution of 6 h were larger than those computed at the accumulated rainfall per 12 h and 18 h. This could be interpreted by the extreme rainfall intensities at the early night times (i.e., 00:00 to 06:00 UTC/GMT). The MAD and RMSE values were matched at a time interval of 6 h since the GSMaP-G had the best performance and followed by the IMERG-E, IMERG-L, GSMaP-S, and IMERG-F in ascending order. On the contrary, there was a different performance, where

GSMaP-G ranked first and was followed by GSMaP-S, IMERG-F, IMERG-L, and IMERG-E at a temporal resolution of 12 h. Furthermore, the smallest MAD and RMSE values were reported by the IMERG-F, i.e., 13.8 mm and 15.77 mm, and GSMaP-G, i.e., 14.24 mm and 16.2 mm, respectively, at 18 h. (Table 2A.8).

2A.4.3. Daily Analysis Utilizing Categorical Metrics per Entire Ground Gauges

In order to calculate the categorical metrics, each day over the whole period of study was considered whether the observations from either both in-situ gauges and GSPEs were available or not. Figure 2A.3 shows that the GSMaP-G, IMERG-L, and a GSMaP-S had the highest POD with a value of approximately 0.7 and 0.4 at the initialization thresholds of 0.00 and 2.5 mm/day, respectively. The IMERG-L and GSMaP-S kept providing most top POD scores, and IMERG-E showed a significant improvement at a initialization threshold of 10 mm. The POD decreased with the rise of rainfall initiation threshold from 0.00 to 10 mm. Low POD might be interpreted by the missed precipitation due to possible occurrences of snow coverage on the top of Al-Jabal Al Khader, and by the incapability of capturing warm rain processes or short-lived convective storms [41], where these conditions prevailed along the Gulf of Oman. The GSMaP-S and GSMaP-G reported the highest CSI values at the three rainfall thresholds. The other GSPEs had close CSI values to those reported by the GSMaP-S and GSMaP-G with a maximum difference of 0.1 in the case of IMERG-F (Figure 2A.3).

At the initialization threshold of 0 mm/day, the GSMaP-S had the best performance with the lowest FAR, i.e., 0.64, while the other GSPEs had closer FAR values with a difference of 0.06 (Figure 2A.3). GSMaP-S again had the lowest FAR, i.e., 0.61 at a rain threshold of 2.5 mm, while the IMERG-L ranked last among the 5 GSPEs with FAR of 0.71. The IMERG-F reported the lowest FAR and was followed by GSMaP-G and GSMaP-S by values of 0.57, 0.59, and 0.63, respectively, at a rain threshold of 10 mm/day. The FBI and FAR scores were consistent, where GSMaP-S reported the best values, i.e., 2.07, 1.06, and at rain thresholds of 0.00 and 2.5 mm/day, respectively. With the increase of the rain threshold value to 10 mm/day, the IMERG-F and GSMaP-G had the best FAR, i.e., approximately 1.

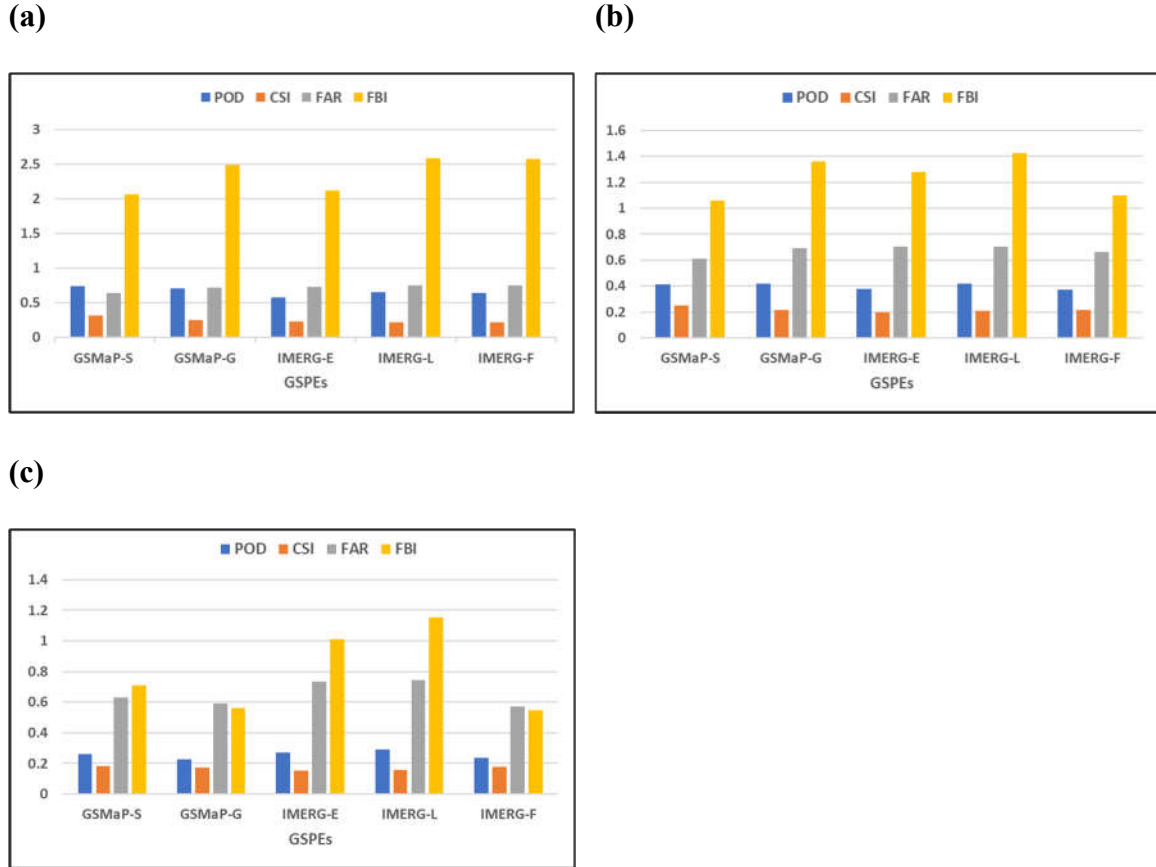


Figure 2A.3. Categorical statistical indices of daily rainfall events at different initialization thresholds: (a) 0.00 mm/day, (b) 2.5 mm/day, and (c) 10 mm/day.

2A.4.4. Sub-daily Analysis Utilizing Categorical Metrics per Entire Ground Gauges

GSMaP-G generally showed the best performance since it came in the first place among other GSPEs at temporal resolutions of 6 h and 12 h, and third at 18 h with POD values of 0.57, 0.66, and 0.64, respectively (Figure 2A.4). The GSMaP-S came in the second rank with reporting POD values of 0.65 and 0.75 at the sub-daily time scales of 12 and 18 h; however, it ranked last in at 6 h (Figure 2A.4). High POD might be interpreted by the domination of convective storms [38]. IMERG-L and IMERG-F reported approximately similar POD values that were lower than those computed from GSMaP-G and GSMaP-S at different latency times (Figure 2A.4). CSI of GSMaP S seems to be better than other GSPEs at daily time scales of 6, 12, and 18 h (Figure 2A.4) by values of 0.19, 0.24, and 0.32, respectively.

In general, the GSMaP-S mostly recorded the lowest FAR and FBI values at different temporal resolutions. The GSMaP-G had the worst FAR and FBA at 6 and 12 h. Its performance improved 18 h, where it ranked first with reporting the lowest FAR and FBI, i.e., 0.67 and 1.97, respectively. The IMERG-L and IMERG-E yielded the highest FAR and FBI scores at the three sub-daily time scales (Figure 2A.4).

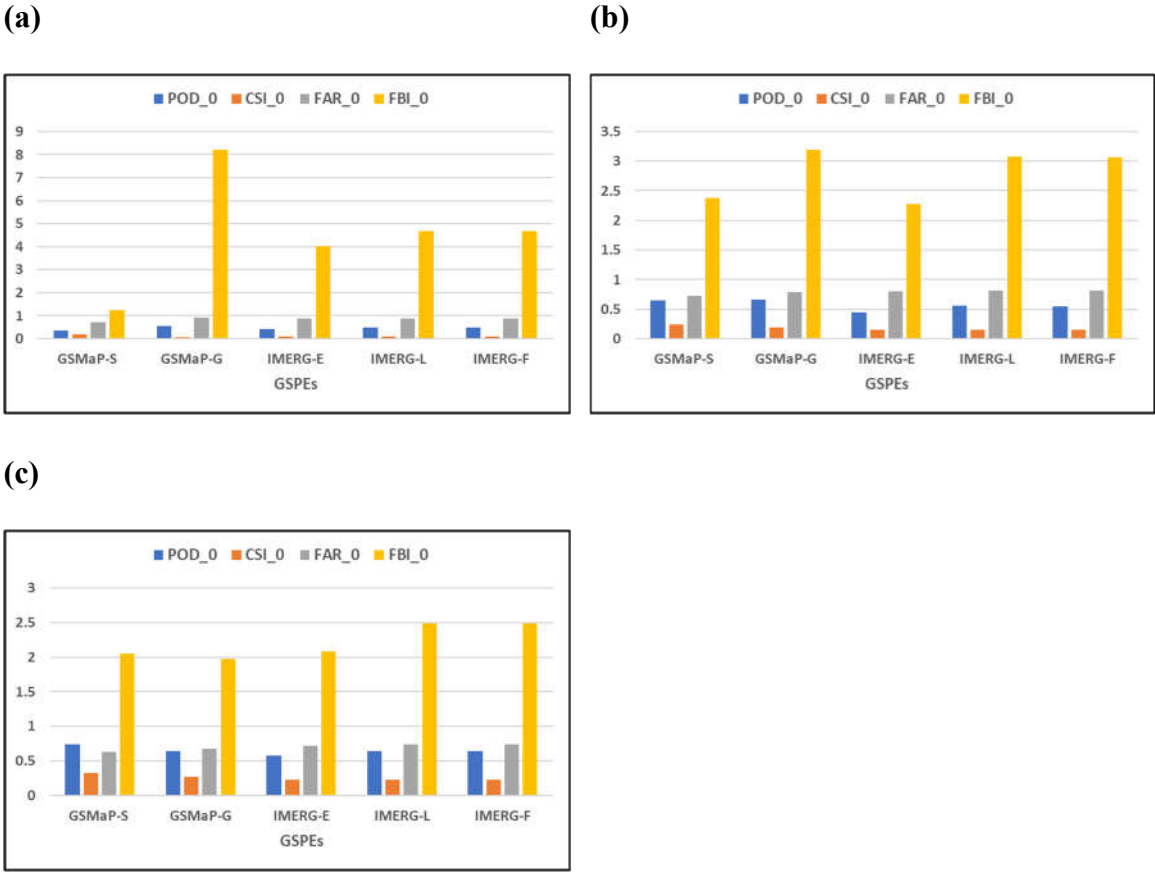


Figure 2A.4. Categorical statistical indices of sub-daily rainfall events using the total rainfall intensity per three temporal resolutions: (a) 6 h, (b) 12 h, and (c) 18 h.

Figure 2A.5 shows the results of evaluating 5 GSPEs using the categorical indices at a light rainfall intensity from 0.00–2.5 mm. Both GSMaP products showed the highest POD and CSI values at different sub-daily and daily times scales. They have equal POD values, i.e., 0.65, at a daily time scale, while GSMaP-G outperformed the GSMaP-S by differences of 0.19 and 0.04 at the time latency of 6 and 12 h, respectively. At a time-scale of 18 h, GSMaP-S had a higher POD value than GSMaP-G. GSMaP-S slightly outperformed

GSMaP-G with reporting higher CSI scores at 6, 12, 18, and 24 h. The IMERG products had the lowest performance with reporting approximately equal POD and CSI scores with a slight improvement in the case of IMERG-F and IMERG-L at different sub-daily and daily scales.

The GSMaP-S had the best performance with the lowest reported FAR values of 0.79, 0.83, 0.78, and 0.78 at time scales of 6, 12, 18, and 24 h, respectively (Figure 2A.5). The GSMaP-G outperformed the other three IMERG products; however, the reported FAR scores from these 4 GSPEs were very close with minimum values of 0.92, 0.87, 0.8, and 0.83 at time latency of 6, 12, 18, and 24 h, respectively (Figure 2A.5). The FBI values also supported that the GSMaP-S had the highest performance among other GSPEs at different time scales. The other GSPEs had fluctuated performance at different times scales. The IMERG-E reported the lowest FBI values except at a time scale of 18 h, where GSMaP-S yielded the lowest value, i.e., 2.94 (Figure 2A.5). IMERG-F and IMERG-L showed the weakest performance with respect to FBI values, except at a temporal resolution of 6 h (Figure 2A.5).

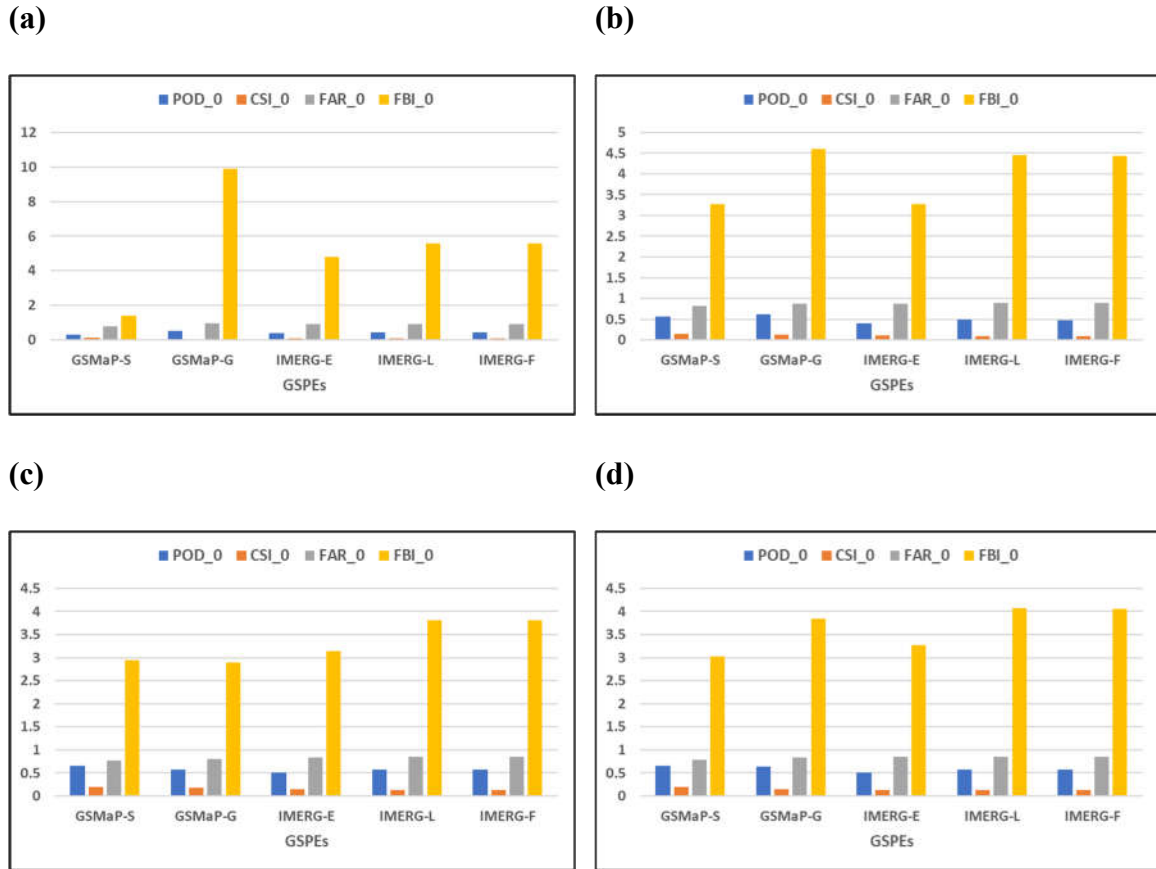


Figure 2A.5. Categorical statistical indices of sub-daily rainfall events at an intensity less than 2.5 mm and three-time scales: (a) 6 h, (b) 12 h, (c) 18 h, and (d) 24 h.

2A.5. Discussion

The use of the daily in-situ rainfall gauges as benchmarks to evaluate the performance of the GSPEs has been less documented by previous studies over the arid Arabian Peninsula. Over entire Saudi Arabia, Mahmoud et al. [21] evaluated the three GPM-IMERG runs using 1455 records from 189 in-situ rain gauges during the period October 2015–April 2016. Utilizing the entire ground stations, the reported RMSE and MAD values ranged from 10 mm/day to greater than 40 mm/day. The reported categorical performance metrics such as POD and CSI were greater than 0.6, 0.7, and 0.9 in case of the early, late, and final IMERG products, respectively. The MAE values of the IMERG-E run ranged from 10–25 mm/day, while they showed slight improvement in the case of IMERG-L. The IMERG-F yielded the lowest MAD with values less than 10 mm/day. The reported RMSE

values ranged from 10 mm/day to greater than 30 mm/day in the case of IMERG-E, and they provided considerable improvement with reduced RMSE values from 40 mm/day to 20 mm/day over some regions. The IMERG-F mostly yielded RMSE values less than 10 mm/day, with few exceptions at some regions where they reached 30 mm/day. Based on the individual stations, the estimated RMSE, MD, and MAD ranged from 15 mm/day to greater than 55 mm/day, -20 mm/day to greater than 20 mm/day, and 5 mm/day to greater than 40 mm/day, respectively. The reported categorical performance metrics such as POD and CSI values ranged from less than 0.5 to greater than 0.85. The IMERG-F showed a higher accuracy over the other two IMERG runs that had fluctuated performance between over- and under-estimation of the in-situ gauge measurements over the different regions of Saudi Arabia.

In 2019, Mahmoud et al. [22] evaluated the accuracy of the three GPM-IMERG products utilizing 1600 in-situ measurements recorded from 81 rain gauges from January 2015–December 2017 over the entire area of UAE. The IMERG-F reported the highest accuracy and lowest estimation error compared to other IMERG products. The late run showed a slight improvement over the early product. The regional evaluation of the early, late, and final IMERG products reported POD values that ranged from 0.68–0.8, 0.7–greater than 0.8, and greater than 0.85, respectively. On the basis of evaluating the individual stations, an overall high detection accuracy with POD greater than 0.75 was recorded. Based on the evaluation of the IMERG products using the entire ground stations, the early and late runs showed MAD and RMSE values that generally ranged from 10 mm/day to greater than 15 mm/day, and 15 mm/day to 30 mm/day, respectively. The late run showed a higher estimation error than that observed in the early product with an average increment of 15%. The IMERG-F product reported difference error lower than the other IMERG product with MAD and RMSE values that ranged from 9–11 mm/day and from less than 15–21 mm/day. The individual station-based assessment showed similar results to the regional assessment, but the RMSE reached more than 40 mm/day in some locations.

Nashwan et al. [47] validated three GSPEs (IMERG-F V05, GSMaP V07, and Climate Hazards Group InfraRed Precipitation with Stations (CHIRPS)) over Egypt during

the period from March 2014–May 2018. They used 670 rainfall events recorded by 29 in-situ meteorological stations that collected by the US National Climate Data Center Global Summary of Days (GSOD). Although the three GSPEs are gauge-corrected, they did not show consistent performance. Therefore, no single product can be named as the best/worst performing product in Egypt. Without classifying the rainfall intensity, the CHIRPS ranked first with the lowest estimation error, i.e., median RMSE = 2 mm/day. The median values of RMSE reported by the IMERG-F and GSMaP-G were found to be close to that provided by CHIRPS. For the light rainfall intensity class, the GSMaP-G and CHIRPS generally demonstrated similar median RMSE values, i.e., 1.03 mm/day. The same results were reported from the low-moderate rainfall intensity class, but CHIRPS showed a slightly higher median RMSE value, i.e., 2.82 mm/day, than the GSMaP_G. Furthermore, GSMaP-G recorded also the lowest median RMSE at the heavy rainfall intensity class. The three GSPEs reported weak performance for the heavy rainfall class with the highest median RMSE value, i.e., 51 mm/day. The GSMaP-G and IMERG-F similarly captured the spatial distribution of the rainfall, but the GSMaP-G was more consistent with the in-situ observations than the IMERG-F run. In general, the lack of detailed ground rainfall records may contribute significantly to the unsatisfactory performance of the three GSPEs. The accurate detection of rainfall using the GSPEs over the arid climate, particularly the deserts of hot climate is still challenging and open for further studies. Nashwan et al. [47] stated that their research was constrained by the lack of dense in-situ rainfall measurements. More daily and sub-daily ground gauge records are needed to evaluate the diurnal rainfall cycles of the IMERG-F and GSMaP-G at fine temporal resolutions.

The findings of Nashwan et al. [47] were similar to the current results at the daily time scale, but the magnitude of the estimated errors was lower in my case study. Additionally, the previous studies showed that the performance of the different GSPEs was inconsistent with respect to the in-situ gauge measurements. Although this fluctuated performance, current findings agreed with the other authors that GSMaP-G mostly provides the best performance. Additionally, the IMERG-F slightly outperformed the IMERG-E and IMERG-L.

Water was, still, and will be the most influential factor in Earth's evolution [48]. The need for continuous and long precipitation records of high accuracy and free availability is a frequent problem for the environmental modelers [49]. Reliable rainfall records constitute integral inputs of different environmental models, particularly flood inundation modeling (e.g., [50] and their associated watershed (e.g., [51], [52]), runoff (e.g., [53]), groundwater flow and recharge (e.g., [54]), surface and subsurface water pollution (e.g., [55]), soil moisture (e.g., [56]), optimum water management (e.g., [57]), climate prediction and forecasting (e.g., [58], and hazard assessment (e.g., [59]) models. The GSPEs introduce an alternative and promising source of continuous rainfall records for different hydrological and environmental applications, particularly over the arid area [47], [60]. There is no perfect rainfall data, but selecting the optimum datasets depend mainly on the purpose of the given application [49]. Additionally, choosing precipitation records depend on the method, spatial, and temporal resolutions [61], which can give the advantage of using GSPEs over the traditional gauge data in various environmental applications.

2A.6. Conclusions

This paper presented a detailed statistical evaluation of 5 GSPEs (GEMaP-S, GSMaP-G, IMERG-E, IMERG-L, and IMERG-F). In general, the performance of the 5 GSPEs enhanced with receiving more spaceborne estimates throughout the day. Both GSMaP products reported the best statistical metrics, among other GSPEs, in most of daily and sub-daily comparisons with the in-situ rain gauge measurements. The IMERG-F slightly outperformed the IMERG-L and IMERG-E. However, the early and late IMERG runs gave promising results, particularly they have shorter latency times (i.e., 4 and 12 h, respectively) and uncorrected with gauge information. The availability of these products within shorter times than the other GSPEs can help in different hydrological applications such as monitoring flash flood over fine sub-daily temporal resolutions. Up to my best knowledge, there were no previous studies concerning evaluating different GSPEs at sub-daily time scales over this extremely arid area of the world. The assessment of the 5 GSPEs over daily and sub-daily time intervals revealed the following:

The overall performance of the 5 GSPEs in capturing daily rainfall events of the total intensity class was acceptable in comparison with the results reported from previous literature mentioned above in the discussion section. With respect to the error difference between GSPEs and ground gauge records, the GSMaP-G, IMERG-F, and GSMaP-S showed the lowest recorded RMSE and MAD values. In terms of MD and UB metrics, The IMERG-L ranked first with reporting the lowest underestimation values, and IMERG-E and GSMaP-G came in the second and third places, respectively.

- The 5 GSPEs generally underestimated the in-situ rainfall measurements at different rainfall intensity classes, except for the light rainfall of an intensity less than 2.5 mm/day. With respect to the underestimation of moderate to heavy in-situ rainfall records per daily basis, the IMERG-L ranked first with reporting the lowest underestimation values and followed by IMERG-E and GSMaP-S.
- The underestimation of ground rainfall measurements per day raised with the increase of the rainfall intensity from less than 2.5 mm/day to greater than 50 mm/day.
- At both daily and sub-daily time scales, the lowest RMSE and MAD values were mostly demonstrated by GSMaP-G, IMERG-F, and GSMaP-S, respectively. The only exception was at a rainfall intensity greater than 50 mm/day, where IMERG-E and IMERG-L came in the first two places with reporting the lowest recorded RMSE and MAD values.
- The daily performance of the 5 GSPEs at a rainfall intensity greater than 50 mm was very low, where they heavily underestimated the ground rainfall measurements. This weak performance could be interpreted by the minor amount of reported rainfall events (i.e., 14) for the short period of mid-March 2014 to October 2016, as well as the erratic behavior of rain over the arid areas.

- For the 5 GSPEs, the POD and CSI values improved, and FAR and FBI measures decreased with the increase of the temporal resolution from 6 to 18 h.
- The GSMaP-G showed the lowest underestimation degree of the ground rainfall measurements of accumulated rain intensity per 6 h, while IMERG-L outperformed the other GSPEs per 12 and 18 h.
- At a rainfall intensity of less than 2.5 mm per sub-daily time intervals, the GSMaP-G and IMERG-F closely matched with ground rainfall measurements with reporting the lowest MD, MAD, and RMSE values, as well as UB scores close to unity.
- Within a rainfall intensity class between 2.5–10 mm/h, GSMaP-G had a good agreement with in-situ rain observations per 6 h, while IMERG-L showed higher matching than the other GSPEs at the time intervals of 12 and 18 h. The GSMaP-G and IMERG-F showed the lowest statistical error differences at the three different temporal resolutions.
- At a rainfall intensity of 10–50 mm/h, the estimated MD and UB values were much larger than those estimated at the light and moderate rainfall intensity classes. These values could be interpreted by the possible occurrence of heavy rainfall events that were captured by the in-situ gauges while massively undervalued by the GSPEs.
- GSMaP-G had the closest matching with the ground rain measurements at the early night hours (i.e., 00:00 to 06:00 UTC/GMT). With moving toward the daytime (i.e., 06:00 to 12:00 and 12:00 to 18:00 UTC/GMT), IMERG-F showed the best performance with reporting the lowest MD among other GSPEs. Additionally, the reported error differences during early night times were larger than those computed in the day time.
- Concerning the accumulated rainfall at a rain threshold of 0.00 mm per different sub-daily time scales, the two GSMaP products kept mostly achieving the top

performance on the basis of POD and CSI metrics. GSMaP-S ranked first with reporting lowest FAR and FBI at different time intervals except at 18 h, where it came second after GSMaP-G.

- With respect to evaluating light rainfall of an intensity of less than 2.5 mm per sub-daily and daily time intervals, the GSMaP products outperformed IMERG runs based on the 4 categorical measures.

Based on the achieved findings and with the difficulties in having continuous and reliable rainfall records from in-situ gauge networks, I would recommend that the researchers in the arid areas should pay more attention to use and assess the available GSPEs in their hydrological and water management studies, and particularly for flood susceptibility modeling.

Author Contributions

Conceptualization, M.S., A.M., Q.K.H., and N.E.-S.; Formal Analysis, M.S.; Data Curation, M.S.; Writing-Original Draft Preparation, M.S.; Writing-Review & Editing, A.M., Q.K.H., and N.E.-S.; Supervision, Q.K.H., and N.E.-S.; Funding Acquisition, M.S.

Acknowledgments

The authors would like to thank: (i) both NASA and JAXA for providing various types of the satellite precipitation products; and (ii) Ministry of Regional Municipalities and Water Resources, the Sultanate of Oman for providing rain gauge data.

Conflicts of Interest

The authors declare no conflict of interest

(2B) QUANTIFYING UNCERTAINTIES ASSOCIATED WITH DIFFERENT GLOBAL SATELLITE ESTIMATES USING STATISTICAL ERROR MODELS

2B.1. Introduction and Background

Quantifying precipitation is a complex process since it is highly variable at a small scale and time [1], [2]. A variety of satellite platforms have been used to build a global precipitation network by combining from visible, infrared (IR), and/or passive microwave (PMW) data [62]. Global Satellite Precipitation Estimates (GSPEs) such as Precipitation Estimation from Remotely Sensed Information using Artificial Neural Networks (PERSIANN) [63], the US National Oceanic Atmospheric Administration (NOAA) Climate Prediction Center's (CPC) morphing technique (CMORPH) [64], and the National Aeronautics and Space Administration (NASA) Tropical Rainfall Measuring Mission (TRMM) Multi-satellite Precipitation Analysis (TMPA) [2] have great potential for scientific research on climate and hydrology. However, numerous studies have revealed that GSPEs showed non-negligible bias when compared with in-situ gauge observations (e.g., [65], [66]). GSPEs involve indirect precipitation estimates from visible-, IR-, and/or PMW-based cloud properties information. Therefore, they include Inherent biases, and quantifying uncertainties in the satellite precipitation estimates is essential to overcome the underestimation or exaggeration of the actual rainfall values [67].

Considerable progress has been achieved in recent years in the development and availability of real-time GSPEs' algorithms. However, GSPEs still include major biases that need to be quantified and adjusted before the precipitation products can be used in different hydrological applications. These inherent biases are mainly due to the inaccurate estimation of climate variables and their temporal variations, or the incorrect detection of rainfall events [68].

Different bias correction schemes for GSPEs were utilized in various studies such as the study by Kim et al. [69]. They indicated that GSPEs require post-processing of bias

adjustment. Different approaches for modeling the errors in the GSPEs were introduced such as the linear scaling (e.g., [70]), additive error model (e.g., [71][72]), and multiplicative error model (e.g., [71][73]).

GSPEs are prone to systematic and random errors because the satellite precipitation products are indirect rainfall estimates from visible, IR, and/or MW based information of cloud properties [74]. Bias is defined as the systematic error or difference between rain gauge estimates and GSPEs and can be positive or negative [75]. Bias can express rainfall depth, occurrence, and intensity [67]. Quantifying the deviation of the GSPEs from the reference datasets serve to correct for systematic errors of the GSPEs and aim to improve the reliability of GSPEs [76]. Statistical error models rely on assumptions that adjust for rainfall variability in space and time [77].

On the one side, many studies of modeling errors in the GSPEs have carried out over different areas of the world such as North America (e.g., [76]), South America (e.g., [66]), Asia (e.g., [78]), Africa (e.g., [68]), Europe (e.g., [60]), and Australia (e.g., [79]). On the other side and up to my best knowledge, there is no studies have been performed to model the daily errors in the GSPEs over the arid Arabian Peninsula. There were two analyses reported by Wehbi et al. [23] and Almazroui et al. [80] over the United Arab Emirates (UAE) and Saudi Arabia, respectively. These studies used the linear regression to quantify the bias associated with TRMM data based on the in-situ monthly-averaged rainfall records throughout 2003–2010 and 1998–2009, respectively.

The GSPEs' errors are mostly related to sampling and retrieval of rain rates [81], [82]. The sampling errors result from estimating the precipitation amount for a continuous spatial and temporal domain with measurements at discrete space and time intervals, such as computing the daily or monthly total precipitation from instantaneous observations at a 3 h interval. The sampling error has studied extensively, and its relationship with rain-rate and spatial/temporal resolution have established both empirically and theoretically (e.g., [83], [84]). As well, this part of the errors is beyond the scope of this research.

The retrieval error arises from the remote-sensing procedures involved to convert satellite observations (brightness temperature) to rain rate. This error type is more complex, because of its dependencies on many factors, including sensor type (i.e., conical vs. cross-track, active vs. passive MW), sensor resolution and viewing geometry, precipitation type, surface type, atmospheric condition, cloud microphysics, and retrieval algorithm itself (e.g., [85], [86]). The retrieval biases can be further decomposed into systematic and random errors. The systematic errors reflect predictable, consistent error behaviors often associated with instrument or algorithm characteristics (e.g., miss calibration), and it can be further decomposed into miss (M), false (F), and hit (H) errors (e.g., [87], [88]). It is, therefore, necessary to assess the contributions of each source of uncertainties in GSPEs before these products used for operational applications. However, validation datasets are limited in terms of both coverage and quality [82]. For these reasons, there is a great difficulty in unambiguously identifying a specific product as “best” in terms of precipitation amount and rate over most of the globe [89], [90]. The random error is the stochastic component that its magnitude directly determines the uncertainty [82].

GSPEs are not always reliable, and consensus has been reached that they require the quantification of the uncertainties associated with these estimates. The in-situ rain gauges’ measurements considered to be the reference data [91] to assess the reliability and accuracy of GSPEs. Tian et al. [71] assumed that the ground rain gauge records are error-free, where the associated biases considered much smaller than those in the GSPEs. Furthermore, it is simple to take these errors into account if they are available or can be determined [92].

Defining and quantifying the uncertainties in GSPEs depend mainly on the underlying mathematical error model that expressed the deviation of satellite estimates from the truth datasets [93]. The error model can predict the precipitation measurements and their associated biases when the reference in-situ rain gauges are available and vice versa [71]. Although there were many studies aimed at evaluating GPSEs, they were limited to specific regions, and modeling the errors in the daily GSPEs in the arid Arabian Peninsula has not systematically investigated enough to date. The different performance of GSPEs makes it mandatory to determine whether a product is suitable for a specific environment or region.

In the current research, the performance of the Global Precipitation Mission (GPM)-Integrated Multi-satellitE Retrievals for the GPM (IMERG) and Global Satellite Mapping of Precipitation (GSMaP) the in the arid region of the Sultanate of Oman using rain measurements from 38 in-situ ground gauges were performed. The statistical additive and multiplicative error models were used to quantify the deviation of the GSPEs from the in-situ reference data.

2B.2. Methods

In this study, the error decomposition method introduced by Tian et al. [71] and Habib et al. [88] was utilized, where the total errors were divided into three different components (i.e., H, M, and F, see section 2A.3.2.2. for more details). These components can have substantial magnitudes with coarse spatial and temporal variations.

Next, multiplicative and additive error models [71] have been utilized to quantify the hit errors derived from the above-described error decomposition. The additive and multiplicative models define the bias as the difference and as the ratio between the GSPEs and in-situ rainfall measurements (i.e., the truth), respectively [71]. The additive error model is defined as:

$$Y_i = a + bX_i + \varepsilon_i \quad (2B.1)$$

where i refers to a single in-situ gauge at a certain grid center of the GSPEs (i.e., index), X_i refers to the reference datasets assumed error-free, Y_i points to the estimates, a denotes the offset, b is a scale parameter to compute the differences in the dynamic ranges between the ground rainfall observations and GSPEs, and ε_i is a random error of zero mean and variance of σ^2 . This model is defined by three parameters, namely, a , b , and σ , where a and b quantify the deterministic systematic error and σ specify the random error in the estimates Y_i .

While the multiplicative model is presented by the following equation:

$$Y_i = aX_i^b e^{\varepsilon_i} \quad (2B.2)$$

where a and b denote for the systematic error that represents a non-linear function of the reference data. The random error e^{ε_i} is a multiplicative factor, with the average of being zero and the variance σ^2 .

The three parameters (a , b , and σ) of both models (Equations 2B.1 and 2B.2) can be estimated with the ordinary least squares (OLS) assuming the residuals (random errors) are uncorrelated with a constant variance σ^2 (e.g., [43]).

Meanwhile, if a natural logarithm transformation of the variables in Equation (2B.2) was performed, the multiplicative model becomes as follows:

$$\ln(Y)_i = \ln(a) + b \ln(X_i) + \varepsilon_i \quad (2B.3)$$

which is also a simple linear regression in the transformed domain, and the parameters can be estimated with the same OLS procedure. To have statistically reliable results, the entire in-situ rain gauge measurements and the corresponding GSPEs were divided for training (70%) and testing (30%) both additive and multiplicative error models and cross-validated for ten times (i.e., runs). The statistical metrics (i.e., mean difference (MD) and root mean square error (RMSE)) were used to evaluate the performances of both additive and multiplicative models in quantifying the errors associated with different GSPEs at accumulated and classified rainfall intensities per day.

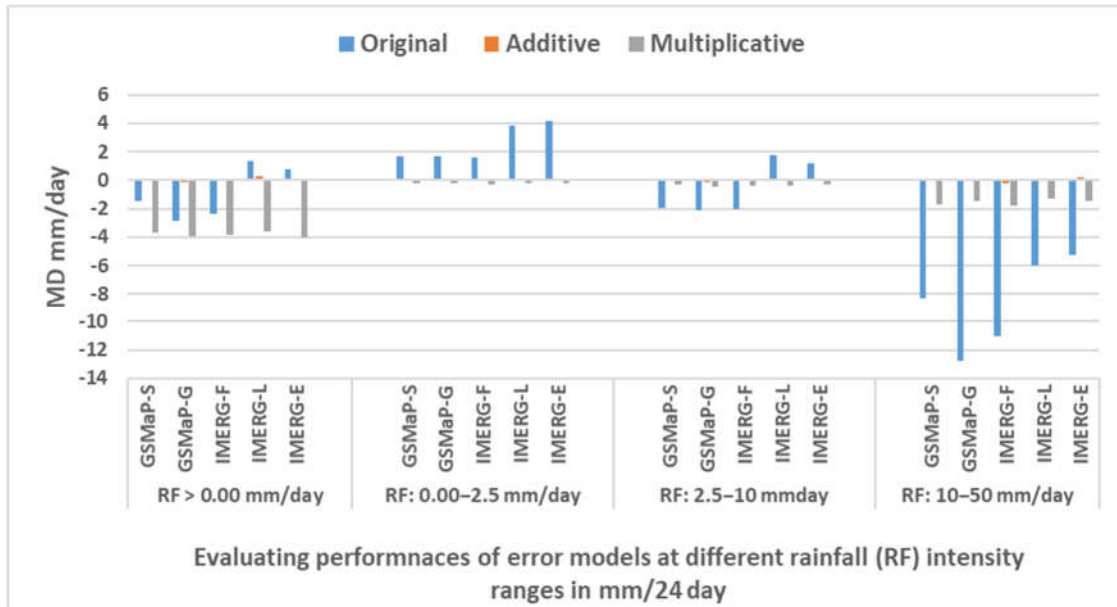
2B.3. Results

In general, based on the estimated RMSE's small values and MD close to zero values, the additive and multiplicative error models were able to quantify the deviation of the GSPEs from the in-situ reference data at classified rainfall intensities per day (Figures 2B.1a, and 2B.1b) (Appendix A).

After using the error models, the performance metrics were calculated with respect to predicted GSPEs and associated uncertainties based on the reference datasets. Using the MD measure, Figure 2B.1a shows that the additive error model was able to significantly reduce the rate of the under- and over-estimation per the total and classified rainfall intensities. The multiplicative model provided close performance to the additive one, but with reporting lower performance's values than those reported by additive model at the three classified rainfall intensities.

Figure 2B.1b displays RMSE values that were resulted from utilizing error models. The RMSE values were generally low after using the additive and multiplicative models, particularly at categorized rainfall intensities. At the total rainfall intensity per day, the additive model showed a slight improvement in providing lower RMSE values than those reported before using error models. The multiplicative model failed to improve the results in the latter case except in the case of IMERG-E. Though the additive model was superior to the performance of the multiplicative one in modeling the errors in the GSPEs, where both models showed low RMSEs at different rainfall intensity classes. The results reported by both additive and multiplicative error models were statistically significant [94], [95], with reporting p-values of less than 0.001 ($< .001$) at each run at total and classified rainfall intensities. There were few runs in case of GSMaP where p-values were less than 0.01 ($< .01$).

(a)



(b)

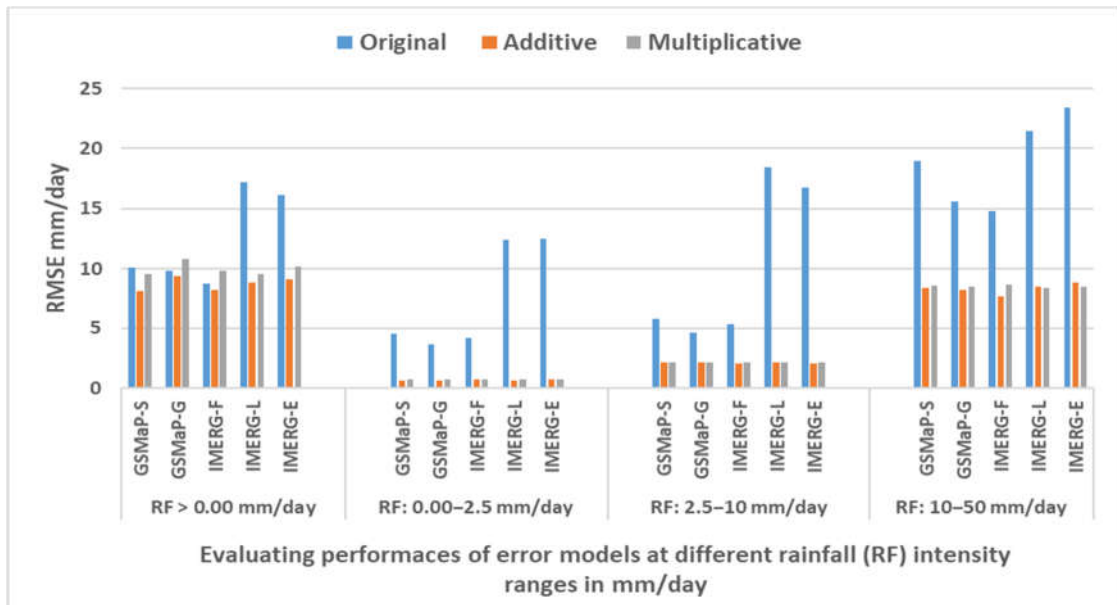


Figure 2B.1. Evaluating performance of the additive and multiplicative error models in quantifying the uncertainties in the GSPEs at different rainfall intensity classes using: (a) MD and (b) RMSE.

2B.4. Discussion

The additive error model essentially defines the error as the difference between the measurement and the truth data, while the multiplicative error model expresses the error as the ratio between the two. The current findings indicated that the additive scheme was able to quantify the uncertainties associated with GSPEs per the accumulated total rainfall per day. In general, the additive model outperformed multiplicative one in computing the errors in the five daily GSPEs at different rainfall intensity classes.

Tian et al. [71] noted that the multiplicative error model is a better choice than the adaptive model in estimating the deviation of the GSPEs from the truth datasets. It was more consistent with the large variability of precipitation estimates and can detect systematic errors more cleanly and equally well on a daily scale. On the one side, the current results contradict with Tian et al. [71], where the multiplicative error model failed to quantify the uncertainties in the GSPEs at the accumulated rainfall intensity per day. On the other hand, the current outcomes matched with Tian et al. [71], where the multiplicative error approach showed better performance for quantifying the errors associated with the daily GSPEs at rainfall intensity classes of 0.00–2.5, 2.5–10, and 10–50 mm/day. However, based on MD and RMSE values, the additive error model provided better performance than the multiplicative model at most of the rainfall intensity classes. The differences between both findings could be interpreted by: (1) different scale of both studies, where the current analysis was carried out at local scale over a particular area at the Sultanate of Oman, and the other study was performed with a regional scale over the entire USA, (2) the climate were mostly consistent over the current area of study, while it was varied over the USA, (3) different data used in both studies, wherein the present study, the GSMaP and GPM-IMERG products with spatial resolution 10 km were utilized, while the other study used TRMM-3B42RT with a spatial details of 25 km, and (4) different reference datasets where the current research utilized in-situ rain gauge measurements of point scales, and other study used the pixel-based Climate Prediction Center (CPC) Unified Daily Gauge Dataset [96].

2B.5. Conclusions

In this study, the additive and multiplicative error models were used to model the errors in the daily GSPEs. The daily 38 rainfall gauges stations for the period 2014–2016 were used for the purpose of evaluation at the Sultanate of Oman. The additive bias method was more effective than the multiplicative method in computing the uncertainties associated with GSPEs at different rainfall classes. It is worth mentioning that the multiplicative error scheme also performs in some cases closely to the additive one at different rainfall classes. The analyses showed that the statistical additive approach performed well in case of GSMaP-G and GSMaP-S products. Additionally, the other IMERG products behaved reasonably with the two error approaches. This finding is very important because based on the required application and degree of accuracy, it could be possible to use the IMERG products with shorter time latencies. The current results indicated that modeling the errors in the GSPEs, in regions of arid climate, can be carried out using an additive approach. The achieved finding can be valuable for both algorithm developers and end-data users. It is recommended to explore the role of additional error models in quantifying the uncertainties associated with GSPEs over other arid areas and over longer evaluation periods.

References

- [1] L. A. Blacutt, D. L. Herdies, L. G. G. de Gonçalves, D. A. Vila, and M. Andrade, “Precipitation comparison for the CFSR, MERRA, TRMM3B42 and Combined Scheme datasets in Bolivia,” *Atmos. Res.*, vol. 163, pp. 117–131, Sep. 2015.
- [2] G. J. Huffman *et al.*, “The TRMM Multisatellite Precipitation Analysis (TMPA): Quasi-Global, Multiyear, Combined-Sensor Precipitation Estimates at Fine Scales,” *J. Hydrometeorol.*, vol. 8, no. 1, pp. 38–55, Feb. 2007.
- [3] B. Alhammoud, C. Claud, B. Funatsu, K. Béranger, and J.-P. Chaboureau, “Patterns of Precipitation and Convection Occurrence over the Mediterranean Basin Derived from a Decade of Microwave Satellite Observations,” *Atmosphere (Basel)*, vol. 5, no. 2, pp. 370–398, May 2014.
- [4] E. De Coning and E. Poolman, “South African Weather Service operational satellite based precipitation estimation technique: Applications and improvements,” *Hydrol. Earth Syst. Sci.*, vol. 15, no. 4, pp. 1131–1145, Apr. 2011.
- [5] T. Bangira, B. H. P. Maathuis, T. Dube, and T. W. Gara, “Investigating flash floods potential areas using ASCAT and TRMM satellites in the Western Cape Province, South Africa,” *Geocarto Int.*, vol. 6049, no. 7, pp. 1–18, Aug. 2015.
- [6] U. Germann, G. Galli, M. Boscacci, and M. Bolliger, “Radar precipitation measurement in a mountainous region,” *Q. J. R. Meteorol. Soc.*, vol. 132, no. 618, pp. 1669–1692, Jul. 2006.
- [7] A. Y. Hou *et al.*, “The Global Precipitation Measurement Mission,” *Bull. Am. Meteorol. Soc.*, vol. 95, no. 5, pp. 701–722, May 2014.
- [8] K. O. Asante, R. D. Macuacua, G. A. Artan, R. W. Lietzow, and J. P. Verdin, “Developing a flood monitoring system from remotely sensed data for the Limpopo

- basin,” *IEEE Trans. Geosci. Remote Sens.*, vol. 45, no. 6, pp. 1709–1714, Jun. 2007.
- [9] A. S. Gebregiorgis and F. Hossain, “How well can we estimate error variance of satellite precipitation data around the world?,” *Atmos. Res.*, vol. 154, pp. 39–59, Mar. 2015.
- [10] C. Kidd, D. R. Kniveton, M. C. Todd, and T. J. Bellerby, “Satellite Rainfall Estimation Using Combined Passive Microwave and Infrared Algorithms,” *J. Hydrometeorol.*, vol. 4, no. 6, pp. 1088–1104, Dec. 2003.
- [11] F. J. Tapiador *et al.*, “Global precipitation measurement: Methods, datasets and applications,” *Atmos. Res.*, vol. 104–105, no. 1, pp. 70–97, Feb. 2012.
- [12] S. Michaelides, V. Levizzani, E. Anagnostou, P. Bauer, T. Kasparis, and J. E. Lane, “Precipitation: Measurement, remote sensing, climatology and modeling,” *Atmos. Res.*, vol. 94, no. 4, pp. 512–533, Sep. 2009.
- [13] I. Strangeways, “Improving precipitation measurement,” *Int. J. Climatol.*, vol. 24, no. 11, pp. 1443–1460, Sep. 2004.
- [14] T. Cohen Liechti, J. P. Matos, J. L. Boillat, and A. J. Schleiss, “Comparison and evaluation of satellite derived precipitation products for hydrological modeling of the Zambezi River Basin,” *Hydrol. Earth Syst. Sci.*, vol. 16, no. 2, pp. 489–500, Feb. 2012.
- [15] M. Pan, H. Li, and E. Wood, “Assessing the skill of satellite-based precipitation estimates in hydrologic applications,” *Water Resour. Res.*, vol. 46, no. 9, p. W09535, Sep. 2010.
- [16] H. Zhao, S. Yang, S. You, Y. Huang, Q. Wang, and Q. Zhou, “Comprehensive Evaluation of Two Successive V3 and V4 IMERG Final Run Precipitation Products over Mainland China,” *Remote Sens.*, vol. 10, no. 2, p. 34, Dec. 2017.

- [17] J. Su, H. Lü, Y. Zhu, X. Wang, and G. Wei, “Component Analysis of Errors in Four GPM-Based Precipitation Estimations over Mainland China,” *Remote Sens.*, vol. 10, no. 9, p. 1420, Sep. 2018.
- [18] A. Milewski, R. Elkadiri, M. Durham, A. Milewski, R. Elkadiri, and M. Durham, “Assessment and Comparison of TMPA Satellite Precipitation Products in Varying Climatic and Topographic Regimes in Morocco,” *Remote Sens.*, vol. 7, no. 5, pp. 5697–5717, May 2015.
- [19] F. Satgé *et al.*, “Benefits of the Successive GPM Based Satellite Precipitation Estimates IMERG–V03, –V04, –V05 and GSMaP–V06, –V07 Over Diverse Geomorphic and Meteorological Regions of Pakistan,” *Remote Sens.*, vol. 10, no. 9, p. 1373, Aug. 2018.
- [20] J. R. Rozante, D. A. Vila, J. Barboza Chiquetto, A. D. A. Fernandes, and D. Souza Alvim, “Evaluation of TRMM/GPM Blended Daily Products over Brazil,” *Remote Sens.*, vol. 10, no. 6, p. 882, Jun. 2018.
- [21] M. T. Mahmoud, M. A. Al-Zahrani, and H. O. Sharif, “Assessment of global precipitation measurement satellite products over Saudi Arabia,” *J. Hydrol.*, vol. 559, pp. 1–12, Apr. 2018.
- [22] M. T. Mahmoud, M. A. Hamouda, M. Mostafa, and M. M. Mohamed, “Spatiotemporal evaluation of the GPM satellite precipitation products over the United Arab Emirates,” *Atmos. Res.*, vol. 219, no. January, pp. 200–212, May 2019.
- [23] Y. Wehbe, D. Ghebreyesus, M. Temimi, A. Milewski, and A. Al Mandous, “Assessment of the consistency among global precipitation products over the United Arab Emirates,” *J. Hydrol. Reg. Stud.*, vol. 12, no. December 2016, pp. 122–135, Aug. 2017.
- [24] A. Y. Kwarteng, A. S. Dorvlo, and G. T. Vijaya Kumar, “Analysis of a 27-year rainfall

- data (1977-2003) in the Sultanate of Oman,” *Int. J. Climatol.*, vol. 29, no. 4, pp. 605–617, Mar. 2009.
- [25] M. S. Al-Kalbani, J. C. Martin FP, and M. F. Price, “Recent Trends in Temperature and Precipitation in Al Jabal Al Akhdar, Sultanate of Oman, and the Implications for Future Climate Change,” *J. Earth Sci. Clim. Change*, vol. 06, no. 08, p. 9, Sep. 2015.
- [26] C. FAO, Mountain Partnership Secretariat, UNCCD, SDC, *Highlands and Drylands: Mountains, a Source of Resilience in Arid Regions*. FAO, UNCCD, Mountain Partnership, Swiss Agency for Development and Cooperation, and CDE, with the support of an international group of experts. Rome, 2011.
- [27] G. Al-Rawas and C. Valeo, “Relationship between wadi drainage characteristics and peak-flood flows in arid northern Oman,” *Hydrol. Sci. J.*, vol. 55, no. 3, pp. 377–393, Apr. 2010.
- [28] F. El-Baz *et al.*, *Wadis of Oman : Satellite Image Atlas*. Stacey International, 2002.
- [29] G. A. Al-Rawas and C. Valeo, “Characteristics of rainstorm temporal distributions in arid mountainous and coastal regions,” *J. Hydrol.*, vol. 376, no. 1–2, pp. 318–326, Sep. 2009.
- [30] Y. Charabi, “Arabian summer monsoon variability: Teleconexion to ENSO and IOD,” *Atmos. Res.*, vol. 91, no. 1, pp. 105–117, Jan. 2009.
- [31] J. Laurencelle, T. Logan, and R. Gens, “Alaska Satellite Facility (ASF) - Radiometrically terrain corrected ALOS PALSAR products,” 2015.
- [32] Environmental Systems Research Institute (ESRI), “World Imagery: DigitalGlobe, GeoEye, i-cubed, USDA FSA, USGS, AEX, Getmapping, Aerogrid, IGN, IGP, swisstopo, and the GIS User Community,” 2018. [Online]. Available: <https://www.arcgis.com/home/item.html?id=10df2279f9684e4a9f6a7f08febac2a9>. [Accessed: 04-Jan-2019].

- [33] G. J. Huffman, N. Gsfc, D. T. Bolvin, D. Braithwaite, K. Hsu, and R. Joyce, “Algorithm Theoretical Basis Document (ATBD) NASA Global Precipitation Measurement (GPM) Integrated Multi-satellitE Retrievals for GPM (IMERG),” NASA Goddard Earth Sciences Data and Information Services Center, Greenbelt, MD, USA, 2017.
- [34] G. J. Huffman, D. T. Bolvin, E. J. Nelkin, and E. F. Stocker, “V04 IMERG Early and Late Run Release Notes,” NASA Goddard Earth Sciences Data and Information Services Center, Greenbelt, MD, USA, 2017.
- [35] G. J. Huffman, D. T. Bolvin, E. J. Nelkin, and E. F. Stocker, “V04 IMERG Final Run Release Notes,” NASA Goddard Earth Sciences Data and Information Services Center, Greenbelt, MD, USA, 2017.
- [36] T. Ushio *et al.*, “A Kalman filter approach to the global satellite mapping of precipitation (GSMaP) from combined passive microwave and infrared radiometric data,” *J. Meteorol. Soc. Japan*, vol. 87A, pp. 137–151, Mar. 2009.
- [37] K. Aonashi *et al.*, “GSMaP passive microwave precipitation retrieval algorithm : Algorithm description and validation,” *J. Meteorol. Soc. Japan*, vol. 87A, pp. 119–136, Mar. 2009.
- [38] T. Kubota *et al.*, “Global precipitation map Using satellite-borne microwave radiometers by the GSMaP project: production and validation,” *IEEE Trans. Geosci. Remote Sens.*, vol. 45, no. 7, pp. 2259–2275, Jul. 2007.
- [39] Goddard Earth Sciences Data and Information Services Center (GES DISC) - NASA, “How to Import HDF5-formatted IMERG GPM Precipitation Data into ArcGIS.” [Online]. Available: <https://disc.gsfc.nasa.gov/information/howto?title=How to Import HDF5-formatted IMERG GPM Precipitation Data into ArcGIS>. [Accessed: 28-Nov-2019].

- [40] M. Llasat, “An objective classification of rainfall events on the basis of their convective features: application to rainfall intensity in the northeast of Spain,” *Int. J. Climatol.*, vol. 21, no. 11, pp. 1385–1400, Sep. 2001.
- [41] E. Sharifi, R. Steinacker, and B. Saghafian, “Assessment of GPM-IMERG and Other Precipitation Products against Gauge Data under Different Topographic and Climatic Conditions in Iran: Preliminary Results,” *Remote Sens.*, vol. 8, no. 2, p. 135, Feb. 2016.
- [42] A. Milewski *et al.*, “A remote sensing solution for estimating runoff and recharge in arid environments,” *J. Hydrol.*, vol. 373, no. 1–2, pp. 1–14, Jun. 2009.
- [43] D. S. Wilks, *Statistical Methods in the Atmospheric Sciences*, vol. 100. Elsevier; 3rd ed., 2011.
- [44] A. Rossa, P. Nurmi, and E. Ebert, “Overview of methods for the verification of quantitative precipitation forecasts,” in *In: Michaelides S. (eds) Precipitation: Advances in Measurement, Estimation and Prediction*, Springer, Berlin, Heidelberg, 2008, pp. 419–452.
- [45] A. Boluwade, T. Stadnyk, V. Fortin, and G. Roy, “Assimilation of precipitation Estimates from the Integrated Multisatellite Retrievals for GPM (IMERG, early Run) in the Canadian Precipitation Analysis (CaPA),” *J. Hydrol. Reg. Stud.*, vol. 14, pp. 10–22, Dec. 2017.
- [46] V. Fortin, G. Roy, N. Donaldson, and A. Mahidjiba, “Assimilation of radar quantitative precipitation estimations in the Canadian Precipitation Analysis (CaPA),” *J. Hydrol.*, vol. 531, pp. 296–307, Dec. 2015.
- [47] M. S. Nashwan, S. Shahid, and X. Wang, “Assessment of satellite-based precipitation measurement products over the hot desert climate of Egypt,” *Remote Sens.*, vol. 11, no. 5, p. 555, Mar. 2019.

- [48] M. T. Chahine, “The hydrological cycle and its influence on climate,” *Nature*, vol. 359, no. 6394, pp. 373–380, Oct. 1992.
- [49] J. Sitterson *et al.*, “A Survey of Precipitation Data for Environmental Modeling,” Washington, DC, 2017.
- [50] S. Saksena, V. Merwade, and P. J. Singhofen, “Flood inundation modeling and mapping by integrating surface and subsurface hydrology with river hydrodynamics,” *J. Hydrol.*, vol. 575, pp. 1155–1177, Aug. 2019.
- [51] M. Shawky, A. Moussa, Q. K. Hassan, and N. El-Sheimy, “Pixel-based geometric assessment of channel networks/orders derived from global spaceborne digital elevation models,” *Remote Sens.*, vol. 11, no. 3, p. 235, Jan. 2019.
- [52] M. L. Kavvas *et al.*, “Watershed Environmental Hydrology (WEHY) Model Based on Upscaled Conservation Equations: Hydrologic Module,” *J. Hydrol. Eng.*, vol. 9, no. 6, pp. 450–464, Nov. 2004.
- [53] Q. Ma, L. Xiong, D. Liu, C.-Y. Xu, and S. Guo, “Evaluating the Temporal Dynamics of Uncertainty Contribution from Satellite Precipitation Input in Rainfall-Runoff Modeling Using the Variance Decomposition Method,” *Remote Sens.*, vol. 10, no. 12, p. 1876, Nov. 2018.
- [54] Y. Shu, H. Li, and Y. Lei, “Modelling Groundwater Flow with MIKE SHE Using Conventional Climate Data and Satellite Data as Model Forcing in Haihe Plain, China,” *Water*, vol. 10, no. 10, p. 1295, Sep. 2018.
- [55] M. Park *et al.*, “A Comparison Study of Runoff Characteristics of Non-Point Source Pollution from Three Watersheds in South Korea,” *Water*, vol. 11, no. 5, p. 966, May 2019.
- [56] L. Yi, W. Zhang, and X. Li, “Assessing Hydrological Modelling Driven by Different Precipitation Datasets via the SMAP Soil Moisture Product and Gauged Streamflow

- Data,” *Remote Sens.*, vol. 10, no. 12, p. 1872, Nov. 2018.
- [57] A. H. M. Siddique-E-Akbor *et al.*, “Satellite Precipitation Data–Driven Hydrological Modeling for Water Resources Management in the Ganges, Brahmaputra, and Meghna Basins,” *Earth Interact.*, vol. 18, no. 17, pp. 1–25, Nov. 2014.
- [58] J. Sillmann *et al.*, “Understanding, modeling and predicting weather and climate extremes: Challenges and opportunities,” *Weather Clim. Extrem.*, vol. 18, pp. 65–74, Dec. 2017.
- [59] A. M. Dewan, *Floods in a megacity: Geospatial techniques in assessing hazards, risk and vulnerability*. Springer, 2013.
- [60] M. Saber and K. Yilmaz, “Evaluation and Bias Correction of Satellite-Based Rainfall Estimates for Modelling Flash Floods over the Mediterranean region: Application to Karpuz River Basin, Turkey,” *Water*, vol. 10, no. 5, p. 657, May 2018.
- [61] Y. Tuo, Z. Duan, M. Disse, and G. Chiogna, “Evaluation of precipitation input for SWAT modeling in Alpine catchment: A case study in the Adige river basin (Italy),” *Sci. Total Environ.*, vol. 573, pp. 66–82, Dec. 2016.
- [62] Y. Yang and Y. Luo, “Evaluating the performance of remote sensing precipitation products CMORPH, PERSIANN, and TMPA, in the arid region of northwest China,” *Theor. Appl. Climatol.*, vol. 118, no. 3, pp. 429–445, Jan. 2014.
- [63] K. Hsu *et al.*, “Precipitation Estimation from Remotely Sensed Information Using Artificial Neural Networks,” *J. Appl. Meteorol.*, vol. 36, no. 9, pp. 1176–1190, Sep. 1997.
- [64] R. J. Joyce *et al.*, “CMORPH: A Method that Produces Global Precipitation Estimates from Passive Microwave and Infrared Data at High Spatial and Temporal Resolution,” *J. Hydrometeorol.*, vol. 5, no. 3, pp. 487–503, Jun. 2004.

- [65] W. Sun *et al.*, “Evaluation and Correction of GPM IMERG Precipitation Products over the Capital Circle in Northeast China at Multiple Spatiotemporal Scales,” *Adv. Meteorol.*, vol. 2018, pp. 1–14, Dec. 2018.
- [66] A. Beaufort, F. Gibier, and P. Palany, “Assessment and correction of three satellite rainfall estimate products for improving flood prevention in French Guiana,” *Int. J. Remote Sens.*, vol. 40, no. 1, pp. 171–196, Jan. 2019.
- [67] W. Gumindoga, T. H. M. Rientjes, A. T. Haile, H. Makurira, and P. Reggiani, “Bias correction schemes for CMORPH satellite rainfall estimates in the Zambezi River Basin,” *Hydrol. Earth Syst. Sci. Discuss.*, vol. 23, no. 7, pp. 1–36, Jul. 2016.
- [68] R. Valdés-Pineda, E. M. C. Demaría, J. B. Valdés, S. Wi, and A. Serrat-Capdevilla, “Bias correction of daily satellite-based rainfall estimates for hydrologic forecasting in the Upper Zambezi, Africa,” *Hydrol. Earth Syst. Sci. Discuss.*, pp. 1–28, Sep. 2016.
- [69] K. B. Kim, M. Bray, and D. Han, “An improved bias correction scheme based on comparative precipitation characteristics,” *Hydrol. Process.*, vol. 29, no. 9, pp. 2258–2266, Apr. 2015.
- [70] M. Luo *et al.*, “Comparing Bias Correction Methods Used in Downscaling Precipitation and Temperature from Regional Climate Models: A Case Study from the Kaidu River Basin in Western China,” *Water*, vol. 10, no. 8, p. 1046, Aug. 2018.
- [71] Y. Tian *et al.*, “Modeling errors in daily precipitation measurements: Additive or multiplicative?,” *Geophys. Res. Lett.*, vol. 40, no. 1–6, pp. 2060–2065, Mar. 2013.
- [72] R. Roca *et al.*, “Comparing Satellite and Surface Rainfall Products over West Africa at Meteorologically Relevant Scales during the AMMA Campaign Using Error Estimates,” *J. Appl. Meteorol. Climatol.*, vol. 49, no. 4, pp. 715–731, Apr. 2010.
- [73] G. J. Ciach, W. F. Krajewski, G. Villarini, G. J. Ciach, W. F. Krajewski, and G. Villarini, “Product-Error-Driven Uncertainty Model for Probabilistic Quantitative

- Precipitation Estimation with NEXRAD Data,” *J. Hydrometeorol.*, vol. 8, no. 6, pp. 1325–1347, Dec. 2007.
- [74] A. J. Pereira Filho *et al.*, “Satellite rainfall estimates over South America - Possible applicability to the water management of large watersheds1,” *J. Am. Water Resour. Assoc.*, vol. 46, no. 2, pp. 344–360, Apr. 2010.
- [75] S. Moazami, S. Golian, M. R. Kavianpour, and Y. Hong, “Uncertainty analysis of bias from satellite rainfall estimates using copula method,” *Atmos. Res.*, vol. 137, pp. 145–166, 2014.
- [76] K. Tesfagiorgis, S. E. Mahani, N. Y. Krakauer, and R. Khanbilvardi, “Bias correction of satellite rainfall estimates using a radar-gauge product – a case study in Oklahoma (USA),” *Hydrol. Earth Syst. Sci.*, vol. 15, no. 8, pp. 2631–2647, Aug. 2011.
- [77] E. Habib, A. Haile, N. Sazib, Y. Zhang, and T. Rientjes, “Effect of Bias Correction of Satellite-Rainfall Estimates on Runoff Simulations at the Source of the Upper Blue Nile,” *Remote Sens.*, vol. 6, no. 7, pp. 6688–6708, Jul. 2014.
- [78] H. Le, J. Sutton, D. Bui, J. Bolten, and V. Lakshmi, “Comparison and Bias Correction of TMPA Precipitation Products over the Lower Part of Red–Thai Binh River Basin of Vietnam,” *Remote Sens.*, vol. 10, no. 10, p. 1582, Oct. 2018.
- [79] R. C. Pipunic, D. Ryu, J. F. Costelloe, and C.-H. Su, “An evaluation and regional error modeling methodology for near-real-time satellite rainfall data over Australia,” *J. Geophys. Res. Atmos.*, vol. 120, no. 20, p. 10,767–10,783, Oct. 2015.
- [80] M. Almazroui, “Calibration of TRMM rainfall climatology over Saudi Arabia during 1998–2009,” *Atmos. Res.*, vol. 99, no. 3–4, pp. 400–414, 2011.
- [81] M. Gebremichael and W. F. Krajewski, “Characterization of the temporal sampling error in space-time-averaged rainfall estimates from satellites,” *J. Geophys. Res.*, vol.

- 109, no. D11, p. D11110, Jun. 2004.
- [82] L. Tang, Y. Tian, F. Yan, and E. Habib, “An improved procedure for the validation of satellite-based precipitation estimates,” *Atmos. Res.*, vol. 163, pp. 61–73, Sep. 2015.
- [83] B. Nijssen and D. P. Lettenmaier, “Effect of precipitation sampling error on simulated hydrological fluxes and states: Anticipating the Global Precipitation Measurement satellites,” *J. Geophys. Res.*, vol. 109, no. D2, p. D02103, Jan. 2004.
- [84] T. L. Bell, P. K. Kundu, C. D. Kummerow, T. L. Bell, P. K. Kundu, and C. D. Kummerow, “Sampling Errors of SSM/I and TRMM Rainfall Averages: Comparison with Error Estimates from Surface Data and a Simple Model,” *J. Appl. Meteorol.*, vol. 40, no. 5, pp. 938–954, May 2001.
- [85] L. Tang, Y. Tian, and X. Lin, “Validation of precipitation retrievals over land from satellite-based passive microwave sensors,” *J. Geophys. Res. Atmos.*, vol. 119, no. 8, pp. 4546–4567, Apr. 2014.
- [86] Y. Tian and C. D. Peters-Lidard, “Systematic anomalies over inland water bodies in satellite-based precipitation estimates,” *Geophys. Res. Lett.*, vol. 34, no. 14, p. L14403, Jul. 2007.
- [87] F. Hossain and E. N. Anagnostou, “A two-dimensional satellite rainfall error model,” *IEEE Trans. Geosci. Remote Sens.*, vol. 44, no. 6, pp. 1511–1522, Jun. 2006.
- [88] E. Habib, A. Henschke, and R. F. Adler, “Evaluation of TMPA satellite-based research and real-time rainfall estimates during six tropical-related heavy rainfall events over Louisiana, USA,” *Atmos. Res.*, vol. 94, no. 3, pp. 373–388, Nov. 2009.
- [89] A. T. Haile, F. Yan, and E. Habib, “Accuracy of the CMORPH satellite-rainfall product over Lake Tana Basin in Eastern Africa,” *Atmos. Res.*, vol. 163, pp. 177–187, Sep. 2015.

- [90] R. F. Adler *et al.*, “Intercomparison of Global Precipitation Products: The Third Precipitation Intercomparison Project (PIP-3),” *Bull. Am. Meteorol. Soc.*, vol. 82, no. 7, pp. 1377–1396, Jul. 2001.
- [91] H. A. Bhatti, T. Rientjes, A. T. Haile, E. Habib, and W. Verhoef, “Evaluation of bias correction method for satellite-based rainfall data,” *Sensors*, vol. 16, no. 6, Jun. 2016.
- [92] W. F. Krajewski, G. J. Ciach, J. R. McCollum, and C. Bacotiu, “Initial Validation of the Global Precipitation Climatology Project Monthly Rainfall over the United States,” *J. Appl. Meteorol.*, vol. 39, no. 7, pp. 1071–1086, Jul. 2000.
- [93] W. G. Lawson, J. A. Hansen, W. G. Lawson, and J. A. Hansen, “Alignment Error Models and Ensemble-Based Data Assimilation,” *Mon. Weather Rev.*, vol. 133, no. 6, pp. 1687–1709, Jun. 2005.
- [94] S. Liu, D. Yan, T. Qin, B. Weng, and M. Li, “Correction of TRMM 3B42V7 Based on Linear Regression Models over China,” *Adv. Meteorol.*, vol. 2016, p. 13, Dec. 2016.
- [95] S. Wang, J. Liu, J. Wang, X. Qiao, and J. Zhang, “Evaluation of GPM IMERG V05B and TRMM 3B42V7 Precipitation Products over High Mountainous Tributaries in Lhasa with Dense Rain Gauges,” *Remote Sens.*, vol. 11, no. 18, p. 2080, Sep. 2019.
- [96] M. Chen *et al.*, “Assessing objective techniques for gauge-based analyses of global daily precipitation,” *J. Geophys. Res.*, vol. 113, no. D4, p. D04110, Feb. 2008.

CHAPTER THREE

Pixel-Based Geometric Assessment of Channel Networks/Orders Derived from Global Spaceborne Digital Elevation Models

M. Shawky, A. Moussa, Q. K. Hassan, and N. El-Sheimy, “Pixel-based geometric assessment of channel networks/orders derived from global spaceborne digital elevation models,” *Remote Sens.*, vol. 11, no. 3, p. 235, Jan. 2019.

Abstract

Digital Elevation Models (DEMs) contribute to geomorphological and hydrological applications. DEMs can be derived using different remote sensing-based datasets, such as Interferometric Synthetic Aperture Radar (InSAR) (e.g., Advanced Land Observing Satellite (ALOS) Phased Array type L-band SAR (PALSAR) and Shuttle Radar Topography Mission (SRTM) DEMs). In addition, there is also the Digital Surface Model (DSM) derived from optical tri-stereo ALOS Panchromatic Remote-sensing Instrument for Stereo Mapping (PRISM) imagery. In this study, the satellite-based DEMs, SRTM (Global) GL1 DEM V003 28.5 m, ALOS DSM 28.5 m, and PALSAR DEMs 12.5 m and 28.5 m, and their derived channel networks/orders were evaluated. These assessments were carried out using Light Detection and Ranging (LiDAR) Digital Surface Models (DSMs) and Digital Terrain Models (DTMs) and their derived channel networks and Strahler orders as reference datasets at comparable spatial resolutions. A pixel-based method was introduced for the quantitative horizontal evaluation of the channel networks and Strahler orders derived from global DEMs utilizing confusion matrices at different flow accumulation area thresholds (ATs) and pixel buffer tolerance values (PBTVs) in both $\pm X$ and $\pm Y$ directions. A new Python toolbox for ArcGIS was developed to automate the introduced method. A set of evaluation metrics—(i) producer accuracy (PA), (ii) user accuracy (UA), (iii) F-score (F), and (iv) Cohen's kappa index (KI)—were computed to evaluate the accuracy of the horizontal matching between channel networks/orders extracted from global DEMs and those derived from LiDAR DTMs and DSMs. PALSAR DEM 12.5 m ranked first among the other global DEMs with the lowest root mean square error (RMSE) and mean difference (MD) values of 4.57 m and 0.78 m, respectively, when compared to the LiDAR DTM 12.5 m. The ALOS DSM 28.5 m had the highest vertical accuracy with the lowest recorded RMSE and MD values of 4.01 m and -0.29 m, respectively, when compared to the LiDAR DSM 28.5 m. PALSAR DEM 12.5 m and ALOS DSM 28.5 m-derived channel networks/orders yielded the highest horizontal accuracy when compared to those delineated from LiDAR DTM 12.5 m and LiDAR DSM 28.5 m, respectively. The number of unmatched channels decreased when the PBTV increased from 0 to 3 pixels using different ATs.

3.1. Introduction

Current advances in remote sensing techniques are essential in producing high-quality Digital Elevation Models (DEMs). Because of the general availability of different optical and microwave satellite data-based DEMs, many authors have extensively used these elevation datasets for a wide range of applications, particularly for various hydrological and geomorphological models. The outcomes of these models depend mainly on the accuracy and quality of the utilized DEMs [1]–[6].

In general, a DEM is an umbrella term for any electronically accessible elevation datasets, such as Digital Terrain Models (DTMs) and Digital Surface Models (DSMs). It includes elevation measures of the Earth's terrain, in addition to natural- and human-based objects above a certain vertical datum [7]. Some researchers apply the terms bare-earth DEM and DTM interchangeably, because of their opposite usage in the United States of America (USA) and Europe [8]. A DEM (hereinafter referred to as both DTM and DSM) can be represented mainly by vector- and raster-based spatial representations [9]. The elevation datasets required to create a DEM can be collected using various ground- and satellite-based techniques, including conventional topographic surveys [10], digitizing and interpolation of contours [11], kinematic global navigation satellite system surveys [12], stereo-photogrammetry [13], Synthetic Aperture Radar (SAR) interferometry [14], airborne laser scanning [15], and fusion of data from different sources [16].

The spatial resolution of a DEM is expressed by the geometric size of a cell in the X and Y horizontal directions, in addition to the distance between two adjacent cells [17]. The accuracy of a DEM in representing the land surface mainly depends on its source data's spatial resolution [18]. The more accurate the information, the higher the spatial resolution the DEM can have. A DEM's spatial resolution has been shown to affect the outcomes of many hydrological parameters. For example, it was found that the DEM resolution had a significant effect on the prediction outputs of different hydrologic models, such as the topography-based hydrological model [19] and the soil and water assessment tool model [20]. Furthermore, different DEM sources introduce various levels of spatial details and

accuracies (either horizontal or vertical). Therefore, many hydrological studies fail to provide consistent results. For instance, the DEM source profoundly affected the accuracy of river hydrodynamic modeling outputs, particularly flood extents and depths [21]. The difference between DEM sources and extracted channel networks explicitly affected the outputs of different hydrological models [22], [23]. Schumann et al. [24] noted the impact of an accurate bare-earth DEM on flood modeling. Li and Wong 2010 [3] reported that the simulation results of flood inundation areas varied significantly using channel networks derived from different DEM datasets (Shuttle Radar Topography Mission (SRTM), Light Detection and Ranging (LiDAR), and the National Elevation Dataset). They emphasized the need for evaluating the channel networks extracted from different DEM sources before utilizing them in further hydrologic applications. Vaze et al. [25] confirmed that a LiDAR-based DTM with high accuracy and resolution improved the overall quality of the extracted hydrological features.

In this article, two abbreviations are used to describe DEMs. First is the DTM, which provides information about the heights of bare soil in terms of X, Y, and Z coordinates [26]. X and Y stand for the horizontal position of a point that can be defined by geographic coordinates or by grid coordinates in a map projection system, while Z represents the orthometric or ellipsoidal elevation. Second is the DSM, which represents top faces of all objects situated on a terrain, such as human-made features and natural canopy, in addition to the bare ground itself in open areas [27].

Most of the available global DEM datasets can be considered as compromises between DTM and DSM. For instance, the SRTM DEM was originally generated to provide near-global DTMs for the Earth's land surface. However, a significant positive bias in the SRTM (C-band) DEM was observed in areas with extensive tree and/or shrub coverage (e.g., boreal and Amazon regions) [28]. In addition, the C-band radar imagery used by the NASA Jet Propulsion Laboratory to generate the SRTM DEM could not fully penetrate the vegetation canopy for a region of the Amazon Basin to the ground [29]. Consequently, the SRTM C-band DEM might be more appropriately identified as a DSM. Moreover, for DTM-

based applications requiring accurate estimates of bald-earth elevations, the SRTM DEM may prove unsuitable in its current form [30].

A channel network consists of a set of tributaries and master streams along which the water and sediments are transported under the effect of gravity from higher- to lower-elevation landscapes in a drainage basin [31], [32]. Extracting channel networks from DEMs is mandatory in various hydrological [33] and geomorphological [32] studies. In fact, a drainage system's evolution over time is profoundly affected by different variables, such as geomorphology, geologic units, soil, tectonics, landscape topography, and land cover [34]. The detailed morphometric analysis of a channel network and its watershed can help to characterize the impact of channel morphometry on the landforms [35]. Furthermore, it was used to explicate the hydrological behavior of drainage basins and to quantify surface water potentialities [36].

The widespread availability of remote sensing-based DEMs facilitates the development of new approaches to extract channel networks (e.g., [32], [37]–[40]), as well as precise algorithms to derive surface flow direction (e.g., [37], [39], [41], [42]). DEMs-derived channel networks proved to be more efficient for computing hillslope travel distances [43] and measuring hydrological proximities [44] than traditionally mapped channel networks (i.e., derived from topographic maps, aerial photographs, and field surveying). Vaze et al. [25] stated that channel networks extracted from LiDAR-based DEMs should be used instead of those derived from contour-derived DEMs. Furthermore, the direct delineation of the channel networks from DEMs significantly reduces the amount of human labor [45].

The horizontal assessment of channel networks was rarely discussed in the literature, where Anderson et al. [46] and Mozas-Calvache et al. [47] proposed two vector-based approaches for the horizontal evaluation of stream networks. However, both methods had some constraints in the selection and preparation of the channels for the evaluation.

Requirements for accurate DTMs and DSMs with enhanced spatial details are mandatory for different fields of environmental applications. DSMs are of considerable interest for various applications, such as urban planning [48] and three-dimensional (3-D) city modeling [49]. DTMs are more applicable to different hydrological-related research than DSMs. The DTMs have been applied successfully to determine the spatial distributions of many topographic (e.g., aspect, slope, surface curvature, and gully morphology) [50]–[53] and hydrologic (e.g., flow direction, length, and accumulation) attributes [40]. Furthermore, many hydrologists have used DTMs to extract channel networks accurately [50], [54], [55]. Different geomorphometric measures (e.g., stream order, frequency, density) can be estimated utilizing channel networks. These topographic, hydrologic, and geomorphometric parameters contribute as the primary inputs to various physical and conceptual hydrological models that address the link between hydrological and geomorphic processes operating on the Earth's surface [10], [51].

Recently, airborne LiDAR-based DTMs have been broadly used for various hydrological modeling studies [54], [56], [57], as well as channel network delineation [58], [59]. LiDAR point cloud datasets can be obtained by using airborne or terrestrial instruments. It is a surveying method that measures distances to a target frequently and precisely, and usually LiDAR point cloud measurements render a so-called DSM. It is possible to derive a DTM from a DSM if the distinction between ground and non-ground pixels can be automated (e.g., Sharma et al. [60]).

Note that airborne LiDAR-based DEMs are only available over a small percentage of the Earth's landmass, due to their high cost. Therefore, for many studies—particularly for flood monitoring and flood hazard zoning—researchers have used the freely available remote sensing-based DEMs with global coverage (e.g., Reference [61]–[68]). However, most of these researchers did not investigate the nature of the DEM used (i.e., either a DSM or a DTM) and errors that could profoundly affect their developed models. In addition, most of these studies did not evaluate the horizontal accuracy of the channel networks extracted from different global DEMs to select the optimum channel network for their environmental research.

Each DEM source has intrinsic errors, because of data acquisition technology and processing methodology in relation to specific terrains and land cover types [69]. Many studies have evaluated the vertical elevation accuracy of various DEM datasets using ground truth points of known accurate elevations [14] and pairwise comparisons of different DEMs and/or their surface derivatives (e.g., slope and aspect) by means of conventional statistical metrics, such as root mean square error (RMSE) or mean difference (MD) [25], [69]. Other researchers have assessed different DEMs' vertical accuracy by evaluating the channel network-derived geomorphometric parameters [69]–[72].

Considering the above-mentioned issues, my objectives were five-fold: (i) To evaluate the pixel-based vertical elevation accuracies of spaceborne-based global DEMs (i.e., SRTM DEM 28.5 m, Advanced Land Observing Satellite (ALOS) DSM 28.5 m, and Phased Array type L-band SAR (PALSAR) DEMs 28.5 m and 12.5 m) based on LiDAR-based DTM and DSM utilizing traditional statistical metrics, such as the root mean square error (RMSE) and mean difference (MD), (ii) to introduce a pixel-based technique to assess the horizontal spatial variability in the channel networks/orders extracted from the global elevation sources using those delineated from LiDAR DTM and DSM at similar spatial resolutions and at different pixel buffer tolerance values (PBTVs), (iii) to develop a new Python toolbox for ArcGIS to automate the previous objectives, (iv) to determine which global DEM dataset would be closer in performance to the airborne LiDAR DTM or LiDAR DSM in the study area, and (v) to compare the outcomes of the first and the second objectives to depict the degree of matching between the results achieved from both methods.

3.2. Materials

3.2.1. Study Area

An area covering 235.56 km² in San Luis Obispo County along the western coast of California, USA, was used to test the introduced method. The study area is geographically located between 672,000 m E to 696,000 m E and 3,924,000 m N to 3,940,000 m N (Figure 3.1). It is moderately rugged and has significant variations in the relief height, ranging from

-1 m to +437 m above sea level. Geomorphologically, the area is characterized by a narrow coastal area of steep cliffs, in addition to a coastal range sculpted by hills and valleys [73]. It is also characterized by the presence of the Whale Rock Reservoir to the south. It has a watershed area of 53 km², and the reservoir has a capacity of 50.156 m³ and the maximum water height of 66 m [74]. Geologically, the study area is dominated mainly by sandstone, in addition to exposures of serpentinites, rhyolite, basalt and alluvium terraces [75]. The dominant forests are evergreen, deciduous, and mixed, and their density varies from low to scattered [76], [77]. Furthermore, the area is covered by grassland, and scattered vegetation is present on both sides of the lake. Figure 3.1 shows the area of study at San Luis Obispo County, California, United States of America (USA), where the source of the satellite imagery (top left) is ESRI, 2018 [78].

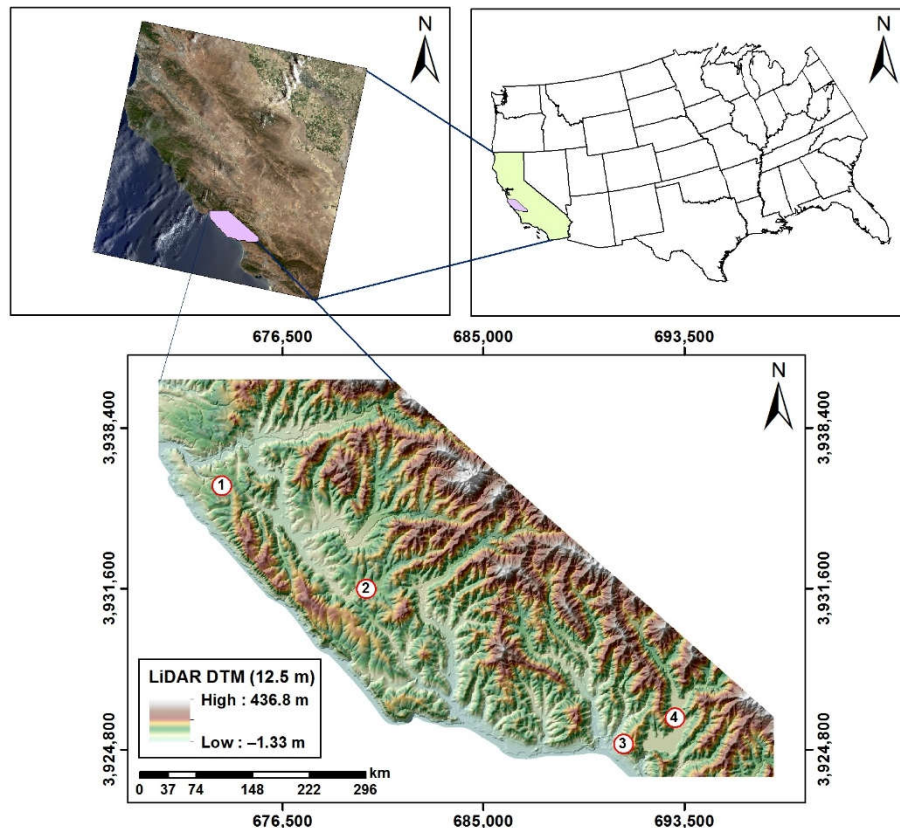


Figure 3.1. The study area in San Luis Obispo County, the western part of the central coast of California, USA. (1 to 4) refer to Cambria, Harmony, Cayucos, and Whale Reservoir, respectively. The source of the satellite imagery (top left) is ESRI, 2018 [78].

3.2.2. Data Requirements

In this study, two types of data were used. One was the global DEM datasets [13], [79]–[81]; their major characteristics are summarized in Table 3.1. The other was the LiDAR point cloud datasets that were acquired for the Diablo Canyon Power Plant (DCCP) San Simeon project for the Pacific Gas and Electric Company (PG&E) [82], California, USA. Although these data were over an area of 810 km², this study deals with an area of 235.56 km² in order to demonstrate the effectiveness and applicability of the proposed approach. The airborne LiDAR point cloud datasets were acquired, calibrated, and verified by Quantum Spatial for the funder PG&E. These LiDAR data were made available to the public through OpenTopography (a public data domain: <https://opentopography.org/>) on 29 March 2013.

Table 3.1. Descriptions of the three global Digital Elevation Models (DEMs). SRTM, Shuttle Radar Topography Mission; ALOS, Advanced Land Observing Satellite; PALSAR, Phased Array type L-band Synthetic Aperture Radar; DSM, Digital Surface Model; ASF DAAC, Alaska Satellite Facility Distributed Active Archive Data Center; JAXA, Japan Aerospace Exploration Agency.

Feature	SRTM GL1 V003 DEM	ALOS PALSAR DEM	ALOS World 3D (ALOS DSM)
Spatial Extent	Near global (60° N to 56° S)	Near global (60° N to 59° S)	Near global (60° N to 60° S)
Spatial Resolution	≈ 28.5 m	12.5 m	≈ 28.5 m
Horizontal Reference	WGS 1984	NAD 83	WGS 1984
Vertical Reference	WGS 1984/EGM 96	NAVD 88	WGS 1984/EGM 96
Sensor Type	Radar (C band)	Radar (L band)	Optical (pan-chromatic band)
Generation Techniques	SAR interferometry	SAR interferometry	Optical stereo matching
Data Access	OpenTopography	ASF DAAC	OpenTopography
Owner Agency	NASA, NGA, DLR	JAXA, NASA	JAXA
Data Type	16-bit signed integer	16-bit signed integer	16-bit signed integer
File Format	GeoTIFF	GeoTIFF	GeoTIFF
Temporal Extent	02/11/2000 - 02/21/2000	2006 - 2011	2017
Additional Details	[79]	[80]	[13], [81]

The LiDAR survey was accomplished using a Leica ALS70 sensor mounted on a Cessna Grand Caravan. The ALS70 system was set to capture a scan angle of 15° from nadir to yield high-resolution data of more than 15 pulses per square meter and a swath width of 191 m over terrestrial surfaces. It flew 1100 m above ground level and acquired at least 240,000 laser pulses per second. The LiDAR scanning was achieved without data voids and gaps, excluding non-reflective surfaces (e.g., open water, wet asphalt). The LiDAR data were acquired under optimum conditions with minimal to no cloud cover (i.e., less than 10% cloud shadow) and maximum solar zenith angles. In addition, consistent aircraft altitude over the terrain was obtained to eliminate the potential for data gaps related to acquisition and laser shadowing of targets. Furthermore, an accurate ground survey was achieved by Watershed Sciences Inc. in parallel with the airborne LiDAR scanning.

The absolute vertical accuracy of the LiDAR datasets was initially assessed using ground checkpoints collected from bare earth surfaces of constant slope. For this project, the reported RMSE and MD values of the absolute and average relative vertical accuracies of the LiDAR datasets were 2.6 cm and 5 cm, respectively (see Wilson and Steinberg 2013 [82] for additional details).

3.3. Methods

Figure 3.2 shows our proposed method in the form of a schematic diagram. It consisted of 4 distinct components: (i) Data preparation, (ii) evaluation of the vertical elevation accuracy of the global DEMs utilizing LiDAR DTM/DSM, (iii) extraction of the channel networks, and (iv) development of ArcGIS Python toolbox for the geometric assessment of channel networks/orders. They are described in the following sub-sections.

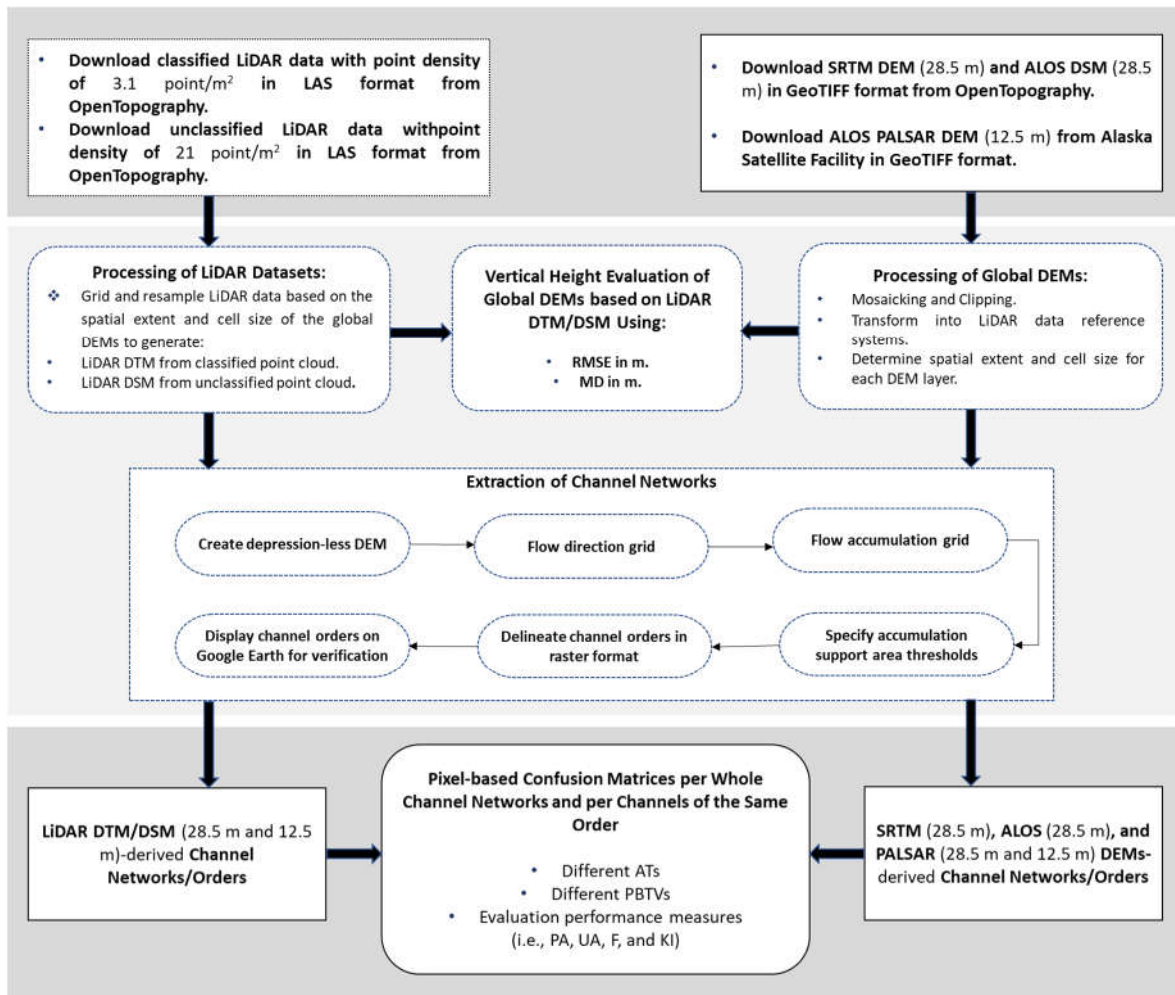


Figure 3.2. Methodology flow chart for the per-pixel geometric evaluation of channel networks/Strahler orders.

3.3.1. Data Preparation

The global SRTM DEM and ALOS DSM were obtained from the OpenTopography (High-Resolution Topography Data and Tools) website in GeoTIFF format with a horizontal resolution of approximately 1 arcsec/28.5 m (Table 3.1). The PALSAR DEM was downloaded from the Alaska Satellite Facility Distributed Active Archive Data Center (ASF DAAC) in geographic information systems (GIS)-ready GeoTIFF format with a horizontal resolution of 12.5 m. For full coverage of the area under study, two dual-polarization (HH +

HV) PALSAR scenes operating in fine beam mode (FBD) were obtained from an ascending path on 15 June 2007.

The ground and unclassified LiDAR point cloud data, with a point density of 3.1 and 21 pts/m², were downloaded from the OpenTopography domain in a compressed LAS file format. LAS is a public file format for the interchange of 3-D LiDAR point cloud datasets. The LAS binary file format is an alternative to proprietary systems or a generic ASCII file interchange system and is compatible with many commercial and open source software packages. Each point within the LiDAR datasets was classified by whether it was returned from the ground, vegetation, or building/structure. The vertical and horizontal references of the LiDAR point cloud data are NADV 88 and NAD 83. The LiDAR point cloud datasets were geocoded to the Universal Transverse Mercator (UTM) projection system, Zone 10N.

Both ground and unclassified LiDAR points were gridded, resampled, and averaged based on the spatial extent and resolution of the SRTM DEM 28.5 m, ALOS DSM 28.5 m, PALSAR DEM 12.5 m, and resampled PALSAR DEM 28.5 m.

Before the global elevation datasets (SRTM DEM V003 28.5 m, ALOS DSM 28.5 m, and PALSAR DEMs 12.5 m and 28.5 m) could be directly compared with LiDAR DTM/DSM of similar spatial resolution, it was imperative to have them in a common reference system. The global elevation products were transformed into the LiDAR reference system. Additionally, the projected coordinate systems were made consistent among the global elevation products and LiDAR datasets. Each pair of comparable DEMs had the same number of rows and columns and were well aligned.

3.3.2. Evaluating the Vertical Elevation Accuracy of Global DEMs Based on LiDAR DTM/DSM

Elevation differences among LiDAR DTM and DSM (reference datasets) and the other global DEMs were assessed by computing the traditional statistical metrics (RMSE and MD) grids at the co-located pixels.

Validation accuracy measures the closeness of observation to a true value [7]. RMSE has become a standard statistical tool for analyzing DEM accuracy and has been used in many studies to quantify the vertical accuracy in DEMs [83], [84]. RMSE is a single measure that characterizes the error surface, while MD indicates the bias of the error surface and their equations are as follows:

$$\text{RMSE} = \sqrt{\frac{1}{N} \sum_{i=1}^N (\text{LDEM}_{\text{ref}} - \text{GDEM})^2} \quad (3.1)$$

$$\text{MD} = \frac{1}{N} \sum_{i=1}^N (\text{LDEM}_{\text{ref}} - \text{GDEM}) \quad (3.2)$$

where N is the number of pixels; LDEM_{ref} is the reference LiDAR DEM (DTM or DSM); and GDEM is the global DEM (SRTM DEM V003, ALOS DSM, or PALSAR DEM).

For the purpose of this paper, the elevations values are represented by the geometric centers of all DEM cells included in the evaluation.

3.3.3. Extraction of the Channel Networks/Orders

The channel network is the most significant terrain parameter derived from DEMs; along its tributaries, fluvial processes act to transport water and sediments from an upstream high-elevated region by gravity downslope to a lower, flat landscape [32]. The hydrology geoprocessing tools assembled in the ArcGIS ModelBuilder [85] were utilized to extract channel networks/orders from the global DEMs, as well as from LiDAR DTM and DSM.

Delineating a channel network depends mainly on detecting the flow path of every cell in the DEM grid through a series of consecutive steps [38], [86]. The first step was to create a depression-less DEM by filling the pits [37]. The presence of sinks within DEMs is a common problem that affects the proper detection of flow directions. Therefore, to have a

hydrologically-corrected DEM, it is necessary to first fill these sinks [32], [39]. The algorithm developed by Jenson and Dominique 1988 [39] has been widely used in many GIS software packages for sink filling [39], where every depression is converted to a flat area by raising each cell's elevation to the lowest elevation of its neighbors.

Based on the availability of high-resolution remote sensing-based DEMs, many authors developed accurate flow direction algorithms. They derived paths of surface flow using a nondispersive single (e.g., [39], [41], [42]) and dispersive multiple (e.g., Reference [87]) flow direction methods. Orlandini and Moretti 2009 [42] stated that nondispersive algorithms should be used when the extraction of channel systems and surface flow directions is the main focus of the study. Furthermore, Zhu et al. [88] mentioned that most pit filling algorithms were based on a 1-D single flow direction (e.g., Reference [32], [39]). Therefore, in the second step, the flow direction grid was derived from the conditioned DEM by using the nondispersive eight-direction (D8) surface flow method [39]. The flow path was determined by comparing each cell's elevation with its eight adjacent or diagonal 3×3 cell neighbors, where the cell with the steepest downward direction is identified as the flow path based on the underlying topography [39], [42]. The direction of flow determines the ultimate destination of the surface water flowing across the land toward downslope zones.

Third, using the predetermined flow direction spatial layer, it was possible to define cells with high flow concentration to detect how the flow would be accumulated and where small groups of cells could turn into streams [37], [39]. In fact, cells with flow accumulation values greater than a certain threshold would constitute an effective part of the stream. The threshold is called the flow accumulation area threshold (AT), and it defines the minimum contributing area required to initiate the channels [32], [86], [89]. The AT is the main factor in extracting the channel networks, where it determines the channels' initiation and differentiates between stream and non-stream pixels. The AT is strongly affected by topography, geomorphology, geology, climate, vegetation, and human influence [40], [90]. The determination of the AT is a matter of debate, but utilizing a constant value for delineating DEM-based channels network has been well-accepted among different researchers [32], [91]. Most GIS software used 1% of the maximum flow accumulation value

as a default to determine the AT [92]. Orlandini et al. [86] specified the AT by comparing the predicted and observed channel heads determined from LiDAR DEM and field measurements, respectively. Tarboton et al. [37] extracted channel networks of high density from DEMs that satisfy the scaling laws computed from the contour DEMs-derived networks (blue lines). Tribe 1992 [90] selected the optimum AT when there was a close match between the channel networks extracted from DEMs and manually drawn blue lines. Jones 2002 [93] visually determined the flow accumulation support AT by a trial and error approach.

The channel network extracted from LiDAR DEM had higher accuracy than that delineated from contour-based DEM [25]. The Google Earth Pro tool provides rich spatial details for determining individual objects [94]. Therefore, it is widely and efficiently used in different remote sensing applications, in particular for land use/cover mapping (e.g., Reference [94]–[96]). In this study, the approach of a trial and error [93] was used with a subsequent visual verification using Google Earth imagery to detect 4 ATs to test the developed method for evaluating the horizontal accuracy of channel networks. The ATs were equal to at least 0.004 km², 0.008 km², 0.012 km², and 0.016 km², and 0.020 km², 0.041 km², 0.061 km², and 0.081 km² for spatial resolutions of 12.5 m and 28.5 m, respectively. The ATs corresponded to at least 25, 50, 75, and 100 pixels at spatial resolutions of 12.5 m and 28.5 m. Applying the predetermined threshold values to the flow accumulation grid, the real channels of the network began to be defined. Then, the extracted channel grids were converted to vector layers and then exported them to keyhole markup language (KML) format to visually check the quality of the extracted channels using Google Earth Pro. The delineated channels were well matched with the actual watercourses of Google Earth 3-D imagery. To obtain the equivalent AT values among multiple DEM grids with different spatial resolutions, a simple derived mathematical relationship was used based on the following equation:

$$CAT = \left(\frac{LRD}{HRD} \right)^2 \times OAT \quad (3.3)$$

where CAT is the comparable area threshold that needs to be estimated; LRD is the lower-resolution DEM (test DEM); HRD is the higher-resolution DEM (reference DEM);

and OAT is the original area threshold based on which the channel network/orders were extracted.

Finally, the channel segment links were generated with unique identifications by using the most common [34] stream order designation method (i.e., the Strahler method [97], modified from Horton 1945 [98]), which was applied to delineate the order of stream segments in the network. The channel order is in direct proportion to the channel size, watershed dimension, and discharge of water and sediments [97]. The Strahler ordering approach [97] assigned a numeric order for each channel segment based on a hierarchy of tributaries. In this method, the unbranched fingertip tributaries are designated as first order, and the order increases to the next higher one when branches of the same orders are joined. For instance, the joining of 2 first-order channels at a specific point will generate a second-order channel (Figure 3.3a,b), and so on. The stream ordering method can be simplified using the following relationships:

$$\text{Order}_A \text{ "v" } \text{Order}_A = \text{Order}_{\text{Next to A in rank}} \quad \text{If A = A} \quad (3.4)$$

$$\text{Order}_A \text{ "v" } \text{Order}_B = \text{Order}_{\text{Highest of A \& B}} \quad \text{If A } \neq \text{ B} \quad (3.5)$$

where A and B denote the ranks of channel orders and “v” refers to the joining between 2 channels. The trunk stream through which water and sediments discharge downstream was assigned the highest order [97].

3.3.4. Developing ArcGIS Python Toolbox for Geometric Assessment of Channel Networks

A new Python toolbox for ArcGIS were developed for the purpose of pixel-based geometric evaluation of the channel networks/orders derived from open-source global DEMs based on those extracted from LiDAR DTMs/DSMs (Appendix B). The availability of numerous GIS software packages enabled the extraction of channel networks from remote sensing-based DEMs such as ArcGIS [85], Geographic Resources Analysis Support System (GRASS) GIS [99], and Quantum GIS [100]. In this study, the ArcGIS environment was

used to introduce the developed toolbox, because ArcGIS and its powerful geoprocessing toolboxes have been widely used by different authors in different hydrological and geomorphological related research (e.g., [57], [66], [101]).

Accuracy assessment is a mandatory step in evaluating the results of different remote sensing related studies [102], [103]. Users with different applications should be able to assess whether the accuracy of their outcomes (e.g., map) fits their objectives [104]. In the remote sensing literature, the confusion matrix is the most commonly endorsed and utilized method (i.e., the core) of the accuracy assessment [102], [103]. It consists of a simple cross-tabulation that introduces the foundation to define the classification accuracy and characterize errors (Tables 3.2 and 3.3). It has been widely used by different authors to evaluate the accuracy of different remote sensing-based models (e.g., fragmented agricultural landscapes [105], automatic classification of LiDAR datasets in an urban area [106], global climatic maps [107], object extraction [108], change detection [109], and land cover/use classifications [110]–[112]).

In this study, the calculated two-class (Figure 3.3c and Table 3.2) and multiclass (Figure 3.3d and Table 3.3) confusion matrices arranged the channel networks (Table 3.2), and channel orders (Table 3.3) of the reference data in the rows and the test datasets in the columns. The PBTVs (Figure 3.4) around the LiDAR DTMs/DSMs 12.5 m and 28.5 m-derived networks/orders were set to 0, 1, 2, and 3 pixels, to detect the horizontal matching with those derived from global DEMs in both $\pm X$ and $\pm Y$ directions and at comparable spatial resolutions.

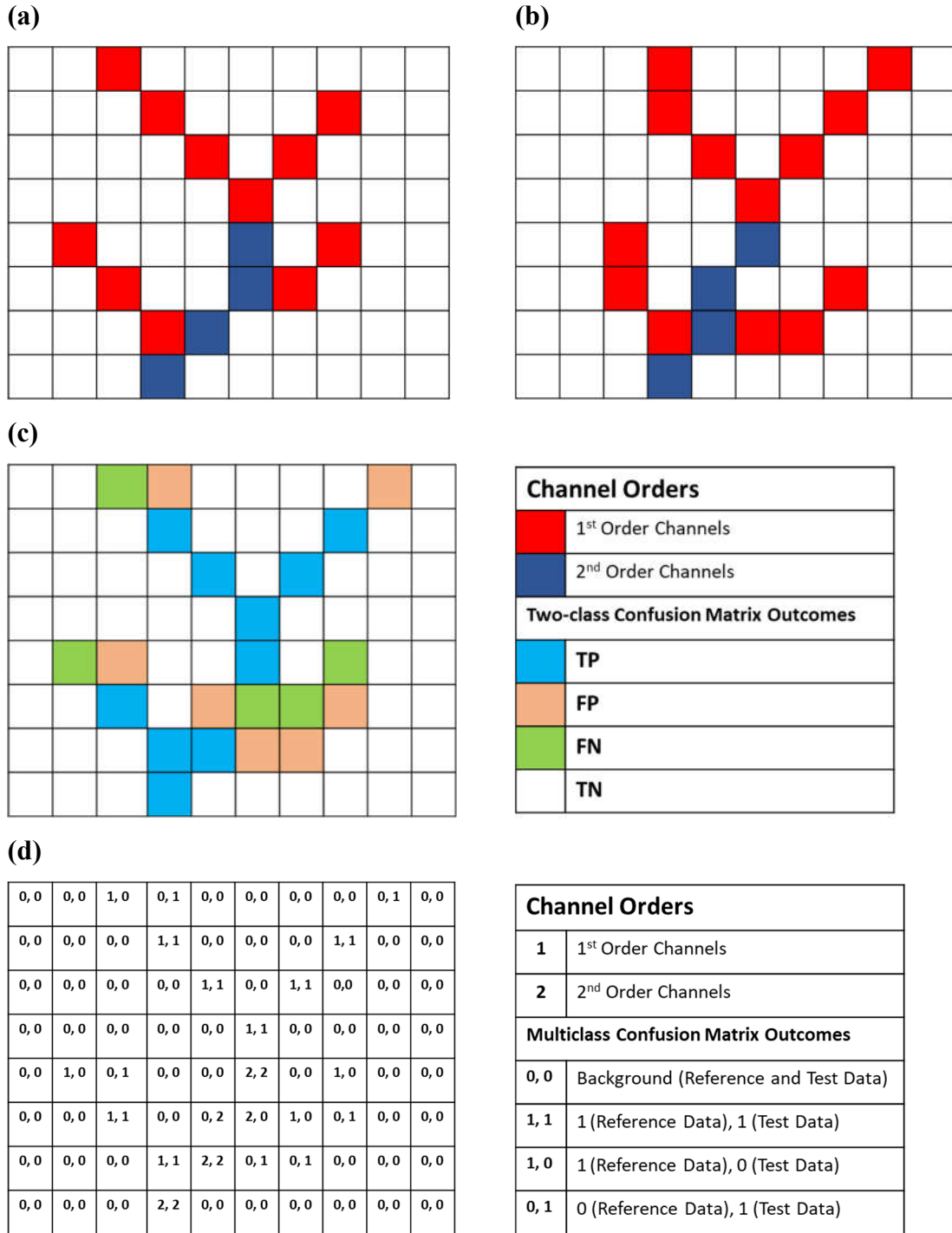


Figure 3.3. Sketch for comparing pixels of channel networks/orders using error matrices: (a) reference datasets, (b) test datasets, (c) two-class confusion matrix outcomes resulting from matching between the whole networks in a and b (regardless of the channels' of the channels' orders), and (d) multiclass error matrix outcomes resulting from matching between channels that have the same order in a and b. TP, true positive; FP, false positive; FN, false negative; and TN, true negative.

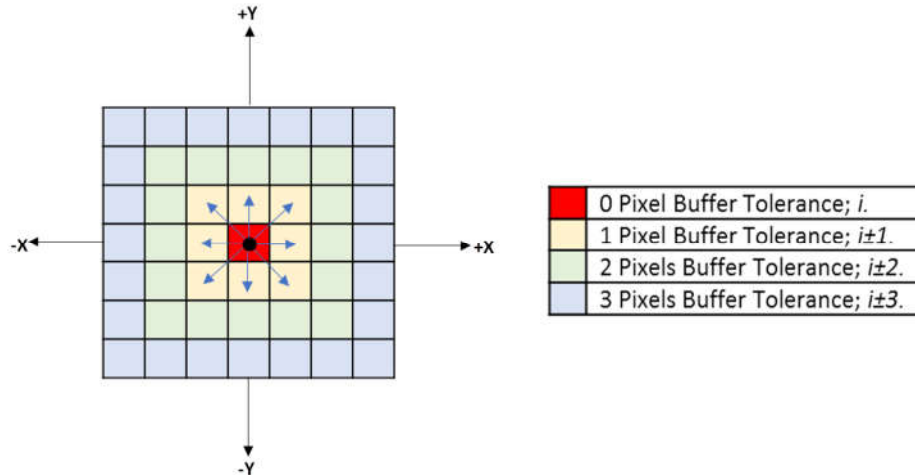


Figure 3.4. Concept of the pixel buffer tolerance values (PBTVs).

In general, a confusion matrix is a statistical technique for summarizing the performance of a classification algorithm [113], [114]. In this study, an $N \times N$ error matrix (Figure 3.3 and Table 3.2) was used to geometrically evaluate the channel networks, where N is equal to the number of classes (whole channel networks) in the case of the simplest 2×2 array (Table 3.2). When separately evaluating the channels having the same order, N was equal to the number of classes (orders) (Table 3.3). Each column and row of the matrix corresponds to the test (one of the global DEMs-derived networks/orders) and reference (one of the LiDAR DTMs/DSMs-based networks/orders) classes, respectively. The counts of correct and incorrect agreements (i.e., disagreements) were then filled into the confusion matrices (Tables 3.2 and 3.3).

The results of the geometric evaluation of the channel networks/orders derived from global DEMs (test data) and LiDAR DTMs/DSMs (reference data) were arranged in a matrix format (Tables 3.2 and 3.3) with the following 4 outcomes: (i) True positive (TP), where the matched pixels were correctly classified as the same channel segment of the networks/orders of both test and reference datasets, (ii) true negative (TN), where co-located pixels were correctly classified as non-channel networks/orders of both test and reference classes (iii) false positive (FP), where pixels of the test data were unmatched with the reference data (i.e., the test pixels corresponded to a channel of another order or to the background), and (iv) false negative (FN), where pixels of the reference data were incorrectly matched by the test

data (i.e., the reference pixels corresponded to the background or to a channel belonging to another order).

Table 3.2. Outcomes of classification matrix resulting from comparing a LiDAR DTM/DSM-derived channel network (reference class) and a global DEM-based network (test class); where Net denotes network.

Test Class		
Reference Class	Net ₀	Net ₁
Net ₀	Net _{0,0} (TN) = Number of Net ₀ pixels classified correctly as Net ₀	Net _{0,1} (FP) = Number of Net ₀ pixels classified incorrectly as Net ₁
Net ₁	Net _{1,0} (FN) = Number of Net ₁ pixels classified incorrectly as Net ₀	Net _{1,1} (TP) = Number of Net ₁ pixels classified correctly as Net ₁

Table 3.3. Outputs of multiclass error matrix resulting from comparing a LiDAR DTM/DSM (reference data)-derived channel orders and a global DEM (test data)-based orders with a channel having a higher order of n; where Ord denotes channel order and B₀ refers to the background of 0 value.

		Test Data						
		Global DEMs-based Channel Orders						
		B_0	Ord_1	Ord_2	Ord_3	Ord_4	Ord_5	Ord_n
Reference Data LiDAR DTM/DSM-based Orders	B_0	B ₀ , B ₀	B ₀ , Ord ₁	B ₀ , Ord ₂	B ₀ , Ord ₃	B ₀ , Ord ₄	B ₀ , Ord ₅	B ₀ , Ord _n
	Ord_1	Ord ₁ , B ₀	Ord _{1,1} (TP)	Ord _{1,2}	Ord _{1,3}	Ord _{1,4}	Ord _{1,5}	Ord _{1,n}
	Ord_2	Ord ₂ , B ₀	Ord _{2,1}	Ord _{2,2} (TP)	Ord _{2,3}	Ord _{2,4}	Ord _{2,5}	Ord _{2,n}
	Ord_3	Ord ₃ , B ₀	Ord _{3,1}	Ord _{3,2}	Ord _{3,3} (TP)	Ord _{3,4}	Ord _{3,5}	Ord _{3,n}
	Ord_4	Ord ₄ , B ₀	Ord _{4,1}	Ord _{4,2}	Ord _{4,3}	Ord _{4,4} (TP)	Ord _{4,5}	Ord _{4,n}
	Ord_5	Ord ₅ , B ₀	Ord _{5,1}	Ord _{5,2}	Ord _{5,3}	Ord _{5,4}	Ord _{5,5} (TP)	Ord _{5,n}
	Ord_n	Ord _n , B ₀	Ord _{n,1}	Ord _{n,2}	Ord _{n,3}	Ord _{n,4}	Ord _{n,5}	Ord _{n,n} (TP)

The auto-extracted channel networks/orders from global DEM grids were geometrically evaluated using those derived from LiDAR DTMs and DSMs at similar spatial resolutions. The maximum PBTVs around each channel segment-based reference LiDAR DTMs/DSMs were set to 0, 1, 2, and 3 pixels (Figure 3.4). These PBTVs were equal to

horizontal distances of 0 m, 12.5 m, 25 m, and 37.5 m, and 0 m, 28.5 m, 57 m, and 86.5 m, at spatial resolutions of 12.5 m and 28.5 m, respectively. The developed algorithm was first checked for the matched co-located non-classified or classified (i.e., ordered) channels' pixels (i.e., a PBTv of 0) from the test data with respect to the reference datasets. If there were no more matched pixels, the algorithm kept running to locate the closest horizontal matching between the remainder of the deviated pixels within the subsequent nearest 1-pixel, 2- pixels, and 3-pixels neighbors with respect to the reference datasets (i.e., PBTv of 1 to 3 pixels) (Figure 3.4).

3.3.5. Categorical Performance Measures for Assessing the Horizontal Accuracy of Channel Networks/Orders

In this study, different evaluation measures, such as producer accuracy (PA), user accuracy (UA), F-score (F), and Cohen's kappa index (KI), from the error matrices at different ATs and PBTvs were used to quantify the reliability and accuracy of the matching between networks/orders. Many studies have used these measures to evaluate the accuracy of various remote sensing datasets and models (e.g., [106], [108], [115], [116]).

The PA and UA [114] were calculated using the marginal row or column of the matrix, respectively. PA (i.e., row values) was computed considering the agreement of a particular class with the summation of all classes in that row (Tables 3.2 and 3.3). The rows of the table represent the actual class (LiDAR DTM/DSM-based network/orders), while the columns represent the test class (global DEM-derived network/orders). TP and TN (Tables 3.2 and 3.3) denote the correctly classified pixels, while FP and FN represent the incorrectly classified cells.

UA (i.e., column values) was similarly calculated, but with respect to the summation of all classes in that column (Tables 3.2 and 3.3). PA and UA represent measures of completeness and correctness, respectively. The difference between PA and UA lies in the definitions of how well the channel networks/orders can be matched (PA) versus how reliable the matching accuracy is (UA). Therefore, both PA and UA are of interest and

considered as important accuracy metrics. In particular, the accuracy of each channel order using PA and UA is useful in determining how different models perform (see Congalton 1991 [102] and Stehman 1997 [117]) for an in-depth discussion). In Table 3.3, for channels of order 1 (i.e., Ord_1 class), the TP, FN, FP, and TN outcomes were labeled in yellow, green, orange, and gray, respectively. In other words, the total number of FN outputs for an Ord_1 (i.e., channels that had the order of 1) (Table 3.3) equalled the summation of values in the corresponding row, excluding the TP. If a channel pixel of order 1 was located in the reference class (LiDAR DEM-based orders), and no corresponding channel pixel of the same order was reported in the test data (global DEM-based orders) (i.e., a channel of another order or a background pixel of 0 value was recorded), this cell was assigned the value of (1, the other order recorded in the test data) or (1, 0) in the error matrix, respectively. In the same way, the total number of the FP outcomes for an Ord_1 (Table 3.3) equalled the summation of values in the corresponding column, excluding the TP. If a channel pixel of order 1 was not located in the reference data, but was recorded in the test data, this cell was assigned the value of (0, the other order recorded in the test data) or (0, 1), in the matrix.

The F metric represents the harmonic mean (i.e., weighted average) of PA and UA [118]. It measures the accuracy of the compared whole networks, as well as the channels with the same order. The F value provides the balance between precision (UA) and recall (PA). Therefore, it takes both FP and FN into account, and it addresses how similar the PA and UA values are. The F-score can summarize UA and PA into a single value, which makes it simple to determine the level of matching between the networks/orders extracted from different DEMs at different ATs and PBTVs.

The higher the PA, UA, and F values, the better the performance of the matching between the channel networks/orders. A score of 1 means perfect matching. The lowest possible score of the PA, UA, and F is 0, which denotes no horizontal matching between the networks/orders.

The KI is a measure of the overall agreement of a matrix, calculating the proportion of agreement beyond chance agreement and expected disagreement [119]. It was introduced

to the remote sensing community in the early 1980s [113], [120] and has become a widely accepted measure for classification accuracy [102]. The KI provides an overall assessment of the accuracy of the classification [121]. It has a negative value if the chance agreement increases, a positive value if the strength of the agreement increases, and a value of zero when the agreement between reference and test datasets equal the chance agreement (i.e., no agreement) [122]. The KI uses both the overall accuracy of the model and the accuracy within each class; therefore, it has the advantage of statistically comparing two classification outcomes. In contrast to the overall accuracy [113], the KI takes the non-diagonal elements into consideration as expressed by Equation (9) [119]. The equations for computing PA [114], UA [114], KI, and F [118] are as follows:

$$PA = \frac{TP}{(TP + FN)} \quad (3.6)$$

$$UA = \frac{TP}{(TP + FP)} \quad (3.7)$$

$$F = \frac{2 \times TP}{(2 \times TP + FP + FN)} \quad (3.8)$$

$$KI = \frac{N \sum_{i=1}^m s_{ii} - N \sum_{i=1}^m (s_{i+} \times s_{+i})}{N^2 - \sum_{i=1}^m (s_{i+} \times s_{+i})} \quad (3.9)$$

where m is the numbers of rows; s_{ii} is the numbers of channel network/order pixels in row i and column i (on the major diagonal); s_{i+} is the total number of the channel network/order pixels in row i ; s_{+i} is the total number of the observations in column i ; and N is the total number of observations.

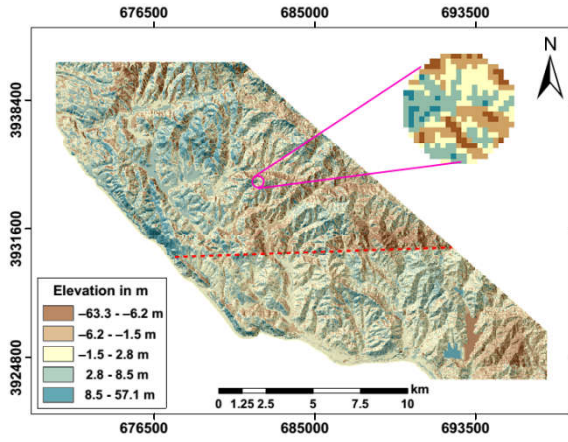
3.4. Results

3.4.1. Traditional Statistical Indices for Evaluating the Vertical Height Accuracy of Global DEMs

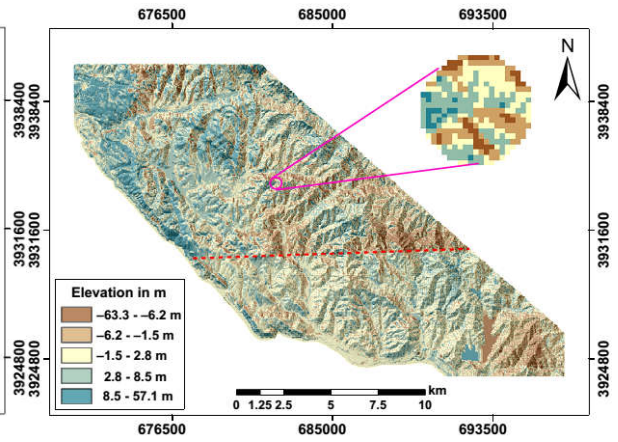
The vertical accuracies of the global DEMs (SRTM DEM V003 28.5 m, ALOS DSM 28.5 m, and PALSAR DEMs 12.5 m and 28.5 m) were assessed by computing the per-pixel difference with the LiDAR DTMs/DSMs at similar spatial details. The continuous elevation differences were generated and pairwise RMSE and MD values were calculated for each error surface in meters (Figure 3.5). In general, LiDAR DTMs and DSMs had higher elevation values than PALSAR DEMs with spatial resolutions of 12.5 m and 28.5 m. Significant positive height differences were observed in the northwestern part of the study area, comparing the PALSAR DEM 12.5 m to LiDAR DTM and DSM (Figure 3.5c,d). Negative elevation differences were dominant in the comparison between SRTM DEM 28.5 m and ALOS DSM 28.5 m against LiDAR DTM 28.5 m and DSM 28.5 m, respectively.

Based on the comparison results using LiDAR DTM (Table 3.4), the PALSAR DEM 12.5 m reported the lowest overall RMSE of 4.57 m. The ALOS DSM 28.5 m and PALSAR DEM 28.5 m provided acceptable RMSE values of approximately 4.6 m and 4.9 m, respectively. The SRTM DSM ranked last, with the lowest accuracy and the highest RMSE of 5.172 m. The ALOS DSM 28.5 m showed better vertical accuracy, with RMSE of 4.012 m than the SRTM DEM 28.5 m and PALSAR DEMs 12.5 m and 28.5 m when compared to the LiDAR DSMs at comparable spatial resolution, with RMSE values of 4.53 m, 5.19 m, and 5.43 m, respectively.

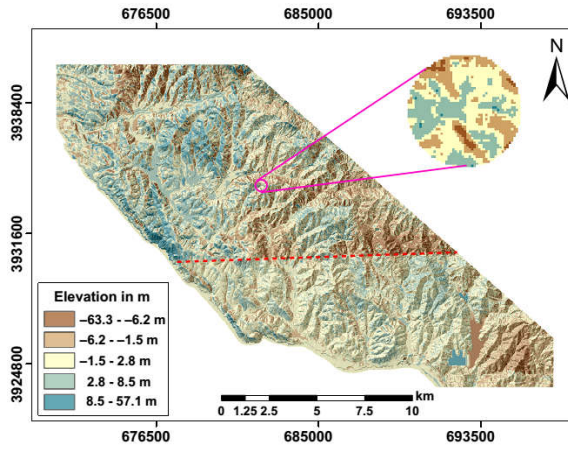
(a)



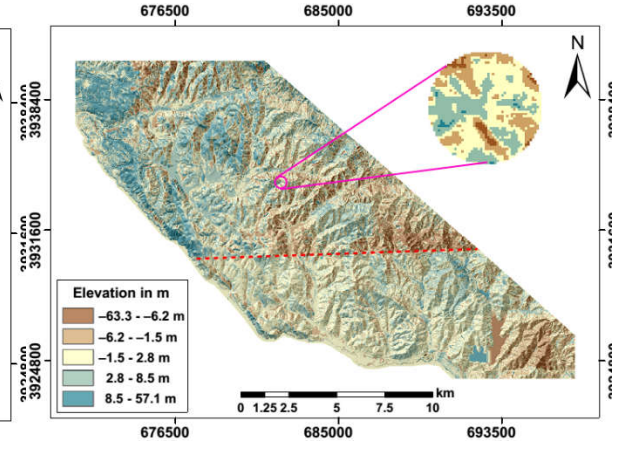
(b)



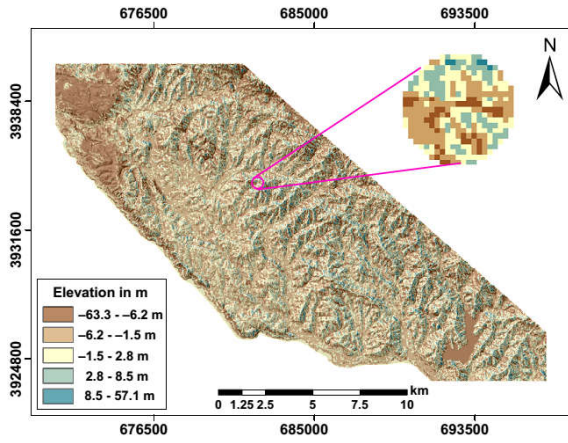
(c)



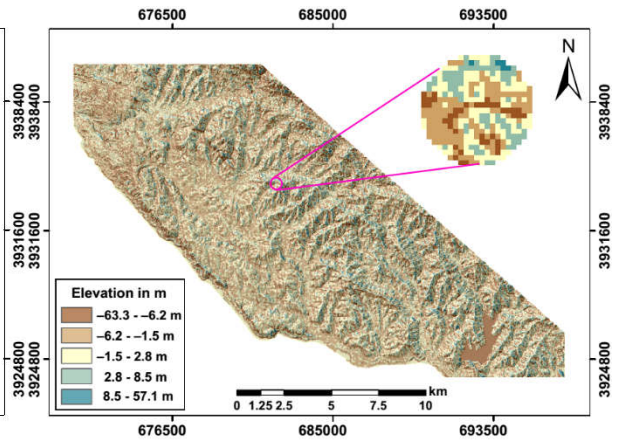
(d)



(e)



(f)



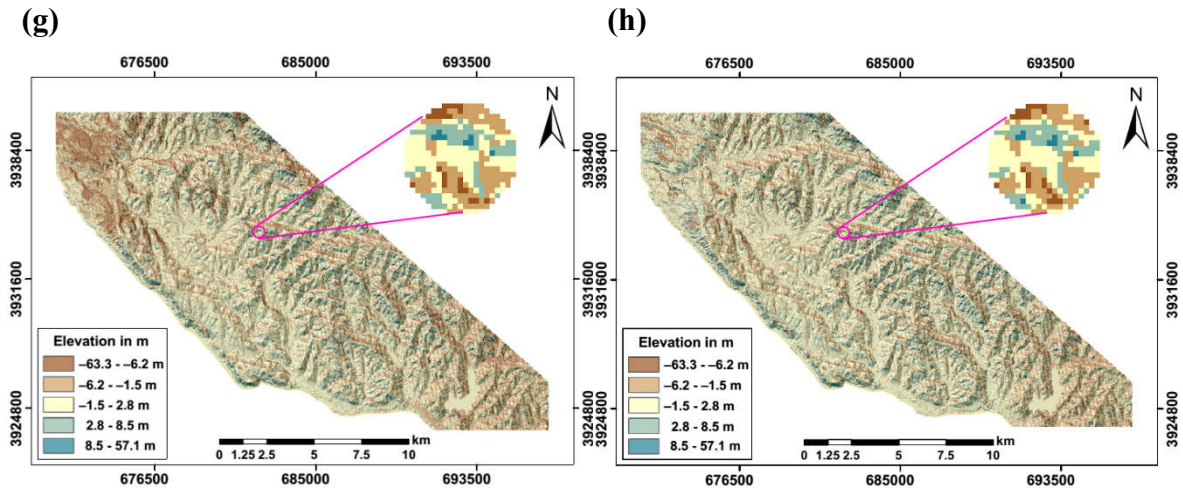


Figure 3.5. Elevation surface differences between: (a) LiDAR DTM and PALSAR DEM 28.5 m, (b) LiDAR DSM and PALSAR DEM 28.5 m, (c) LiDAR DTM and PALSAR DEM 12.5 m, (d) LiDAR DSM and PALSAR DEM 12.5 m, (e) LiDAR DTM and SRTM DEM 28.5 m, (f) LiDAR DSM and SRTM DEM 28.

Table 3.4 shows four positive MD values, with PALSAR DEMs with spatial resolutions of 12.5 m and 28.5 m underestimating the LiDAR DTMs 12.5 m and 28.5 m by 0.78 m and 1.93 m, respectively. In addition, the ALOS DSM 28.5 m showed the lowest MD (−0.29 m) when compared to LiDAR DSM 28.5 m. Furthermore, the SRTM DEM 28.5 m ranked last when compared to LiDAR DTM 28.5 m with an MD of −2.66 m. The differences between the remote sensing-based elevation products were likely due to the nature and capabilities of the acquired sensors and generation algorithms [69]. On the other hand, four negative MD values were recorded (Table 3.4) in the evaluation of SRTM DEM 28.5 m and ALOS DSM 28.5 m using LiDAR DTM 28.5 m and DSM 28.5 m. SRTM DEM 28.5 m and ALOS DSM 28.5 m overestimated the elevation values of LiDAR DTM and DSM, respectively. The best-matched elevation values were recorded in the comparison of ALOS DSM 28.5 m against LiDAR DSM, with an MD value of −0.29 m.

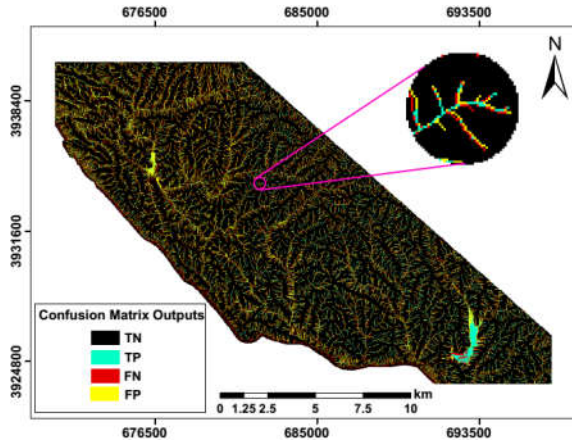
Table 3.4. Statistical vertical differences between global DEMs and LiDAR DTMs/DSMs expressed in terms of RMSE and MD in m.

Reference Data	Test Data	Spatial Resolution	RMSE (m)	MD (m)
LiDAR DTM	ALOS DSM	28.5 m	4.695	-1.260
LiDAR DTM	SRTM DEM	28.5 m	5.172	-2.655
LiDAR DTM	PALSAR DEM	28.5 m	4.988	0.952
LiDAR DTM	PALSAR DEM	12.5 m	4.571	0.777
LiDAR DSM	ALOS DSM	28.5 m	4.012	-0.288
LiDAR DSM	SRTM DEM	28.5 m	4.537	-1.699
LiDAR DSM	PALSAR DEM	28.5 m	5.434	1.929
LiDAR DSM	PALSAR DEM	12.5 m	5.186	1.741

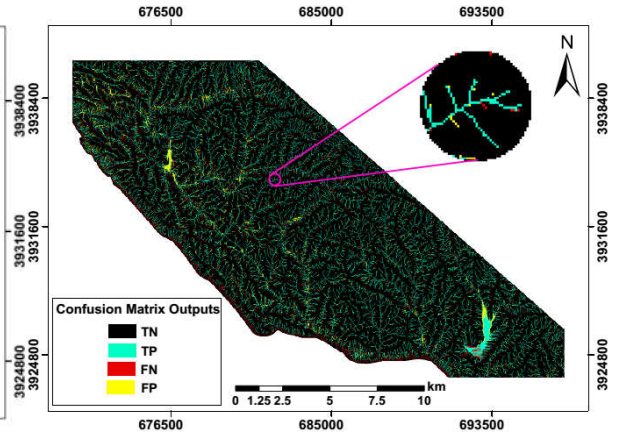
3.4.2. Horizontal Evaluation of the Channel Networks

The whole networks were evaluated using the four categorical measures (PA, UA, F, and KI) derived from the two-class pixel-based confusion matrix outcomes (Table 3.2 and Figure 3.3c). The flow accumulation ATs were set to correspond to at least 25, 50, 75, and 100 pixels. Figure 3.6 shows some examples of the outcomes of the confusion matrices (TP, FP, TN, and FN) resulting from comparing the whole networks extracted from global DEMs based on those derived from LiDAR DTMs/DSMs. In general, the values of these metrics were improved with the increase the PBTVs from 0 to 3 pixels. Slight differences were recorded among these measures in the comparison between networks extracted from global DEMs 28.5 m and LiDAR DTM/DSM 28.5 m at comparable ATs and PBTVs (Tables 3.5–3.8).

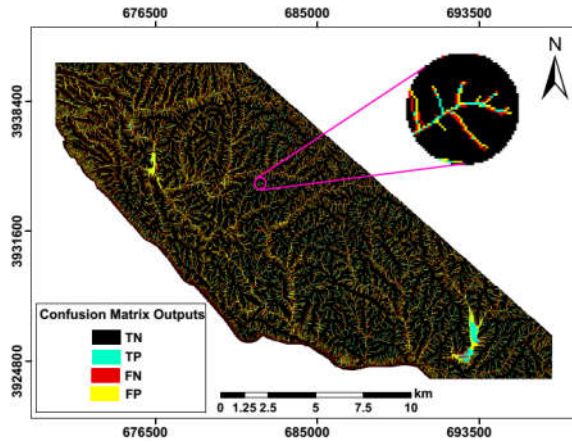
(a)



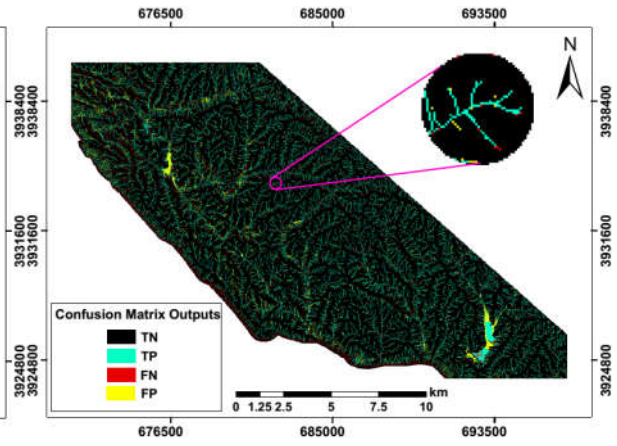
(b)



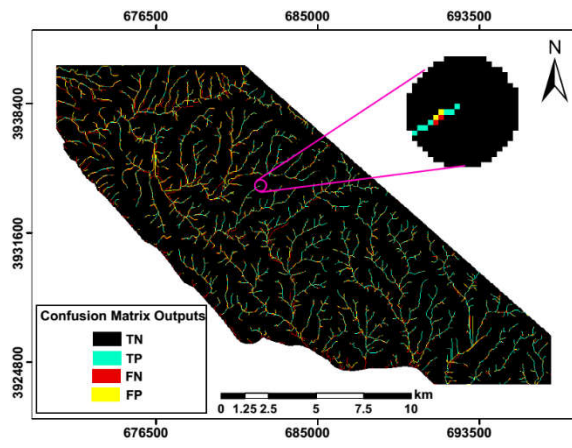
(c)



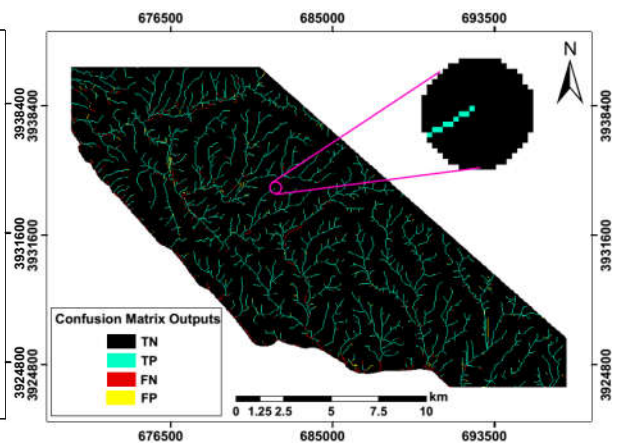
(d)



(e)



(f)



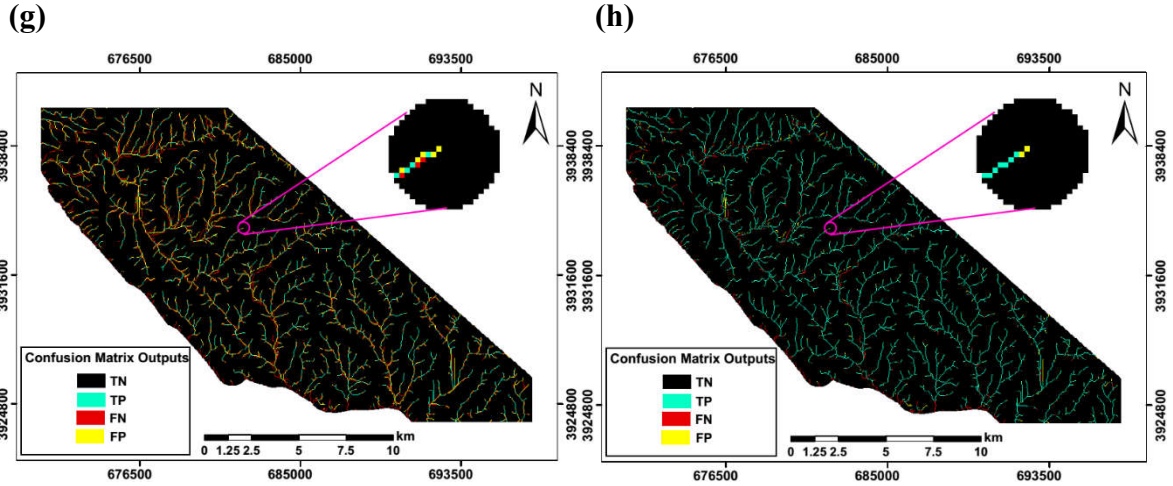


Figure 3.6. Confusion matrix outcomes resulting from comparing channel networks extracted from: **(a,b)** LiDAR DTM and PALSAR DEM 12.5 m at an area threshold (AT) corresponding to 25 pixels and pixel buffer tolerance value (PBTv) of 0 and 3 pixels, respectively, **(c,d)** LiDAR DSM and PALSAR DEM 12.5 m using an AT corresponding to 25 pixels and PBTv of 0 and 3 pixels, respectively, **(e,f)** LiDAR DTM and PALSAR DEM 28.5 m using an AT corresponding to 100 pixels and PBTv of 0 and 3 pixels, respectively, and **(g,h)** LiDAR DSM and PALSAR DEM 28.5 m using an AT corresponding to 100 pixels and PBTv of 0 and 3 pixels, respectively.

For the evaluation using the networks extracted from LiDAR DTM 28.5 m, the networks derived from PALSAR DEM 28.5 m (Table 3.7) reported the highest performance measure values. There were a few insignificant exceptions where the ALOS DSM 28.5 m-based network (Table 3.5) slightly outperformed that derived from PALSAR DEM 28.5 m (Table 3.7) using a PBTv of 3. The PA, UA, F, and KI values computed in the assessment of the PALSAR DEM 28.5 m-based network (Table 3.7) were higher than those estimated from evaluating the ALOS DSM 28.5 m-derived network (Table 3.5) by 0.025, 0.064, 0.045, and 0.052 and 0.056, 0.081, 0.068, and 0.073, respectively, using a PBTv of 0 and ATs corresponding to 25 and 100 pixels. Additionally, using the previously mentioned conditions, but employing a PBTv of 3, the differences were -0.039 , 0.029 , -0.005 , and -0.005 and -0.025 , 0.019 , -0.003 , and -0.003 , respectively.

Table 3.5. Performance accuracy metrics computed based on a comparison between whole channel networks/orders extracted from the LiDAR DTM/DSM 28.5 m and the ALOS DSM 28.5 m at different ATs expressed in the corresponding number of pixels and PBTv in pixels.

Reference LiDAR-based Net	DTM	DSM	DTM	DSM	DTM	DSM	DTM	DSM
PBTv_AT	0_25	0_25	3_25	3_25	0_100	0_100	3_100	3_100
PA_Net	0.505	0.518	0.938	0.929	0.453	0.476	0.916	0.919
UA_Net	0.483	0.506	0.897	0.907	0.456	0.476	0.920	0.919
F_Net	0.494	0.512	0.917	0.918	0.455	0.476	0.918	0.919
KI_Net	0.431	0.444	0.907	0.907	0.423	0.446	0.913	0.914
KI_Ords	0.389	0.403	0.766	0.766	0.395	0.419	0.816	0.827
PA_Ord1	0.423	0.417	0.751	0.733	0.426	0.439	0.771	0.784
PA_Ord2	0.371	0.380	0.588	0.581	0.382	0.425	0.736	0.757
PA_Ord3	0.354	0.389	0.605	0.610	0.287	0.345	0.638	0.680
PA_Ord4	0.294	0.340	0.544	0.563	0.280	0.262	0.585	0.627
PA_Ord5	0.222	0.147	0.452	0.347	0.113	0.160	0.437	0.564
PA_Ord6	0.057	0.178	0.179	0.377				
UA_Ord1	0.385	0.393	0.683	0.691	0.432	0.443	0.781	0.790
UA_Ord2	0.372	0.381	0.590	0.583	0.379	0.416	0.730	0.742
UA_Ord3	0.360	0.399	0.616	0.626	0.287	0.334	0.637	0.659
UA_Ord4	0.316	0.315	0.585	0.521	0.251	0.273	0.523	0.652
UA_Ord5	0.135	0.195	0.275	0.460	0.143	0.187	0.554	0.659
UA_Ord6	0.167	0.280	0.520	0.593				

The SRTM DEM-derived network ranked third in comparison with the LiDAR DTM 28.5 m-based network (Table 3.6). Employing the previously mentioned conditions, the measures were 0.910, 0.891, 0.900, and 0.887 and 0.891, 0.912, 0.902, and 0.896, respectively, in the comparison between networks extracted from SRTM DEM and LiDAR DTM (Table 3.6). The performance metrics calculated from comparing the networks delineated from PALSAR DEM and LiDAR DTM at a spatial resolution of 28.5 m (Table

3.7) were higher than those reported at spatial details of 12.5 m (Table 3.8) by average values of 0.068 and 0.075 using a comparable PBTv of 3 and ATs corresponding to 25 and 100 pixels, respectively.

Using different PBTvs and ATs, the metrics computed from comparing networks extracted from ALOS and LiDAR DSM 28.5 m (Table 3.5) were almost equal to those reported from evaluating networks derived from ALOS DSM and LiDAR DTM 28.5 m (Table 3.5), with a maximum absolute difference of 0.024. The channel network-based ALOS DSM 28.5 m (Table 3.5) reported the best evaluation metrics when compared to that extracted from LiDAR DSM. The PALSAR DEM 28.5 m and SRTM DEM 28.5 m (Table 3.6)-derived networks ranked second and third in accuracy performance when compared to the LiDAR DSM 28.5 m-based network.

The average of the differences between the performance measures reported from comparing the network delineated from ALOS DSM 28.5 m (Table 3.5) against networks extracted from PALSAR DEM 28.5 m (Table 3.7) and SRTM DEM 28.5 m (Table 3.6) was 0.006 and 0.016, and 0.074 and 0.014 using an AT corresponding to 25 pixels and PBTv of 0 and 3, respectively. Under the previously mentioned conditions, but with using an AT corresponding to 100 pixels, the average of differences was 0.012 and 0.018, and 0.066 and 0.015, respectively. The PALSAR DEM 12.5 m-derived channel network (Table 3.8) reported the lowest accuracy measures compared to that extracted from LiDAR DSM.

Table 3.6. Performance accuracy metrics computed based on a comparison between whole channel networks/orders extracted from the LiDAR DTM/DSM 28.5 m and the SRTM DEM 28.5 m at different ATs expressed in the corresponding number of pixels and PBTv in pixels.

Reference LiDAR-based Net	DTM	DSM	DTM	DSM	DTM	DSM	DTM	DSM
PBTv_AT	0_25	0_25	3_25	3_25	0_100	0_100	3_100	3_100
PA_Net	0.429	0.439	0.910	0.905	0.384	0.406	0.891	0.895
UA_Net	0.420	0.438	0.891	0.904	0.394	0.414	0.912	0.913
F_Net	0.425	0.438	0.900	0.905	0.389	0.410	0.902	0.904
KI_Net	0.354	0.369	0.887	0.892	0.354	0.377	0.896	0.898
KI_Ords	0.305	0.319	0.721	0.725	0.326	0.348	0.793	0.797
PA_Ord1	0.311	0.311	0.675	0.667	0.355	0.369	0.759	0.764
PA_Ord2	0.300	0.310	0.534	0.523	0.322	0.338	0.675	0.670
PA_Ord3	0.287	0.311	0.499	0.500	0.188	0.239	0.515	0.529
PA_Ord4	0.190	0.293	0.422	0.501	0.203	0.245	0.683	0.679
PA_Ord5	0.109	0.130	0.343	0.317	0.115	0.147	0.522	0.603
PA_Ord6	0.101	0.110	0.336	0.407				
UA_Ord1	0.298	0.308	0.647	0.662	0.353	0.364	0.753	0.754
UA_Ord2	0.298	0.307	0.529	0.518	0.349	0.361	0.730	0.716
UA_Ord3	0.315	0.345	0.550	0.554	0.233	0.288	0.639	0.638
UA_Ord4	0.193	0.256	0.428	0.437	0.132	0.184	0.443	0.512
UA_Ord5	0.056	0.145	0.176	0.355	0.144	0.170	0.654	0.697
UA_Ord6	0.147	0.087	0.488	0.321				

3.4.3. Performance Evaluation Metrics of the Geometric Assessment of Channel Orders

Three performance measures (PA, UA, and KI) were computed using the outcomes of the multiclass error matrices (Figure 3.3d and Table 3.3) derived from the comparison between channels of similar orders (Tables 2.5–2.8).

In general, comparing the PALSAR DEM 28.5 m and LiDAR DTM 28.5 m-derived orders (Table 3.7) at similar ATs and PBTVs showed the best evaluation measures with few exceptions. Using a PBTV of 3 and an AT corresponding to 100 pixels, the estimated PA and UA values for channels of orders 1, 2, 3, 4, and 5 were equal to 0.790, 0.699, 0.691, 0.568, and 503 and 0.806, 0.809, 0.682, 0.548, 0.742, respectively (Table 3.7). Using the previously mentioned conditions, the measures computed from assessing the orders extracted from PALSAR DEM (Table 3.7) were slightly higher than those estimated from evaluating orders derived from ALOS DSM (Table 3.5) and SRTM DEM (Table 3.6), when compared to the LiDAR DTM 28.5 m-based orders with absolute differences ranging from 0.017 to 0.188 and from 0.025 to 0.177, respectively. The estimated KIs per orders using a PBTV of 3 confirmed the previous results, since they were equal to 0.766, 0.721, and 0.769 and 0.816, 0.793, and 0.828 in the evaluation of orders delineated from ALOS DSM (Table 3.5), SRTM DEM (Table 3.6), and PALSAR DEM (Table 3.7) using those extracted from LiDAR DTM 28.5 m at ATs corresponding to 25 and 100 pixels, respectively. The average of the differences between the PA and UA values for channels of orders 1 to 5 resulting from comparing orders delineated from PALSAR DEM 28.5 m (Table 3.7) and LiDAR DTM was 0.184 and 0.181 using an AT corresponding to 25 pixels and PBTV of 0 and 3, respectively. Using the previously mentioned conditions, but with an AT corresponding to 100 pixels, the average of differences was 0.266 and 0.300, respectively (Table 3.7). The PA and UA values estimated from evaluating orders extracted from PALSAR DEM 28.5 m (Table 3.7) were higher than those computed from assessing PALSAR DEM 12.5 m-derived orders (Table 3.8), when compared to those delineated from LiDAR DTMs, at equivalent spatial resolutions, with average values of 0.117 and 0.123 at an AT corresponding to 100 pixels, respectively. In addition, the estimated KI from evaluating orders delineated from PALSAR DEM 28.5 m was higher than that reported from assessing orders derived from PALSAR DEM 12.5 m when compared to LiDAR DTMs by difference values of 0.127 and 0.112 utilizing a PBTV of 3 and ATs corresponding to 25 and 100 pixels, respectively.

The performance metrics of the orders derived from ALOS DSM 28.5 m (Table 3.5) had the highest accuracy when compared to those extracted from LiDAR DTM. Employing a PBTV of 3 and an AT corresponding to 25 pixels, the PA and UA values calculated from

comparing ALOS and LiDAR DSMs-derived channels having orders of 1 to 6 were equal to 0.733, 0.581, 0.610, 0.563, 0.347, and 0.377 and 0.691, 0.583, 0.626, 0.521, 0.460, and 0.593, respectively (Table 3.5). Using a PBTv of 3 and an AT corresponding to 100 pixels, the differences between the PA values of channels having orders 1 to 5 reported from evaluating ALOS DSM 28.5 m (Table 3.5) and those derived from SRTM DEM (Table 3.6) and PALSAR DEM (Table 3.7) were 0.020, 0.087, 0.151, -0.052, and -0.040 and 0.015, 0.067, 0.037, 0.135, and 0.127, respectively, when compared to those derived from LiDAR DSM 28.5 m. Additionally, the UA differences for channels of orders 1 to 5 were 0.036, 0.025, 0.022, 0.140, and 0.039 and 0.009, -0.047, 0.043, 0.101, and 0.066, respectively. There were minor exceptions where the performance of orders delineated from SRTM DEM 28.5 m (Table 3.6) exceeded that of PALSAR DEM 28.5 m-derived orders (Table 3.7), particularly for PA values of orders 4 and 5 and UA of order 5, using an AT corresponding to 100 pixels and PBTv of 0 and 3, respectively. The estimated KIs per orders assured the previous results, since they were equal to 0.766, 0.725, and 0.749 and 0.827, 0.797, and 0.806, respectively, when assessing orders delineated from ALOS DSM (Table 3.5), SRTM DEM (Table 3.6), and PALSAR DEM (Table 3.7) based on those extracted from LiDAR DSM using a PBTv of 3 and ATs corresponding to 25 and 100 pixels.

Table 3.7. Performance accuracy metrics computed based on a comparison between whole networks/orders extracted from the LiDAR DTM/DSM 28.5 m and the PALSAR DEM 28.5 m at different ATs expressed in the corresponding number of pixels and PBTv in pixels.

Reference LiDAR-based Net	DTM	DSM	DTM	DSM	DTM	DSM	DTM	DSM
PBTv_AT	0_25	0_25	3_25	3_25	0_100	0_100	3_100	3_100
PA_Net	0.530	0.491	0.899	0.880	0.509	0.452	0.892	0.880
UA_Net	0.547	0.517	0.927	0.926	0.537	0.475	0.940	0.923
F_Net	0.538	0.504	0.913	0.902	0.523	0.463	0.915	0.901
KI_Net	0.483	0.444	0.902	0.890	0.496	0.433	0.910	0.895
KI_Ords	0.440	0.404	0.769	0.749	0.471	0.409	0.828	0.806
PA_Ord1	0.438	0.414	0.731	0.695	0.475	0.428	0.790	0.769
PA_Ord2	0.407	0.370	0.585	0.555	0.430	0.410	0.699	0.690
PA_Ord3	0.403	0.368	0.576	0.546	0.437	0.336	0.691	0.643
PA_Ord4	0.404	0.340	0.570	0.541	0.360	0.176	0.568	0.492
PA_Ord5	0.355	0.147	0.466	0.341	0.221	0.112	0.503	0.436
UA_Ord1	0.433	0.424	0.722	0.712	0.484	0.434	0.806	0.781
UA_Ord2	0.436	0.396	0.626	0.595	0.497	0.469	0.809	0.788
UA_Ord3	0.476	0.437	0.679	0.649	0.431	0.322	0.682	0.617
UA_Ord4	0.402	0.292	0.568	0.464	0.347	0.197	0.548	0.551
UA_Ord5	0.186	0.168	0.244	0.390	0.325	0.153	0.742	0.593

3.4.4. Effect of Global DEM Spatial Resolution on the Evaluation of Channel Networks/Orders

Although the previously mentioned results, the PALSAR DEM 12.5 m-derived channel network and Strahler orders (Table 3.8) was still the most accurate and had the best agreement with those extracted from LiDAR DTM, with taking into the account the fine spatial resolution it had.

Table 3.8. Performance accuracy metrics computed based on the comparison between whole networks/orders extracted from the LiDAR DTM/DSM 12.5 m and the PALSAR DEM 12.5 m at different ATs expressed in the corresponding number of pixels and PBTVs in pixels.

Reference LiDAR-based Net	DTM	DSM	DTM	DSM	DTM	DSM	DTM	DSM
PBTV_AT	0_25	0_25	3_25	3_25	0_100	0_100	3_100	3_100
PA_Net	0.378	0.347	0.852	0.831	0.331	0.291	0.813	0.782
UA_Net	0.367	0.345	0.826	0.825	0.354	0.318	0.870	0.853
F_Net	0.373	0.346	0.838	0.828	0.342	0.304	0.841	0.816
KI_Net	0.294	0.263	0.817	0.805	0.305	0.265	0.832	0.805
KI_Ords	0.243	0.218	0.643	0.627	0.275	0.239	0.716	0.686
PA_Ord1	0.250	0.229	0.607	0.579	0.271	0.243	0.661	0.623
PA_Ord2	0.221	0.200	0.422	0.399	0.248	0.215	0.544	0.507
PA_Ord3	0.212	0.194	0.382	0.375	0.219	0.188	0.497	0.499
PA_Ord4	0.208	0.189	0.386	0.391	0.216	0.188	0.475	0.484
PA_Ord5	0.215	0.189	0.381	0.380	0.191	0.074	0.462	0.240
PA_Ord6	0.233	0.088	0.412	0.217	0.253	0.062	0.625	0.192
PA_Ord7	0.253	0.144	0.515	0.313				
UA_Ord1	0.223	0.209	0.543	0.528	0.273	0.254	0.667	0.652
UA_Ord2	0.224	0.214	0.428	0.426	0.270	0.245	0.591	0.577
UA_Ord3	0.237	0.229	0.428	0.442	0.256	0.230	0.581	0.610
UA_Ord4	0.241	0.227	0.448	0.470	0.279	0.177	0.616	0.454
UA_Ord5	0.263	0.176	0.466	0.355	0.227	0.090	0.548	0.293
UA_Ord6	0.264	0.112	0.467	0.277	0.274	0.155	0.676	0.481
UA_Ord7	0.274	0.155	0.557	0.335				

An AT corresponding to 519 pixels (equivalent to an AT corresponding to 100 pixels at a spatial resolution of 28.5 m using Equation (3)) was used to compare the channel network and orders extracted from PALSAR DEM versus those derived from LiDAR DTM 12.5 m (Table 3.9). It was found that the calculated performance measures were improved. These measures were found to be closer to those estimated from the comparison between networks

extracted from ALOS DSM (Table 3.5) and PALSAR DEM (Table 3.7) with that delineated from LiDAR DTM 28.5 m. Furthermore, the differences between PA and UA values resulted from comparing channels of orders 1 to 5 delineated from PALSAR DEM 12.5 m, PALSAR DEM 28.5 m, and ALOS DSM 28.5 m were 0.020, -0.026, 0.151, -0.005, and 0.081 and 0.002, 0.011, 0.098, 0.011, and 0.014, respectively, when compared to those derived from LiDAR DTMs using a PBTv of 3 and ATs corresponding to 519 and 100 for spatial resolutions of 12.5 m and 28.5 m, respectively (Table 3.9). Additionally, the UA differences for channels of orders 1 to 5 were -0.064, -0.072, -0.022, -0.002, and 0.195 and -0.088, -0.151, -0.068, -0.026, and 0.007, respectively (Table 3.9). Moreover, the KI differences were 0.061 and -0.052 using the same previously mentioned conditions (Table 3.9).

In the comparison of channel network and orders extracted from PALSAR DEM 12.5 m with those derived from LiDAR DTM at an AT corresponding to 100 pixels, it has been found the performance metrics started to noticeably improve after utilizing only one pixel as a buffer tolerance. This means that an approximate deviation of only one pixel (corresponding to a horizontal distance of 12.5 m) was required to directly gain an obvious improvement in the matching accuracy. A horizontal offset of three pixels (corresponding to a horizontal distance of 87.5 m) was required to achieve an apparent enhancement in matching during the assessment of the networks/orders extracted from ALOS DSM and PALSAR DEM based on those delineated from LiDAR DTM at a spatial resolution of 28.5 m (Table 3.9).

Table 3.9. Performance metrics computed based on the comparison between networks/orders extracted from LiDAR DTMs and global DEMs at different ATs expressed in the corresponding number of pixels, PBTv in pixels, and spatial resolution in m.

Reference Nets	LiDAR DTMs-based Nets					
	PALSAR DEMs-based Nets				ALOS DSM-based Net	SRTM DEM-based Net
Test Nets						
Spatial Resolution	12.5 m	12.5 m	12.5 m	28.5 m	28.5 m	28.5 m
PBTv_AT	3_519	3_25	3_100	3_100	3_100	3_100
PA_Net	0.804	0.852	0.813	0.892	0.916	0.891
UA_Net	0.900	0.826	0.870	0.940	0.920	0.912
F_Net	0.849	0.838	0.841	0.915	0.918	0.902
KI_Net	0.846	0.817	0.832	0.910	0.913	0.896
KI_Ords	0.776	0.643	0.716	0.828	0.816	0.793
PA_Ord1	0.792	0.607	0.661	0.790	0.771	0.759
PA_Ord2	0.710	0.422	0.544	0.699	0.736	0.675
PA_Ord3	0.789	0.382	0.497	0.691	0.638	0.515
PA_Ord4	0.580	0.386	0.475	0.568	0.585	0.683
PA_Ord5	0.518	0.381	0.462	0.503	0.437	0.522
PA_Ord6		0.412	0.625			
PA_Ord7		0.515				
UA_Ord1	0.717	0.543	0.667	0.806	0.781	0.753
UA_Ord2	0.658	0.428	0.591	0.809	0.730	0.730
UA_Ord3	0.615	0.428	0.581	0.682	0.637	0.639
UA_Ord4	0.522	0.448	0.616	0.548	0.523	0.443
UA_Ord5	0.749	0.466	0.548	0.742	0.554	0.654
UA_Ord6		0.467	0.676			
UA_Ord7		0.557				

3.4.5. Characterizing the Horizontal Offset Between the Extracted Channel Networks

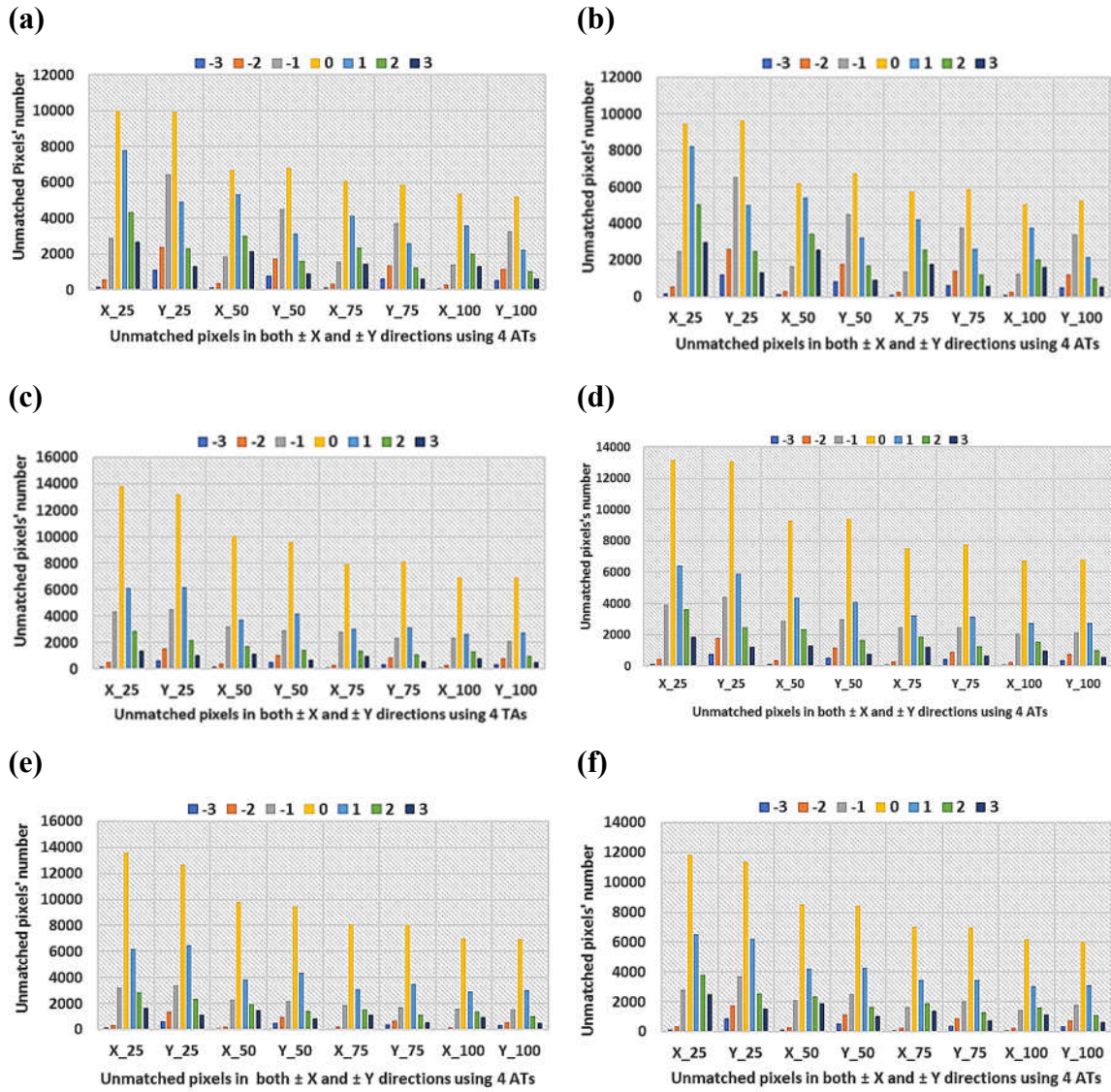
Figure 3.7 shows the histograms estimated based on the comparison between channel networks extracted from global DEMs based on those derived from the reference LiDAR

DTMs/DSMs. They displayed each channel segment's displacement in both $\pm X$ and $\pm Y$ directions, at PBTVs ranging from 0 to 3 pixels and four ATs (corresponding to at least 25, 50, 75, and 100 pixels). The number of co-located channels' pixels using a PBTV of 0 was always higher than that reported using other PBTVs (1 to 3 pixels). Employing larger ATs and a PBTV of 3, the number of unmatched pixels decreased (Figure 3.7). Moreover, using different ATs, the number of displaced channels' pixels reduced with the increase of PBTV from 0 to 3 pixels (Figure 3.7). The number of channels' pixels that remained without displacement (i.e., had 0 PBTV) was always greater when comparing the networks extracted from global DEMs based on those derived from LiDAR DTMs rather than LiDAR DSMs. The highest, and a nearly equal number of co-located pixels (using a PBTV of 0) were reported from evaluating the networks derived from ALOS DSM (Figure 3.7c) and PALSAR DEM (Figure 3.7e) when compared to that extracted from LiDAR DTM with a similar spatial resolution of 28.5 m. Due to the fine spatial details of the PALSAR DEM 12.5 m, the number of matched pixels using a PBTV of 0 was higher than that with a spatial resolution of 28.5 m.

Using a PBTV of 3 pixels and ATs corresponding to 25 and 100, the PALSAR DEM 28.5 m-derived channel segments shifted 1689 and 973 pixels in +X direction and 1151 and 541 pixels in +Y direction, and 159 pixels and 54 pixels in -X direction and 653 and 325 pixels in -Y direction, respectively; with respect to LiDAR DTM-based channels' pixels (Figure 3.7e).

The number of unmatched pixels was higher in evaluating the network extracted from PALSAR DEM 12.5 m (Figure 3.7g), due to its finer details than at a spatial resolution of 28.5 m (Figure 3.7e). Using a PBTV of 3 and an AT corresponding to 100 pixels, a shifting in the channel segments by 8342 and 5655 pixels toward the +X and +Y directions, and 754 and 2300 pixels toward the -X and -Y directions, respectively, in the assessment of channels' pixels derived from PALSAR DEM and LiDAR DTM 12.5 m was found (Figure 3.7g).

In the comparison between the channels extracted from ALOS DSM and LiDAR DSM 28.5 m, the ALOS DSM-derived network was displaced by 1163 and 667 pixels in the +X and +Y directions, and 82 and 366 pixels in the -X and -Y direction, respectively, with respect to LiDAR DSM-based network at a PBTv of 3 pixels and an AT corresponding to 100 pixels (Figure 3.7d).



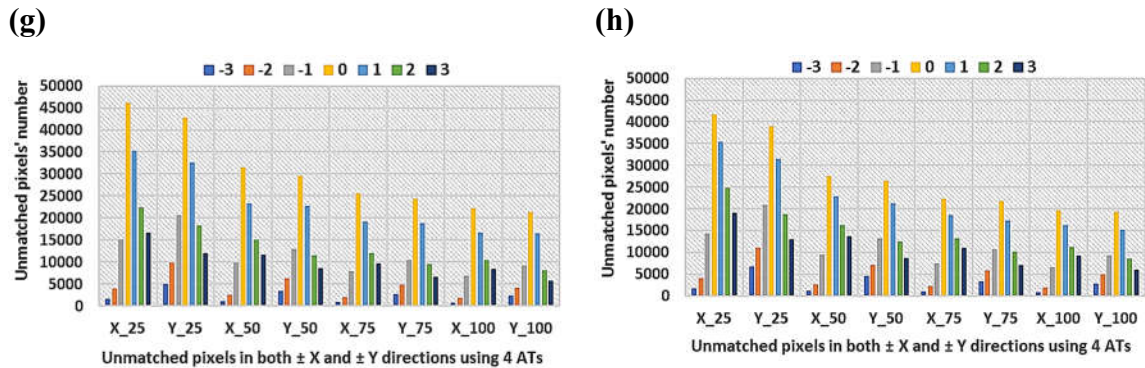


Figure 3.7. Deviations of channels' pixels in in both $\pm X$ and $\pm Y$ directions at different ATs and PBTVs in a comparison between the networks extracted from both: **(a)** LiDAR DTM and SRTM 28.5 m, **(b)** LiDAR DSM and SRTM 28.5 m, **(c)** LiDAR DTM and ALOS DSM 28.5 m, **(d)** LiDAR DSM and ALOS DSM 28.5 m, **(e)** LiDAR DTM and PALSAR DEM 28.5 m, **(f)** LiDAR DSM and PALSAR DEM 28.5 m, **(g)** LiDAR DTM and PALSAR DEM 12.5 m, and **(h)** LiDAR DSM and PALSAR DEM 12.5 m.

3.5. Discussion

3.5.1. Vertical Accuracy of Global DEM

The use of LiDAR DEMs with fine spatial resolutions as benchmarks to assess global spaceborne DEM sources has been well documented by previous studies. Dewitt et al. [123] employed the LiDAR DEM as a reference to evaluate the SRTM DEM 30 m over a heavily forested section in West Virginia, USA. The SRTM DEM showed low accuracy with an RMSE of 16.77 m and systematic negative bias. Acharya et al. [124] evaluated both SRTM DEM and ALOS DSM using LiDAR DEM 30 m in Chuncheon, Korea. The ALOS DSM outperformed the SRTM DEM when compared to the LiDAR DTM, with RMSE values of 12.232 m and 16.843 m, respectively. Furthermore, Liu et al. [125] found that the vertical difference between ALOS DSM and resampled LiDAR DSM 30 m ranged from 0 to 2.75 m with a standard deviation of 1.58 m over Tsengwen, Taiwan.

Many other researchers have used ground control points (GCPs) to evaluate different open DEM sources. Alganci et al. [126] computed the relative accuracies of the SRTM DEM V03 30 m and ALOS DSM 30 m utilizing different sets of ground checkpoints in the Istanbul metropolitan area, Turkey. Under bare terrain condition, the ALOS DSM had better performance than the SRTM DEM, with RMSE values of 2.41 m and 3.53 m, respectively. With respect to different land cover classes, the ALOS DSM still provided higher accuracy than the SRTM DEM. Santillan and Makinano-Santillan 2016 [127] conducted vertical accuracy assessment of recent releases of the ALOS DSM 30 m and SRTM DEM 30 m using scattered control points in Mindanao, Philippines. Their results showed that the ALOS DSM 30 m and SRTM DEM 30 m had RMSE values of 5.68 m and 8.28 m, respectively.

Tadono et al. [13] estimated the vertical height difference between ALOS DSM and SRTM-3 V02 over different sites and the computed RMSE values ranged from 1.91 m to 5.19 m. Takaku et al. [81] reported that the height difference between the ALOS DSM and SRTM-3 V02 had RMSE values ranging from 1.93 m to 11.38 m. In addition, an evaluation of the LiDAR DSM using GCPs resulted in an RMSE of 3.94 m. Moreover, the ALOS DSM 30 m showed similar accuracy to the SRTM 1 DEM 30 m when compared to a 1: 50,000 cm reference DEM over different types of terrain in China [128]. Alganci et al. [126] explained the higher accuracy of the ALOS DSM 30 m by its generation process through down-sampling of a 5 m mesh version utilizing statistical central tendency measures (i.e., average and median).

To my best knowledge, there have been no studies to evaluate the PALSAR DEM 12.5 m using LiDAR datasets. However, the higher accuracy of the PALSAR DEM 12.5 m could be interpreted by the use of high-quality DEMs with fine spatial resolutions (i.e., the National Elevation Dataset (NED)) in the detailed radiometric and geometric correction of PALSAR imagery (see [80], [129] for more details).

Some previous studies reported findings that were similar to the current results, but with different RMSE values. Therefore, a number of factors would be worthwhile to consider when quantifying the vertical height accuracy of optical and radar satellite data-based

DEMs,, such as the presence of: (i) An extensive topographic change (e.g., due to surface mining excavations) (e.g., Reference [126]), (ii) rugged mountainous regions, particularly for interferometric SAR returns that may potentially be affected by foreshortening, layover, and shadow [130], (iii) vegetation canopy of varied roughness (e.g., [126], [131]), (iv) different dates for collecting the original data to generate various DEMs, possible land use changes, and growth of trees during extended time spans (e.g., Reference [128]), (v) slope change due to abrupt change in relief, where it was proved that DEM errors rapidly increased if the slope was greater than 20° [69], (vi) significant differences in the elevation ranges (i.e., difference between minimum and maximum relief) within a particular study area, where a high elevation variance can reduce the DEM's vertical accuracy [69], and (vii) various versions of the same global elevation dataset with different levels of accuracy.

3.5.2. Horizontal Accuracy of Channel Networks

To my best knowledge, there are two similar studies in the literature, in which Anderson et al. [46] and Mozas-Calvache et al. [47] introduced two methods for the quantitative comparison of vector-based stream networks. Anderson et al. [46] mentioned that it is a complex and challenging task to compare and evaluate the degree of matching between two networks of several sets of polylines. They proposed the relative sinuosity, and longitudinal root mean square error (LRMSE) techniques for the quantitative evaluation of the quality and variation in linear stream features. They found that matched sinuosity could indicate a similar level of meandering but did not imply that both channel network polylines were well matched. Therefore, they recommended using the LRMSE technique to evaluate the horizontal similarity between channel lines rather than sinuosity deviation. However, they stated that both techniques must be carefully reviewed before being used to avoid the no-data anomalies, such as significantly unequal polyline lengths.

Mozas-Calvache et al. [47] proposed a method to determine the maximum and mean positional displacements of DEMs-based drainage networks. They used the adapted Hausdorff distance (i.e., a 2-D maximum distance between channels) and vertex influence (i.e., weighting each vector of the 3-D channel by the segments' lengths adjacent to each

vertex) methods [132] to determine the horizontal displacement between the networks. Their findings demonstrated their method's applicability to determine the positional displacement of the selected channels [47]. However, the proposed methods by Mozas-Calvache et al. [47] and Anderson et al. [46] had similar limitations in the selection and preparation of channels for evaluation. They selected only a subset of channels; also, they checked that there were a one-to-one correspondence and proximity between the channels' polylines in both the reference and test datasets. Moreover, they edited the selected channels, and if a particular channel was missed in the test data, they either ignored or deleted the reference channel of interest. The last consideration was that they manually trimmed the more extended channels around the missing branches.

In this study, the introduced method overcame all the previously mentioned constraints, so it is a practical method that can be used without any prior selection, adjustment, trimming, and deletion of the comparable channel networks/orders. It directly considered all the channels in both the reference and test datasets, whether they were co-located or not. Furthermore, the introduced method and the developed toolbox can automate the quantification and visualization of the horizontal spatial variations between channel networks/orders, as well as they have the advantage of evaluating unmatched pixels using different PBTVs (any number of pixels).

3.5.3. Similarity Between the Findings of the Vertical Assessment of Global DEMs and the Horizontal Evaluation of Their Derived Channel Networks/Orders

The achieved results in Section 4 demonstrated that the findings of both methods (pixel-based vertical accuracy of global DEMs and horizontal accuracy of their derived networks/orders) were similar in some cases, but not in others.

Using traditional statistical indices (RMSE and MD), it was found that PALSAR DEM 12.5 m had the best performance with respect to the PALSAR DEM 28.5 m, ALOS DSM 28.5 m, and SRTM DEM 28.5 m, when compared to the LiDAR DTMs at comparable spatial resolutions. The channel network/orders derived from PALSAR DEM 28.5 m had

the highest accuracy, followed by those extracted from ALOS DSM 28.5 m and SRTM DEM 28.5 m in comparison with those derived from LiDAR DTM 28.5 m. The findings of both methods were similar, except for the performance of networks/orders delineated from PALSAR DTM 12.5 m using ATs corresponding to at least 25, 50, 75, and 100 pixels. However, employing an equivalent AT to that at a spatial resolution of 28.5 m, it was found that the performance of channel network/orders extracted from PALSAR DEM 12.5 m was obviously improved. I suggest selecting the channel network/orders extracted from the DEM with the finest spatial resolution for using in geomorphological and hydrological applications if the accuracy metrics evaluating both original DEMs and their derived drainage networks/orders were high and close to each other. Consequently, the channel network and Strahler orders extracted from PALSAR DEM 12.5 m were considered to have the best accuracy performance (see Section 4.4 for more details) when compared to those delineated from LiDAR DTM (i.e., the findings of both methods were considered similar in the cases mentioned above).

Employing the RMSE and MD statistical measures, the ALOS DSM showed the highest vertical accuracy, followed by SRTM DEM 28.5 m, PALSAR DEM 12.5 m, and PALSAR DEM 28.5 m, when compared to the LiDAR DSMs at comparable spatial resolutions. Channel networks/orders derived from ALOS DSM 28.5 m and PALSAR DEM 12.5 m also showed the highest and lowest performance, respectively, when compared to those extracted from LiDAR DSMs at similar spatial resolutions. Therefore, the reported results from both methods were similar in the latter case. However, there were two exceptions where the networks/orders extracted from PALSAR DEM 28.5 m and SRTM DEM 28.5 m ranked second and third in the horizontal accuracy, respectively, contrary to the performance of the original DEMs. Therefore, the findings of the two methods were dissimilar when comparing PALSAR DEM 28.5 m and SRTM DEM 28.5 and their derived networks/orders with LiDAR DSM 28.5 m and its extracted network/orders.

3.5.4. Potential Applications of the Introduced Method

In terms of other potential applications related to remote sensing research, the introduced method can also be used to: (i) Determine the optimum AT by comparing the extracted drainage network from any remote sensing technology-based DEM with a reference network derived from high-quality DEM source (e.g., high-quality satellite imagery and aerial photographs, with the help of topographic maps and field measurements), (ii) assess the effectiveness of different channel networks' extraction algorithms, and (iii) quantify the degree of horizontal variation between other linear geologic and geomorphological features (e.g., structural lineaments, surface geologic contacts, and shorelines) extracted from remote sensing-based geospatial datasets of simultaneous or different temporal series, after converting them to raster format. For extended applications, and even if the LiDAR point cloud datasets are not available elsewhere in the world, other accurate DEM sources and their derived channel networks/orders can be used as benchmarks to quantify the vertical height accuracy of the DEMs used, as well as the horizontal accuracy of their channel networks/orders.

3.6. Conclusions

This paper presents a pixel-based method to evaluate the horizontal accuracy of channel networks and Strahler orders delineated from three global DEMs with four spatial resolutions using reference LiDAR DTMs/DSMs and their derived networks/orders at comparable spatial resolutions and different ATs and PBTVs. The horizontal displacements between the extracted channels in both the $\pm X$ and $\pm Y$ directions were quantified. The pixel-based vertical elevation accuracies of SRTM DEM 28.5 m, ALOS DSM 28.5 m, and PALSAR DEMs 12.5 m and 28.5 m were also determined using traditional statistical metrics (RMSE, MD). In particular, the vertical accuracy of the newly released ALOS PALSAR DEM with two spatial resolutions, 12.5 and 28.5 m, as well as their derived channel networks/orders were thoroughly studied. The similarity between the findings of the vertical assessment of the remote sensing-based DEMs and the horizontal variation of their delineated channel networks/orders were examined. Additionally, a new Python toolbox for

ArcGIS to automate the introduced method has been developed. The presented method effectively determines the horizontal accuracy of the different networks/orders. It was able to detect the performance of the networks/orders beyond the co-located channels' pixels using different PBTVs. In general, the PALSAR DEM 12.5 m and ALOS DSM 28.5 m and their derived channel networks/orders were very close in performance to the LiDAR DTM 12.5 m and DSM 28.5 m and their extracted networks/orders, respectively, at comparable spatial resolutions.

The evaluations of the vertical accuracy of spaceborne DEMs and their derived channel networks and Strahler orders revealed the following:

- The ALOS DSM 28.5 m and PALSAR DEM 12.5 m had the best performance when compared to the LiDAR DSM 28.5 m and LiDAR DTMs 12.5 m, respectively.
- The categorical performance measures were improved with the increase of PBTVs from 0 to 3 pixels. When evaluating the horizontal accuracy using LiDAR DTM 28.5 m derived-channel networks/orders, it was found that networks/orders delineated from PALSAR DEM 28.5 had the highest performance, followed by those from ALOS DSM 28.5 and SRTM DEM 28.5 m. However, taking into consideration the high spatial details of the PALSAR DEM 12.5 m, there was an extended possibility for observing more unmatched pixels, particularly with the use of an AT corresponding to 100 pixels. However, using an AT corresponding to 519 pixels (equivalent to an AT corresponding to 100 pixels at a spatial resolution of 28.5 m), the evaluation performance of the network/orders derived from LiDAR DEM 12.5 m was noticeably improved with the use of only one pixel as a PBTV. Therefore, the channel network and Strahler orders derived from PALSAR DEM 12.5 m were considered to have high horizontal accuracy (see Sections 4.4 and 5.3 for additional details).
- Using a PBTV of 0, the number of co-located channels' pixels was higher than those resulting from the use of more PBTVs. The number of unmatched pixels decreased

with the increase of PBTv from 0 to 3 at different ATs. The number of channels that remained without displacement (a PBTv of 0) was greater when evaluating the networks delineated from global DEMs using those derived from LiDAR DTMs rather than LiDAR DSMs at comparable spatial resolutions. Furthermore, the highest number of matched co-located pixels was recorded in the comparison of the PALSAR DEM 28.5 m- and ALOS DSM 28.5 m-derived networks with that derived from LiDAR DTM 28.5 m.

The findings of the two methods (pixel-based vertical accuracy of global DEMs and horizontal accuracy of their derived channel networks/orders) were mostly similar, but there were exceptions, particularly in comparison with LiDAR DSM 28.5 m and its derived network/orders.

I recommend that other researchers evaluate DEMs and their channel networks/orders before involving them in their geomorphological and hydrological studies. Additionally, I suggest using the introduced method over areas of different land covers, geomorphic units, lithology, and climatic zones elsewhere in the world.

Author Contributions

Conceptualization, M.Sh.; methodology, M.Sh., and A.M.; software, M.Sh., and A.M.; validation, M.Sh., A.M., Q.K.H., and N.El.; formal analysis, M.Sh; investigation, M.Sh; resources, N.El.; writing—original draft preparation, M.Sh.; writing—review and editing, N.El., Q.K.H., and M.sh.; visualization, M.Sh; supervision, N.El., and Q.K.H.; funding acquisition, M.Sh.

Acknowledgments

The authors do acknowledge and appreciate the anonymous reviewers that have taken out time to read our manuscript and provide valuable feedback. This study and the first author have been funded by the Ministry of The Higher Education, Egypt. The acknowledgment extended to the Mobile Multi-Sensor Research Team, Department of Geomatics Engineering, University of Calgary, Canada. The ALOS DSM data provided by the Japan Aerospace Exploration Agency (JAXA) and the Japanese Ministry of Economy, Trade, and Industry (METI). The SRTM DEM provided by National Aeronautics and Space Administration “NASA.” Both datasets were accessed through OpenTopography web-domain. The ALOS PALSAR DEM original data were provided by JAXA and modified by Alaska Satellite Facility (ASF DAAC), 2017; “<https://www.asf.alaska.edu/doi/105067/z97hfcnkr6va/>”. These datasets were also accessed through ASF DAAC. “Dataset: ASF DAAC, ALOS PALSAR_Radiometric_Terrain_Corrected_high_res; Includes Material © JAXA/METI 2007. Accessed through ASF DAAC 2018. 10.5067/Z97HFCNKR6VA”. The LiDAR point cloud data has acquired and processed for the Pacific Gas and Electric Company (PG&E) by Watershed Sciences, Inc. (WSI) across the DCP San Simeon survey area from 29 January 2013 to 25 February 2013. It was accessed in 2017 through OpenTopography web domain. The authors are grateful for the above-mentioned organizations and companies and do appreciate their contribution and support to the scientific community.

Conflicts of Interest

The authors declare no conflict of interest.

References

- [1] T. H. Tarekegn, A. T. Haile, T. Rientjes, P. Reggiani, and D. Alkema, “Assessment of an ASTER-generated DEM for 2D hydrodynamic flood modeling,” *Int. J. Appl. Earth Obs. Geoinf.*, vol. 12, no. 6, pp. 457–465, Jun. 2010.
- [2] A. Casas, G. Benito, V. R. Thorndycraft, and M. Rico, “The topographic data source of digital terrain models as a key element in the accuracy of hydraulic flood modelling,” *Earth Surf. Process. Landforms*, vol. 31, no. 4, pp. 444–456, Apr. 2006.
- [3] J. Li and D. W. S. Wong, “Effects of DEM sources on hydrologic applications,” *Comput. Environ. Urban Syst.*, vol. 34, no. 3, pp. 251–261, May 2010.
- [4] A. A. Jarihani, J. N. Callow, T. R. McVicar, T. G. Van Niel, and J. R. Larsen, “Satellite-derived Digital Elevation Model (DEM) selection, preparation and correction for hydrodynamic modelling in large, low-gradient and data-sparse catchments,” *J. Hydrol.*, vol. 524, pp. 489–506, May 2015.
- [5] A. R. Ghumman, I. S. Al-Salamah, S. S. AlSaleem, and H. Haider, “Evaluating the impact of lower resolutions of digital elevation model on rainfall-runoff modeling for ungauged catchments,” *Environ. Monit. Assess.*, vol. 189, no. 2, p. 54, Feb. 2017.
- [6] B. Purinton and B. Bookhagen, “Validation of digital elevation models (DEMs) and comparison of geomorphic metrics on the southern Central Andean Plateau,” *Earth Surf. Dyn.*, vol. 5, no. 2, pp. 211–237, Apr. 2017.
- [7] D. F. (David F. Maune and American Society for Photogrammetry and Remote Sensing., *Digital elevation model technologies and applications: the DEM users manual*. 2001.
- [8] J. C. Fernandez-Diaz, W. E. Carter, R. L. Shrestha, and C. L. Glennie, “Now you see it... Now you don’t: Understanding airborne mapping LiDAR collection and data

- product generation for archaeological research in Mesoamerica,” *Remote Sens.*, vol. 6, no. 10, pp. 9951–10001, Oct. 2014.
- [9] K. Jedlika, “Accuracy of surface models acquired from different sources —important information for geomorphological research,” *Geomorphol. Slovaca Bohem.*, vol. 1, pp. 17–28, 2009.
- [10] J. P. Wilson and J. C. Gallant, *Terrain analysis : principles and applications*. Wiley, 2000.
- [11] H. Taud, J. F. Parrot, and R. Alvarez, “DEM generation by contour line dilation,” *Comput. Geosci.*, vol. 25, no. 7, pp. 775–783, Aug. 1999.
- [12] N. El-Sheimy, C. (Caterina) Valeo, and A. (Ayman) Habib, *Digital terrain modeling : acquisition, manipulation, and applications*. Artech House, 2005.
- [13] T. Tadono, H. Ishida, F. Oda, S. Naito, K. Minakawa, and H. Iwamoto, “Precise global DEM generation by ALOS PRISM,” *ISPRS Ann. Photogramm. Remote Sens. Spat. Inf. Sci.*, vol. II-4, pp. 71–76, May 2014.
- [14] L. Yap, L. H. Kandé, R. Nouayou, J. Kamguia, N. A. Ngouh, and M. B. Makuate, “Vertical accuracy evaluation of freely available latest high-resolution (30 m) global digital elevation models over Cameroon (Central Africa) with GPS/leveling ground control points,” *Int. J. Digit. Earth*, vol. 12, no. 5, pp. 500–524, Apr. 2018.
- [15] K. A. Razak, M. Santangelo, C. J. Van Westen, M. W. Straatsma, and S. M. de Jong, “Generating an optimal DTM from airborne laser scanning data for landslide mapping in a tropical forest environment,” *Geomorphology*, vol. 190, pp. 112–125, May 2013.
- [16] C. Y. Fu and J. R. Tsay, “Statistic tests aided multi-source DEM fusion,” *Int. Arch. Photogramm. Remote Sens. Spat. Inf. Sci. - ISPRS Arch.*, vol. XLI-B6, pp. 227–233, Jul. 2016.

- [17] B. Basso, “Digital terrain analysis : data source , resolution and applications for modeling physical processes in agroecosystems,” *Riv. Ital. di Agrometeorol.*, vol. 2, pp. 5–14, 2005.
- [18] W. Shi, B. Wang, and Y. Tian, “Accuracy analysis of digital elevation model relating to spatial resolution and terrain slope by bilinear interpolation,” *Math. Geosci.*, vol. 46, no. 4, pp. 445–481, Jan. 2014.
- [19] K. Lin, Q. Zhang, and X. Chen, “An evaluation of impacts of DEM resolution and parameter correlation on TOPMODEL modeling uncertainty,” *J. Hydrol.*, vol. 394, no. 3–4, pp. 370–383, Nov. 2010.
- [20] S. Lin *et al.*, “Effect of DEM resolution on SWAT outputs of runoff, sediment and nutrients,” *Hydrol. Earth Syst. Sci. Discuss.*, vol. 7, no. 4, pp. 4411–4435, Jul. 2010.
- [21] B. F. Sanders, “Evaluation of on-line DEMs for flood inundation modeling,” *Adv. Water Resour.*, vol. 30, no. 8, pp. 1831–1843, Aug. 2007.
- [22] S. Sarachi, K. Hsu, and S. Sorooshian, “A statistical model for the uncertainty analysis of satellite precipitation products,” *J. Hydrometeorol.*, vol. 16, no. 5, pp. 2101–2117, Aug. 2015.
- [23] S. Saksena and V. Merwade, “Incorporating the effect of DEM resolution and accuracy for improved flood inundation mapping,” *J. Hydrol.*, vol. 530, pp. 180–194, Apr. 2015.
- [24] G. J.-P. Schumann, P. D. Bates, J. C. Neal, and K. M. Andreadis, “Technology: fight floods on a global scale,” *Nature*, vol. 507, no. 7491, pp. 169–169, Mar. 2014.
- [25] J. Vaze, J. Teng, and G. Spencer, “Impact of DEM accuracy and resolution on topographic indices,” *Environ. Model. Softw.*, vol. 25, no. 10, pp. 1086–1098, Apr. 2010.

- [26] C. L. Miller and R. A. Laflamme, "The Digital Terrain Model Theory & Application," *Photogramm. Eng. Remote Sens.*, vol. 24, no. 3, pp. 433–442, 1958.
- [27] G. Priestnall, J. Jaafar, and A. Duncan, "Extracting urban features from LiDAR digital surface models," *Comput. Environ. Urban Syst.*, vol. 24, no. 2, pp. 65–78, Feb. 2000.
- [28] W. S. Walker, J. M. Kelndorfer, and L. E. Pierce, "Quality assessment of SRTM C- and X-band interferometric data: Implications for the retrieval of vegetation canopy height," *Remote Sens. Environ.*, vol. 106, no. 4, pp. 428–448, Feb. 2007.
- [29] C. A. Baugh, P. D. Bates, G. Schumann, and M. A. Trigg, "SRTM vegetation removal and hydrodynamic modeling accuracy," *Water Resour. Res.*, vol. 49, no. 9, pp. 5276–5289, Sep. 2013.
- [30] G. Kocak, G. Buyuksalih, and K. Jacobsen, "Analysis of digital elevation models determined by high resolution space images," *Int. Arch. Photogramm. Remote Sens.*, vol. 35 (B4), p. 636–641, 2004.
- [31] L. B. Leopold, M. G. Wolman, and J. P. Miller, *Fluvial processes in geomorphology*. New York: Dover Publications, 1995.
- [32] J. F. O'Callaghan and D. M. Mark, "The extraction of drainage networks from digital elevation data," *Comput. Vision, Graph. Image Process.*, vol. 28, no. 3, p. 247, Dec. 1984.
- [33] W. Yang, K. Hou, F. Yu, Z. Liu, and T. Sun, "A novel algorithm with heuristic information for extracting drainage networks from raster DEMs," *Hydrol. Earth Syst. Sci. Discuss.*, vol. 7, no. 1, pp. 441–459, Jan. 2010.
- [34] A. Omran, S. Dietrich, A. Abouelmagd, and M. Michael, "New ArcGIS tools developed for stream network extraction and basin delineations using Python and java script," *Comput. Geosci.*, vol. 94, pp. 140–149, Sep. 2016.

- [35] H. Chandrashekar, K. V. Lokesh, M. Sameena, J. Roopa, and G. Ranganna, “GIS – based morphometric analysis of two reservoir catchments of Arkavati river, Ramanagaram district, Karnataka,” *Aquat. Procedia*, vol. 4, pp. 1345–1353, Jan. 2015.
- [36] M. Y. E. Angillieri, “Morphometric characterization of the Carrizal basin applied to the evaluation of flash floods hazard, San Juan, Argentina,” *Quat. Int.*, vol. 253, pp. 74–79, Mar. 2012.
- [37] D. G. Tarboton, R. L. Bras, I. Rodriguez-Iturbet, and R. M. Parsons, “On the extraction of channel networks from digital elevation data,” *Hydrol. Process.*, vol. 5, no. 1, pp. 81–100, Jan. 1991.
- [38] G. Moretti and S. Orlandini, “Hydrography-driven coarsening of grid digital elevation models,” *Water Resour. Res.*, vol. 54, no. 5, pp. 3654–3672, May 2018.
- [39] S. K. Jenson and J. O. Dominique, “Extracting topographic structure from digital elevation data for {Geographic Information System} analysis,” *Photogramm. Eng. Remote Sensing*, vol. 54, no. 11, pp. 1593–1600, Nov. 1988.
- [40] W.-T. T. Lin, W.-C. C. Chou, C.-Y. Y. Lin, P.-H. H. Huang, and J.-S. S. Tsai, “Automated suitable drainage network extraction from digital elevation models in Taiwan’s upstream watersheds,” *Hydrol. Process.*, vol. 20, no. 2, pp. 289–306, Feb. 2006.
- [41] S. Orlandini, G. Moretti, M. Franchini, B. Aldighieri, and B. Testa, “Path-based methods for the determination of nondispersive drainage directions in grid-based digital elevation models,” *Water Resour. Res.*, vol. 39, no. 6, Jun. 2003.
- [42] S. Orlandini and G. Moretti, “Determination of surface flow paths from gridded elevation data,” *Water Resour. Res.*, vol. 45, no. 3, pp. 1–14, Mar. 2009.
- [43] F. L. Ogden, J. Garbrecht, P. A. DeBarry, and L. E. Johnson, “GIS and Distributed

- Watershed Models. II: Modules, Interfaces, and Models,” *J. Hydrol. Eng.*, vol. 6, no. 6, pp. 515–523, Dec. 2001.
- [44] T. K. Tesfa, D. G. Tarboton, D. W. Watson, K. A. T. Schreuders, M. E. Baker, and R. M. Wallace, “Extraction of hydrological proximity measures from DEMs using parallel processing,” *Environ. Model. Softw.*, vol. 26, no. 12, pp. 1696–1709, Dec. 2011.
- [45] M. Wu, P. Shi, A. Chen, C. Shen, and P. Wang, “Impacts of DEM resolution and area threshold value uncertainty on the drainage network derived using SWAT,” *Water SA*, vol. 43, no. 3, pp. 450–462, Jul. 2017.
- [46] D. L. Anderson, D. P. Ames, and P. Yang, “Quantitative methods for comparing different polyline stream network models,” *J. Geogr. Inf. Syst.*, vol. 6, no. 2, pp. 88–98, Apr. 2014.
- [47] A. T. Mozas-Calvache, M. A. Ureña-Cámara, and F. J. Ariza-López, “Determination of 3D displacements of drainage networks extracted from digital elevation models (DEMs) using linear-based methods,” *ISPRS Int. J. Geo-Information*, vol. 6, no. 8, p. 234, Aug. 2017.
- [48] C. Beumier and M. Idrissa, “Digital terrain models derived from digital surface model uniform regions in urban areas,” *Int. J. Remote Sens.*, vol. 37, no. 15, pp. 3477–3493, Aug. 2016.
- [49] Y. Zheng, Q. Weng, and Y. Zheng, “A hybrid approach for three-dimensional building reconstruction in indianapolis from LiDAR data,” *Remote Sens.*, vol. 9, no. 4, p. 310, Mar. 2017.
- [50] A. Vianello, M. Cavalli, and P. Tarolli, “LiDAR-derived slopes for headwater channel network analysis,” *Catena*, vol. 76, no. 2, pp. 97–106, Jan. 2009.
- [51] N. Thommeret, J. S. Bailly, and C. Puech, “Extraction of thalweg networks from

- DTMs: Application to badlands,” *Hydrol. Earth Syst. Sci.*, vol. 14, no. 8, pp. 1527–1536, Aug. 2010.
- [52] D. Godone and G. Garnero, “The role of morphometric parameters in Digital Terrain Models interpolation accuracy: A case study,” *Eur. J. Remote Sens.*, vol. 46, no. 1, pp. 198–214, Jan. 2013.
- [53] B. Höfle, L. Griesbaum, and M. Forbriger, “GIS-Based detection of gullies in terrestrial lidar data of the cerro llamoca peatland (peru),” *Remote Sens.*, vol. 5, no. 11, pp. 5851–5870, Nov. 2013.
- [54] M. Cavalli, S. Trevisani, B. Goldin, E. Mion, S. Crema, and R. Valentinotti, “Semi-automatic derivation of channel network from a high-resolution DTM: The example of an italian alpine region,” *Eur. J. Remote Sens.*, vol. 46, no. 1, pp. 152–174, Feb. 2013.
- [55] P. Passalacqua, T. Do Trung, E. Foufoula-Georgiou, G. Sapiro, and W. E. Dietrich, “A geometric framework for channel network extraction from lidar: Nonlinear diffusion and geodesic paths,” *J. Geophys. Res.*, vol. 115, no. F1, p. F01002, Mar. 2010.
- [56] J. F. Parrot and C. Ramírez Núñez, “Artefactos y correcciones a los modelos digitales de Terreno provenientes del LiDAR,” *Investig. Geogr.*, vol. 2016, no. 90, pp. 28–39, Oct. 2016.
- [57] P. Yang *et al.*, “What is the effect of LiDAR-derived DEM resolution on large-scale watershed model results?,” *Environ. Model. Softw.*, vol. 58, pp. 48–57, Aug. 2014.
- [58] J. Roelens, I. Rosier, S. Dondeyne, J. Van Orshoven, and J. Diels, “Extracting drainage networks and their connectivity using LiDAR data,” *Hydrol. Process.*, vol. 32, no. 8, pp. 1026–1037, Apr. 2018.
- [59] F. Cazorzi, G. D. Fontana, A. De Luca, G. Sofia, and P. Tarolli, “Drainage network

- detection and assessment of network storage capacity in agrarian landscape,” *Hydrol. Process.*, vol. 27, no. 4, pp. 541–553, Feb. 2013.
- [60] M. Sharma, G. B. Paige, S. N. Miller, M. Sharma, G. B. Paige, and S. N. Miller, “DEM development from ground-based LiDAR data: A method to remove non-surface objects,” *Remote Sens.*, vol. 2, no. 11, pp. 2629–2642, Nov. 2010.
- [61] F. Altaf, G. Meraj, and S. A. Romshoo, “Morphometric analysis to infer hydrological behavior of Lidder watershed, western Himalaya, India,” *Geogr. J.*, vol. 2013, p. 14, Apr. 2013.
- [62] S. Bhatt and S. A. Ahmed, “Morphometric analysis to determine floods in the Upper Krishna basin using Cartosat DEM,” *Geocarto Int.*, vol. 29, no. 8, pp. 878–894, 2014.
- [63] M. M. El Osta and M. H. Masoud, “Implementation of a hydrologic model and GIS for estimating Wadi runoff in Dernah area, Al Jabal Al Akhadar, NE Libya,” *J. African Earth Sci.*, vol. 107, pp. 36–56, Jul. 2015.
- [64] S. Abuzied, M. Yuan, S. Ibrahim, M. Kaiser, and T. Saleem, “Geospatial risk assessment of flash floods in Nuweiba area, Egypt,” *J. Arid Environ.*, vol. 133, pp. 54–72, Oct. 2016.
- [65] R. Kannan, S. Venkateswaran, M. Vijay Prabhu, and K. Sankar, “Drainage morphometric analysis of the Nagavathi watershed, Cauvery river basin in Dharmapuri district, Tamil Nadu, India using SRTM data and GIS,” *Data Br.*, vol. 19, pp. 2420–2426, Aug. 2018.
- [66] N. Hassan Syed, A. Adbul Rehman, D. Hussain, S. Ishaq, and A. Ahmed Khan, “Morphometric analysis to prioritize sub-watershed for flood risk assessment in Central Karakoram National Park using GIS / RS approach,” in *ISPRS Annals of the Photogrammetry, Remote Sensing and Spatial Information Sciences, Volume IV-4/W4*, 2017, vol. IV, pp. 14–15.

- [67] C. S. Jahan, M. F. Rahaman, R. Arefin, S. Ali, and Q. H. Mazumder, “Morphometric analysis and hydrological inference for water resource management in Atrai-Sib river basin, NW Bangladesh using remote sensing and GIS technique,” *J. Geol. Soc. India*, vol. 91, no. 5, pp. 613–620, May 2018.
- [68] P. Kumar, R. Rajeev, S. Chandel, V. Narayan, and M. Prafull, “Hydrological inferences through morphometric analysis of lower Kosi river basin of India for water resource management based on remote sensing data,” *Appl. Water Sci.*, vol. 8, no. 1, pp. 1–16, Mar. 2018.
- [69] S. Mukherjee, P. K. Joshi, S. Mukherjee, A. Ghosh, R. D. Garg, and A. Mukhopadhyay, “Evaluation of vertical accuracy of open source digital elevation model (DEM),” *Int. J. Appl. Earth Obs. Geoinf.*, vol. 21, pp. 205–217, Apr. 2012.
- [70] J. Thomas, S. Joseph, K. P. Thrivikramji, and K. S. Arunkumar, “Sensitivity of digital elevation models: The scenario from two tropical mountain river basins of the Western Ghats, India,” *Geosci. Front.*, vol. 5, no. 6, pp. 893–909, Nov. 2014.
- [71] J. Thomas and V. Prasannakumar, “Comparison of basin morphometry derived from topographic maps, ASTER and SRTM DEMs: an example from Kerala, India,” *Geocarto Int.*, vol. 30, no. 3, pp. 346–364, Mar. 2015.
- [72] S. Das, P. P. Patel, and S. Sengupta, “Evaluation of different digital elevation models for analyzing drainage morphometric parameters in a mountainous terrain: a case study of the Supin–Upper Tons Basin, Indian Himalayas,” *Springerplus*, vol. 5, no. 1, pp. 1–38, Sep. 2016.
- [73] B. J. T. Watt, S. Y. Johnson, S. R. Hartwell, M. Roberts, and S. Jewell, “Offshore geology and geomorphology from Point Piedras Blancas to Pismo Beach, San Luis Obispo County, California,” 2015.
- [74] City of San Luis Obispo Utilities Department, “Whale Rock Reservoir | City of San

- Luis Obispo, CA,” 2019. [Online]. Available: <https://www.slocity.org/government/department-directory/utilities-department/water/water-sources/whale-rock-reservoir>. [Accessed: 02-Jan-2019].
- [75] C. A. Hall and S. W. Prior, “Geologic map of the Cayucos-San Luis Obispo Region, San Luis Obispo County, California,” 1975.
- [76] J. R. Griffin and W. B. Critchfield, “The distribution of forest trees in California,” *Res. Pap. PSW-RP-82. Berkeley, CA Pacific Southwest For. Range Exp. Station. For. Serv. U.S. Dep. Agric.*, vol. 82, pp. 1–124, 1972.
- [77] P. V. Wells, “Vegetation in relation to geological substratum and fire in the San Luis Obispo Quadrangle, California,” *Ecol. Monogr.*, vol. 32, no. 1, pp. 79–103, Feb. 1962.
- [78] Environmental Systems Research Institute (ESRI), “World Imagery: DigitalGlobe, GeoEye, i-cubed, USDA FSA, USGS, AEX, Getmapping, Aerogrid, IGN, IGP, swisstopo, and the GIS User Community,” 2018. [Online]. Available: <https://www.arcgis.com/home/item.html?id=10df2279f9684e4a9f6a7f08febac2a9>. [Accessed: 04-Jan-2019].
- [79] T. Farr *et al.*, “The shuttle radar topography mission,” *Rev. Geophys.*, vol. 45, no. 2, pp. 1–33, Jun. 2007.
- [80] J. Laurencelle, T. Logan, and R. Gens, “Alaska Satellite Facility (ASF) - Radiometrically terrain corrected ALOS PALSAR products,” 2015.
- [81] J. Takaku, T. Tadono, and K. Tsutsui, “Generation of high resolution global DSM from ALOS PRISM,” *Int. Arch. Photogramm. Remote Sens. Spat. Inf. Sci. - ISPRS Arch.*, vol. XL-4, pp. 243–248, May 2014.
- [82] S. Wilson and S. Steinberg, “Technical Data Report - Diablo Canyon Power Plant (DCCP) San Simeon - LiDAR & Orthoimagery Survey,” California, 2013.

- [83] K. Pakoksung and M. Takagi, “Digital elevation models on accuracy validation and bias correction in vertical,” *Model. Earth Syst. Environ.*, vol. 2, no. 1, pp. 1–13, Dec. 2016.
- [84] A. Sharma, K. N. Tiwari, and P. B. S. Bhadoria, “Vertical accuracy of digital elevation model from Shuttle Radar Topographic Mission - a case study,” *Geocarto Int.*, vol. 25, no. 4, pp. 257–267, Sep. 2010.
- [85] Environmental Systems Research Institute (ESRI), *What is ArcGIS?* Redlands, 2001.
- [86] S. Orlandini, P. Tarolli, G. Moretti, and G. Dalla Fontana, “On the prediction of channel heads in a complex alpine terrain using gridded elevation data,” *Water Resour. Res.*, vol. 47, no. 2, pp. 1–13, Feb. 2011.
- [87] J. Seibert and B. L. McGlynn, “A new triangular multiple flow direction algorithm for computing upslope areas from gridded digital elevation models,” *Water Resour. Res.*, vol. 43, no. 4, Apr. 2007.
- [88] D. Zhu, Q. Ren, Y. Xuan, Y. Chen, and I. D. Cluckie, “An effective depression filling algorithm for DEM-based 2-D surface flow modelling,” *Hydrol. Earth Syst. Sci.*, vol. 17, no. 2, pp. 495–505, Feb. 2013.
- [89] D. G. Tarboton, R. L. Bras, and I. Rodriguez-Iturbe, “The fractal nature of river networks,” *Water Resour. Res.*, vol. 24, no. 8, pp. 1317–1322, Aug. 1988.
- [90] A. Tribe, “Automated recognition of valley lines and drainage networks from grid digital elevation models: a review and a new method,” *J. Hydrol.*, vol. 139, no. 1–4, pp. 263–293, Nov. 1992.
- [91] D. R. Montgomery and W. E. Dietrich, “Channel initiation and the problem of landscape scale,” *Science*, vol. 255, no. 5046, pp. 826–830, Feb. 1992.

- [92] D. R. Maidment, *Arc hydro : GIS for water resources*. ESRI Press, 2002.
- [93] R. Jones, “Algorithms for using a DEM for mapping catchment areas of stream sediment samples,” *Comput. Geosci.*, vol. 28, no. 9, pp. 1051–1060, Nov. 2002.
- [94] Q. Hu *et al.*, “Exploring the use of Google Earth imagery and object-based methods in land use/cover mapping,” *Remote Sens.*, vol. 5, no. 11, pp. 6026–6042, Nov. 2013.
- [95] M. L. Clark, T. M. Aide, H. R. Grau, and G. Riner, “A scalable approach to mapping annual land cover at 250 m using MODIS time series data: A case study in the Dry Chaco ecoregion of South America,” *Remote Sens. Environ.*, vol. 114, no. 11, pp. 2816–2832, Nov. 2010.
- [96] C. Mering, J. Baro, and E. Upegui, “Retrieving urban areas on Google Earth images: application to towns of West Africa,” *Int. J. Remote Sens.*, vol. 31, no. 22, pp. 5867–5877, Dec. 2010.
- [97] A. N. Strahler, “Quantitative analysis of watershed geomorphology,” *Trans. Am. Geophys. Union*, vol. 38, no. 6, p. 913, Dec. 1957.
- [98] R. E. Horton, “Erosional development of streams and their drainage basins: hydro-physical approach to quantitative morphology,” *Geol. Soc. Am. Bull.*, vol. 56, no. 3, pp. 275–370, Mar. 1945.
- [99] GRASS Development Team, “Geographic Resources Analysis Support System (GRASS) (Open Source Geospatial Foundation Project),” 2014. [Online]. Available: https://live.osgeo.org/en/overview/grass_overview.html. [Accessed: 02-Jan-2019].
- [100] QGIS Development Team, “Quantum GIS Geographic Information System (Open Source Geospatial Foundation Project),” 2014. [Online]. Available: https://live.osgeo.org/en/overview/qgis_overview.html. [Accessed: 02-Jan-2019].
- [101] M. S. Tehrany, B. Pradhan, and M. N. Jebur, “Spatial prediction of flood susceptible

- areas using rule based decision tree (DT) and a novel ensemble bivariate and multivariate statistical models in GIS,” *J. Hydrol.*, vol. 504, pp. 69–79, Nov. 2013.
- [102] R. G. Congalton, “A review of assessing the accuracy of classifications of remotely sensed data,” *Remote Sens. Environ.*, vol. 37, no. 1, pp. 35–46, Jul. 1991.
- [103] G. M. Foody, “Status of land cover classification accuracy assessment,” *Remote Sens. Environ.*, vol. 80, no. 1, pp. 185–201, Apr. 2002.
- [104] S. D. A. Aronoff, “The map accuracy report: A user’s view,” *Photogramm. Eng. Remote Sensing*, vol. 48, no. 8, pp. 1309–1312, Aug. 1982.
- [105] A. Garcia-Pedrero, C. Gonzalo-Martin, D. Fonseca-Luengo, and M. Lillo-Saavedra, “A GEOBIA methodology for fragmented agricultural landscapes,” *Remote Sens.*, vol. 7, no. 1, pp. 767–787, Jan. 2015.
- [106] Z. Ao, Y. Su, W. Li, Q. Guo, and J. Zhang, “One-class classification of airborne LiDAR data in urban areas using a presence and background learning algorithm,” *Remote Sens.*, vol. 9, no. 10, p. 1001, Sep. 2017.
- [107] C. Qiu, M. Schmitt, L. Mou, P. Ghamisi, and X. X. Zhu, “Feature importance analysis for local climate zone classification using a residual convolutional neural network with multi-source datasets,” *Remote Sens.*, vol. 10, no. 10, p. 1572, Oct. 2018.
- [108] L. Cai, W. Shi, Z. Miao, and M. Hao, “Accuracy assessment measures for object extraction from remote sensing images,” *Remote Sens.*, vol. 10, no. 2, p. 303, Feb. 2018.
- [109] K. B. Pierce, “Accuracy optimization for high resolution object-based change detection: An example mapping regional urbanization with 1-m aerial imagery,” *Remote Sens.*, vol. 7, no. 10, pp. 12654–12679, Sep. 2015.
- [110] R. Gaetano, D. Ienco, K. Ose, and R. Cresson, “MRFusion: a deep learning

- architecture to fuse PAN and MS imagery for land cover mapping,” *Computer Vision and Pattern Recognition - arXiv:1806.11452 [cs.CV]*, Jun-2018. [Online]. Available: <http://arxiv.org/abs/1806.11452>.
- [111] C. Hütt, W. Koppe, Y. Miao, and G. Bareth, “Best accuracy land use/land cover (LULC) classification to derive crop types using multitemporal, multisensor, and multi-polarization SAR satellite images,” *Remote Sens.*, vol. 8, no. 8, p. 684, Aug. 2016.
- [112] Y. Li, X. Zhu, Y. Pan, J. Gu, A. Zhao, and X. Liu, “A comparison of model-assisted estimators to infer land cover/use class area using satellite imagery,” *Remote Sens.*, vol. 6, no. 9, pp. 8904–8922, Sep. 2014.
- [113] R. G. Congalton, R. G. Oderwald, and R. A. Mead, “Assessing Landsat classification accuracy using discrete multivariate analysis statistical techniques,” *Photogramm. Eng. Remote Sensing*, vol. 49, no. No. 12, pp. 1671–1678, Dec. 1983.
- [114] M. Story and R. G. Congalton, “Remote sensing brief accuracy assessment: a user’s perspective,” *Photogramm. Eng. Remote Sensing*, vol. 52, no. 3, pp. 397–399, Mar. 1986.
- [115] O. Rozenstein and A. Karnieli, “Comparison of methods for land-use classification incorporating remote sensing and GIS inputs,” *Appl. Geogr.*, vol. 31, no. 2, pp. 533–544, Apr. 2011.
- [116] J. Radoux and P. Bogaert, “Good practices for object-based accuracy assessment,” *Remote Sens.*, vol. 9, no. 7, p. 646, Jun. 2017.
- [117] S. V. Stehman, “Selecting and interpreting measures of thematic classification accuracy,” *Remote Sens. Environ.*, vol. 62, no. 1, pp. 77–89, Oct. 1997.
- [118] P.-N. Tan, M. Steinbach, and V. Kumar, *Introduction to data mining*. Pearson Addison Wesley, 2005.

- [119] J. Cohen, “A Coefficient of agreement for nominal scales,” *Educ. Psychol. Meas.*, vol. 20, no. 1, pp. 37–46, Apr. 1960.
- [120] R. Congalton and R. Mead, “A quantitative method to test for consistency and correctness in photointerpretation,” *Photogramm. Eng. Remote Sensing*, vol. 49, no. 1, pp. 69–74, Jan. 1983.
- [121] P. C. Smits, S. G. Dellepiane, and R. A. Schowengerdt, “Quality assessment of image classification algorithms for land-cover mapping: A review and a proposal for a cost-based approach,” *Int. J. Remote Sens.*, vol. 20, no. 8, pp. 1461–1486, Jan. 1999.
- [122] M. Boschetti *et al.*, “Comparative analysis of normalised difference spectral indices derived from MODIS for detecting surface water in flooded rice cropping systems,” *PLoS One*, vol. 9, no. 2, p. e88741, Feb. 2014.
- [123] J. D. Dewitt, T. A. Warner, and J. F. Conley, “Comparison of DEMs derived from USGS DLG, SRTM, a statewide photogrammetry program, ASTER GDEM and LiDAR: Implications for change detection,” *GIScience Remote Sens.*, vol. 52, no. 2, pp. 179–197, Mar. 2015.
- [124] T. D. Acharya, D. Lee, and I. T. Yang, “Comparative analysis of digital elevation models between AW3D30 , SRTM30 and airborne LiDAR : a case of Chuncheon, South Korea,” *J. Korean Soc. Surv. Geod. Photogramm. Cartogr.*, vol. 36, no. 1, pp. 17–24, 2018.
- [125] J. Liu *et al.*, “Accuracy evaluation of ALOS DEM with airborne Lidar data in Southern Taiwan,” in *International Geoscience and Remote Sensing Symposium (IGARSS)*, 2015, pp. 3025–3028.
- [126] U. Alganci, B. Besol, and E. Sertel, “Accuracy assessment of different digital surface models,” *ISPRS Int. J. Geo-Information*, vol. 7, no. 3, p. 114, Jul. 2018.
- [127] J. R. Santillan and M. Makinano-Santillan, “Vertical accuracy assessment of 30-M

- resolution ALOS, ASTER, and SRTM global DEMS over Northeastern Mindanao, Philippines,” *Int. Arch. Photogramm. Remote Sens. Spat. Inf. Sci. - ISPRS Arch.*, vol. 41, no. XLI-B4, pp. 149–156, Jun. 2016.
- [128] Z. Hu, J. Peng, Y. Hou, and J. Shan, “Evaluation of recently released open global digital elevation models of Hubei, China,” *Remote Sens.*, vol. 9, no. 3, p. 262, Mar. 2017.
- [129] G. R. Alaska Satellite Facility (ASF), “ASF radiometric terrain corrected products - Algorithm Theoretical Basis Document,” 2015.
- [130] M. Shimada, “Ortho-rectification and slope correction of SAR data using DEM and its Accuracy evaluation,” *IEEE J. Sel. Top. Appl. Earth Obs. Remote Sens.*, vol. 3, no. 4, pp. 657–671, Dec. 2010.
- [131] M. Hofton, R. Dubayah, J. B. Blair, and D. Rabine, “Validation of SRTM elevations over vegetated and non-vegetated terrain using medium footprint lidar,” *Photogramm. Eng. Remote Sensing*, vol. 72, no. 3, pp. 279–285, Mar. 2006.
- [132] A. T. Mozas-Calvache and F. J. Ariza-López, “Adapting 2D positional control methodologies based on linear elements to 3D,” *Surv. Rev.*, vol. 47, no. 342, pp. 195–201, May 2015.

CHAPTER FOUR

**REMOTE SENSING-BASED AN ENHANCED FLASH
FLOOD SUSCEPTIBILITY MAPPING USING
INTEGRATED BIVARIATE AND MULTIVARIATE
STATISTICAL MODELS**

Abstract

In recent years, flash floods are frequently occurring with accelerated severity in at Ad Dakhiliyah Governate, north of the Sultanate of Oman. Thus, developing flood susceptibility models is necessary to detect flood zones with different degrees of hazards to improve the mitigation of the negative consequences of flooding. Additionally, these predictive models can allow decision makers to develop their plans for the optimum sustainable development of the areas under flood hazards. The current study employed improved, combined bivariate and multivariate statistical approaches-based flood predictive modeling to predict flood-prone areas at fine watershed spatial details (i.e., 12.5 m). The geospatial inputs included thirteen flood triggering factors—namely, geology, soil, altitude (m), height above nearest drainage network (HAND) (m), Melton ruggedness number (MRN), drainage line density (DLD) km/km², topographic position index (TPI), aspect (°), valley depth (VD), topographic wetness index (TWI), convergence index (CI), flow length in the downstream direction (FL_DS), and Global Satellite Mapping of Precipitation-Gauge calibrated (GSMaP-G). The flood inventory map was generated through processing Sentinel-1A images for a specific flood event, with the help of volunteer geographic information (VGI). The equal stratified flood and non-flood points were randomly selected for training and testing flood susceptibility models. Using different confusion matrix-based evaluation measures such as the overall accuracy (OA), producer accuracy (PA), user accuracy (UA), F-measure (F), and Kappa index (KI), I found that the integrated statistical index (SI) – logistic regression (LR) provided the best predictive ability of flood zones. Utilizing the area under curve (AUC) metric through plotting flood probability index against the cumulative percentage of flood occurrences, it was found that the SI predictive flood susceptibility model scored the highest prediction and success rate curves (i.e., approximately 94%). However, paying more attention to the hybrid bivariate and multivariate methods in predicting flood-prone areas is required, because these models were trained and tested using random and well-spatially distributed flood and non-flood locations.

4.1. Introduction

Natural disasters are deemed to be the principal cause of irrecoverable damages worldwide [1]. Schick et al. [2] reported that although flash floods have been considered for many decades as an environmental hazard, the exact processes triggering its initiation and controlling its attributes remain uncertain or less than adequately documented. The combination of the flood event itself, its receptors and pathways (i.e., the channel networks that transport the hazard of the flood to the targets), determines the magnitude of the flood risk [3]. Many infrastructures, such as towns and roads, are inadequately located and unprotected from flood hazards to mitigate the potential damage of future flood events [4]. It is mandatory to analyze past flash floods' events thoroughly [5]. Less attention has given to flash floods in arid areas due to the existence of some years with long intervals between flood events. This lack of awareness makes the local population have a false sense of security from catastrophic flash floods.

Furthermore, newcomers to flood-prone areas usually settle and develop the land without consideration of the expected hazards [2]. Accurate prediction of the vulnerable areas to flash floods would help in designing measures to protect such zones from future damage and assist in preparing new developments such as roads and housing [2]. The hydrological response of the flood-prone basin to rainfall is governed intrinsically by its geomorphometric and land cover characteristics. Additionally, the response of the basin is very sensitive to the depth, the size, and the location of the rainstorm [4]. Although flash flood is one of the main hazards in the arid regions, it is considered a vital natural recharge source of groundwater [5].

Systems of field-based monitoring that are required to record detailed rainfall and runoff datasets are limited or absent [6], especially in many countries in the Arabian Peninsula. To date, it is questionable that such field monitoring systems will be installed shortly because of the enormous efforts and resources entailed to create and maintain such systems. This situation makes it difficult to characterize and to monitor the flood extent. Besides, field-based mapping of flooded zones is limited in terms of the spatial and temporal

extent and can be labor-intensive and costly [7]. In natural hazards research, massive databases are often needed [8]. These data are not easy to collect, and in some cases, the lack of appropriate data can impede such research [9]. Most studies related to flash flooding in arid and semi-arid areas were mostly performed in the absence of real- and near-real time rainfall data (e.g., [10]–[14]). The current advances in remote sensing and GIS methods that have introduced valuable contributions in flood modeling and prediction, and have held the promise to address the abovementioned inadequacies.

Many studies have been carried out on flash floods in the arid and semi-arid regions, but rainfall data were usually not considered in the different developed models. Taha et al. [5] evaluated the geoenvironmental hazards, including flash floods in the Nabq Protectorate, Sinai, Egypt. The assessment involved many analyses of geospatial data extracted from Landsat Enhanced Thematic Mapper Plus (ETM+) (30 m), topographical, and other ancillary geological and geomorphological data. The elevation data were obtained from 30 m SRTM DEM as well as from the digitized contour lines from topographic maps (1:50,000 scale). Quantitative drainage morphometry and DEM derivatives were statistically investigated to determine the zones of low, moderate, and high flood probabilities.

Ghoneim and Foody [4] used a modeling approach to locate the vulnerable sites to flood risks at Marsa Alam, Egypt, through deriving the hydrological properties from surface topography of the terrain (e.g., slope, flow path), DEM, and land cover characteristics. The Watershed-oriented Hydrological Modeling System (HMS) has been employed to model the rainfall-runoff process and to predict basin behaviors through the creation of hydrographs. The Soil Conservation Service Curve Number (SCS-CN) method has been employed to determine water loss due to infiltration and to determine soil texture effect (e.g., [15]). The derived information was classified into four different types based on their runoff potentiality. Their results showed that wadi El-Alam required a rainstorm intensity of at least 40 mm to initiate surface runoff with a noticeable flood peak at its main outlet. They also showed that the location of rainstorms had a major effect on the shape of the basin hydrograph. The drawback of this study that it was performed in the absence of rainfall and surface runoff datasets. Additionally, Cools et al. [16] matched the corresponding flash flood and rainfall

(TRMM) events in a wadi Watir basin, Sinai that has similar topographic and climatic conditions to Marsa Alam. They found that were flood events initiated and occurred from rainfall intensity of less than 1 mm to 5 mm. The HMS software highly overestimated the rainfall intensity required to initiate flood peak.

During their attempts to detect the potential sites for managing stormwater in Riyadh, Saudi Arabia, Mahmoud and Alazba [11] developed a GIS-based decision support system to monitor the flash floods. They incorporated spatial data from different sources such as the soil map, and land cover and land use, slope maps, and TRMM to calculate the runoff coefficient. They also estimated the rainfall surplus from the subtraction of annual rainfall data from the evaporation map. With these data, the authors were able to determine the highest potential zones for flood risk. However, the drawbacks of this paper were that the authors used annual (i.e., generalized model) ground and satellite rainfall data, which ignored the rainfall measurements corresponding to the specific flood events and failed to mimic the flood dynamics.

Alhasanat [17] created floodplain zonation maps in wadi Mousa, northeastern Jordan. Despite the lack of in-situ runoff flow for wadi Mousa, all the required data (e.g., rainfall, topographical maps, and other remote sensing data) were prepared and processed in ArcGIS environment to estimate the surface runoff. A hydrological model was developed to detect the flood risk according to the runoff in the main channels of wadi Mousa. Alhasanat (2014) recognized four levels of the floodplain at 25, 50, 75 and 100 return periods, where the highest probability of flooding associated with the 25-year floodplain zone. Still, the author depended on yearly climatic data, which could not capture the dynamicity of the flash floods.

In 2016, Yousef et al. [12] studied the two 2009 and 2011 Jaddeh flood events employing the bivariate probability (i.e., frequency ratio) and logistic regression models over an area covering 219 km². Seven independent variables (i.e., slope, elevation, curvature, geology, land use, soil drain, and distance from streams) were used to generate two flood susceptibility maps. These variables were reclassified and weighted based on the bivariate

statistics. The normalized variables were involved in multivariate logistic analyses. The flood inventory map generated from IKONOS imagery of 1 m resolution to represent 127 flooded locations in 2009 and 2011. Finally, flood susceptibility maps were developed by classifying the probability flood index into five classes: very low, low, medium, high, and very high susceptibility. This model did not involve rainfall data, and the flood point was collected only along the main valleys.

Preparing flood inundation maps is a mandatory step to outline the hazardous areas and to control the potential flooding risks. In wadi Hali and wadi Yibah, southwestern Saudi Arabia, Sen et al. [18] utilized topographic maps and field measurements to create inundation maps. A number of cross-sections along the possible flood plain were measured, and the average flow velocity in each channel was determined based on the geometric, hydraulic, and material characteristics of each area. The obtained information was employed to assemble synthetic rating curves in control sections by generating an empirical formula to determine both flood depth and width. The authors identified flood levels at various cross-sections. They found that the middle and downstream parts were more dangerous than the upstream portions of the wadis. They reported that empirical field measurements should be employed to develop inundation maps. Also, they concluded that flood assessment in arid areas should not be performed with the same methods applied to humid areas since further modifications are required [18]. This study did not include rainfall and surface runoff measurements.

In the watershed area of Jabal Al-Hajar Mountains (3000 m), northern Oman, Al-Rawas and Valeo [19] attempted to predict flash flood by investigating the relationship between wadi flood peaks discharge and the watershed characteristics. Parameters of 14 sub-watersheds were extracted from a 40 m DEM. The correlation and multiple regression analyses were conducted on the extracted parameters to examine the effect of these physical characteristics including land use on wadis' mean peak flow (QMPF) for various periods of recurrence flood peaks at 5, 10, 20, 50, and 100 years. The main network attributes that affected flood flows were drainage area, wadi slope, and mean elevation. The developed model underestimated the average peak flow in some sub-watersheds. Lack of the required

rainfall data indeed affected the results [19]. Also, the derived relationship was not applicable to apply in other locations in Oman itself even under a slight difference in the climatic conditions as the authors tested their model in Salalah (humid climate) in southern Oman.

Predictive global climate change models indicate that changing precipitation patterns and the increasing number of extreme rainfall events will raise the magnitude and frequency of future flooding events [20]. Real-time flood extent mapping allows the emergency responders to handle extreme flood events, and to direct their limited resources to the highest priority areas [21]. Flash floods are very challenging to be predicted as they characterized by rapid and intense run-off generation leading to a rapid rise in water levels and high peak discharge over a short duration after the onset of the generating storm [22]. Flood management can be achieved through four significant steps: prediction, preparation, prevention, and damage assessment [23].

Earth observation satellites datasets and GIS techniques introduce valuable methods to study flash floods (e.g. [10], [22], [24]–[27]) since they (1) provide essential tools for observing and investigating the spatial dynamics of floods, (2) have relatively low or no acquisition and mapping costs, (3) allow mapping over large, and sometimes, over inaccessible regions, in a time repetitive manner, (4) grant a compelling set of tools for analyzing and extracting spatial information to support decision making reliably and consistently, and (5) present tools to process big digital data volumes since the repeated acquisitions offer a wealth of archive data required to detect flash floods changes over time.

Field-based monitoring of flooded areas requires much time and effort, as well as it requires high degrees of safety and multiple precautions [5]. Currently, different satellite sensors (i.e., microwave and optical) provide a real contribution to monitoring flash floods at real-time and near real-time scales. On the one side, the microwave sensors such as the synthetic aperture Radar (SAR) instruments provide their illumination source, record data at both day and night, and penetrate cloud cover ([28]–[30]). However, SAR data are mostly of high cost and usually have speckled noise [31]. They have coarse spatial and temporal

resolutions that affect their applicability in monitoring flooding [32]. Vegetation covers increase the roughness of SAR imagery [7]. Moreover, the complex procedures that are required to process SAR imagery add more difficulties in mapping flooded areas [7], [33]. The recently launched Sentinel-1 mission can help in solving most of the previously-mentioned issues related to the role of SAR data in monitoring a flood inundation.

On the other side, though multispectral optical sensors mounted on board of both near-polar or geostationary satellites are capable of offering medium to high spatial and spectral details, they often restricted by the presence of clouds and long revisit times [34]. For example, Enhanced Landsat Thematic Mapper (ETM+) and Moderate Resolution Imaging Spectroradiometer (MODIS) have (16 days, 12 bands, 30 m) and (1 day, 36 bands, 1 km) spatial, spectral, and temporal resolutions, respectively. Therefore, the optical sensors are not a practical solution to detect a flood extent.

In the case of determining future flash flood extent based on conditioning factors (flood susceptibility assessment), the central concept used in most of the research is to develop a model to detect flash flood extent and relating it to a set of input factors. Such models were developed using either statistical or machine learning or integration between both techniques [35]. It is imperative to have a spatial association in all input factors to gain accurate results [36].

Flood susceptibility (i.e., potential) map can be defined as the likelihood of future flash floods' extent depending on the intrinsic properties of a given area such as rainfall, slope angle, geologic units, soil type, and more [37]. It can assess the historical and future spatial extent of flood events [38] and classified the hazard degree in the prone areas [39]. It can help the policymakers and authorities concerned to prepare the emergency plans and extract mitigation measures to reduce life and property losses. Over past years, various methods for flood susceptibility mapping such as probabilistic and statistical models [40], multi-criteria evaluation [41], fuzzy logic [42], weights-of-evidence (WoE) [43], artificial neural network (ANN) [44], and decision tree (DT) [45] have been introduced. Dixon [46] and Kia et al. [47] outlined the advantages of applying the ANN in the flash flooding research

since it can deal with uncertainties in the input dataset, and can extract information from the incomplete or contradictory dataset. It can determine linear as well as non-linear functional relationships based on pattern recognition [48]. However, the ANN has some drawbacks [46], [47] such as: (i) it represents a black box, (ii) it needs a high computer capacity (i.e., time-consuming, especially for the training part), and (iii) it requires extensive data as weak predictions can occur when the validation data contain values that are not included in training range. The fuzzy logic model has a more transparent structure than the ANN and has employed in a variety of hydrological applications [49]. Additionally, the adaptive network-based fuzzy inference system (ANFIS) represents a combination of ANN and FIS models. It was found to be optimal in monitoring and forecasting flash floods, where it needs minimum input from experts, and performs fast [50]. However, it entails a large number of parameters, which limits its use due to the difficulty of data collection [51]. The decision tree (DT)-based models have been proved to applicable for flash flooding susceptibility modeling [45], [52]–[55] since they (i) have no statistical assumptions, (ii) can handle data from various measurement scales, and (iii) facilitate the construction of the rules to build predictions about individual cases and for complex relationships. However, they are susceptible to noisy data, and multiple output attributes are not allowed. Support vector machines (SVMs) techniques are efficient and reliable tools in flood susceptibility assessment and can be beneficial in flood mitigation strategies [56]. However, SVM parameterization can be time-consuming and requires many trails for selecting the appropriate kernel type [56]. The analytic hierarchy process (AHP) mostly applied to regional flood susceptibility studies [57]–[59], but it requires expert knowledge and contains many biases due to subjective rules. It is unable to determine the uncertainty that may occur during selection, comparison, and ranking of multiple criteria.

Statistical approaches adopted to generate flood susceptibility maps provide reliable, rapid, and understandable tools to facilitate flood extent mapping. In general, they require the testing of a set of assumptions before initiating the study, which considered as drawbacks of such approaches [60]. The statistical-based logistic regression (LR) model can overcome some of the disadvantages of the abovementioned machine learning approaches and can be combined with other bivariate methods such as frequency ratios (FR) and evidential belief

functions approaches to develop efficient flood susceptibility maps [39], [61]. In contrast, the LR model itself has some disadvantages to analyze the classes of each flood-influencing parameter. Some studies used LR as bivariate to solve this problem, but LR has some limitations to perform bivariate statistical analysis as it manipulated the classes as indicators and does not consider them in the study [45]. The bivariate statistical methods (e.g., FR) analyze the impact of each input factor on flooding [45], but the mutual relationship between the variables cannot be determined. Therefore, a combination of bivariate and multivariate statistical methods can produce a comprehensive and efficient approach to generate flood susceptibility model, which can analyze the influence of each class of every triggering factor on flooding.

The concept of inventory mapping was originally developed for landslide susceptibility studies [62]–[64]. The geomorphic inventory map can be defined as a spatial distribution of landslides at a predefined cartographic scale and prepared by gathering historical information on landslide events [65]. An inventory map shows the locations, the date of occurrence, and landslide events that have left discernible traces in an area [65], [66]. Development of an inventory map depends on the following principal hypotheses [63]: (1) landslide events leave noticeable marks on the land, so visual interpretation of aerial photographs, satellite images, or digital elevation data may support the identification process, (2) changes in image intensity, texture, and shape, in addition to structural lineaments, should be related to the landforms linked with potential slope instability processes [67], and (3) “the past and present are keys to the future” [68] (i.e., landslide inventory maps are applied to study landslide hazard zonation being probable to happen under the same conditions recognized in the past).

Traditional methods for generating an inventory map were field investigation and aerial photographs. The limitations of these conventional methods were described in Malamud et al. [65] and Guzzetti et al. [66]. Nowadays, remote sensing techniques constitute the primary source of information for the creation of an inventory map, in addition to the small contribution from field surveys [62]. Landslides are commonly associated with rainstorm-induced flash floods [69]–[71] and the conditioning factors of landslides such as

altitude, slope, morphology, and geology of the study area, drainage basin parameters, and land use classes are similar to those that control the flash floods. Therefore, in recent years, some authors attempted to create flash flood inventory maps to contribute as a reference standard to validate their developed flash flood susceptibility maps [12], [72].

In the current research, a flash flood inventory map (i.e., information about the locations and characteristics of flash floods events) extracted mainly using Sentinel-1A images. The generated flood map was verified using Google Earth Pro, volunteered geographic data provided by the rainfall hunters in the Sultanate of Oman, and the available historical flood information from previous literature in arid areas of similar topography.

Volunteered geographic information (VGI) is a quickly growing data source for natural hazards research [73]. A vast amount of real-time ground data has become available as a result of internet spreading. Some authors used volunteered data in their studies about such hazardous events, particularly to estimate flood inundation extent [74]–[80]. Notwithstanding the non-scientific nature of volunteered datasets, they can provide critical and vital information. The integration of these data with conventional ones introduces valuable information for mapping the flash flood extent. The proposed inventory map is expected to improve the detection of flash flood extent due to the integration of various sources of information, especially from remote sensing techniques.

Additionally, most of the previous authors used different sources to map the flood inventory such as in-situ mapping through field investigation, literature review, historical multiple flood records, and remote sensing imagery. Due to the complex topography usually covers the upstream watershed and required extensive field survey, most of these authors collected only a few points to represent flood locations such as 211 points [39], 112 points [81], and 137 points [61]. For the non-flood points, these authors used Google Earth to determine non-flood points equal to the pre-collected flood points. However, these non-flood points were restricted only to the upstream (i.e., elevated hills and mountains that are not affected by the flood). Although this assumption could be valid, the non-flood points can be existing everywhere in the mid and low-lying downstream areas.

Therefore, the overall goal of the current study is to introduce improved and integrated statistical based-susceptibility models to differentiate and refine the flood zones susceptible with the highest potential hazards over an arid watershed in the Sultanate of Oman. The main objectives consisted of: (i) including a detailed a spatio-temporal flood information to the models through using the Radar-based inventory flood map, for a certain flood event, to select well-spatially stratified flood and non-flood points among the whole area of study, (ii) introducing a new combination of the flood triggering factors such as near-real-time rainfall data, DEM derivatives (e.g., altitude, aspect, and convergence spatial data), lithologic units, soil type, and topographic wetness index, (iii) applying integrated statistical bivariate (i.e., FR and SI) and multivariate (LR) approaches to generate the flood susceptibility maps, and (iv) comparing the findings of the different flood susceptibility models to depict the model with the top performance.

4.2. Materials

4.2.1. Study Area

The current study was carried out at the foothill of the Al-Jabal Al-Akhdar chain at Ad Dakhiliyah Governate, north of the Sultanate of Oman (Figure 4.1). It includes the wilayats (i.e., cities) of El Hamra, Bahla, and Nizwa and located between $57^{\circ} 0' 0''$ to $57^{\circ} 54' 0''$ Latitude and $22^{\circ} 23' 0''$ to $23^{\circ} 15' 0''$ Longitude (WGS 1984/UTM Zone 40N) (Figure 4.1). The area of study is approximately 4812 km^2 extent and is characterized by sparse rainfed and small dense irrigated vegetation zones [82]. Topography varies across the area (slope = $0-84^{\circ}$; altitude = $783-4178 \text{ m}$) and significantly affects the local climate conditions. Topography varies widely across the study area (altitude = $249-2955 \text{ m}$), which can substantially affect the local climate conditions. The arid climate is associated with hot summer and warm winter. It is highly variable and fluctuated yearly with an average annual rainfall of more than 300 mm in the northern Oman mountains. The convective liquid precipitation storms accompanied by the localized cells of deep atmospheric convection are the main responsible mechanism of rainfall over Al-Jabal Al Akhdar [83]. Notwithstanding the frequency of flash floods in this part of the Sultanate of Oman, no previous research has studied the flood probability in this area. Figure 4.1 demonstrates the study watershed covers an area among wilayats of El Hamra, Bahla, and Nizwa at the Dakhiliyah Governate, the Sultanate of Oman, and the source of the satellite imagery is ESRI, 2018 [84]. According to the Oman Meteorology, the north of Oman received torrential rainfall from December 16-19, 2017, in many parts [85]. Oman's Civil Defense department stated that three people have died, and many homes have been severely damaged with at least 120 people left homeless [85]. Although many people have been rescued from flooded homes and vehicles, dozens of people were injured in road accidents, particularly across to cross wadis (i.e., valleys) and low areas.

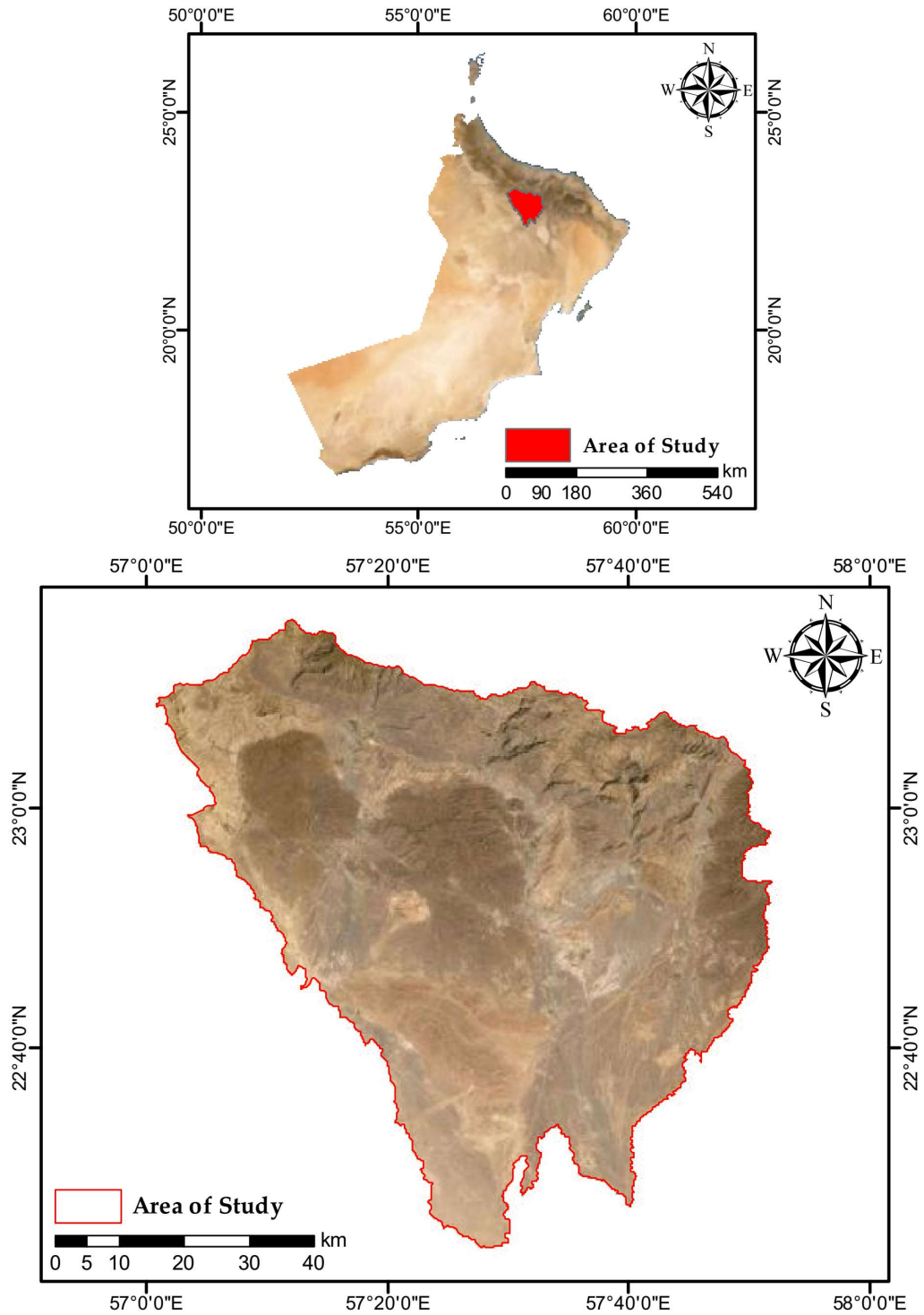


Figure 4.1. The area of the study shows the selected watershed extends among the wilayats of El Hamra, Bahla, and Nizwa at the Dakhiliyah Governate, the Sultanate of Oman. The source of the satellite imagery is ESRI, 2018 [84]. The upper map of the Sultanate of Oman is not an authority on international borders.

4.2.2. Data Requirements

4.2.2.1. *Sentinel-1A*

The ESA-Copernicus (European Space Agency-Commission's Earth Observation Programme) designed the Sentinel-1 Radar observatory mission to provide a continuous mapping of the Earth's surface. The Sentinel-1 mission is a two-satellite constellation (i.e., A and B), of sun-synchronous near-polar orbit, that use an active C-SAR sensor for introducing medium to high-resolution images in all-weather conditions and time (i.e., day and night). Both Sentinel-1A and Sentinel-1B sensors were launched in April 2014 and 2016, respectively, at a 693 km altitude and share the same orbit plane with a phase difference 180°. Therefore, both SAR satellites can image the entire Earth's surface every six days. The key parameters of the mission are to provide improved short revisit time, coverage, frequency bands, polarization, and resolution. For more details, see Torres et al. [86].

Six Sentinel-1A scenes, of a C band frequency (5.405 GHz) and a repeat cycle of 12 days, were downloaded from the Alaska Satellite Facility hub website [87]. The area of study covered mostly by one scene, and about 5% of the area covered by another image. These SAR scenes covered the area of study during the flood event of December 16, 2017, and two pre-flood days on November 10, 2017, and October 17, 2017. The datasets acquired during the same ascending orbits (track-path 30) were selected to have uniform configurations [88]. The incidence angle over the area of study ranged from 36° to 42°. The scenes were acquired in interferometric wide swath (IW) mode of operation that has a wide swath (250 km) and a high spatial resolution (5 m × 20 m) [89]. They delivered as GRDH (Ground Range Detected High Resolution) scenes with dual polarizations (i.e., SAR sensor can transmit and receive signals in both a horizontal and vertical orientation (VV/HV)). High-spatial resolution Sentinel-1 GRD scenes include SAR datasets that have been detected, multi-looked, and projected to ground range using an ellipsoid model of the Earth. The terrain height, of a varied azimuth and constant range, is used to correct the ellipsoid projection of the level-1 GRD products. Because of the multi-look processing, the resulting scene had square pixel spacing with reduced speckle noise at the cost of reduced geometric resolution [90]. They

have spatial details and pixel spacing of about (20×22 m) and (10×10 m), respectively, in the ground range (i.e., range resolution) and azimuth direction [91]. Sentinel-1A SAR images used effectively with a spatial resolution of 10 m in different environmental applications such as extracting surface water map extents, wetlands, and ecosystem units (e.g., [92]–[94]).

4.2.2.2. DEM Dataset

DEM is originally a term reserved for elevation data provided by the United States Geological Survey (USGS). Currently, DEM is used to describe any digital elevation data and to represent the terrain relief where the elevation values over a topographic surface are a regular array of Z-values and referenced to a common world datum [95]. DEM is the leading source to derive various geospatial datasets such as slope, aspect, and curvature.

The ALOS Phased Array type L-band Synthetic Aperture Radar (PALSAR) DEM with a spatial resolution of 12.5 m was adopted in the current study to derive the geospatial layers. It has higher horizontal and vertical accuracies than other freely available global DEMs [96]. It is developed by the Alaska Satellite Facility Distributed Active Archive Data Center (ASF DAAC). The ASF processed ALOS PALSAR scenes using the Gamma remote sensing software package to produce geometrically and radiometrically terrain corrected products. Radiometric Terrain Correction (RTC) overcomes the geometric distortion (e.g., foreshortening, and layover) due to the internal side-looking nature of SAR imagery. The generated products cover landmasses from 60° northern Lat. to 59° southern Lat. The RTC process provides an improved estimation of signal backscattering, which is affected by dielectric constant, surface roughness, scattering mechanism, polarization mode, terrain slope, Radar look angle, and wavelength. Therefore, the enhanced RTC outputs can be utilized for such applications (e.g., flash flood detection, land-cover classification, and monitoring of deforestation). RTC products are distributed at two resolutions. High-resolution RT1 DEM products that are generated with a pixel size of 12.5 m. Layover and shadow masks, and incidence angle maps are available for the same product resolution. More details about PALSAR DEM are available from Laurencelle et al. [97].

4.2.2.3. GSMaP-G

The Global Satellite Mapping of Precipitation (GSMaP) is a global rainfall data derived from blending different space-borne passive microwave (PMW) and infrared (IR) data collected by various satellite platforms such as Global Precipitation Measurement (GPM) Microwave Imager (GMI), Tropical Rainfall Measuring Mission (TRMM) Microwave Imager (TMI), TRMM Precipitation Radar (PR), Geostationary Infrared instruments among others. The GSMaP product is developed and disseminated by the Japan Aerospace Exploration Agency (JAXA) through the Earth Observation Research Center (EORC). It is an hourly product with a spatial resolution of 10 km and time latency of fewer than three days that covers from 60°N–60°S. The GSMaP-Gauge (GSMaP-G) is adjusted GSMaP using the Climate Prediction Center (CPC) unified gauge-based analysis of global daily precipitation data analysis with a 50 km spatial coverage. Additional details about GSMaP V06 algorithms and validation can be obtained from [98]–[100].

4.3. Methods

The workflow of the adopted methodology in the current study is illustrated in Figure 4.2 as follows: (i) producing the flood inventory (i.e., inundation) map by the use of Sentinel-1A Radar images, (ii) deriving a set of flood conditioning explanatory factors from ALOS PALSAR (12.5 m), (iii) extracting drainage network from ALOS PALSAR (12.5 m) to extract the other set of the independent variables, (iv) generating the geologic map utilizing Landsat-8 image (30 m) and geologic maps of scales 1:250.000 [101] and 1:1000.000 [102], (v) digitizing and georeferencing the soil map, (vi) performing multicollinearity quantification, (vii) using the bivariate and multivariate statistical methods to develop predictive modeling of flash flood occurrences; (viii) validating the models, (ix) comparing flood susceptibility classes, and (x) compiling flash flood probability maps.

4.3.1. Flash Flood Inventory Map

The SNAP (Sentinel Application Platform) software [103] was used in most of the major steps to process Sentinel-1A SAR scenes [104] for extracting a flood inundation map. The workflow designed to reduce error propagation associated with the following subsequent processing steps (for more details, see [90]). In the case of utilizing the Sentinel-1A to detect the flood inundation map, the polarized wavelength VV showed improved results over other polarization [105], [106]. The processing steps started by masking the mosaic SAR VV (i.e., single co-polarization types, vertical transmit/vertical receive) scenes to the exact extent of the study area.

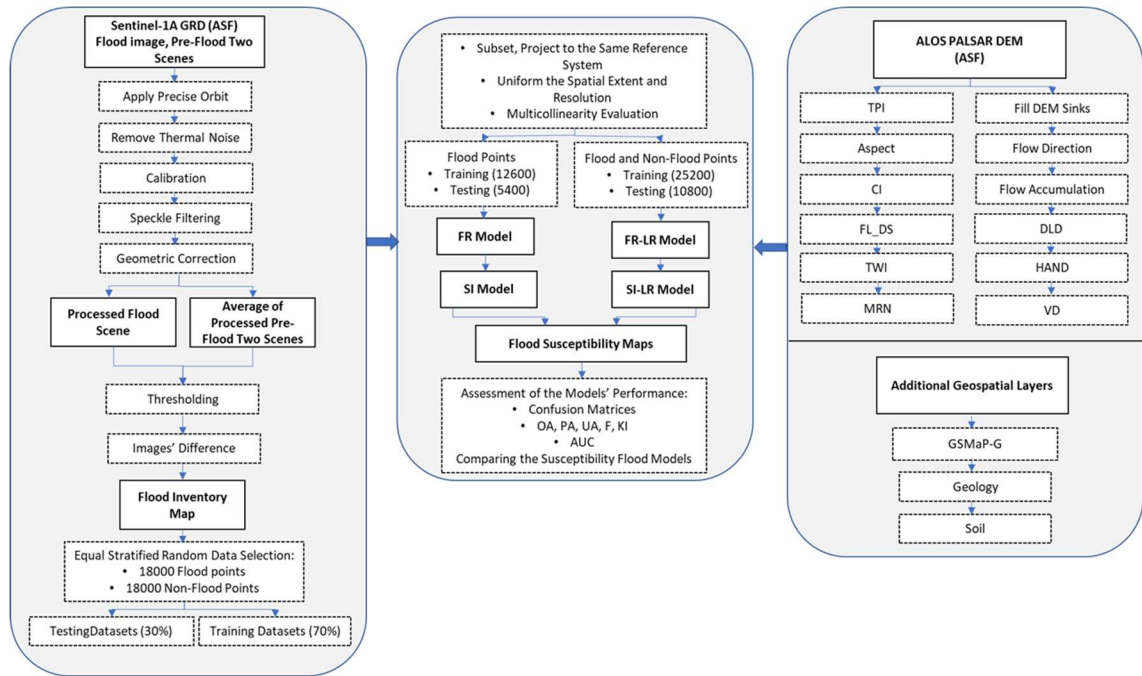


Figure 4.2. Methodology flow chart for the improved flood susceptibility models.

The abstract metadata of Sentinel-1A scenes generally have inaccurate information about the orbit state vectors. The precise orbits available in SNAP allowed automatic download of updated and accurate orbit vectors that are usually available several days after generating the original SAR images. These updated orbits provide precise information about the satellite velocity and position.

The additive thermal noise associated with Sentinel-1A images prevents the precision of SAR reflectivity estimates. It is the receiver’s background energy that shifts SAR reflectivity towards higher values. The thermal noise removal operator available in the SNAP toolkit was used to reduce noise through normalizing the backscatter signals within the entire Sentinel-1A scene.

Level-1 SAR images can have a significant bias because they are not radiometrically-calibrated. The process of relating the digital pixel values of the SAR scenes directly to the true radar backscatter from the reflecting surfaces is called radiometric calibration. It is a mandatory process to compare scenes captured by different SAR sensors, or the same sensor but at different times and/or beam modes. The Sentinel-1A GRD products contain the

required calibration vector, as an annotation, to convert images' intensity values into sigma nought values.

SAR scenes mostly have granular noise or speckles (i.e., inherent salt and pepper texture) that reduce the image quality and cause the features' interpretation to be more difficult. These speckles are due to the random interference (i.e., constructive and destructive) of waves caused by multiple scattering sources within each resolution cell [107]–[109]. The refined Lee 5×5 pixel filter has been applied on during and pre-flood images, after some initial trail on the window size [110], to have smooth scenes of high quality and free of speckles. The refined Lee filter was found to be superior to other speckle filters, for visual interpretation, due to its capability to preserve linear features, point target, and texture information [107].

SAR images are acquired with a varying viewing angle (i.e., side-looking geometry) greater than 0° , resulting in distorted scenes. As a result of topographical variations in the SAR imagery and tilting of the spaceborne sensors, the distances can be distorted within the scenes. Therefore, the range of doppler terrain correction was applied to compensate for the distortions (i.e., to be close to the real world). The SAR scenes then re-projected to the UTM projection Zone 40 N of the Sultanate of Oman. Range Doppler geometric terrain correction is a correction method of geometric SAR distortions as a result of topography (i.e., foreshortening and shadows), utilizing a DEM to derive the precise geolocation information of each pixel [111]. The range Doppler operator allows selecting the image resampling method and the target pixel spacing.

Flood inundation mapping can be defined as how to identify a highly precise binary mask of flood and non-flood water. Multiple SAR-based flood water detection approaches have been proposed in the literature such as unsupervised and supervised methods (e.g. [112]–[114]), threshold determination (e.g. [110], [115], [116]), and change detection (e.g. [117], [118]). The accuracy of different flood inundation algorithms considerably differs based on the dominant land cover. For example, detecting Flood in urban areas is challenging because of the shadow effect of building due to the side-looking viewing geometry of SAR

sensors [119]. Additionally, it is strenuous to sense the water below vegetation cover as a result of double bounce signal scattering in such areas [120]. Furthermore, the strong wind can roughen water surfaces that can cause misclassification errors.

The thresholding method is the most commonly used method for SAR images to differentiate between flood and non-flood water areas [110]. The thresholding method depends mainly on the contrast between low and high Radar returns from water bodies and the surrounding terrain [110]. The steep slope filtering (i.e., slope less than or equal to 3°) [105], [121] step was implemented to mask any Sentinel-1A's pixels that might display a brightness change due to the angle of the SAR signals' return from the steep, rugged hills and slopes [121]–[123]. Additionally, this filter could help in reducing the areas with Radar shadow [105], particularly in the upstream area dominated by rugged and complex mountain structures. The chosen slope threshold is considered as a standard conservative slope that can include rough and steep hill slopes [121], and the sloped pixels were assigned to class 0. For the current area of study, a slope mask of less than or equal to 3° includes mostly the upstream mountainous non-flood area; therefore, it was a convenient and reliable threshold.

In the current study, the backscattering of collocated SAR pixels in and before the flood events were compared and generate a single mask object (flood water or non-flood water). The Otsu method [124] is utilized to reduce a grayscale image to a binary image. This binarization algorithm assumes that the monochrome includes two classes of pixels following a bi-modal histogram (i.e., foreground and background pixels). To separate the two categories, an optimum threshold is estimated by iterating through all possible threshold values to detect the minimum intra-class variance for the pixels that either follow the foreground or background class.

The drawback of the Otsu method that it can be applied only on images that have bimodal grey-level histograms [125], which was not available in the current study. Therefore, a segmentation algorithm that can threshold the Sentinel-1A images with close to unimodal or unimodal grey-level histograms was required to extract flood areas in the current study. The neighborhood valley-emphasis (NVE) [125] method (i.e., a technique that

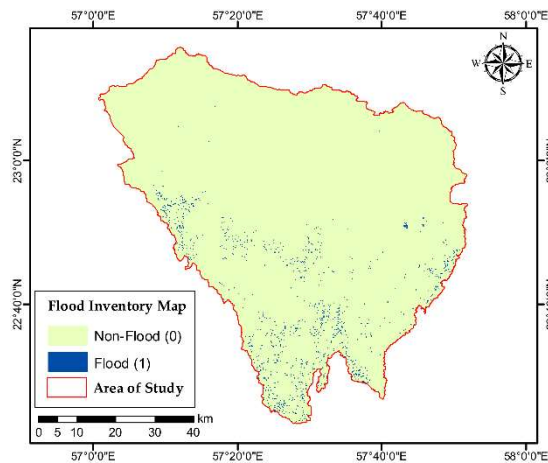
uses the neighborhood information of the actual valley point within an unimodal histogram) has been applied successfully by Nakmuenwai et al. 2017 [126] to auto-extract the inundated areas from RADARSAT-2 images. In the current study, the NVE developed by [125] and implemented by [127], [128] was utilized to auto-select the optimal thresholds to differentiate between flood and non-flood classes.

Change detection technique used to compare backscattering signal intensities of pre- and during-flood images to detect only significantly changed pixels as inundation candidates to reduce false classified flood pixels [129]. It can overcome the over-detection error of water-like surfaces (e.g., Giustarini et al. [117]). However, it is sensitive to speckle-related noise [130] that can be diminished using an appropriate speckle filter [110], and geometric dislocation error that can be reduced through assessing the change from the binary water masks [129]. The image difference was carried out through subtracting binary reference flood image from the binary pre-flood average image. The final flood inventory map (Figure 4.3a) had 357971 pixels within the flood class (i.e., assigned the value of 1), and 30413754 pixels in the non-flood zone (i.e., allocated the value of 0). Additionally, it had 36125 pixels with the value of -1, which might be related to the human activities and using of Aflaj irrigation system for agricultural purposes, during this time of the season, and seeping of the water to the terrain surface in limited locations. These pixels with negative values were assigned the value of 0 (i.e., non-flood class). A sample equal to 10% of the number of flood pixels was acquired using the equal stratified random sampling technique from flood and non-flood classes to ensure the coverage of most classes of the flood causative factors in the study area. The selected sample was divided into training (Figure 4.3b) and testing (Figure 4.3c) datasets with percentages of 70% and 30% to be used in the hybrid flood susceptibility modeling, respectively.

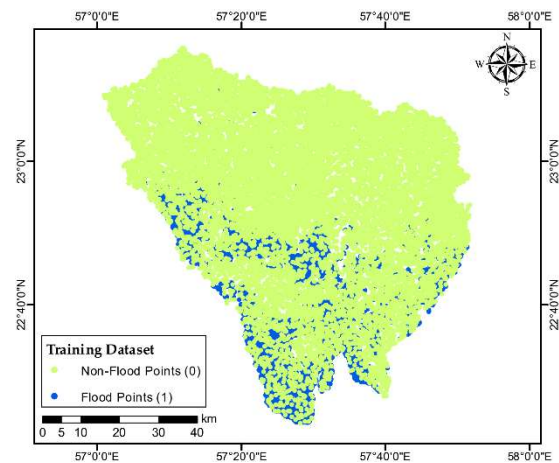
The volunteered geographic information (VGI) was used for the validation purpose of the flood generated flood inventory map. Some of the Omani people have the enthusiasm for regularly following and tracking the rainfall events, and they published their video, images, and description of rainfall and flood events on the online forums and websites. One of the major Omani forums called “Sabalet Oman” has a complete division for the weather

and climatic events over the Sultanate of Oman. By keep following the different reported flood events over the wilayats of El Hamra, Bahla, and Nizwa at the Dakhiliyah Governate [131], a complete picture of the flood frequent spatial distribution had gained. Through using the acquired information, it was possible to visually validate the developed flood inventory map (Figure 4.3a). It is worth mentioning that Martinis et al. 2018 [116] used Sentinel-1A images to extract near real-time flood inundated areas over Somalia, Ethiopia, and Iraq [116], [132]. They used different frequency classes with thresholds of -10, -15, and -20 db to reduce sand interference. Their applied method successfully reduced overestimated flood extents.

(a) Flood inventory map



(b) Training dataset



(c) Testing dataset

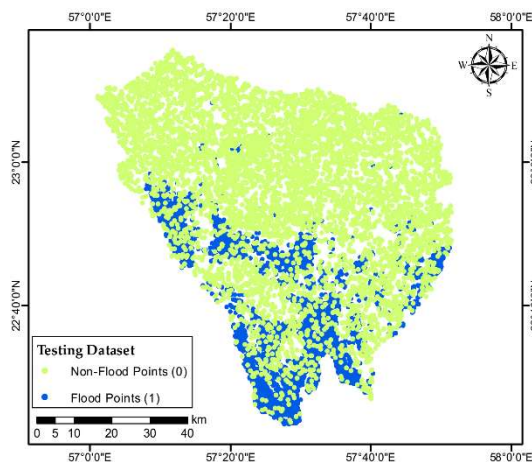


Figure 4.3. (a) the flood inventory map, (b) and (c) training and testing datasets, respectively.

4.3.2. Flood-Affecting Independent Factors

Identifying a set of factors that are in control (i.e., can significantly contribute to the occurrence) of a flash flood is the main task in the flooding predictive modeling. Despite there is no complete agreement on selecting the optimum set of flood-controlling factors [72], there were some independent variables frequently used by other researchers (e.g. [72], [133], [134]). Most of the latest studies aimed to develop precise susceptibility models with the use of the least number of independent parameters [44]. The explanatory factors should be measurable and have spatial relations with the dependent reference variable (i.e., flood inundation map). The numerical morphometric parameters-derived DEM can provide beneficial information about missed observed hydrologic data (e.g., runoff) in the case of the ungauged basin, as well as geologic and physiographic information of watersheds [135]–[137].

Thirteen explanatory variables that represent the local physical and climatic characteristics of the study area were proposed through the knowledge attained from the previous literature (e.g., [5], [12], [39], [133], [138]) and the previous fieldwork experience in similar areas. They included geology, soil, altitude (m), height above nearest drainage network (HAND) (m), Melton ruggedness number (MRN), drainage line density (DLD) km/km², topographic position index (TPI), aspect (°), valley depth (VD), topographic wetness index (TWI), convergence index (CI), flow length in the downstream direction (FL_DS), and Global Satellite Mapping of Precipitation-Gauge calibrated (GSMaP-G). The flood influencing factors were processed and compiled into a geospatial database utilizing ArcGIS and SAGA GIS software. Additionally, SPSS software was used in some analysis steps.

Each parameter was resampled to the spatial resolution of the ALOS PALSAR DEM (i.e., 12.5 m), where the study area grid was bounded by 7013 and 7710 columns and rows, respectively. Each independent variable was classified using the natural break classification method within the ArcGIS environment [139]. This approach automatically determines the class breaks and maintains similar values together (i.e., minimizing the variance within

classes), while maximizing the differences between different classes. It was used in various previous flood susceptibility studies (e.g., [140]) due to its efficiency.

To extract the lithologic units (i.e., geology) (Figure 4.4a), the Landsat 8 surface reflectance scene of zero-cloud, acquired on April 10, 2017, for path 158 and row 44, was downloaded from the United States Geological Survey (USGS) Earth Explorer data portal. The maximum likelihood classification (MLC) algorithm was used to perform supervised classification of the multiband Landsat 8 image to generate the geologic map for the study area with a spatial resolution of 30 m. The signatures of the geologic units were captured by overlying the georeferenced resampled geologic maps with scales of 1:250.000 [101] and 1:1000.000 [102] above the Landsat 8 scene (RGB = 742 [141]) and Google Earth Pro imagery. MLC is one of the most frequent and accurate supervised classifiers in remote sensing studies [142], [143]. It depends on the hypothesis that the probability density function for each class is a multivariate, and the unidentified pixel is assigned to the lithologic class with the highest probability of being a member [142], [144].

The hard copy of the soil map for the under study was georeferenced to Oman local reference system and vectorized in the ArcGIS environment to demonstrate the spatial distribution of soil units in the study area (Figure 4.4b). The source of the soil map was the “Oman Soil Atlas” with a scale of 1:250.000 developed by the Ministry of Agriculture and Fisheries (MAF), Oman, in 1992 [145]. The United Nations Food and Agriculture Organization (FAO), in partnership with the UN Development Programme (UNDP), collaborated with MAF in the project “OMA/87/011-Soil Survey and Land Classification” to generate the Oman Soil Atlas.

The ALOS PALSAR DEM with a spatial resolution of 12.5 m was used to directly express the altitude (i.e., digital elevation) (Figure 4.4c). Additionally, it contributed significantly in direct and indirect ways to extract most of the following derivatives (i.e., flood causative factors).

Height above nearest drainage (HAND) (Figure 4.4d) normalizes the elevation of a drainage basin with respect to the relative height along with its channel network [146], [147]. It is the relative altitude difference between a specific cell on the original DEM and its corresponding hydrologically linked cell in the channel network. The outcome is a normalized local altitude map in a meter. In other words, HAND is a normalized DEM that can provide valuable information about the relative drainage potential, runoff generation mechanisms, soil properties of a given area. The high HAND values prevail in regions with large draining potential such as a subsurface rapid (i.e., slope zone) and deep percolation (i.e., plateau zone) flow. Additionally, low HAND values prevail in the zone with a saturated response (i.e., area with saturation excess overland flow), where draining water generates a pool and causes waterlogging due to low draining potential and proximity to the groundwater table. HAND has been applied in different applications such as hydrological modeling [147], [148], spatial distribution of the stationary soil moisture [148], [149], geomorphological landscape studies [150], groundwater potential zones [151]–[153], filtration, verification, and change detection of flood inundation flood-based SAR images [105], [154], flood mapping and monitoring [155], [156], and surface water mapping [157]. Though the successful applications of HAND in different environmental models, only one study (i.e., Rosim et al. [158]), based on my best knowledge, have adopted the HAND in flood susceptibility modeling. More details about the HAND concept, algorithm, implementation steps are available in Rennó et al. [146], Nobre et al. [147], and Rahmati et al. [152].

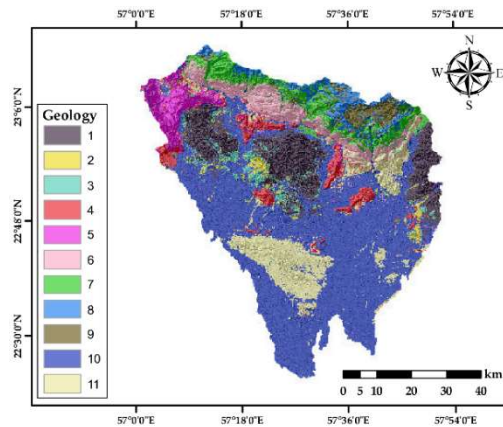
Melton ruggedness number (MNR) (Figure 4.4f) is a morphometric index related to the flow accumulation. It computed per each grid cell as the difference between the minimum and maximum elevation divided by the square root of the watershed area size [159]–[161].

Drainage line density (DLD) was derived using the line density toolbox within the ArcGIS environment. The drainage network was extracted from PALSAR DEM 12.5 following the steps illustrated briefly in Figure 4.2. Then, the tool computed the density of the linear channel features within the neighborhood of every raster cell in units of length per unit of area (i.e., km/km²) [162].

The topographic position index (TPI) (Figure 4.4g) measure the difference between the altitude of the focused (i.e., central) pixel and the average elevation of the surrounding cells, within the range of predetermined radius (i.e., 100 m in the current study) in a DEM [163], [164]. If that central cell is located higher than its average neighboring pixels, the TPI yielded positive values. Additionally, negative TPI values reveal that the focused pixel has a lower elevation than the surroundings and represented by valleys [165]. Large radius values identify the major landscape features, while small values reveal the smaller geomorphic features (i.e., minor valleys and ridges) [165].

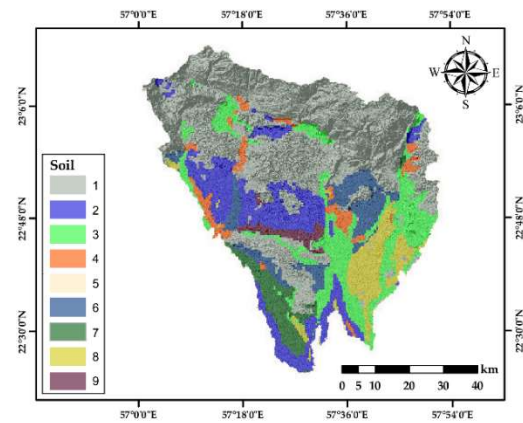
The aspect (Figure 4.3h) represents the slope direction of the maximum magnitude value [95]. It estimates the steepest downslope direction between each cell and its neighbors. It is the direction that is perpendicular to the contour lines on the surface [166]. Terrain aspect values are calculated clockwise in degrees from 0° (north) to 360°. It can be derived directly from a DEM. Areas with no downslope direction assigned an aspect value of -1.

(a) Geology



- (1) Rock Outcrop Torriorthents: strongly dissected rocky plateaus and mountains
- (2) Calciorthids–Torriorthents: loamy and sandy-skeletal, deep soils
- (3) Torriorthents: extremely gravelly sandy, deep soils
- (4) Torriorthents–Torrifluvents: sandy and loamy deep soils
- (5) Gypsiorthids: loamy-skeletal and sandy-skeletal soils, gypsum pan

(b) Soil



- (1) Samail Ophiolite: middle to late Cretaceous mantle sequence - harzburgite
- (2) Samail Ophiolite: middle to late Cretaceous cumulate and high-level gabbro
- (3) Samail Ophiolite: middle to late Cretaceous intrusive peridotite - gabbro
- (4) Sumeini and Hawasina Nappes: Triassic to Cretaceous - Umar Group - volcanic rocks, basin facies

(6) Torriorthents–Gypsiorthids: sandy-skeletal on a young alluvial fan

(7) Gypsiorthids: sandy to loamy-skeletal soils on moderately dissected high alluvial terraces and fans

(8) Calciorthids: loamy, deep soils

(9) Calciorthids–Gypsiorthids: loamy to loamy-skeletal, deep and moderately deep soils

(5) Sumeini and Hawasina Nappes: Triassic to Cretaceous - Kawr Group - volcanic rocks, platform facies

(6) Arabian platform: middle Cretaceous - Wasia Group - shelf facies

(7) Arabian platform: end Jurassic to middle Cretaceous - Kahmah Group - basinal, slope and shelf facies

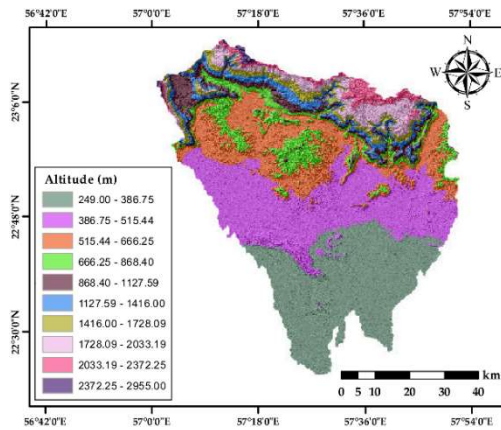
(8) Arabian platform: Jurassic - Sahtan Group - shelf facies

(9) Sedimentary Basement: lower Huqf Group - shelf facies

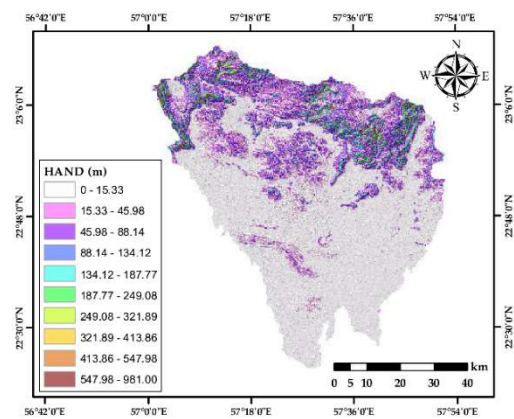
(10) Quaternary alluvial deposits

(11) Sumeini and Hawasina Nappes: late Permian to late Cretaceous - Hamrat Duru Group - volcanic rocks, basin facies

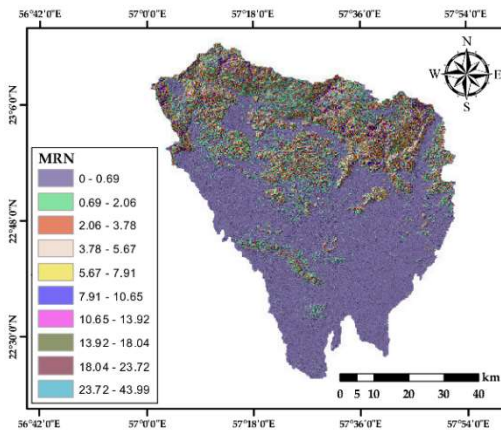
(c) Altitude



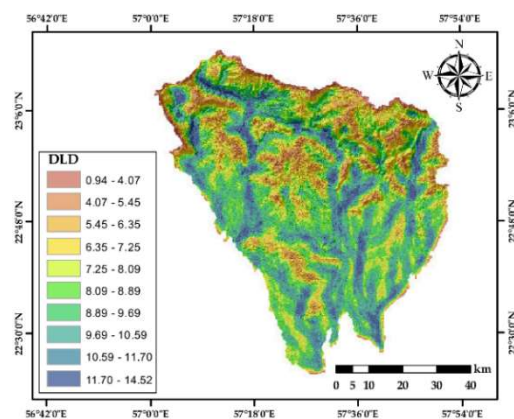
(d) HAND



(e) MRN

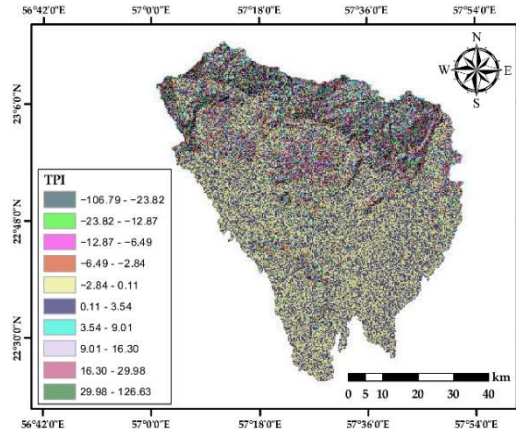


(f) DLD

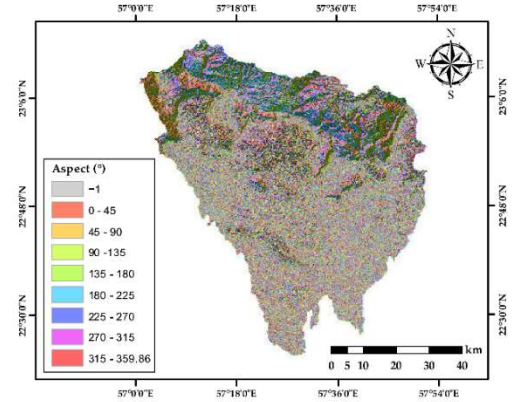


(g) TPI

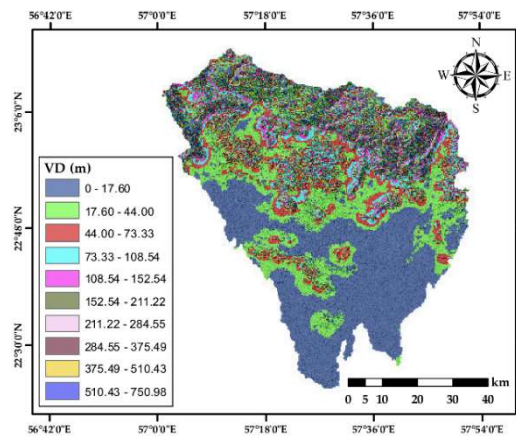
(h) Aspect



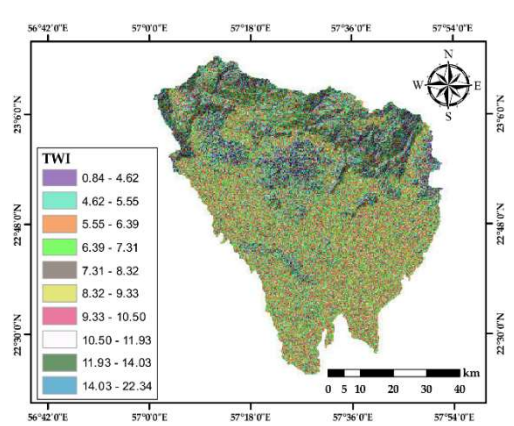
(i) VD



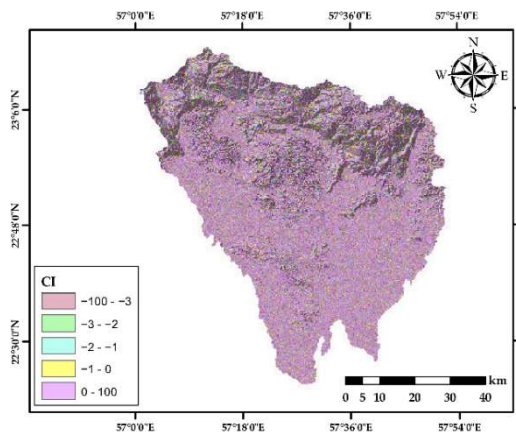
(j) TWI



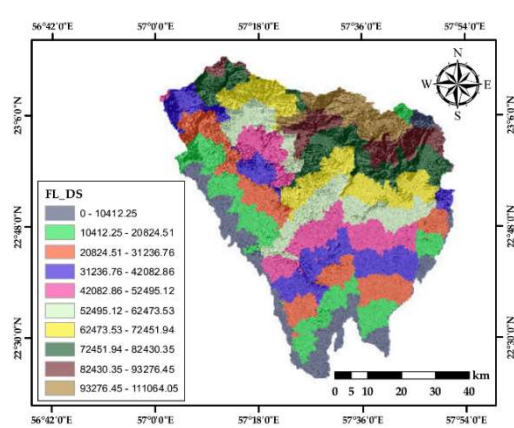
(k) CI



(l) FL_DS



(m) GSMaP-G



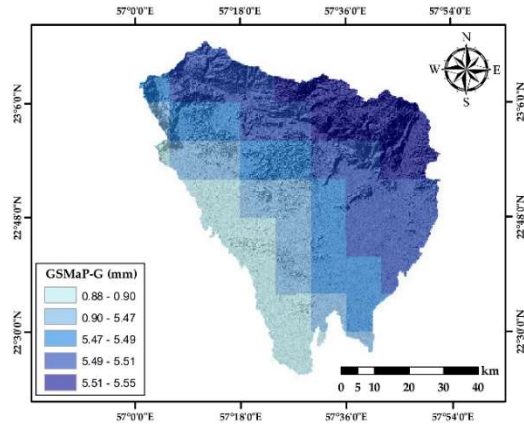


Figure 4.4. Reclassified flash flood triggering factor in the selected area of study: **(a)** geology, **(b)** soil, **(c)** altitude (m), **(d)** height above nearest drainage network (HAND) (m), **(e)** Melton ruggedness number (MRN), **(f)** drainage line density (DLD) (km/km²), **(g)** topographic position index (TPI), **(h)** Aspect (°), **(i)** valley depth (VD), **(j)** topographic wetness index (TWI), **(k)** convergence index (CI), **(l)** flow length in the downstream direction (FL_DS), and **(m)** Global Satellite Mapping of Precipitation-Gauge calibrated (GSMaP-G).

Valley depth (VD) (Figure 4.4i) is the difference between interpolated ridges' levels and the original elevation of the terrain [160], [167].

The topographic wetness index (TWI) (Figure 4.4j) is a morphometric factor that can represent the soil moisture and water distribution on soil [168]. It can quantify the effect of topography on runoff generation (i.e., zones of surface saturation) and define the spatial distribution areas of relative wetness or dryness [169]. It defines the flow accumulation's amount at any given point in a basin and the water ability to move downslope as a result of gravity [170]. Areas with similar TWI values, within the same catchment area, are considered to have a comparable hydrological response to rainfall when other prevailing conditions (e.g., soil, geology) are similar [171]. It can be considered as a function of specific catchment area and local slope [168].

Convergence index (CI) (Figure 4.4l) is a terrain morphometric factor [160] used to quantify the degree of river network convergence and relief structure [172].

Convergent negative areas denoted the valleys, while positive values characterized areas occupied by ridges.

Flow length in the downstream direction (FL_DS) is the weighted distance alongside the flow path in the downstream direction for each cell to an outlet or a sink on the boundary of the sub-watershed [173].

The hourly GSMaP-G (Figure 4.4m) with a $0.1^\circ \times 0.1^\circ$ spatial resolution was utilized in the current study. The hourly GSMaP-G was accumulated to 24 h product directly before the capturing date of the Sentinel-1A GRD Radar images. The additive bias correction method, while stations represent the dependent variable, was applied to ensure achieving the most optimum rainfall measurements.

4.3.3. Multicollinearity Assessment of the Flood Causative Variables

Involving highly correlated variables in the bivariate and multivariate statistical methods can significantly reduce the accuracy of the developed models [174], [175]. Therefore, it was mandatory to exclude the highly intercorrelated explanatory factors before developing such models. In the current study, two indicators (i.e., variance inflation factor (VIF) and tolerance (TOL)) were used to determine the multicollinearity problem. The VIF is the quotient of the variance in a multiple term-based model by the variance of a single term model, while TOL is the reciprocal of VIF. Independent variables with VIF values greater than 5 or tolerance values less than 0.2 defined multicollinear variables [176] that needed to be removed from the model under development.

4.3.4. Bivariate and Multivariate Statistical Models

The future flash floods tend to occur under comparable local conditions that triggered them in the past. Flash flood predictive modeling can be compiled in the following steps: (i) detecting flood occurrence for a specific event through processing of Sentinel-1A SAR

scenes, (ii) investigating a set of flood influencing parameters, (iii) quantifying the relationships between the controlling factors and the flash flood extent by adopting different bi and multi-variate statistical methods, (iv) computing a spatially-distributed map for the flood extent probability, and (v) evaluating the reliability of the probability map and its utility for predicting future flash flood locations.

Flash flood susceptibility map is a binomial classification task where the flood index (i.e., inventory map) is categorized into two class classes (i.e., flood and non-flood sets). The flood and non-flood pixels denoted 1 and 0 values, respectively, and nodata pixels assigned the value of -9999. A random 25.200 and 10.800 pixels were used to create the training and testing datasets (Figure 4.3b,c), respectively.

4.3.4.1. Relative Frequency Ratio (FR)

The first step was to take a completely random, well-spatially distributed, and stratified sample of 18000 points from the flood inventory map in the ArcGIS environment. Based on the previous studies (e.g., [72], [134]), the pre-selected random flood sample was subdivided into training (70%) and testing (30%) data subsets.

$$FR = (FF/CA) / \Sigma (TFF/TCA) \quad (4.1)$$

where (FF) is the flood frequency within a certain class of one covariate divided by total occurrences of flood within the whole class (TFF), and (CA) is the area of a particular class divided by the total area of all classes (TCA) of one parameter.

Flood probability index (FBI) measured by summing the FR of all factors triggering flash flood in the area under study.

$$FBI = \sum_{j=1}^m FR \quad (4.2)$$

where m is the number of factors affecting flood initiation and spreading in the study area.

4.3.4.2. Statistical Index (SI)

The statistical index (SI) is a bivariate analytical method introduced by van Westen et al. [177]. It has been successfully used in the susceptibility mapping of landslides' natural hazards [178]. In the SI model, a weight for each variable class is the quotient of the natural logarithm of the flood density in that class by the flash flood occurrences in the entire area under study. It is formulated in the following equation [177]:

$$SI_{ij} = \ln \left(\frac{FO_{ij}}{FO_T} \right) = \ln \left(\frac{FPN_{ij}/FPN_T}{FPX_{ij}/FPX_T} \right) \quad (4.3)$$

where SI_{ij} denotes the weight given to a particular category “i” of a factor “j,” FO_{ij} refers to the flood occurrences within class “i” of variable “j,” FO_T is the total flood occurrences within the entire area of study, FPN_{ij} and FPX_{ij} are the number of spatial flood points and pixels, respectively, in a specific category “i” of parameter “j,” and FPN_T and FPX_T are the total numbers of flood points and pixels in the entire area of study.

The SI approach can be computed using the modeling capabilities in a GIS environment. It is a fast and reasonable simple technique that can be used efficiently for flood hazard modeling [72]. Every conditioning parameter was intersected with the flash flood inventory map and the flood density (i.e., occurrences) in each class of the entire variables was computed. Then, each factor was reclassified using the derived weights to generate the final flood probability map. Positive weights indicated a direct relationship between a class of a specific parameter and flood density. The higher positive score demonstrated a strong relationship, while negative one showed that the class under consideration is not relevant for developing flood.

4.3.4.3. Logistic Regression (LR)

Logistic regression (LR) is one of the main multivariate statistical methods that has been widely applied to quantify the susceptibility for different natural hazards such as landslides, forest fires, and flood [61], [179]–[181]. It supports any possible type of the

triggering variables [182], [183] (e.g., continuous, nominal, and categorical). The flash flood inventory represented by a binary image that demonstrated the occurrences (i.e., 1) and non-occurrence (i.e., 0) of the flash flood. Using the binomial LR, a regression association has been established among the flood conditioning factors and dichotomous inventory map with two possible values (i.e., flood (0) and non-flood (1)). The RapidMiner Studio software [184] was utilized to build a statistical regression model in order to predict the logit transformation of the probability occurrence of the dependent binary variable (i.e., flash flood).

LR evaluates a dependent variable of a particular flood event and depicts the spatial association with the independent variables (i.e., triggering factors) that can contribute to the probability of occurrences of that event. It directed to determine the best fitting model that can demonstrate the relationship between the normalized (i.e., in the range of zero to one) independent flood-related factors by calculating the likelihood changes of falling in each class of the flood inventory map [39]. The quantitative spatial relationships between flood occurrence and its related dependent factors can be expressed as:

$$P = \frac{1}{(1 + e^{-z})} \quad (4.4)$$

where P denotes the flood probability index (i.e., occurrence). It ranges between zero and one on an S-shaped curve. z is the linear combination of the explanatory factors and it varies from $-\infty$ to $+\infty$. It can be estimated using the following LR equation:

$$\text{Logit}(z) = \beta_0 + \beta_1 x_1 + \beta_2 x_2 + \dots + \beta_n x_n \quad (4.5)$$

where β_0 refers to the constant or intercept of the LR model, the β_i (i = 0, 1, 2, ... , n) denotes the slope coefficients (i.e.,) of the LR model, and the x_i (i = 0, 1, 2, ... , n) are the independent covariates.

4.3.5. Models' Performance Validation

In the current study, different metrics were used to evaluate the performance of the individual bivariate and integrated bivariate and multivariate-based flood susceptibility

models. In the bivariate statistical models, flood points were utilized for training and testing such models, while flood and non-flood points were employed for the same purpose in case of the ensemble bivariate and multivariate models.

The confusion matrix is a statistical method to summarize of a classification algorithm’s performance [185], [186]. In the 2 by 2 error matrix, the number of correct and incorrect flood pixels’ predictions were listed and differentiated into 4 outputs (i.e., true positive (TP), true negative (TN), false positive (FP), and false negative (FN)) (Table 4.1).

Table 4.1. Classification matrix’s outcomes of the comparison between actual flood inundation and predicted flood extent datasets. F and NF denote flood and non-flood, respectively.

		Predicted Class	
		NF	F
Actual Class	NF	NF_NF (TN) = Number of NF pixels classified correctly as NF	NF_F (FP) = Number of NF pixels classified incorrectly as F
	F	F_NF (FN) = Number of F pixels classified incorrectly as NF	F_F (TP) = Number of F pixels classified correctly as F

Overall accuracy (OA), producer accuracy (PA) (i.e., sensitivity, recall, or true positive rate), user accuracy (UA) (i.e., precision), F-score (F), specificity (SP) (i.e., selectivity or true negative rate), and Cohen’s kappa index (KI) were computed to evaluate the performance of the integrated flood susceptibility models (Table 4.2). These metrics have been frequently used to assess the accuracy of various remote sensing-based models (e.g., [106,108,115,116]).

Table 4.2. The metrics for measuring the predictive performance of the flood susceptibility models.

Metric	Formula	Definition	Reference	Equation No
OA	$\frac{TP + TN}{TP + FP + FN + TN}$	the ratio of the correct predictions to entire predictions	[186]	(4.6)
PA	$\frac{TP}{TP + FN}$	the proportion of actual flood pixels, which were predicted as true positive	[186] [191]	(4.7)
UA	$\frac{TP}{TP + FP}$	the proportion of positive flood pixels that were correct	[186] [191]	(4.8)
F	$\frac{2 * TP}{2 * TP + FP + FN}$	the weighted average of PA and UA	[192]	(4.9)
SP	$\frac{TN}{TN + FP}$	the proportion of actual non-flood pixels, that were predicted as true negative	[193]	(4.10)
KI	$\frac{N \sum_{i=1}^m x_{ii} - N \sum_{i=1}^m (x_{i+} * x_{+i})}{N^2 - \sum_{i=1}^m (x_{i+} * x_{+i})}$	difference between observed and expected agreements	[194]	(4.11)

where m is the numbers of rows, X_{ii} is the numbers of channel network/order pixels in row i and column i (on the major diagonal), X_{i+} is the total number of the channel network/order pixels in row I, X_{+i} is the total number of the observations in column I, and N is the total number of observations.

The higher the PA, UA, F, and SP values, the better the performance of ensemble bi and multivariate flood susceptibility models. If the chance agreement and strength of the agreement increase, the KI provides negative and positive values, respectively.

Without validation, the identified flood-prone areas (i.e., susceptibility maps) have no scientific significance [195], [196]. Therefore, for evaluating the performance of bivariate flood susceptibility models (i.e., FR and SI), the area under the receiver operating characteristics (AUROC) curves-based cumulative percentages of flood occurrences were used.

ROC is a curve of probability curve, and AUC is a measure of separability between classes. It is used frequently in evaluating the performance of the natural hazards susceptibility models [133], [197], [198]. AUC shows the capability of a model tells to

distinguish between different classes and it ranges between zero and one. The higher the AUC, the sharper the differentiation between classes, and the better the model is at the prediction. In the current research, the 18,000 flood locations were divided into 70% and 30%, using the stratified random sampling method, for training and validation of the bivariate susceptibility models, respectively. The outputs of the flood susceptibility maps were evaluated using the training and testing flood points by means of prediction and success rates' curves, respectively [196]. To gain the relative ranks for the developed flood probability maps for the training and validation datasets, the calculated probability index values of all pixels, in the area under study, were sorted in descending order [199]. Next, the ordered cell values were divided into 100 classes, using an equal interval classification method, with accumulated 1% intervals. Then, the AUC can be quantified using the trapezoid area mathematical formula.

4.4. Results

4.4.1. Multicollinearity Assessment

In the current study, a detailed multicollinearity evaluation has been carried out to exclude the highly inter-associated variables from the flood susceptibility models under development. The VIF and TOL metrics used to select the optimal flood predictive factors, where VIF and TOL values greater than 5 and less than 0.2, respectively, indicated a multicollinearity problem [39]. The results of multicollinearity assessment among the 13 independent variables showed that no factor exceeded the critical values of VIF and TOL (Figure 4.5).

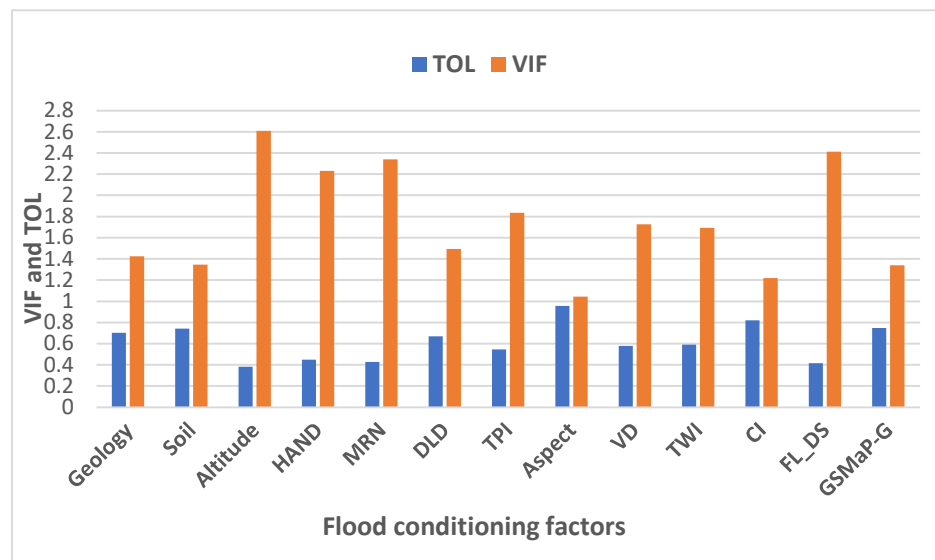


Figure 4.5. Multicollinearity assessment of the flood triggering factors.

4.4.1. FR Model-based Flood Susceptibility

The FR computed by dividing the ratios of flash flood occurrences by the areas occupied by each class of every flood causative factors (Table 4.3). The greater the FR's class weight, the stronger the spatial association between that class and the flood occurrence is. The surficial alluvial deposits had a higher probability of the flash flood occurrence than the other geologic classes (Figure 4.4a). The mountainous and strongly dissected rocky

plateaus, and Loamy and sandy-skeletal deep soils had the lowest and highest impacts, respectively, on the flood spreading (Figure 4.4b). The part of terrain with an altitude of less than 555 m showed a strong association with the flood occurrence (Figure 4.4c). For the HAND and MRN factors, the classes with the lowest values had significant effects on the flood density probability (Figures 4.4d,e). The classes ranged from 9.69 - 10.59 and 10.59 - 11.70 km/km² of DLD (Figure 4.4f) had remarkable influences on the spatial distribution of flash flood. The TPI ranged from -2.84 - 0.11 and 0.11 - -3.54 m (Figure 4.4g) had obvious effects on the flood occurrence. Due to the complex topography of the study area, most of the aspect's classes showed noticeable connections to the flood probability (Figure 4.4h). VD of less than 44 m (Figure 4.4i) provided a favorable condition for flood occurrences. For the TWI (Figure 4.4j), the four classes ranged from 6.39 - 10.5 had an apparent impact on the flood occurrence rather than the remaining classes. For the CI (Figure 4.4k) and GSMaP-G (Figure 4.4m) variables, most of the categories had remarkable spatial associations with the flood. The class 0 - 10412.25 of the FL_DS (Figure 4.4l) showed a higher connection to the flood occurrence than the other entire classes of all other flood causative factors. Each FR weight was multiplied by its related class and the sum of the FR-based reclassified causative factors were computed to derive the FR-based spatial flood susceptibility index. The natural break classification method [139] used to classify the FR-based flood probability index map into five hazard categories of the flood-prone zones (i.e., very low, low, moderate, high, and very high) (Figure 4.6a).

Table 4.3. The spatial relationships between flood occurrence and each class of the flood causative factors based on estimating FR and SI.

Factor	Class No.	Class	Flood Hazards	Class Area (m ²)	RF*100	SI*100
	1	Mantle sequence - harzburgite	51562.5	3894328	21	-157
	2	Cumulate and high-level gabbro	5781.25	443342	20	-159
	3	Intrusive peridotite - gabbro	3281.25	797582	6	-274
	4	Volcanic rocks, basin facies	8281.25	1452062	9	-242
Geology	5	Volcanic rocks, platform facies	2031.25	1280412	2	-370
	6	Shelf facies	625	1902484	1	-527
	7	Basinal, slope and shelf facies	781.25	1938965	1	-507
	8	Shelf facies	781.25	1226269	1	-461
	9	Shelf facies	312.5	783120	1	-508
	10	Surficial alluvial deposits	1733750	13659615	199	69
	11	Volcanic rocks, basin facies	160781.25	3422212	74	-31
	1	Mountains and dissected rocks	55625	15076610	6	-285
	2	Loamy and sandy-skeletal, deep soils	917031.25	4302551	334	120
	3	Gravelly sandy, deep soils	332656.25	4442940	117	16
	4	Sandy and loamy deep soils	161250	1121292	225	81
Soil	5	Loamy- and sand-skeletal soils, gypsum	13593.75	77396	275	101
	6	Sandy-skeletal	128593.75	2085371	97	-4
	7	Sandy to loamy-skeletal soils	189062.5	1322504	224	81
	8	Loamy, deep soils	96562.5	1867315	81	-21
	9	Loamy to loamy-skeletal deep soils	73593.75	504412	228	83
	1	249.00 - 386.75	1250781.25	7886252	248	91
	2	386.75 - 515.44	704687.5	8244396	134	29
	3	515.44 - 666.25	9375	5382553	3	-360
	4	666.25 - 868.40	468.75	2587269	0	-587
Altitude (m)	5	868.40 - 1127.59	781.25	1750194	1	-496
	6	1127.59 - 1416.00	312.5	1330667	0	-561
	7	1416.00 - 1728.09	625	1181741	1	-479

	8	1728.09 - 2033.19	781.25	1531817	1	-483
	9	2033.19 - 2372.25	156.25	797401	0	-579
	10	2372.25 - 2955.00	0	108101	0	—
	1	0 - 15.33	1966875	21559536	143	36
	2	15.33 - 45.98	625	4009204	0	-602
	3	45.98 - 88.14	312.5	2577679	0	-627
	4	88.14 - 134.12	0	1222669	0	—
HAND (m)	5	134.12 - 187.77	156.25	661081	0	-560
	6	187.77 - 249.08	0	379821	0	—
	7	249.08 - 321.89	0	210375	0	—
	8	321.89 - 413.86	0	110783	0	—
	9	413.86 - 547.98	0	52694	0	—
	10	547.980- 981.00	0	16549	0	—
	1	0 - 0.69	1963125	21022209	146	38
	2	0.69 - 2.06	4218.75	3965109	2	-410
	3	2.06 - 3.78	312.5	2686285	0	-631
	4	3.78 - 5.67	312.5	1501628	0	-573
MRN	5	5.67 - 7.91	0	806327	0	—
	6	7.91 - 10.65	0	429522	0	—
	7	10.65 - 13.92	0	212824	0	—
	8	13.92 - 18.04	0	109269	0	—
	9	18.04 - 23.72	0	49424	0	—
	10	23.72 - 43.99	0	17794	0	—
	1	0.94 - 4.07	468.75	346737	2	-386
	2	4.07 - 5.45	6250	1423873	7	-268
	3	5.45 - 6.35	15312.5	2485259	10	-234
	4	6.35 - 7.25	42343.75	3625113	18	-170
DLD	5	7.25 - 8.09	176250	4570790	60	-51
km/km²	6	8.09 - 8.89	363593.75	5092869	112	11
	7	8.89 - 9.69	476406.25	4904429	152	42
	8	9.69 - 10.59	500312.5	4159527	188	63

	9	10.59 - 11.70	337031.25	2880523	183	60
	10	11.70 - 14.52	50000	1311271	60	-52
	1	-106.79 - -23.82	0	38707	0	—
	2	-23.82 - -12.87	312.5	307533	2	-414
	3	-12.87 - -6.49	1250	1308055	1	-420
	4	-6.49 - -2.84	5937.5	2618480	4	-334
TPI	5	-2.84 - 0.11	1115937.5	12323706	142	35
	6	0.11 - 3.54	808593.75	10554197	120	18
	7	3.54 - 9.01	35468.75	2560916	22	-153
	8	9.01 - 16.30	312.5	853568	1	-516
	9	16.30 - 29.98	156.25	209324	1	-445
	10	29.98 - 126.63	0	25905	0	—
	1	-1	328750	1953988	263	97
	2	0 - 45	211093.75	3252562	102	2
	3	45 - 90	219687.5	3188856	108	8
	4	90 - 135	220468.75	3841265	90	-11
Aspect (°)	5	135 - 180	237343.75	4432081	84	-18
	6	180 - 225	228437.5	5134570	70	-36
	7	225 - 270	221875	3606772	96	-4
	8	270 - 315	211875	3152985	105	5
	9	315 - 360	88437.5	2237312	62	-48
	1	0 - 17.60	1682500	13244222	199	69
	2	17.60 - 44.00	253593.75	8365568	47	-75
	3	44.00 - 73.33	26875	4809868	9	-244
	4	73.33 - 108.54	3281.25	2434115	2	-386
VD (m)	5	108.54 - 152.54	1093.75	1028658	2	-410
	6	152.54 - 211.22	0	451153	0	—
	7	211.22 - 284.55	156.25	246578	1	-461
	8	284.55 - 375.49	468.75	139633	5	-295
	9	375.49 - 510.43	0	62119	0	—
	10	510.43 - 750.98	0	18477	0	—

	1	0.84 - 4.62	23593.75	3375087	11	-221
	2	4.62 - 5.55	400000	6450431	97	-3
	3	5.55 - 6.39	420000	7264398	90	-10
	4	6.39 - 7.31	403125	5229595	121	19
TWI	5	7.31 - 8.32	350625	3647198	150	41
	6	8.32 - 9.33	205000	2327494	138	32
	7	9.33 - 10.50	112343.75	1363313	129	25
	8	10.50 - 11.93	41093.75	752221	86	-16
	9	11.93 - 14.03	12187.5	314517	61	-50
	10	14.03 - 22.34	0	76137	0	—
	1	-100 - -3	809062.5	8530288	148	40
	2	-3 - -2	53281.25	1474208	57	-57
CI	3	-2 - -1	62812.5	1898749	52	-66
	4	-1 - 0	88906.25	2407283	58	-55
	5	0 - 100	953906.25	16489863	91	-10
	1	0 - 10412.25	767500	3003849	400	139
	2	10412.25 - 20824.51	585781.25	3864957	237	86
	3	20824.51 - 31236.76	260937.5	3711271	110	10
	4	31236.76 - 42082.86	124218.75	3725271	52	-65
FL_DS	5	42082.86 - 52495.12	169062.5	3225372	82	-20
	6	52495.12 - 62473.53	39531.25	3288155	19	-167
	7	62473.53 - 72451.94	19062.5	3401034	9	-243
	8	72451.94 - 82430.35	312.5	2979188	0	-641
	9	82430.35 - 93276.45	625	1876719	1	-526
	10	93276.45 - 111064.05	937.5	1724575	1	-477
	1	0.88 - 0.90	843281.25	4742178	278	102
	2	0.90 - 5.47	547343.75	5249323	163	49
GSMaP-G	3	5.47 - 5.49	353906.25	6814821	81	-21
(mm)	4	5.49 - 5.51	222031.25	9447062	37	-100
	5	5.51 - 5.55	1406.25	4547007	0	-533

4.4.3. SI-based Flood Susceptibility Model

The weight of each class of every flood causative parameter had been calculated through quantifying the spatial relationship with the flooding inventory map (Table 4.3). The SI of each class is directly proportional to the probability of flood occurrence. Negative values (i.e., weights) of the SI denote weak relationships between flood probability and the class under consideration. On the contrary, the greater the positive value of the SI of a particular class, the stronger the possibility of the flash flood within this class is. Classes with no flood occurrence do not have any association with the flash flood inventory map. Most of the lithologic units had negative relationships with the flood occurrence except for the alluvial deposit class. (Figure 4.4a). The loamy and sandy-skeletal deep soils (Figure 4.4b) had the most significant positive SI value. The different classes of DEM (Figure 4.4c) had negative influences on the flood initiation and spreading, except for the low terrain with elevation less than 515 m that showed a positive association with the flood possibility. HAND's 0 - 15.33 m (Figure 4.4d) was the only class that had a positive influence on the flood probability, while HAND in the ranges of 15.33 - 45.98, 45.98 - 88.14, and 134.12 – 187.77 m had the highest SI negative values. MRN's classes (Figure 4.4e) had mostly weak or no relationships with the flood occurrence.

The first five classes of DLD showed no effect on the flood extent (Figure 4.4f). Most of the TPI's classes (Figure 4.4g) showed no influences on the flood density. The flat area class of the aspect parameter (Figure 4.4h) yielded the greatest effect on the flood occurrence and followed by classes ranged from 0 – 90°. The entire classes of VD (Figure 4.4i) had negative influences on the flood probability, except for the classes ranged from 0 – 17.6 m. The first class of TWI (Figure 4.4j) yielded the greatest negative SI value (i.e., -212) with respect to other TWI's classes. CI's categories (Figure 4.4k) showed mostly weak influences on the flash flood occurrence except for the first class (-100 – -3) that had a positive relationship with the flood probability. The FL_DS class (Figure 4.4l) with value ranged from 72451.94 - 82430.35 had the lowest minimal effect on the flood probability when compared to the other classes of all flood conditioning factors. However, the first three units of the FL_DS in the range between 0 and 31236.76 had positive impacts on the

probability of flooding. The different classes of the GSMaP-G (Figure 4.4m) showed mixed effects on the flood occurrence.

The SI-based flood susceptibility index was computed using the reclassified triggering factors based on the derived SI values. The flash flood susceptibility map (Figure 4.6b) was developed by differentiating that susceptibility index into five degrees (i.e., very low, low, moderate, high, and very high) of flood susceptibility.

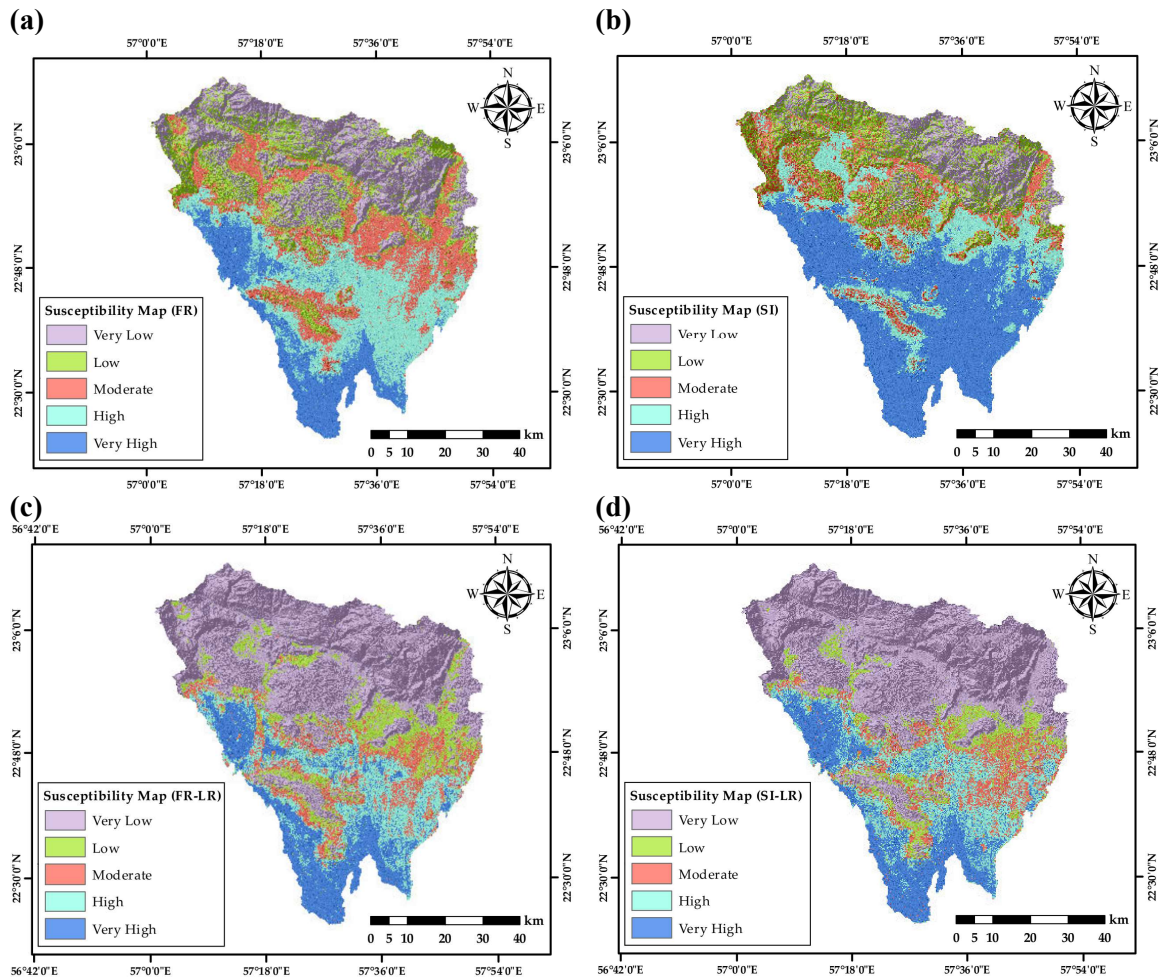


Figure 4.6. Flash flood susceptibility maps generated using: (a) FR, (b) SI, (c) FR-LR, and (d) SI-LR models.

4.4.4. Integrated Bivariate and Multivariate Derived Flood Susceptibility Models

The LR analyses were carried out utilizing RapidMiner software [184], and LR coefficients were estimated for the normalized explanatory flood parameters. Negative LR coefficients (i.e., weights) denoted that the flood causative factors were negatively associated with the flood inundation map (i.e., dependent variable) [81]. The multicollinearity among the independent variables has been re-assessed after weighting the 13 flood triggering factors using FR and SI methods. The results showed that there was no multicollinearity, where no factor exceeded the critical values of VIF and TOL. FR- and SI-based LR models were trained using the equal stratified random flood and non-flood sample (i.e., 70%), and tested utilizing the remaining unseen 30% of the dataset. Table 4.4 shows the flood triggering variables and their corresponding LR coefficients and p-values. The geology and TPI variables of the integrated FR-LR model, and the TPI factor of the and SI-LR model had negative coefficients, and other flood causative parameters received positive weights in both hybrid models.

The p-value is a probability that is used to determine if the spatial association between each independent variable and the response variable (i.e., flood inventory map) is statistically significant. It is statistical evidence against the null hypothesis (i.e., the feature's coefficient is equal to zero) based on a significance level (i.e., α or alpha) of 0.05. In the current study, the p-value is less than α for eleven features (Table 4.4), which indicates significant statistical associations between the independent variable and these explanatory variables. More details about the p-value can be obtained from [200]. Variables (e.g., geology and TPI) with no significant p-values were tested by being removed and added to the hybrid LR based susceptibility maps and checking the areas occupied by different flood classes in both cases.

Table 4.4. The results of fitting the FR-LR and SI-LR models on the flash flood datasets. The parameters utilized in both models, their estimated weights and p-values is shown below.

Attribute	FR-LR Model		SI-LR Model	
	β	P-Value	β	P-Value
Geology	-0.005	0.936	0.234	0.166
Soil	2.093	0.000	1.914	0.000
Altitude	2.119	0.000	2.654	0.000
HAND	2.808	0.000	2.196	0.000
MRN	2.423	0.000	3.248	0.000
DLD	0.950	0.000	1.461	0.000
TPI	-0.187	0.125	-0.127	0.593
Aspect	0.690	0.000	0.767	0.000
VD	1.029	0.000	1.675	0.000
TWI	1.133	0.000	2.741	0.000
CI	0.407	0.000	0.413	0.000
FL_DS	1.251	0.000	3.934	0.000
GSMaP-G	0.188	0.014	1.279	0.000
Intercept	-10.415	0.000	-18.884	0.000

The linear combination (i.e., z values) of the constants (i.e., intercepts) of the two hybrid LR models and the product of multiplying every coefficient with the corresponding flood conditioning factor are given in the following equations:

$$z(\text{FR-LR}) = -10.415 + (\text{Soil} * 2.093) + (\text{Altitude} * 2.119) + (\text{HAND} * 2.808) + (\text{MRN} * 2.423) + (\text{DLD} * 0.950) + (\text{Aspect} * 0.690) + (\text{VD} * 1.029) + (\text{TWI} * 1.133) + (\text{CI} * 0.407) + (\text{FL_DS} * 1.251) + (\text{GSMP-G} * 0.188) \quad (4.12)$$

$$z(\text{SI-LR}) = -18.884 + (\text{Soil} * 1.914) + (\text{Altitude} * 2.654) + (\text{HAND} * 2.196) + (\text{MRN} * 3.248) + (\text{DLD} * 1.461) + (\text{Aspect} * 0.767) + (\text{VD} * 1.675) + (\text{TWI} * 2.741) + (\text{CI} * 0.413) + (\text{FL_DS} * 3.934) + (\text{GSMP-G} * 1.279) \quad (4.13)$$

$$\text{Flood susceptibility map (FR-LR)} = P = \frac{1}{(1 + e^{-z(\text{FR-LR})})} \quad (4.14)$$

$$\text{Flood susceptibility map (SI-LR)} = P = \frac{1}{(1 + e^{-z(\text{SI-LR})})} \quad (4.15)$$

The FR-LR and SI-LR flood probability maps were generated using equations (4.14 and 4.15), and subdivided into five classes (i.e., very low, low, moderate, high, and very high) to predict potentiality for flash flood occurrence in each zone of the study area (Figures 4.6c,d).

4.5.5. Evaluation of the Flash Flood Susceptibility Models

In the current study, evaluating the performance of the flash flood susceptibility models were performed using different statistical metrics such as overall accuracy (OA), producer accuracy (PA), user accuracy (UA), specificity (SP), and Kappa index (KI) (Table 4.5). On the one hand, the bivariate statistical approaches (i.e., FR and SI) were trained and tested using only the random stratified flood points (i.e., no use of non-flood locations at this step). However, by determining the flood-prone areas, it could be possible to distinguish the non-flood zones, which assumed to be matched with low flood susceptibility classes. On the other hand, the multivariate statistical methods (i.e., FR-LR and SI-LR) utilized both flood

and non-flood points for developing the flood predictive models. Therefore, to have a consistent base of models' evaluations, a similar probability threshold to that used in the multivariate techniques (i.e., 0.5) was used to distinguish between flood and non-flood events of the bivariate susceptibility models [72]. It was possible at that case to use the equal random stratified flood and non-flood points to evaluate the performance of the bivariate FR- and SI-based susceptibility models.

Regarding the OA, all flood susceptibility models achieved high OA of about 85% for both training and testing phases except for the SI method. The SI susceptibility model scored low OA values of 70.77% and 70.82% for the training and testing datasets, respectively, due to reporting deficient records of TN and FN with respect to the other predictions (Table 4.5). The SI-LR approach achieved the best score among other models and slightly outperformed the FR-LR one with minimally reporting more TP.

Table 4.5. Evaluation metrics for quantifying the predictive performance of the four flood susceptibility models.

	Training	Testing	Training	Testing	Training	Testing	Training	Testing
Metrics	FR	FR	FR-LR	FR-LR	SI	SI	SI-LR	SI-LR
OA	84.49%	84.83%	86.24%	86.56%	70.77%	70.82%	86.64%	86.83%
PA	97.51%	97.39%	92.27%	92.31%	99.87%	99.00%	94.30%	94.63%
UA	77.35%	77.84%	82.34%	82.79%	63.13%	63.15%	81.77%	81.86%
F	86.27%	86.52%	87.02%	87.30%	77.36%	77.39%	87.59%	87.79%
SP	71.46%	72.28%	80.21%	80.81%	41.68%	41.72%	78.98%	79.04%
K	0.690	0.697	0.725	0.731	0.416	0.416	0.733	0.737
AUC	76.98	77.02	80.89	81.07	94.33	94.38	79.16	79.35

In general, the four susceptibility techniques achieved high PA values over 92%. The bivariate statistical models reported higher accuracy than the hybrid susceptibility approaches (i.e., FR-LR and SI-LR) with scoring higher values of TP and lower values of FN. The great number of TP values that were recorded in case of SI and FR models was expected because the bivariate susceptibility models were trained and tested using only flood points. However, SI-LR and FR-LR models still reported a close number of TP to those recorded by SI and FR techniques and simultaneously reported a better number of TN.

The FR-LR model achieved the best UA score and followed directly by the SI-LR approach. The SI model yielded the lowest value of UA (i.e., 63.13% and 63.15% for the training and testing data, respectively), due to reporting the highest number of FP (Table 4.5). For the F-measure (Table 4.5), the SI-LR model performed the best among others and achieved the highest F-score and followed by the FR-LR approach by differences of 0.57 and 0.49 in the case of the training and testing phases, respectively. It was expected that the SI susceptibility model showed the lowest F-score due to its low UA (Table 4.5).

Regarding the evaluation of predicting the non-flood locations, the FR-LR ranked first with SP's values of 80.21% and 80.81% in case of training and validation data, respectively, with reporting the highest number of TN and lowest number of FP among other models (Table 4.5). The bivariate-based susceptibility models generally scored low values of SP, particularly SI model that reported 41.68% and 41.72% in case of training and testing modeling steps, respectively. The very low SP score of the SI model because the lowest number of TN was reported in this case.

The KI value of less than or equal to 0 indicates by or less than chance agreement, 0.01–0.20 as a slight, 0.21–0.40 as a fair, 0.41– 0.60 as a moderate, 0.61–0.80 as a substantial, and 0.81–1.00 as nearly perfect agreement [201]. Three flood susceptibility models out of four showed substantial agreements except for SI method that had a moderate performance with reporting the lowest number of TN among other models (Table 4.5). The SI-LR model slightly outperformed the FR-LR models with KI's differences of 0.007 and 0.004 in the case of training and testing steps, respectively.

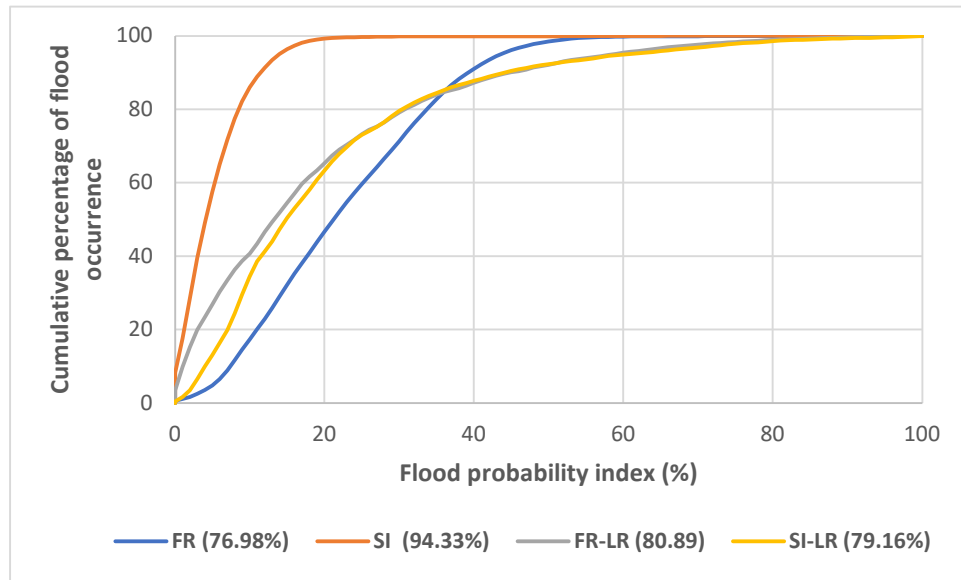
In general, the statistical difference between GSPEs and ground stations were minor, especially for the light and moderate rainfall classes (See Chapter 2 for more details). Therefore, the GSPEs can be used directly in the flood susceptibility modeling, particularly for the bivariate statistical models that categorized GSPEs into classes instead of using separate pixels values. In the trial for developing the individual bivariate flood susceptibility models, the direct GSMaP-G product was tested in these models and it provided close results to the corrected GSMaP-G. In addition, it gave close results in the case of integrated bivariate and multivariate statistical methods.

To have a complementary evaluation of the performance of different statistical-based flood susceptibility models, the ROC and AUC described above in section 4.3.5 were used. Most of the previous researches for flood susceptibility mapping used these metrics successfully to determine the performance of various statistical and machine learning-based models (e.g., [39], [45]). The current study utilized the success and prediction rate curves to validate the developed susceptibility models. The success rate curve is comparing the predicted flood hazard zones to existing flood hazard locations. The prediction curve determines how well the susceptibility model predicts the probability of the flood zones [196]. The computed percentages of the success and prediction rates of each flood susceptibility model were generated utilizing the random stratified flood training (70%) and testing (30%) datasets, respectively. The closer to one and the larger the AUC value, the better the predictive capability of the flood model is.

The values of prediction rates of the four flood susceptibility models slightly outperformed the success rate curves (Figure 4.7). In general, the AUC value of 0.9438 of the SI flood susceptibility model represented a superior predictive accuracy of 94.38% (Figure 4.7). On the one side, although the statistical bivariate FR-based flood susceptibility model yielded the lowest prediction accuracy rate (i.e., 77.02%), the integrated FR-LR method demonstrated a better flood predictive capability (i.e., 81.07%) (Figure 4.7). On the other side, the SI flood susceptibility model showed a better accuracy prediction rate (i.e., 94.38%) than the SI-LR flood method (i.e., 79.35%) (Figure 4.7). This result was expected

because the SI model was tested using only flood locations, but the SI-LR method was validated using flood and non-flood points.

(a)



(b)

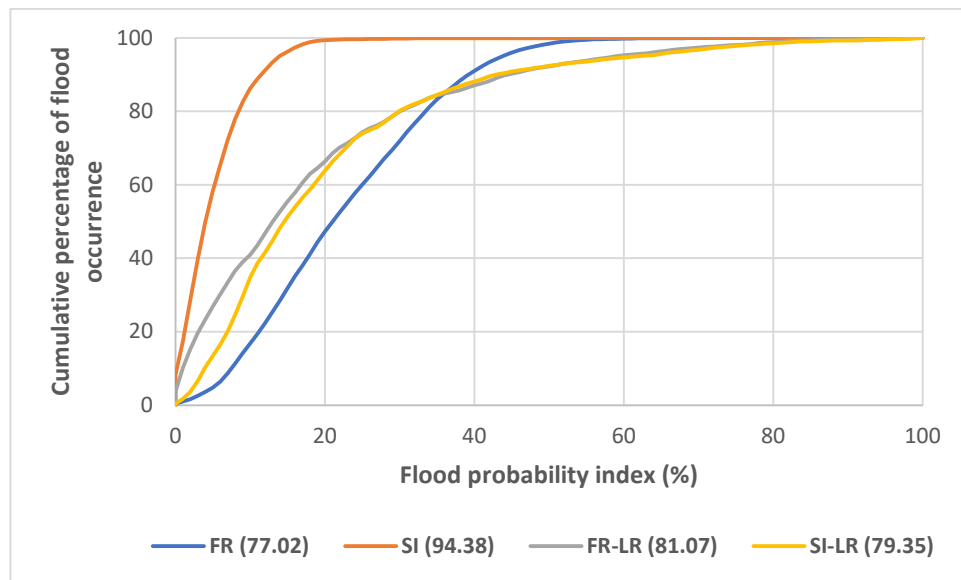


Figure 4.7. The success (a) and (b) prediction rate curves for the four statistical models-based flash flood susceptibility maps.

4.5.6. Comparing Five Classes' Percentages Derived from Four Flood susceptibility Models

The zones of very low and low occupied the lowest area percentages in the case of SI- and FR-based flood susceptibility maps with values of 32.66% and 44.03%, respectively. After integration with the multivariate LR, the hybrid SI-LR and FR-LR models increased the share percentages of these zones to about 61% (i.e., the major part of the map) (Figure 4.8).

The very high and high flash flood susceptibility categories covered an area of 54.64% in the case of SI model and reduced to be 36.85, 29.79, and 29.03% in the case of FR, SI-LR, and FR-LR methods. Therefore, the areas of the very low and low susceptibility classes increased at the expense of very high and high categories while transferring from individual bivariate to integrated bivariate and multivariate susceptibility models in case of including 11 variables. The moderate susceptibility class area reduced in the case of the hybrid flood models (Figure 4.8).

The latter results reflected the performance of the four susceptibility models, where the hybrid models (i.e., SI-LR and FR-LR) were able to detect very low and low susceptibility classes more than the individual bivariate models (i.e., SI and FR). The use of non-flood points beside flood points to train the integrated SI-LR and FR-LR provided these models with more capabilities to determine non-flood zones (i.e., areas with low flood probability) and to refine flood locations. Utilizing the flood points to train and validate the bivariate statistical models (i.e., SI and FR) provided the chance for these models to focus only on determining the flood locations, particularly in the case of SI technique. However, the final results of these models may need to be refined with the outcomes of the hybrid models (Figure 4.8).

Tehrany et al., [81] added all the flood conditioning factors in her study to the LR model. In the current study, by including the 13 variables to generate the flood susceptibility maps, it was found that the areas occupied by very low and low flood classes increased by

1.27%, while the high and very high susceptible zones decreased by 1.9% In case of the FR-LR susceptibility model. In contrast, the predictive high and very high flood classes in the SI-LR susceptibility map increased by 0.12 %, and very low and low flood categories decreased by 0.26%.

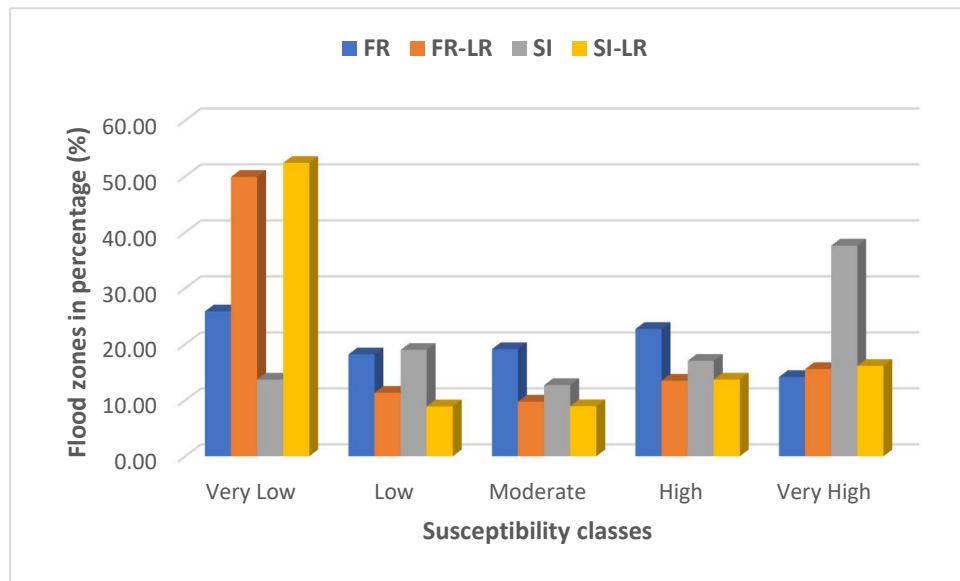


Figure 4.8. The area percentage of the flash flood zones located within the five classes of the developed susceptibility maps.

4.6. Discussion and Conclusions

In general, the overall effective performance of the four flood susceptibility maps was affirmed by the obvious agreement between flood and non-flood locations and developed susceptible flood-prone classes (Figure 4.6). However, possible arguments and improvements in the current study with respect to other research are discussed in the following paragraphs.

There is no agreement regarding the optimum number of conditioning factors required to generate an efficient flood susceptibility map. In the current study, thirteen flood causative parameters were selected in the case of the individual bivariate and integrated bivariate and multivariate statistical models, respectively. Tehrany et al. [72] employed thirteen variables, while Bui et al. [39] and Khosravi et al. [202] utilized ten parameters. Mahmoud and Gan [203] recommended to use more than six factors to avoid predicting misleading flood-prone areas that could be affected by a single weight of a specific class and related over-rating of the probability of certain contributing variables.

The bivariate flood susceptibility models showed that flood occurrence was mostly controlled by soil, rainfall, FL_DS, and DLD factors. The achieved results of the hybrid models (i.e., SI-LR and FR-LR) could be interpreted by using both flood and non-flood points for the training and testing of these models. The use of non-flood points added more spatial details to the ensemble models and allowed them to better distinguish between different susceptible flood zones, and to refine between flood and non-flood locations. The non-flood areas were mostly associated with low and very low flood vulnerable-zones (Figure 4.6c,d).

Youssef et al. [12] found that FR flood susceptibility modeling over Jeddah, Saudi Arabia, slightly outperformed the LR model with reporting AUC values of 0.914 and 0.904, respectively. Tehrany et al. [72] stated that the prediction rates of the FR-, SI-, and LR-based flood susceptibility models were equal to 67.33, 78.18, and 79.45%, respectively, over Brisbane catchment, Australia. Bui et al. [39] concluded that the ensemble evidential belief

function (EBF)-LR model was superior to the LR approach in generating the flood susceptibility map. Additionally, the EBF-based flood susceptibility model outperformed the EBF-LR and LR models, with reporting prediction rates of 94.55, 83.19, and 66.41%, respectively.

On the one hand, in the current study, the SI-LR susceptibility model was slightly superior to the FR-LR method. Besides, the FR- and SI-based susceptibility models came in the third and last rank, respectively. The latter evaluation was conducted based on considering flood and no-flood locations. The multivariate LR method managed to improve the performance of the individual bivariate FR- and SI-based flood susceptibility models. On the other hand, considering only flood points, the SI flood susceptibility model achieved the highest prediction and success rates and followed by FR-LR, SI-LR, and FR methods. Although each area of study has its own physical and topographic conditions, my findings were similar to the studies conducted by Bui et al. [39] and Tehrany et al. [72]. However, there were differences in the fine details of the developed flood susceptibility maps from my study and previously mentioned research. It is expected that the current study introduced more precise flood susceptibility maps, with respect to the others for the reasons described in the following paragraphs.

Most of the previous flood susceptibility researchers developed their flood inventory maps based on multiple past flood events and limited field surveys. This means that the generated flood inundation maps were broad and not specific to a certain event. The field survey requires excessive effort and cost and can usually only be carried out after the complete retreat and seepage of the flood water to the underlying soil layers. It is worth mentioning that there are mapping locations representing more rugged, mountainous terrain that are inaccessible by vehicles and very dangerous for researchers to traverse. Therefore, the outcome of the field survey is to collect a few flood points, mostly along the main valleys. Additionally, the obtained field points can represent few flood locations that cannot represent the real and areal spatial distribution of the flash floods' occurrences.

The selection of the non-flood points is also one of the major limitations of the flood susceptibility research. Different authors chose the non-flood points using only the topographic maps and Google Earth, and most of the non-flood locations were set on the upstream rugged mountains. Although their point of view was acceptable, non-flood points could be found anywhere within the stream watershed.

Another imperative constraint for most of the previous flood susceptibility modelers was that they did not include the rainfall data, which is the most essential and key dynamic factor related to floods' triggering. In some cases, the researchers involved the annual average rainfall data, which is a general data, bearing no relation to a certain flood event.

The current study overcame the above-mentioned limitations, whereby it introduced an improved flood susceptibility modeling that included both spatial and temporal details. It employed corresponding flood inventory mapping and satellite-based rainfall data (i.e., GSMaP-G) that contributed to the selected flood event. The achieved enhancement resulted in developing more accurate maps that can mimic the susceptible areas to future flood hazards over space and time, at a similar rainfall intensity.

Developing flash flood susceptibility maps is the cornerstone of research to manage a sustainable plan for mitigating flood risks in any area under consideration for current and future urban planning. Reliable and precise dynamic flood susceptibility maps can efficiently help decision makers and planners develop plans to reduce costs, limit infrastructure damage, and lessen the threat to human life associated with future flash floods. Although the Dakhiliyah Governate at the Sultanate of Oman was frequently exposed to severe flash flooding events, this study is the first to determine the vulnerable locations to the flash flood hazards. The current research aiming to determine which of the individual and integrated statistical techniques (FR, SI, FR-LR, and SI-LR) is more successful in predicting the probability of future flash flood occurrences.

Although flash flooding has, for many decades, been considered an extreme environmental hazard, the processes triggering its initiation and spreading remain uncertain

or less than adequately documented. The current study introduced a new proper combination of flood causative factors such as HAND, TPI, VD, CI, FL_DS, MRN, and GSMaP-G. The new factors covered information about the possible processes affecting the stream watershed and flash floods such as climatic (i.e., GSMaP-G), geomorphic (i.e., Altitude, TPI, VD, CI, MRN, and Aspect), hydrologic (TWI, FL_DS, HAND, and DLD), and lithologic parameters (i.e., soil and geology). The new recipe for the integrated bivariate and multivariate managed in providing flood susceptibility maps with high predictive performances over space and time.

In the current study, the flash flood inventory map was generated using high-resolution and active Sentinel-1A SAR scenes and was verified using detailed volunteer geographic information. The radar sensor can effectively penetrate cloud cover to capture data, day or night, via any possible weather conditions—making it the most precise method to extract a flood inundation. Thresholding, with the help of slope filter, of the during flood SAR imagery was able to determine the overall spatial distribution of flood. However, to have additional refinement, the change detection technique has been applied with respect to other pre-flood scenes. It is recommended to explore more segmentation algorithms of SAR images for the auto-extraction of the flood extents in the arid environments to accommodate with different characteristics of the arid watersheds. Additionally, searching for possible future availability of SAR scenes with frequent coverage of flood events in the arid basins is highly recommended for better extraction of flood extents.

The flash flood is a complex physical process that can be highly variable in space and time. Therefore, the findings of the four developed susceptibility models should be studied and integrated thoroughly to ascertain a complete picture of the flood dynamics. I recommend studying different flood future events with different magnitudes to glean more robust information about the spatio-temporal variability of flash floods, in the areas under considerations and, particularly, juxtaposed with the rapidly changing climate.

References

- [1] S. Vorogushyn, K. E. Lindenschmidt, H. Kreibich, H. Apel, and B. Merz, “Analysis of a detention basin impact on dike failure probabilities and flood risk for a channel-dike-floodplain system along the river Elbe, Germany,” *J. Hydrol.*, vol. 436–437, pp. 120–131, May 2012.
- [2] A. P. Schick, T. Grodek, and J. Lekach, “Sediment management and flood protection of desert towns: effects of small catchments,” *Hum. impact Eros. sedimentation. Proc. Int. Symp. Rabat, Morocco, 1997*, vol. 245, pp. 183–189, Jan. 1997.
- [3] B. Merz, J. Hall, M. Disse, and A. Schumann, “Fluvial flood risk management in a changing world,” *Nat. Hazards Earth Syst. Sci.*, vol. 10, no. 3, pp. 509–527, Mar. 2010.
- [4] E. Ghoneim and G. M. Foody, “Assessing flash flood hazard in an arid mountainous region,” *Arab. J. Geosci.*, vol. 6, no. 4, pp. 1191–1202, Sep. 2011.
- [5] A. H. A. Taha, E. H. Ibrahim, A. S. Shalaby, and M. Shawky, “Evaluation of geological hazards for landuse planning in Nabq protectorate, southeastern Sinai using GIS techniques,” *Int. J. Geosci.*, vol. 04, no. 04, pp. 816–836, Jul. 2013.
- [6] A. Milewski *et al.*, “A remote sensing solution for estimating runoff and recharge in arid environments,” *J. Hydrol.*, vol. 373, no. 1–2, pp. 1–14, Jun. 2009.
- [7] J. D. Giraldo Osorio and S. Gabriela García galiano, “Development of a sub-pixel analysis method applied to dynamic monitoring of floods,” *Int. J. Remote Sens.*, vol. 33, no. 7, pp. 2277–2295, Dec. 2012.
- [8] A. D. Regmi, K. Yoshida, M. R. Dhital, and B. Pradhan, “Weathering and

- mineralogical variation in gneissic rocks and their effect in Sangrumba landslide, East Nepal,” *Environ. Earth Sci.*, vol. 71, no. 6, pp. 2711–2727, 2014.
- [9] Y. B. Liu and F. De Smedt, “Flood modeling for complex terrain using GIS and remote sensed information,” *Water Resour. Manag.*, vol. 19, no. 5, pp. 605–624, Oct. 2005.
- [10] J. Mashaly and E. Ghoneim, “Flash Flood Hazard Using Optical, Radar, and Stereo-Pair Derived DEM: Eastern Desert, Egypt,” *Remote Sens.*, vol. 10, no. 8, p. 1204, Aug. 2018.
- [11] S. H. Mahmoud and A. A. Alazba, “Towards a sustainable capital city: an approach for flood management and artificial recharge in naturally water-scarce regions, Central Region of Saudi Arabia,” *Arab. J. Geosci.*, vol. 9, no. 2, p. 92, Jul. 2016.
- [12] A. M. Youssef, B. Pradhan, and S. A. Sefry, “Flash flood susceptibility assessment in Jeddah city (Kingdom of Saudi Arabia) using bivariate and multivariate statistical models,” *Environ. Earth Sci.*, vol. 75, no. 1, p. 12, Dec. 2016.
- [13] A. M. Youssef, S. a. Sefry, B. Pradhan, and E. A. Alfadail, “Analysis on causes of flash flood in Jeddah city (Kingdom of Saudi Arabia) of 2009 and 2011 using multi-sensor remote sensing data and GIS,” *Geomatics, Nat. Hazards Risk*, vol. 5705, no. 3, pp. 1–25, May 2015.
- [14] M. El Maghraby, M. Masoud, and B. Niyazi, “Assessment of surface runoff in arid, data scarce regions; an approach applied in Wadi Al Hamd, Al Madinah Al Munawarah, Saudi Arabia,” *Life Sci. J.*, vol. 11, no. 4, pp. 271–289, Jan. 2014.
- [15] E. Ghoneim, “Optimum groundwater locations in the northern United Arab Emirates,” *Int. J. Remote Sens.*, vol. 29, no. 20, pp. 5879–5906, Oct. 2008.
- [16] J. Cools *et al.*, “An early warning system for flash floods in hyper-arid Egypt,” *Nat. Hazards Earth Syst. Sci.*, vol. 12, no. 2, pp. 443–457, Feb. 2012.

- [17] H. Alhasanat, “Flash Flood Assessment for Wadi Mousa City-Jordan,” *Procedia Econ. Financ.*, vol. 18, pp. 675–683, Dec. 2014.
- [18] Z. Şen *et al.*, “Flash flood inundation map preparation for wadis in arid regions,” *Arab. J. Geosci.*, vol. 6, no. 9, pp. 3563–3572, Jul. 2012.
- [19] G. Al-Rawas and C. Valeo, “Relationship between wadi drainage characteristics and peak-flood flows in arid northern Oman,” *Hydrol. Sci. J.*, vol. 55, no. 3, pp. 377–393, Apr. 2010.
- [20] R. Khatami and G. Mountrakis, “Implications of classification of methodological decisions in flooding analysis from Hurricane Katrina,” *Remote Sens.*, vol. 4, no. 12, pp. 3877–3891, Dec. 2012.
- [21] D. C. Mason, L. Giustarini, J. Garcia-Pintado, and H. L. Cloke, “Detection of flooded urban areas in high resolution Synthetic Aperture Radar images using double scattering,” *Int. J. Appl. Earth Obs. Geoinf.*, vol. 28, pp. 150–159, May 2014.
- [22] T. Bangira, B. H. P. Maathuis, T. Dube, and T. W. Gara, “Investigating flash floods potential areas using ASCAT and TRMM satellites in the Western Cape Province, South Africa,” *Geocarto Int.*, vol. 6049, no. 7, pp. 1–18, Aug. 2015.
- [23] D. D. Konadu and C. Fosu, “Digital elevation models and GIS for watershed modelling and flood prediction – a case study of Accra Ghana,” in *Yanful E.K. (eds) Appropriate Technologies for Environmental Protection in the Developing World*, Springer, Dordrecht, 2009, pp. 325–332.
- [24] S. M. Abuzied and B. M. H. Mansour, “Geospatial hazard modeling for the delineation of flash flood-prone zones in Wadi Dahab basin, Egypt,” *J. Hydroinformatics*, vol. 21, no. 1, pp. 180–206, Feb. 2019.
- [25] M. Abdulrazzak *et al.*, “Flash flood risk assessment in urban arid environment: case study of Taibah and Islamic universities’ campuses, Medina, Kingdom of Saudi

- Arabia,” *Geomatics, Nat. Hazards Risk*, vol. 10, no. 1, pp. 780–796, Jan. 2019.
- [26] E. Opolot, “Application of remote sensing and geographical information systems in flood management : a review,” *Res. J. Appl. Sci. Eng. Technol.*, vol. 6, no. 10, pp. 1884–1894, May 2013.
- [27] S. S. Durduran, “Coastline change assessment on water reservoirs located in the Konya Basin Area, Turkey, using multitemporal landsat imagery,” *Environ. Monit. Assess.*, vol. 164, no. 1–4, pp. 453–461, May 2010.
- [28] B. Pradhan, U. Hagemann, M. Shafapour Tehrany, and N. Prechtel, “An easy to use ArcMap based texture analysis program for extraction of flooded areas from TerraSAR-X satellite image,” *Comput. Geosci.*, vol. 63, pp. 34–43, Feb. 2014.
- [29] K. Auynirundronkool, N. Chen, C. Peng, C. Yang, J. Gong, and C. Silapathong, “Flood detection and mapping of the Thailand Central plain using RADARSAT and MODIS under a sensor web environment,” *Int. J. Appl. Earth Obs. Geoinf.*, vol. 14, no. 1, pp. 245–255, Feb. 2012.
- [30] L. Giustarini *et al.*, “Assimilating SAR-derived water level data into a hydraulic model: A case study,” *Hydrol. Earth Syst. Sci.*, vol. 15, no. 7, pp. 2349–2365, Jul. 2011.
- [31] G. Schumann, G. Di Baldassarre, and P. D. Bates, “The utility of spaceborne radar to render flood inundation maps based on multialgorithm ensembles,” *IEEE Trans. Geosci. Remote Sens.*, vol. 47, no. 8, pp. 2801–2807, Aug. 2009.
- [32] L. Pulvirenti, N. Pierdicca, M. Chini, and L. Guerriero, “An algorithm for operational flood mapping from Synthetic Aperture Radar (SAR) data using fuzzy logic,” *Nat. Hazards Earth Syst. Sci.*, vol. 11, no. 2, pp. 529–540, Feb. 2011.
- [33] G. Di Baldassarre, G. Schumann, L. Brandimarte, and P. Bates, “Timely low resolution SAR imagery to support floodplain modelling: a case study review,” *Surv.*

Geophys., vol. 32, no. 3, pp. 255–269, Jan. 2011.

- [34] B. Revilla-Romero *et al.*, “On the use of global flood forecasts and satellite-derived inundation maps for flood monitoring in data-sparse regions,” *Remote Sens.*, vol. 7, no. 11, pp. 15702–15728, Nov. 2015.
- [35] V. Meyer, S. Scheuer, and D. Haase, “A multicriteria approach for flood risk mapping exemplified at the Mulde river, Germany,” *Nat. Hazards*, vol. 48, no. 1, pp. 17–39, May 2009.
- [36] J. Sanayl and X. Lu, “Application of remote sensing in flood management with special reference to Monsoon Asia: a review,” *Nat. Hazards*, vol. 33, no. 2, pp. 283–301, Oct. 2004.
- [37] USGS, “What is a landslide hazard map?” [Online]. Available: https://www.usgs.gov/faqs/what-a-landslide-hazard-map?qt-news_science_products=0#qt-news_science_products. [Accessed: 07-Nov-2019].
- [38] M. Rahman *et al.*, “Flood susceptibility assessment in Bangladesh using machine learning and multi-criteria decision analysis,” *Earth Syst. Environ.*, vol. 3, no. 3, pp. 1–17, Oct. 2019.
- [39] D. Tien Bui *et al.*, “Flood spatial modeling in Northern Iran using remote sensing and GIS: a comparison between evidential belief functions and its ensemble with a multivariate logistic regression model,” *Remote Sens.*, vol. 11, no. 13, p. 1589, Jul. 2019.
- [40] M. Lee, J. Kang, and S. Jeon, “Application of frequency ratio model and validation for predictive flooded area susceptibility mapping using GIS,” *Ieee Igarss*, no. 1, pp. 895–898, Jul. 2012.
- [41] J. K. Levy, J. Hartmann, K. W. Li, Y. B. An, and A. Asgary, “Multi-criteria decision support systems for flood hazard mitigation and emergency response in urban

- watersheds,” *JAWRA-Journal Am. Water Resour. Assoc.*, vol. 43, no. 2, pp. 346–358, Apr. 2007.
- [42] A. Mukerji, C. Chatterjee, and N. S. Raghuwanshi, “Flood forecasting using ANN, Neuro-Fuzzy, and Neuro-GA models,” *J. Hydrol. Eng.*, vol. 14, no. 6, pp. 647–652, Jun. 2009.
- [43] M. S. Tehrany, B. Pradhan, and M. N. Jebur, “Flood susceptibility mapping using a novel ensemble weights-of-evidence and support vector machine models in GIS,” *J. Hydrol.*, vol. 512, pp. 332–343, May 2014.
- [44] M. Campolo, A. Soldati, and P. Andreussi, “Artificial neural network approach to flood forecasting in the River Arno,” *Hydrol. Sci. Journal-Journal Des Sci. Hydrol.*, vol. 48, no. 3, pp. 381–398, Jun. 2003.
- [45] M. S. Tehrany, B. Pradhan, and M. N. Jebur, “Spatial prediction of flood susceptible areas using rule based decision tree (DT) and a novel ensemble bivariate and multivariate statistical models in GIS,” *J. Hydrol.*, vol. 504, pp. 69–79, Nov. 2013.
- [46] B. Dixon, “Applicability of neuro-fuzzy techniques in predicting ground-water vulnerability: A GIS-based sensitivity analysis,” *J. Hydrol.*, vol. 309, no. 1–4, pp. 17–38, Jan. 2005.
- [47] M. B. Kia, S. Pirasteh, B. Pradhan, A. R. Mahmud, W. N. A. Sulaiman, and A. Moradi, “An artificial neural network model for flood simulation using GIS: Johor River Basin, Malaysia,” *Environ. Earth Sci.*, vol. 67, no. 1, pp. 251–264, Sep. 2012.
- [48] G. P. Zhang, E. B. Patuwo, and H. Michael Y., “Forecasting with artificial neural networks: The state of the art,” *Int. J. Forecast.*, vol. 14, no. 1, pp. 35–62, Mar. 1998.
- [49] A. Tilmant, M. Vanclooster, L. Duckstein, and E. Persoons, “Comparison of fuzzy and nonfuzzy optimal reservoir operating policies,” *J. Water Resour. Plan. Manag.*, vol. 128, no. 6, pp. 390–398, Nov. 2002.

- [50] S. I. Avadhoot and R. J. Deshmukh, "A study of recurrent neural networks based water level forecasting for flood control: case study on Koyana dam," in *Proceedings of International Conference on Computing, Communication and Energy Systems (ICCCES-16) in Association with IET, UK & sponsored by TEQIP-II*, 2016, p. 4.
- [51] Chau, C. L. Wu, and Y. S. Li, "Comparison of several flood forecasting models in Yangtze river," *J. Hydrol. Eng.*, vol. 10, no. 6, pp. 485–491, Oct. 2005.
- [52] A. Sikorska, D. Viviroli, and J. Seibert, "Flood-type classification in mountainous catchments using crisp and fuzzy decision trees," *Water Resour. Res.*, vol. 51, no. 10, pp. 7959–7976, 2015.
- [53] P. Lamvoec, K. Oštir, and M. Mikoš, "Flash floods and peak discharge estimation," in *12th Congress INTERPRAEVENT*, 2012, pp. 201–210.
- [54] C. C. Tsai, M. C. Lu, and C. C. Wei, "Decision tree-based classifier combined with neural-based predictor for water-stage forecasts in a river basin during typhoons: a case study in Taiwan," *Environ. Eng. Sci.*, vol. 29, no. 2, pp. 108–116, Jan. 2012.
- [55] D. Sun, Y. Yu, and M. D. Goldberg, "Deriving water fraction and flood maps from MODIS images using a decision tree approach," *IEEE J. Sel. Top. Appl. Earth Obs. Remote Sens.*, vol. 4, no. 4, pp. 814–825, Dec. 2011.
- [56] M. S. Tehrany, B. Pradhan, S. Mansor, and N. Ahmad, "Flood susceptibility assessment using GIS-based support vector machine model with different kernel types," *Catena*, vol. 125, pp. 91–101, Feb. 2015.
- [57] G. P. Siddayao, S. E. Valdez, and P. L. Fernandez, "Analytic hierarchy process (AHP) in spatial modeling for floodplain risk assessment," *Int. J. Mach. Learn. Comput.*, vol. 4, no. 5, pp. 450–457, Oct. 2014.
- [58] D. S. Fernández and M. A. Lutz, "Urban flood hazard zoning in Tucuman Province, Argentina, using GIS and multicriteria decision analysis," *Eng. Geol.*, vol. 111, no.

1–4, pp. 90–98, Feb. 2010.

- [59] N.-B. Chang, G. Parvathinathan, and J. B. Breeden, “Combining GIS with fuzzy multicriteria decision-making for landfill siting in a fast-growing urban region,” *J. Environ. Manage.*, vol. 87, no. 1, pp. 139–153, Apr. 2008.
- [60] J. A. Benediktsson, P. H. Swain, and O. K. Ersoy, “Neural network approaches versus statistical methods in classification of multisource remote sensing data,” *IEEE Trans. Geosci. Remote Sens.*, vol. 28, no. 4, pp. 540–552, Jul. 1990.
- [61] M. Shafapour Tehrany, F. Shabani, M. Neamah Jebur, H. Hong, W. Chen, and X. Xie, “GIS-based spatial prediction of flood prone areas using standalone frequency ratio, logistic regression, weight of evidence and their ensemble techniques,” *Geomatics, Nat. Hazards Risk*, vol. 8, no. 2, pp. 1538–1561, Dec. 2017.
- [62] M. Scaioni, L. Longoni, V. Melillo, and M. Papini, “Remote sensing for landslide investigations: an overview of recent achievements and perspectives,” *Remote Sens.*, vol. 6, no. 10, pp. 9600–9652, Dec. 2014.
- [63] F. Guzzetti, A. C. Mondini, M. Cardinali, F. Fiorucci, M. Santangelo, and K. T. Chang, “Landslide inventory maps: New tools for an old problem,” *Earth-Science Rev.*, vol. 112, no. 1–2, pp. 42–66, Apr. 2012.
- [64] A. M. Booth, J. J. Roering, and J. T. Perron, “Automated landslide mapping using spectral analysis and high-resolution topographic data: Puget Sound lowlands, Washington, and Portland Hills, Oregon,” *Geomorphology*, vol. 109, no. 3–4, pp. 132–147, Aug. 2009.
- [65] B. D. Malamud, D. L. Turcotte, F. Guzzetti, and P. Reichenbach, “Landslide inventories and their statistical properties,” *Earth Surf. Process. Landforms*, vol. 29, no. 6, pp. 687–711, Jun. 2004.
- [66] P. Guzzetti, F.; Carrara, A.; Cardinali, M. & Reichenbach, “Landslide hazard

- evaluation: a review of current techniques and their application in a multi-scale study, Central Italy,” *Geomorphology*, vol. 31, no. 1–4, pp. 181–216, Dec. 1999.
- [67] R. Soeters and C. van Westen, “Slope instability recognition analysis and zonation,” in *Landslides: Investigation and Mitigation*, Transportation Research Board Special No. 247; Turner, A.K., Schuster, R.L., Eds.; National Academy Press: Washington, DC, USA, 1996, pp. 129–177.
- [68] D. Varnes and I. Commission on landslides and other mass-movements, *Landslide hazard zonation: A review of principles and practice*. The UNESCO Press: Paris, France, 1984.
- [69] H. Fang, P. Cui, L. Z. Pei, and X. J. Zhou, “Model testing on rainfall-induced landslide of loose soil in Wenchuan earthquake region,” *Nat. Hazards Earth Syst. Sci.*, vol. 12, no. 3, pp. 527–533, Mar. 2012.
- [70] F. Ardizzone, M. Cardinali, M. Galli, F. Guzzetti, and P. Reichenbach, “Identification and mapping of recent rainfall-induced landslides using elevation data collected by airborne Lidar,” *Nat. Hazards Earth Syst. Sci.*, vol. 7, no. 6, pp. 637–650, Nov. 2007.
- [71] G. Wang and K. Sassa, “Pore-pressure generation and movement of rainfall-induced landslides: Effects of grain size and fine-particle content,” *Eng. Geol.*, vol. 69, no. 1–2, pp. 109–125, Apr. 2003.
- [72] M. Shafapour Tehrany, L. Kumar, M. Neamah Jebur, and F. Shabani, “Evaluating the application of the statistical index method in flood susceptibility mapping and its comparison with frequency ratio and logistic regression methods,” *Geomatics, Nat. Hazards Risk*, vol. 10, no. 1, pp. 79–101, Jan. 2019.
- [73] M. F. Goodchild, “Citizens as sensors: the world of volunteered geography,” *GeoJournal*, vol. 69, no. 4, pp. 211–221, Nov. 2007.
- [74] J. P. Albuquerque, B. Herfort, A. Brenning, and A. Zipf, “A geographic approach for

- combining social media and authoritative data towards identifying useful information for disaster management,” *Int. J. Geogr. Inf. Sci.*, vol. 29, no. 4, pp. 1–23, Apr. 2015.
- [75] F. E. A. Horita, J. P. de Albuquerque, L. C. Degrossi, E. M. Mendiondo, and J. Ueyama, “Development of a spatial decision support system for flood risk management in Brazil that combines volunteered geographic information with wireless sensor networks,” *Comput. Geosci.*, vol. 80, pp. 84–94, Jul. 2015.
- [76] M. H. Faizal, Z. A. Latiff, and M. A. M. Iskandar, “A study of volunteered geographic information (VGI) assessment methods for flood hazard mapping: a review,” *J. Teknol.*, vol. 75, no. 10, pp. 127–134, Aug. 2015.
- [77] E. Schnebele and G. Cervone, “Improving remote sensing flood assessment using volunteered geographical data,” *Nat. Hazards Earth Syst. Sci.*, vol. 13, no. 3, pp. 669–677, Mar. 2013.
- [78] E. Schnebele, G. Cervone, S. Kumar, and N. Waters, “Real time estimation of the calgary floods using limited remote sensing data,” *Water*, vol. 6, no. 2, pp. 381–398, Mar. 2014.
- [79] M. Erskine and D. G. Gregg, “Utilizing volunteered geographic information to develop a real-time disaster mapping tool : A prototype and research framework,” in *International Conference on Information Resources Management*, 2012, pp. 1–14.
- [80] K. McDougall, “Using volunteered information to map the Queensland floods,” in *Proceedings of the Surveying and Spatial Sciences Conference*, 2011, no. November, pp. 13–23.
- [81] M. S. Tehrany, M.-J. J. Lee, B. Pradhan, M. N. Jebur, and S. Lee, “Flood susceptibility mapping using integrated bivariate and multivariate statistical models,” *Environ. Earth Sci.*, vol. 72, no. 10, pp. 4001–4015, Nov. 2014.
- [82] F. Megdicke-Kharrat, R. Ragala, and M. Moussa, “Mapping land use and dynamics

of vegetation cover in Southeastern Arabia using remote sensing: the study case of Wilayat Nizwa (Oman) from 1987 to 2016,” *Arab. J. Geosci.*, vol. 12, no. 15, p. 450, Aug. 2019.

- [83] F. El-Baz *et al.*, *Wadis of Oman : Satellite Image Atlas*. Stacey International, 2002.
- [84] Environmental Systems Research Institute (ESRI), “World Imagery: DigitalGlobe, GeoEye, i-cubed, USDA FSA, USGS, AEX, Getmapping, Aerogrid, IGN, IGP, swisstopo, and the GIS User Community,” 2018. [Online]. Available: <https://www.arcgis.com/home/item.html?id=10df2279f9684e4a9f6a7f08febac2a9>. [Accessed: 04-Jan-2019].
- [85] FloodList, “Oman and UAE – Deadly Floods Hit After Torrential Rain – FloodList,” 2017. [Online]. Available: <http://floodlist.com/asia/oman-uae-floods-december-2017>. [Accessed: 10-Jan-2018].
- [86] R. Torres *et al.*, “GMES Sentinel-1 mission,” *Remote Sens. Environ.*, vol. 120, pp. 9–24, May 2012.
- [87] “Copernicus Sentinel Data,” 2019. [Online]. Available: Retrieved from ASF DAAC September 2019, processed by ESA.
- [88] C. Cazals *et al.*, “Mapping and characterization of hydrological dynamics in a coastal marsh using high temporal resolution Sentinel-1A images,” *Remote Sens.*, vol. 8, no. 7, p. 570, Jul. 2016.
- [89] “Sentinel-1 - Mission Summary - Sentinel Online.” [Online]. Available: <https://sentinel.esa.int/web/sentinel/missions/sentinel-1/overview/mission-summary>. [Accessed: 27-Oct-2019].
- [90] F. Filipponi, “Sentinel-1 GRD Preprocessing Workflow,” *Proceedings*, vol. 18, no. 1, p. 11, Jun. 2019.

- [91] “User Guides - Sentinel-1 SAR - Level-1 Ground Range Detected - Sentinel Online.” [Online]. Available: <https://sentinel.esa.int/web/sentinel/user-guides/sentinel-1-sar/resolutions/level-1-ground-range-detected>. [Accessed: 27-Oct-2019].
- [92] W. Huang *et al.*, “Automated extraction of surface water extent from Sentinel-1 data,” *Remote Sens.*, vol. 10, no. 5, p. 797, May 2018.
- [93] A. Whyte, K. P. Ferentinos, and G. P. Petropoulos, “A new synergistic approach for monitoring wetlands using Sentinels -1 and 2 data with object-based machine learning algorithms,” *Environ. Model. Softw.*, vol. 104, pp. 40–54, Jun. 2018.
- [94] J. Haas and Y. Ban, “Sentinel-1A SAR and sentinel-2A MSI data fusion for urban ecosystem service mapping,” *Remote Sens. Appl. Soc. Environ.*, vol. 8, pp. 41–53, Nov. 2017.
- [95] M. De Smith, M. F. Goodchild, and P. a Longley, *Geospatial analysis to principles, techniques and software tools*, 5th ed. Winchelsea Press, Winchelsea, UK Acknowledgements, 2015.
- [96] M. Shawky, A. Moussa, Q. K. Hassan, and N. El-Sheimy, “Pixel-based geometric assessment of channel networks/orders derived from global spaceborne digital elevation models,” *Remote Sens.*, vol. 11, no. 3, p. 235, Jan. 2019.
- [97] J. Laurencelle, T. Logan, and R. Gens, “Alaska Satellite Facility (ASF) - Radiometrically terrain corrected ALOS PALSAR products,” 2015.
- [98] T. Ushio *et al.*, “A Kalman filter approach to the global satellite mapping of precipitation (GSMaP) from combined passive microwave and infrared radiometric data,” *J. Meteorol. Soc. Japan*, vol. 87A, pp. 137–151, Mar. 2009.
- [99] K. Aonashi *et al.*, “GSMaP passive microwave precipitation retrieval algorithm: Algorithm description and validation,” *J. Meteorol. Soc. Japan*, vol. 87A, pp. 119–136, Mar. 2009.

- [100] T. Kubota *et al.*, “Global precipitation map Using satellite-borne microwave radiometers by the GSMAp project: production and validation,” *IEEE Trans. Geosci. Remote Sens.*, vol. 45, no. 7, pp. 2259–2275, Jul. 2007.
- [101] Ministry of Petroleum and Minerals – Directorate General of Minerals, “Geological Map of Oman – Nizwa – Sheet NF40-07 – Scale 1:250,000.” Geological Mapping By R. Wyns, F. Béchenec, , S. Chevrel, J. Le. Métour and J. Roger. Compiled in 1991 by R. Wyns and F. Béchenec. Computer assisted cartography and printing by Cartography Depratment BRGM-Orléans-France, 1992.
- [102] Ministry of Petroleum and Minerals – Directorate General of Minerals, “Geological Map Of Oman – Scale 1:1000,000.” Geological Mapping By J. Le. Métour, J.-P. Platel, F. Béchenec, A. Berthiaux, S. Chevrel, J. Dubreuilh, J. Roger, And R. Wyns (1993). Compiled in 1993 by J. Le. Métour and J.-P. Platel. The cartography was done in the Service Édition Cartographique of the BRGM Département Cartes-France, 1993.
- [103] “SNAP Software, Brockmann Consult, Array Systems Computing and C-S.” [Online]. Available: <https://step.esa.int/main/toolboxes/snap/>.
- [104] “Copernicus Sentinel-1A data [2017]. Retrieved from ASF DAAC [2019], processed by ESA.” .
- [105] M. A. Clement, C. G. Kilsby, and P. Moore, “Multi-temporal synthetic aperture radar flood mapping using change detection,” *J. Flood Risk Manag.*, vol. 11, no. 2, pp. 152–168, Jun. 2018.
- [106] A. Twele, W. Cao, S. Plank, and S. Martinis, “Sentinel-1-based flood mapping: a fully automated processing chain,” *Int. J. Remote Sens.*, vol. 37, no. 13, pp. 2990–3004, Jul. 2016.
- [107] J. S. Lee, I. Jurkevich, P. Dewaele, P. Wambacq, and A. Oosterlinck, “Speckle

- filtering of synthetic aperture radar images: a review,” *Remote Sens. Rev.*, vol. 8, no. 4, pp. 313–340, Feb. 1994.
- [108] L. Giustarini *et al.*, “Accounting for image uncertainty in SAR-based flood mapping,” *Int. J. Appl. Earth Obs. Geoinf.*, vol. 34, pp. 70–77, Feb. 2015.
- [109] T. Esch, A. Schenk, T. Ullmann, M. Thiel, A. Roth, and S. Dech, “Characterization of land cover types in TerraSAR-X images by combined analysis of speckle statistics and intensity information,” *IEEE Trans. Geosci. Remote Sens.*, vol. 49, no. 6 PART 1, pp. 1911–1925, Jun. 2011.
- [110] F. Bioresita, A. Puissant, A. Stumpf, and J.-P. Malet, “A method for automatic and rapid mapping of water surfaces from Sentinel-1 imagery,” *Remote Sens.*, vol. 10, no. 2, p. 217, Feb. 2018.
- [111] SNAP_Software, “Science toolbox exploitation platform-European Space Agency (ESA).” [Online]. Available: <https://step.esa.int/main/toolboxes/snap/>. [Accessed: 04-Jan-2020].
- [112] Y.-S. Song, H.-G. Sohn, and C.-H. Park, “Efficient water area classification using Radarsat-1 SAR imagery in a high relief mountainous environment,” *Photogramm. Eng. Remote Sens.*, vol. 73, no. 3, pp. 285–296, Mar. 2007.
- [113] N. Kussul, A. Shelestov, and S. Skakun, “Grid system for flood extent extraction from satellite images,” *Earth Sci. Informatics*, vol. 1, no. 3–4, pp. 105–117, Nov. 2008.
- [114] K. Uddin, M. A. Matin, and F. J. Meyer, “Operational flood mapping using multi-temporal Sentinel-1 SAR images: A case study from Bangladesh,” *Remote Sens.*, vol. 11, no. 13, p. 1581, Jul. 2019.
- [115] P. Matgen, R. Hostache, G. Schumann, L. Pfister, L. Hoffmann, and H. H. G. Savenije, “Towards an automated SAR-based flood monitoring system: Lessons learned from two case studies,” *Phys. Chem. Earth, Parts A/B/C*, vol. 36, no. 7–8, pp.

241–252, Jan. 2011.

- [116] S. Martinis, S. Plank, and K. Ćwik, “The use of Sentinel-1 time-series data to improve flood monitoring in arid areas,” *Remote Sens.*, vol. 10, no. 4, p. 583, Apr. 2018.
- [117] L. Giustarini, R. Hostache, P. Matgen, G. J.-P. Schumann, P. D. Bates, and D. C. Mason, “A change detection approach to flood mapping in urban areas using TerraSAR-X,” *IEEE Trans. Geosci. Remote Sens.*, vol. 51, no. 4, pp. 2417–2430, Apr. 2013.
- [118] X. Shen, E. N. Anagnostou, G. H. Allen, G. Robert Brakenridge, and A. J. Kettner, “Near-real-time non-obstructed flood inundation mapping using synthetic aperture radar,” *Remote Sens. Environ.*, vol. 221, pp. 302–315, Feb. 2019.
- [119] S. Martinis, “Automatic near real-time flood detection in high resolution X-band synthetic aperture radar satellite data using context-based classification on irregular graphs,” der Fakultät für Geowissenschaften-der Ludwig-Maximilians-Universität München, 2010.
- [120] G. J.-P. Schumann and D. K. Moller, “Microwave remote sensing of flood inundation,” *Phys. Chem. Earth, Parts A/B/C*, vol. 83–84, pp. 84–95, Jan. 2015.
- [121] S. Long, T. E. Fatoyinbo, and F. Policelli, “Flood extent mapping for Namibia using change detection and thresholding with SAR,” *Environ. Res. Lett.*, vol. 9, no. 3, p. 035002, Mar. 2014.
- [122] L. L. Hess, J. M. Melack, and D. S. Simonett, “Radar detection of flooding beneath the forest canopy: A review,” *Int. J. Remote Sens.*, vol. 11, no. 7, pp. 1313–1325, Jul. 1990.
- [123] J. P. Ford, J. B. Cimino, and C. Elachi, “Space Shuttle Columbia Views the World W&h Imaging Radar: the SIR-A Experiment: Jet Propulsion Lab., California Inst. of Tech.; Pasadena, CA, United States, NASA-CR-169932, JPL-PUB-82-95, NAS

1.26:169932,” California, 1983.

- [124] N. Otsu, “A threshold selection method from gray-level histograms,” *IEEE Trans. Syst.*, vol. 9, pp. 62–66, 1979.
- [125] J. L. Fan and B. Lei, “A modified valley-emphasis method for automatic thresholding,” *Pattern Recognit. Lett.*, vol. 33, no. 6, pp. 703–708, Apr. 2012.
- [126] P. Nakmuenwai, F. Yamazaki, and W. Liu, “Automated extraction of inundated areas from multi-temporal dual-polarization RADARSAT-2 images of the 2011 Central Thailand flood,” *Remote Sens.*, vol. 9, no. 1, p. 78, Jan. 2017.
- [127] M. T. N. Truong and S. Kim, “Automatic image thresholding using Otsu’s method and entropy weighting scheme for surface defect detection,” *Soft Comput.*, vol. 22, no. 13, pp. 4197–4203, Jul. 2018.
- [128] M. T. N. Truong and S. Kim, “GitHub - mtntuong/entropy-otsu: MATLAB code and data for the article ‘DOI:10.1007/s00500-017-2709-1.’” [Online]. Available: <https://github.com/mtntuong/entropy-otsu>. [Accessed: 11-Jan-2020].
- [129] X. Shen, D. Wang, K. Mao, E. Anagnostou, and Y. Hong, “Inundation extent mapping by synthetic aperture Radar: A review,” *Remote Sens.*, vol. 11, no. 7, p. 879, Apr. 2019.
- [130] L. Landuyt, A. Van Wesemael, G. J.-P. Schumann, R. Hostache, N. E. C. Verhoest, and F. M. B. Van Coillie, “Flood mapping based on Synthetic Aperture Radar: An assessment of established approaches,” *IEEE Trans. Geosci. Remote Sens.*, vol. 57, no. 2, pp. 722–739, Feb. 2019.
- [131] Sabalet Oman, “Department of Photo Reports Archive/” أرشيف قسم التقارير المصورة, ٢٠٢٠. [Online]. Available: <https://avb.s-oman.net/forumdisplay.php?f=290&s=8ce811aed4d13d3cb905f7b6da9c3597>. [Accessed: 05-Jan-2020].

- [132] K. Cwik, “Flood Mapping with the Sentinel-1 Time-Series Data in Arid Areas,” Technical University of Munich, 2017.
- [133] M. C. Popa, D. Peptenatu, C. C. Drăghici, and D. C. Diaconu, “Flood hazard mapping using the flood and flash-flood potential index in the Buzău River Catchment, Romania,” *Water*, vol. 11, no. 10, p. 2116, Oct. 2019.
- [134] Y. Wang *et al.*, “A hybrid GIS multi-criteria decision-making method for flood susceptibility mapping at Shangyou, China,” *Remote Sens.*, vol. 11, no. 1, p. 62, Dec. 2018.
- [135] F. Altaf, G. Meraj, and S. A. Romshoo, “Morphometric analysis to infer hydrological behavior of Lidder watershed, western Himalaya, India,” *Geogr. J.*, vol. 2013, p. 14, Apr. 2013.
- [136] L. P. Perucca and Y. E. Angilieri, “Morphometric characterization of del Molle Basin applied to the evaluation of flash floods hazard, Iglesia Department, San Juan, Argentina,” *Quat. Int.*, vol. 233, no. 1, pp. 81–86, Mar. 2011.
- [137] G. Kabite and B. Gessesse, “Hydro-geomorphological characterization of Dhidhessa River Basin, Ethiopia,” *Int. Soil Water Conserv. Res.*, vol. 6, no. 2, pp. 175–183, Jun. 2018.
- [138] S. H. Mahmoud and A. A. Alazba, “Hydrological response to land cover changes and human activities in arid regions using a geographic information system and remote sensing,” *PLoS One*, vol. 10, no. 4, pp. 1–19, Apr. 2015.
- [139] Environmental Systems Research Institute (ESRI), “Classifying numerical fields for graduated symbology—Help | ArcGIS for Desktop.” [Online]. Available: <https://desktop.arcgis.com/en/arcmap/10.3/map/working-with-layers/classifying-numerical-fields-for-graduated-symbols.htm>. [Accessed: 03-Jan-2020].
- [140] C. Cao, P. Xu, Y. Wang, J. Chen, L. Zheng, and C. Niu, “Flash flood hazard

susceptibility mapping using frequency ratio and statistical index methods in coalmine subsidence areas,” *Sustain.*, vol. 8, no. 9, p. 948, Sep. 2016.

- [141] E. Hasan, T. Fagin, Z. El Alfy, and Y. Hong, “Spectral angle mapper and aeromagnetic data integration for gold-associated alteration zone mapping: a case study for the Central Eastern Desert Egypt,” *Int. J. Remote Sens.*, vol. 37, no. 8, pp. 1762–1776, Apr. 2016.
- [142] X. Chen, T. A. Warner, and D. J. Campagna, “Integrating visible, near-infrared and short-wave infrared hyperspectral and multispectral thermal imagery for geological mapping at Cuprite, Nevada,” *Remote Sens. Environ.*, vol. 110, no. 3, pp. 344–356, Oct. 2007.
- [143] W. Ge, Q. Cheng, Y. Tang, L. Jing, and C. Gao, “Lithological classification using Sentinel-2A data in the Shibanjing Ophiolite Complex in Inner Mongolia, China,” *Remote Sens.*, vol. 10, no. 4, p. 638, Apr. 2018.
- [144] A. J. Scott and M. J. Symons, “Clustering methods based on likelihood ratio criteria,” *Biometrics*, vol. 27, no. 2, p. 387, Jun. 1971.
- [145] The Ministry of Agriculture and Fisheries (MAF) of Oman, (FAO), and (UNDP), “MAF.pdf,” The Oman Soil Atlas. UNDP/FAO Project OMA/87/011 Soil Survey and Land Classification., 1992.
- [146] C. D. Rennó *et al.*, “HAND, a new terrain descriptor using SRTM-DEM: Mapping terra-firme rainforest environments in Amazonia,” *Remote Sens. Environ.*, vol. 112, no. 9, pp. 3469–3481, Sep. 2008.
- [147] A. D. Nobre *et al.*, “Height Above the Nearest Drainage – a hydrologically relevant new terrain model,” *J. Hydrol.*, vol. 404, no. 1–2, pp. 13–29, Jun. 2011.
- [148] A. D. Nobre, L. A. Cuartas, M. R. Momo, D. L. Severo, A. Pinheiro, and C. A. Nobre, “HAND contour: a new proxy predictor of inundation extent,” *Hydrol. Process.*, vol.

30, no. 2, pp. 320–333, Jan. 2016.

- [149] E. H. Sutanudjaja, S. M. de Jong, F. C. van Geer, and M. F. P. Bierkens, “Using ERS spaceborne microwave soil moisture observations to predict groundwater head in space and time,” *Remote Sens. Environ.*, vol. 138, pp. 172–188, Nov. 2013.
- [150] I. Papageorgaki and I. Nalbantis, “Classification of drainage basins based on readily available information,” *Water Resour. Manag.*, vol. 30, no. 15, pp. 5559–5574, Dec. 2016.
- [151] S. Owusu, M. L. Mul, B. Ghansah, P. K. Osei-Owusu, V. Awotwe-Pratt, and D. Kadyampakeni, “Assessing land suitability for aquifer storage and recharge in northern Ghana using remote sensing and GIS multi-criteria decision analysis technique,” *Model. Earth Syst. Environ.*, vol. 3, no. 4, pp. 1383–1393, Dec. 2017.
- [152] O. Rahmati, A. Kornejady, M. Samadi, A. D. Nobre, and A. M. Melesse, “Development of an automated GIS tool for reproducing the HAND terrain model,” *Environ. Model. Softw.*, vol. 102, pp. 1–12, Apr. 2018.
- [153] N. Hamdani and A. Baali, “Height Above Nearest Drainage (HAND) model coupled with lineament mapping for delineating groundwater potential areas (GPA),” *Groundw. Sustain. Dev.*, vol. 9, p. 100256, Oct. 2019.
- [154] S. Schlaffer, P. Matgen, M. Hollaus, and W. Wagner, “Flood detection from multi-temporal SAR data using harmonic analysis and change detection,” *Int. J. Appl. Earth Obs. Geoinf.*, vol. 38, pp. 15–24, Jun. 2015.
- [155] C. M. Bhatt, G. S. Rao, P. G. Diwakar, and V. K. Dadhwal, “Development of flood inundation extent libraries over a range of potential flood levels: a practical framework for quick flood response,” *Geomatics, Nat. Hazards Risk*, vol. 8, no. 2, pp. 384–401, Nov. 2017.
- [156] V. K. Sharma, G. S. Rao, C. M. Bhatt, A. K. Shukla, A. K. Mishra, and V.

- Bhanumurthy, “Automatic procedures analyzing remote sensing data to minimize flood response time: a step towards National flood mapping service,” *Spat. Inf. Res.*, vol. 25, no. 5, pp. 657–663, Oct. 2017.
- [157] C. Huang, B. D. Nguyen, S. Zhang, S. Cao, and W. Wagner, “A Comparison of terrain indices toward their ability in assisting surface water mapping from Sentinel-1 data,” *ISPRS Int. J. Geo-Information*, vol. 6, no. 5, p. 140, Apr. 2017.
- [158] S. Rosim, J. R. de Freitas Oliveira, J. de Oliveira Ortiz, M. Z. Cuellar, and A. C. Jardim, “Drainage network extraction of Brazilian semiarid region with potential flood indication areas,” in *Proc. SPIE 9239, Remote Sensing for Agriculture, Ecosystems, and Hydrology XVI, 923919*, 2014, pp. 923919-923919–9.
- [159] M. A. Melton, “The geomorphic and paleoclimatic significance of alluvial deposits in Southern Arizona,” *J. Geol.*, vol. 73, no. 1, pp. 1–38, Jan. 1965.
- [160] O. Conrad *et al.*, “System for Automated Geoscientific Analyses (SAGA) v. 2.1.4,” *Geosci. Model Dev.*, vol. 8, no. 7, pp. 1991–2007, Jul. 2015.
- [161] L. Marchi and G. Dalla Fontana, “GIS morphometric indicators for the analysis of sediment dynamics in mountain basins,” *Environ. Geol.*, vol. 48, no. 2, pp. 218–228, Jul. 2005.
- [162] B. W. Silverman, *Density estimation for statistics and data analysis*. Chapman and Hall, 1986.
- [163] A. Guisan, S. B. Weiss, and A. D. Weiss, “GLM versus CCA spatial modeling of plant species distribution,” *Plant Ecol.*, vol. 143, no. 1, pp. 107–122, Jul. 1999.
- [164] J. P. Wilson and J. C. Gallant, *Terrain analysis : principles and applications*. Wiley, 2000.
- [165] J. De Reu *et al.*, “Application of the topographic position index to heterogeneous

- landscapes,” *Geomorphology*, vol. 186, pp. 39–49, Mar. 2013.
- [166] P. A. Burrough and R. A. Mcdonnell, *Principles of Geographical Information Systems*. New York: Oxford University Press, 1998.
- [167] M. Ma *et al.*, “Flash flood risk analysis based on machine learning techniques in the Yunnan Province, China in Advances in Geomorphology and Quaternary Studies in Argentina,” *Remote Sens.*, vol. 11, no. 2, p. 170, Jan. 2019.
- [168] M. W. Raduła, T. H. Szymura, and M. Szymura, “Topographic wetness index explains soil moisture better than bioindication with Ellenberg’s indicator values,” *Ecol. Indic.*, vol. 85, pp. 172–179, Feb. 2018.
- [169] K. J. Beven and M. J. Kirkby, “A physically based, variable contributing area model of basin hydrology / Un modèle à base physique de zone d’appel variable de l’hydrologie du bassin versant,” *Hydrol. Sci. Bull.*, vol. 24, no. 1, pp. 43–69, Mar. 1979.
- [170] C. Gokceoglu, H. Sonmez, H. A. Nefeslioglu, T. Y. Duman, and T. Can, “The 17 March 2005 Kuzulu landslide (Sivas, Turkey) and landslide-susceptibility map of its near vicinity,” *Eng. Geol.*, vol. 81, no. 1, pp. 65–83, Sep. 2005.
- [171] C.-Z. Qin *et al.*, “An approach to computing topographic wetness index based on maximum downslope gradient,” *Precis. Agric.*, vol. 12, no. 1, pp. 32–43, Feb. 2011.
- [172] R. Costache and L. Zaharia, “Flash-flood potential assessment and mapping by integrating the weights-of-evidence and frequency ratio statistical methods in GIS environment – Case study: Bâsca chiojdului river catchment (Romania),” *J. Earth Syst. Sci.*, vol. 126, no. 4, pp. 1–19, Jun. 2017.
- [173] X. Zhu, *GIS for environmental applications : a practical approach*. Abingdon, Oxon ; New York, NY: Routledge, 2016.

- [174] H. R. Pourghasemi and M. Beheshtirad, "Assessment of a data-driven evidential belief function model and GIS for groundwater potential mapping in the Koohrang Watershed, Iran," *Geocarto Int.*, vol. 30, no. 6, pp. 662–685, Jul. 2015.
- [175] A. Jaafari, D. M. Gholami, and E. K. Zenner, "A Bayesian modeling of wildfire probability in the Zagros Mountains, Iran," *Ecol. Inform.*, vol. 39, pp. 32–44, May 2017.
- [176] R. M. O'Brien, "A caution regarding rules of thumb for variance inflation factors," *Qual. Quant.*, vol. 41, no. 5, pp. 673–690, Oct. 2007.
- [177] C. Van Westen, "Statistical landslide hazard analysis," Enschede, The Netherlands., 1997.
- [178] S. Mandal and K. Mandal, "Bivariate statistical index for landslide susceptibility mapping in the Rorachu river basin of eastern Sikkim Himalaya, India," *Spat. Inf. Res.*, vol. 26, no. 1, pp. 59–75, Feb. 2018.
- [179] O. F. Althuwaynee, B. Pradhan, H. J. Park, and J. H. Lee, "A novel ensemble bivariate statistical evidential belief function with knowledge-based analytical hierarchy process and multivariate statistical logistic regression for landslide susceptibility mapping," *Catena*, vol. 114, pp. 21–36, Mar. 2014.
- [180] A. Jaafari, D. Mafi-Gholami, B. Thai Pham, and D. Tien Bui, "Wildfire probability mapping: Bivariate vs. multivariate statistics," *Remote Sens.*, vol. 11, no. 6, p. 618, Mar. 2019.
- [181] L. Ayalew and H. Yamagishi, "The application of GIS-based logistic regression for landslide susceptibility mapping in the Kakuda-Yahiko Mountains, Central Japan," *Geomorphology*, vol. 65, no. 1–2, pp. 15–31, Feb. 2005.
- [182] S. Lee, "Application of logistic regression model and its validation for landslide susceptibility mapping using GIS and remote sensing data," *Int. J. Remote Sens.*, vol.

26, no. 7, pp. 1477–1491, Apr. 2005.

- [183] H. R. Pourghasemi, H. R. Moradi, and S. M. Fatemi Aghda, “Landslide susceptibility mapping by binary logistic regression, analytical hierarchy process, and statistical index models and assessment of their performances,” *Nat. Hazards*, vol. 69, no. 1, pp. 749–779, May 2013.
- [184] I. Mierswa, “Lightning Fast Data Science Platform for Teams | RapidMiner®.” [Online]. Available: <https://rapidminer.com/>. [Accessed: 16-Jan-2020].
- [185] R. G. Congalton, R. G. Oderwald, and R. A. Mead, “Assessing Landsat classification accuracy using discrete multivariate analysis statistical techniques,” *Photogramm. Eng. Remote Sensing*, vol. 49, no. No. 12, pp. 1671–1678, Dec. 1983.
- [186] M. Story and R. G. Congalton, “Remote sensing brief accuracy assessment: a user’s perspective,” *Photogramm. Eng. Remote Sensing*, vol. 52, no. 3, pp. 397–399, Mar. 1986.
- [187] O. Rozenstein and A. Karnieli, “Comparison of methods for land-use classification incorporating remote sensing and GIS inputs,” *Appl. Geogr.*, vol. 31, no. 2, pp. 533–544, Apr. 2011.
- [188] J. Radoux and P. Bogaert, “Good practices for object-based accuracy assessment,” *Remote Sens.*, vol. 9, no. 7, p. 646, Jun. 2017.
- [189] Z. Ao, Y. Su, W. Li, Q. Guo, and J. Zhang, “One-class classification of airborne LiDAR data in urban areas using a presence and background learning algorithm,” *Remote Sens.*, vol. 9, no. 10, p. 1001, Sep. 2017.
- [190] L. Cai, W. Shi, Z. Miao, and M. Hao, “Accuracy assessment measures for object extraction from remote sensing images,” *Remote Sens.*, vol. 10, no. 2, p. 303, Feb. 2018.

- [191] S. V. Stehman, "Selecting and interpreting measures of thematic classification accuracy," *Remote Sens. Environ.*, vol. 62, no. 1, pp. 77–89, Oct. 1997.
- [192] P.-N. Tan, M. Steinbach, and V. Kumar, *Introduction to data mining*. Pearson Addison Wesley, 2005.
- [193] K. M. Ting, "Sensitivity and Specificity," in *Encyclopedia of Machine Learning*, Boston, MA: Springer US, 2011, pp. 901–902.
- [194] J. Cohen, "A Coefficient of agreement for nominal scales," *Educ. Psychol. Meas.*, vol. 20, no. 1, pp. 37–46, Apr. 1960.
- [195] H. Nampak, B. Pradhan, and M. A. Manap, "Application of GIS based data driven evidential belief function model to predict groundwater potential zonation," *J. Hydrol.*, vol. 513, pp. 283–300, May 2014.
- [196] C. J. F. Chung and A. G. Fabbri, "Validation of spatial prediction models for landslide hazard mapping," *Nat. Hazards*, vol. 30, no. 3, pp. 451–472, Nov. 2003.
- [197] Rahmati *et al.*, "Urban flood hazard modeling using self-organizing map neural network," *Water*, vol. 11, no. 11, p. 2370, Nov. 2019.
- [198] Y. Li and W. Chen, "Landslide susceptibility evaluation using hybrid integration of evidential belief function and machine learning techniques," *Water*, vol. 12, no. 1, p. 113, Dec. 2019.
- [199] S. Lee, "Landslide susceptibility mapping using an artificial neural network in the Gangneung are, Korea," *Int. J. Remote Sens.*, vol. 28, no. 21, pp. 4763–4783, Nov. 2007.
- [200] Minitab, "Coefficients for Binary Logistic Regression - Minitab Express." [Online]. Available: <https://support.minitab.com/en-us/minitab-express/1/help-and-how-to/modeling-statistics/regression/how-to/binary-logistic-regression/interpret-the->

results/all-statistics-and-graphs/coefficients/. [Accessed: 05-Jan-2020].

- [201] M. L. McHugh, "Interrater reliability: The kappa statistic," *Biochem. Medica*, vol. 22, no. 3, pp. 276–282, Oct. 2012.
- [202] K. Khosravi, H. R. Pourghasemi, K. Chapi, and M. Bahri, "Flash flood susceptibility analysis and its mapping using different bivariate models in Iran: a comparison between Shannon's entropy, statistical index, and weighting factor models," *Environ. Monit. Assess.*, vol. 188, no. 12, p. 656, Dec. 2016.
- [203] S. H. Mahmoud and T. Y. Gan, "Multi-criteria approach to develop flood susceptibility maps in arid regions of Middle East," *J. Clean. Prod.*, vol. 196, pp. 216–229, Jun. 2018.

CHAPTER FIVE

CONCLUSIONS AND RECOMMENDATIONS

5.1. Concluding Remarks

This section sums up the concluding remarks for every objective.

Objective 1 (Chapter 2):

In this component, the performance of five sub-daily and daily global satellite precipitation estimates (GSPEs) (i.e., Global Precipitation Mission-Integrated Multi-satellitE Retrievals for the GPM (GPM-IMERG), and Global Satellite Mapping of Precipitation (GSMaP)) was evaluated using the in-situ rain gauge measurements between March 2014 and December 2016. A set of continuous difference statistical indices (e.g., mean absolute difference, root mean square error, mean difference, and unconditional bias), and categorical metrics (e.g., probability of detection, critical success index, false alarm ratio, and frequency bias index) were utilized to evaluate recorded precipitation occurrences in . To my best knowledge, there were no previous detailed studies concerning evaluating different GSPEs, particularly at sub-daily time scales and local spatial details over this extremely arid part of the world. The findings showed that the five GSPEs could generally capture the spatial and temporal patterns of rainfall of in-situ gauge measurements at different precipitation intensities. The overall quality of the GSMaP runs outperformed the IMERG products. IMERG-F was slightly superior to the IMERG-E and IMERG-L. In addition, the additive and multiplicative error models were used to quantify the uncertainties associated with five daily GSPEs. The additive scheme was slightly more effective than the multiplicative approach in modeling the errors in the GSPEs at different rainfall intensity classes. Based on the achieved findings, and with the difficulties in having continuous rainfall records from in-situ gauge networks, it is recommended that researchers focus on the arid areas to consider assessing and using the available GSPEs in their hydrological studies such as flood susceptibility modeling.

Objective 2 (Chapter 3):

The scope of the second objective was to select the digital terrain model (DTM) and its derived channel network/orders with the highest accuracy in order to extract the required spatial geomorphic, hydrologic, and topographic layers necessary for flood susceptibility modeling. Therefore, a pixel-based method was developed for the quantitative horizontal evaluation of the channel networks and Strahler orders derived from global digital elevation models (DEMs) utilizing confusion matrices at different flow accumulation area thresholds (ATs) and pixel buffer tolerance values (PBTVs). The horizontal displacements between the extracted channels were quantified using drainage network/order-derived light detection and ranging (LiDAR) datasets. Additionally, the pixel-based vertical elevation accuracies of the three global DEMs (i.e., Advanced Land Observing Satellite (ALOS) Phased Array type L-band Synthetic Aperture Radar (PALSAR) 12.5 and 28.5 m, Shuttle Radar Topography Mission (SRTM) 28.5 m, and ALOS Panchromatic Remote-sensing Instrument for Stereo Mapping (PRISM) 28.5 m) were assessed using traditional statistical metrics. The outcomes demonstrated that PALSAR DTM 12.5 m and its drainage networks had the highest vertical and horizontal accuracies. Therefore, these datasets were used in the next objective to derive various geospatial layers required for generating flood potential maps. It is recommended that other researchers evaluate DEMs and their derived channel networks/orders prior to involving them in their geomorphological and hydrological studies. Additionally, it is suggested to use the developed method with respect to globally diverse areas comprising different land covers, geomorphic units, lithology, and climatic zones.

Objective 3 (Chapter 4):

In this part, improved individual bivariate and integrated bivariate and multivariate statistical methods-based flood susceptibility models were developed to detect flood-prone areas at the watershed scale (12.5 m). The input data of these models were the pre-evaluated satellite precipitation from the first objective and other variables extracted from the DEM and drainage network of choice in the second objective (i.e., PALSAR DTM), as well as soil and geologic maps. This objective had the following sub-tasks: (i) generating flood

inundation (i.e., inventory map) from Sentinel-1A SAR images, with the help of the volunteer geographic information (VGI), (ii) making a vectorized soil map from original data obtained from Ministry of Agriculture, Sultanate of Oman, (iii) preparing a geologic map for the area of study using Landsat-8 and geologic maps with a fine spatial resolution based on an effective and straightforward technique, (iv) deriving many geospatial flood controlling factors (i.e., geomorphic, topographic, and hydrologic features) from PALSAR DEM (12.5 m) and its derived channel network, and (v) comparing the findings of the different flood susceptibility models to depict the model with the top performance. The developed models included applying spatio-temporal flood details through involving a rainfall event matched with a specific flood event. Using SAR-based flood inundation mapping allowed the selection of spatially distributed and stratified flood and non-flood points among the entire area of study for training and testing the models. Furthermore, the chosen new combination of the flood triggering factors was proven to be successful in detecting flood-prone high- and low-land areas.

5.2. Research Outcomes (Contributions)

In-depth application of actual scientific research related to flash floods in the Arabian Peninsula was critical to understanding and mitigating flash floods' impacts on human life and infrastructure in this extremely arid area of the world. Given the complexity and challenges involved in studying flash flooding, known to be one of the most complex physical systems, listed below are the summarized contributions of the current research:

- 1) with the rapidly changing global climate, the developed flood susceptibility models can contribute to mitigating negative impacts of flooding by providing accurate information about their future extent probabilities at a rainfall intensity similar to that prevailed during the past flood event. These developments can help administrators and local settlers avoid the negative consequences of flash floods by providing reasonable information about flood extent at a fine spatial resolution (12.5 m). The introduced susceptibility models demonstrated a significant potential of the integrated bivariate and multivariate statistical methods for operational prediction and classification of flood hazard levels.

- 2) the outcomes of the validation different recent GSPEs' releases can contribute to having continuous and reliable rainfall records that can significantly support studies of future flash floods. To the best of my understanding, the current research introduced the first detailed assessment of sub-daily and daily GSPEs over the watershed scale in the Arabian Peninsula. The achieved findings can overcome the limited availability and coverage of the in-situ rain gauges in the arid areas. It will improve the time factor in predicting the flood extent. Modeling the errors in the GSPEs using the statistical error approaches can help to improve the results of different hydrological applications. The satellite precipitation records can contribute to many hydrogeologic, climatic, and surface- and ground-water resource management in the arid regions. The validation of five continuous sub-daily and daily GSPEs with different time latencies will allow incorporating them among various hydrological models, depending on the type of application and required temporal

resolution (i.e., real-time or near-real-time). It is possible to use the GSPEs for flood studies not only in the selected area of study but also in other remote areas of similar climatic and topographic conditions to the current study watershed.

- 3) the developed new pixel-based method for quantifying the horizontal accuracies of the channels/orders derived from global DEMs, combined with computing vertical accuracies of these DEMs, can effectively help in selecting the DEM and its derived drainage network with the highest accuracies for extracting various geospatial layers required for flood susceptibility models. Additionally, there were other potential applications for the introduced method related to remote sensing research, whereby it can also be used to (i) determine the optimum AT by comparing the extracted drainage network from any remote sensing technology-based DEM with a reference network derived from high-quality DEM source, (ii) assess the effectiveness of different channel networks' extraction algorithms, and (iii) quantify the degree of horizontal variation between other linear geologic and geomorphological features (e.g., structural lineaments, surface geologic contacts, and shorelines) extracted from remote sensing-based geospatial datasets of simultaneous or different temporal series, after converting them to raster format.
- 4) developing flash flood susceptibility maps is the core stage to managing a sustainable plan for mitigating flood risks in any area under consideration for any current, or future, urban planning. Although the Dakhiliyah Governate at the Sultanate of Oman is frequently exposed to severe flash flood events, this study is the first to determine the vulnerable locations underlying flash flood hazards. The developed flood susceptibility models introduced the following improvements: (i) integrating bivariate and multivariate statistical techniques to provide precise susceptibility models taking the advantages of both methods, (ii) including spatio-temporal details by incorporating the corresponding satellite precipitation data that initiated a certain flood event, (iii) introducing a new and proper combination of flood causative factors that covered the entirety of information about the possible factors affecting the stream watershed and flash floods, such as climatic (i.e., GSMaP-G), geomorphic (i.e.,

Altitude, TPI, VD, CI, MRN, and Aspect), hydrologic (TWI, FL_DS, and DLD), and lithologic parameters (i.e., soil and geology). The new recipe provided flood susceptibility models of high predictive performances, (iv) extracting flood inventory map from SAR scenes and verified using VGI, which provided the chance for having spatially distributed and stratified random flood and non-flood points for accurate training and testing of the susceptibility models, (v) using the PALSAR DTM with a fine spatial resolution (12.5 m), and high vertical and horizontal accuracies to derive geospatial layers required for susceptibility models, (vi) selecting proper watershed that has diverse topography, with the developed hybrid susceptibility models yielding high predictive abilities and classification of the flood hazard levels in both mountainous and flat zones. Reliable and precise dynamic flood susceptibility maps can efficiently help the decision makers and environmental planners to develop their strategies to reduce costs and lessen the threats to human life and infrastructure that are commonly associated with future flash floods over space and time.

- 5) for a potential application, it can be possible to adopt the regionalization approach [1]–[4] to apply the trained susceptibility models to other arid watersheds of similar topographic and climatic conditions to the current study area, but with limited or no in-situ rainfall records (e.g., Kingdom of Saudi Arabia, United Arab Emirates, Yemen, and Sinai and the Eastern Desert in Egypt). The latter step could help in mitigating flash flood hazards in these areas, particularly with the limitation of in-situ rainfall data in these countries.

5.3. Recommendations for Future Work

Notwithstanding the reasonable performance of the improved integrated statistical-based flood susceptibility models to predict flood-prone areas and classify the degrees of hazards into five categories in the current research, the following points are to be considered for future efforts:

- using drones for capturing and verifying the flash flood extent, particularly with the inability to use the optical space-borne sensors for this task due to dense cloud coverage usually associated with flood spreading.
- including more dynamic factors (e.g., runoff and shallow groundwater level datasets) by taking into consideration the need for datasets with fine spatial and temporal resolutions.
- testing additional statistical, machine learning, and multi-criteria decision-making algorithms in developing the flood susceptibility models in the arid regions.
- searching the possible future availability of SAR scenes with frequent coverage of the arid basins. Having SAR images that are matched with flood occurrences is not an easy task and requires a lot of time. However, as long as there is a possibility to have more SAR scenes with fine spatial and temporal resolutions in the near future, it is recommended to study multiple future rainfall events of varying intensities, along with corresponding flood events with different magnitudes over the same area, in order to glean more information about the spatio-temporal variability of flash floods' inundations.
- exploring more segmentation algorithms of SAR images for the auto-extraction of the flood extents in the arid environments to accommodate with different characteristics of the arid watersheds.

- highlighting and emphasizing the rule of VGI in studying flash floods, particularly in remote areas with complex topographic and harsh climatic conditions. Raising flood awareness among the local settlers with respect to curated uploading of corresponding reports, images, and videos themed around flash events to give the researchers additional supports and opportunities to better understand the flash floods' dynamics.
- further exploring the assumption that the selected area of study is hydrogeologically connected (i.e., there is a mutual connection between surface and sub-surface processes, and especially those related to water). This type of study might provide additional, previously undiscovered insights into the variability of flash floods over space and time.
- exploring the performance of the developed pixel-based method for quantifying the horizontal variability of channels/orders derived from global DEMs over areas of different land covers, geomorphic units, lithology, and climatic zones throughout the world. It is recommended that researchers evaluate the accuracy of the DEMs and their channel networks/orders prior to involving them in their geomorphological and hydrological studies.
- Exploring the effectiveness on the integrated bivariate and multivariate susceptibility modeling on other hydrological and water resources management studies such as groundwater potentiality.

Finally, I would like to emphasize on the need to install dense streamflow gauges in some selected and representative areas of the arid basins. The extensive cost and labor work can hinder such a step; however, this action can improve predictive flood modeling, as well as other water resource management studies in the arid areas.

References

- [1] A. Milewski *et al.*, “A remote sensing solution for estimating runoff and recharge in arid environments,” *J. Hydrol.*, vol. 373, no. 1–2, pp. 1–14, Jun. 2009.
- [2] X. Yang, J. Magnusson, and C. Y. Xu, “Transferability of regionalization methods under changing climate,” *J. Hydrol.*, vol. 568, pp. 67–81, Jan. 2019.
- [3] J.-H. Song, Y. Her, K. Suh, M.-S. Kang, and H. Kim, “Regionalization of a Rainfall-Runoff Model: Limitations and Potentials,” *Water*, vol. 11, no. 11, p. 2257, Oct. 2019.
- [4] G. Krebs, T. Kokkonen, H. Setälä, and H. Koivusalo, “Parameterization of a Hydrological Model for a Large, Ungauged Urban Catchment,” *Water*, vol. 8, no. 10, p. 443, Oct. 2016.

APPENDICES

APPENDIX A

**RESULTS OF DIFFERENT RUNS FOR QUANTIFYING
UNCERTAINTIES ASSOCIATED WITH DIFFERENT GSPEs**

Table A.1. Traditional statistical metrics (RMSE and MD) estimated before and after using the statistical additive and multiplicative approaches to model the errors in the IMERG-F run at rainfall (RF) intensity classes of > 0.00 and 0.00–2.5 mm/day.

RF > 0.00 mm/day	Original	Additive	Multiplicative	RF: 0.00–2.5 mm/day	Original	Additive	Multiplicative
RMSE_1	8.19494	7.58455	8.74509	RMSE_1	4.34449	0.702298	0.762879
RMSE_2	9.09311	8.46335	10.3472	RMSE_2	3.69271	0.667054	0.743846
RMSE_3	9.31975	9.09022	11.0913	RMSE_3	3.64557	0.677036	0.721522
RMSE_4	9.0483	8.39925	9.56666	RMSE_4	4.60482	0.657251	0.711523
RMSE_5	9.14906	8.36866	9.64368	RMSE_5	4.20075	0.677807	0.736182
RMSE_6	8.22758	7.76944	9.86142	RMSE_6	4.26653	0.67619	0.755552
RMSE_7	8.87702	8.28215	10.2272	RMSE_7	5.07164	0.691121	0.720987
RMSE_8	9.19707	8.53272	9.90838	RMSE_8	4.14935	0.670233	0.705205
RMSE_9	8.28051	7.45878	9.33244	RMSE_9	3.94966	0.650924	0.68499
RMSE_10	8.58557	8.03096	9.68381	RMSE_10	3.63098	0.648234	0.655221
RMSE_All	8.80702	8.21135	9.85885	RMSE_All	4.15565	0.672009	0.720461
MD_1	-1.9417	0.620368	-3.18447	MD_1	1.59705	-0.0995808	-0.328525
MD_2	-2.5606	-0.407801	-4.30028	MD_2	1.5857	-0.110453	-0.344136
MD_3	-2.8086	-0.657388	-4.3337	MD_3	1.25316	-0.0409114	-0.275017
MD_4	-2.2276	0.206866	-3.47685	MD_4	1.72023	-0.0183294	-0.269306

MD_5	-2.4306	- 0.0916355	-3.91107	MD_5	1.75324	-0.0617224	-0.299256
MD_6	-2.1596	0.132678	-3.85395	MD_6	1.41414	-0.124675	-0.371115
MD_7	-2.5345	-0.288927	-4.1147	MD_7	1.96482	0.034178	-0.213938
MD_8	-2.1406	0.273915	-3.5654	MD_8	1.76858	0.0030691	-0.237866
MD_9	-2.3848	- 0.0875967	-4.01569	MD_9	1.55721	0.021726	-0.224966
MD_10	-2.17	0.317059	-3.46721	MD_10	1.4862	0.0924572	-0.154827
MD_All	-2.3359	0.0017537	-3.82233	MD_All	1.61003	-0.0304243	-0.271895

Table A.2. Traditional statistical metrics (RMSE and MD) estimated before and after using the statistical additive and multiplicative approaches to model the errors in the IMERG-F run at rainfall (RF) intensity classes of 2.5–10 and 10–50 mm/ day.

RF: 2.5–10 mm/day	Original	Additive	Multiplicative	RF: 10–50 mm/day	Original	Additive	Multiplicative
RMSE_1	5.23188	2.06858	2.12756	RMSE_1	14.1075	7.53828	8.88468
RMSE_2	4.87854	2.11046	2.10088	RMSE_2	15.1889	7.57147	9.24109
RMSE_3	4.80331	2.07953	2.08673	RMSE_3	15.4651	7.70578	9.07135
RMSE_4	6.88997	2.11378	2.17927	RMSE_4	15.6411	8.40493	9.27696
RMSE_5	5.31003	2.08001	2.1839	RMSE_5	13.4077	6.80406	7.22492
RMSE_6	4.82546	1.85581	1.83109	RMSE_6	13.8577	7.21592	7.85292
RMSE_7	5.00177	2.04321	2.09492	RMSE_7	15.5133	8.36313	8.90278
RMSE_8	6.0442	2.1459	2.21039	RMSE_8	14.5402	7.87773	9.19168
RMSE_9	4.62107	2.12893	2.13469	RMSE_9	15.0874	7.93207	8.77768
RMSE_10	4.98147	2.19449	2.23753	RMSE_10	14.7707	7.51115	8.41898
RMSE_All	5.30016	2.08384	2.12142	RMSE_All	14.7757	7.70633	8.70763
MD_1	-2.14402	-0.087944	-0.469139	MD_1	-10.812	-0.560115	-2.29068
MD_2	-1.79547	0.194883	-0.171694	MD_2	-11.362	-1.08999	-2.6648
MD_3	-1.88228	0.200305	-0.179327	MD_3	-11.9534	-1.68354	-3.36927
MD_4	-1.3916	-0.102785	-0.526609	MD_4	-11.5644	-0.793419	-2.24729

MD_5	-2.16265	-0.235984	-0.645065	MD_5	-9.62572	2.01708	0.244625
MD_6	-1.99503	0.341895	-0.069629	MD_6	-9.81106	1.09167	-0.415375
MD_7	-2.11983	-0.127682	-0.515639	MD_7	-12.0983	-0.695264	-1.83918
MD_8	-2.01128	-0.089895	-0.478022	MD_8	-11.5679	-0.768374	-2.1104
MD_9	-2.60512	0.168731	-0.200492	MD_9	-10.4291	0.150952	-1.86471
MD_10	-2.10667	-0.055512	-0.409761	MD_10	-10.9847	0.094957	-1.47033
MD_All	-2.02139	0.0206011	-0.366538	MD_All	-11.0209	-0.223604	-1.80274

Table A.3. Traditional statistical metrics (RMSE and MD) estimated before and after using the statistical additive and multiplicative approaches to model the errors in the GSMaP-S product at rainfall (RF) intensity classes of > 0.00 and 0.00–2.5 mm/day.

RF > 0.00 mm/day	Original	Additive	Multiplicative	RF: 0.00–2.5 mm/day	Original	Additive	Multiplicative
RMSE_1	9.40465	7.96618	9.69162	RMSE_1	5.06112	0.663037	0.686668
RMSE_2	12.0926	9.28296	10.5742	RMSE_2	4.37254	0.645827	0.675495
RMSE_3	9.19592	8.02473	9.9008	RMSE_3	4.24058	0.690975	0.735317
RMSE_4	9.69161	8.65375	10.1718	RMSE_4	4.14466	0.665934	0.702964
RMSE_5	9.52329	7.7892	10.2062	RMSE_5	4.68967	0.6518	0.663914
RMSE_6	10.5838	8.02567	8.10248	RMSE_6	4.02414	0.685558	0.728514
RMSE_7	9.07057	7.51479	9.79286	RMSE_7	5.15865	0.668903	0.706823
RMSE_8	9.41774	8.09856	9.90795	RMSE_8	4.85241	0.683232	0.740694
RMSE_9	10.8303	8.04058	8.08768	RMSE_9	4.79336	0.665987	0.68535
RMSE_10	11.0216	7.89267	8.95027	RMSE_10	4.13338	0.672139	0.736503
RMSE_All	10.1273	8.14251	9.57411	RMSE_All	4.56399	0.669478	0.70672
MD_1	-1.71157	- 0.116454	-3.7769	MD_1	2.10754	0.0599775	-0.195062
MD_2	-1.49033	- 0.345035	-4.28862	MD_2	1.73802	0.0517978	-0.210962
MD_3	-1.43211	0.085911	-3.66871	MD_3	1.62052	-0.0065173	-0.256952
MD_4	-1.98683	- 0.428307	-3.86512	MD_4	1.51963	0.025202	-0.232987

MD_5	-1.4124	-0.42809	-4.29788	MD_5	1.52795	0.0982697	-0.165741
MD_6	-1.68421	0.356043	-2.95653	MD_6	1.49597	0.0011869	-0.249867
MD_7	-1.51725	-0.2616	-4.16248	MD_7	1.72093	0.0174148	-0.242256
MD_8	-1.46313	-0.16691	-3.89783	MD_8	1.72149	-0.0250895	-0.275877
MD_9	-0.84526	1.13039	-2.5705	MD_9	1.89899	0.073386	-0.185996
MD_10	-1.10424	0.497095	-3.4385	MD_10	1.46765	-0.0513285	-0.305876
MD_All	-1.46473	0.032303	-3.69231	MD_All	1.68187	0.02443	-0.232158

Table A.4. Traditional statistical metrics (RMSE and MD) estimated before and after using the statistical additive and multiplicative approaches to model the errors in the GSMaP-S product at rainfall (RF) intensity classes of 2.5–10 and 10–50 mm/ day.

RF: 2.5–10 mm/day	Original	Additive	Multiplicative	RF: 10–50 mm/day	Original	Additive	Multiplicative
RMSE_1	5.68049	2.06686	2.08995	RMSE_1	15.4429	7.20637	7.89165
RMSE_2	5.8724	2.07071	2.05529	RMSE_2	16.6304	7.55031	8.54653
RMSE_3	5.38183	2.06411	2.08423	RMSE_3	17.228	8.06739	8.92401
RMSE_4	5.61602	2.03621	2.08086	RMSE_4	18.9159	8.82278	9.39542
RMSE_5	5.14934	2.1206	2.12707	RMSE_5	17.006	7.33655	7.93568
RMSE_6	5.74702	2.261	2.33021	RMSE_6	17.0953	8.13362	9.14803
RMSE_7	6.39771	2.0925	2.11932	RMSE_7	21.8281	8.44388	6.79206
RMSE_8	5.56253	2.14947	2.19042	RMSE_8	18.231	9.00443	9.90524
RMSE_9	5.3839	1.99262	2.02521	RMSE_9	23.0849	10.0822	9.56863
RMSE_10	6.32902	2.17334	2.19222	RMSE_10	22.3618	9.14485	7.29892
RMSE_All	5.72465	2.104	2.13113	RMSE_All	18.955	8.42319	8.59636
MD_1	-2.18018	0.0507466	-0.347591	MD_1	-8.80279	1.42379	-0.140546
MD_2	-1.91387	0.30936	-0.105419	MD_2	-6.83595	0.218244	-1.63259
MD_3	-2.06708	0.0086633	-0.357177	MD_3	-6.43559	0.691662	-1.12098
MD_4	-1.89464	0.0914719	-0.270328	MD_4	-11.5957	-1.87707	-3.03484

MD_5	-2.4028	0.146668	-0.24135	MD_5	-8.41288	0.53205	-1.17886
MD_6	-1.87125	-0.272902	-0.644116	MD_6	-8.03892	-1.27842	-2.92725
MD_7	-1.56869	0.125797	-0.262164	MD_7	-8.50802	0.893403	-0.625024
MD_8	-2.40173	0.0711913	-0.304381	MD_8	-8.49811	-1.21242	-2.64442
MD_9	-1.9569	0.0166328	-0.372464	MD_9	-9.45811	-1.58259	-3.24367
MD_10	-1.60238	0.0548565	-0.31082	MD_10	-6.81	1.72255	-0.260294
MD_All	-1.98595	0.0602486	-0.321581	MD_All	-8.3396	-0.04688	-1.68085

Table A.5. Traditional statistical metrics (RMSE and MD) estimated before and after using the statistical additive and multiplicative approaches to model the errors in the GSMaP-G at rainfall (RF) intensity classes of > 0.00 and 0.00–2.5 mm/day.

RF > 0.00 mm/day	Original	Additive	Multiplicative	RF: 0.00–2.5 mm/day	Original	Additive	Multiplicative
RMSE_1	8.76415	8.29818	9.87831	RMSE_1	3.47401	0.642517	0.674242
RMSE_2	9.20133	8.74592	10.2117	RMSE_2	3.94027	0.67529	0.730407
RMSE_3	9.58939	9.11235	10.9444	RMSE_3	3.80893	0.66784	0.721882
RMSE_4	8.72093	8.35891	9.77021	RMSE_4	3.92266	0.653395	0.698969
RMSE_5	12.58470	12.4569	12.9424	RMSE_5	3.54275	0.677931	0.7003
RMSE_6	8.54834	8.09268	9.8831	RMSE_6	3.58692	0.680321	0.723018
RMSE_7	9.03263	8.56311	10.3096	RMSE_7	3.74093	0.642221	0.674433
RMSE_8	8.77107	8.32042	9.46801	RMSE_8	3.44284	0.647114	0.688751
RMSE_9	13.29100	12.8745	14.1131	RMSE_9	3.48938	0.664531	0.704718
RMSE_10	8.22586	7.77766	9.35505	RMSE_10	3.7626	0.648433	0.70826
RMSE_All	9.81717	9.42192	10.7931	RMSE_All	3.67542	0.660112	0.70274
MD_1	-2.86396	-0.1482	-3.88542	MD_1	1.5816	0.0370762	-0.218083
MD_2	-2.84839	-0.146282	-3.99121	MD_2	1.80619	-0.0430076	-0.290379
MD_3	-3.26203	-0.715161	-4.34997	MD_3	1.6991	-0.0388932	-0.289812
MD_4	-2.56953	0.273689	-3.52452	MD_4	1.6859	0.000361147	-0.255126

MD_5	-2.24345	0.73822	-3.33157	MD_5	1.59821	0.0422155	-0.202401
MD_6	-2.77742	-0.0532836	-4.0075	MD_6	1.60854	-0.016978	-0.260589
MD_7	-2.96712	-0.303259	-4.12578	MD_7	1.70608	0.0474019	-0.201289
MD_8	-2.72994	0.0357547	-3.64507	MD_8	1.55201	0.000105997	-0.249899
MD_9	-3.42451	-0.960899	-4.5419	MD_9	1.63295	-0.00010314	-0.247379
MD_10	-2.74074	0.0427212	-3.69103	MD_10	1.72205	-0.0359255	-0.292469
MD_All	-2.84271	-0.12367	-3.9094	MD_All	1.65926	-0.00077467	-0.250743

Table A.6. Traditional statistical metrics (RMSE MD) estimated before and after using the statistical additive and multiplicative approaches to model the errors in the GSMaP-G product at rainfall (RF) intensity classes of 2.5–10 and 10–50 mm/ day.

RF: 2.5–10 mm/day	Original	Additive	Multiplicative	RF: 10–50 mm/day	Original	Additive	Multiplicative
RMSE_1	4.72093	2.0511	2.09669	RMSE_1	15.9161	8.09711	8.2097
RMSE_2	4.7203	1.99279	2.04004	RMSE_2	15.6209	8.2343	8.83605
RMSE_3	4.93557	2.20368	2.2245	RMSE_3	16.3363	8.77816	9.14802
RMSE_4	4.47495	2.14631	2.19962	RMSE_4	15.782	8.01936	8.02776
RMSE_5	4.09138	2.045	2.04127	RMSE_5	15.8593	7.80983	8.32069
RMSE_6	4.71779	2.13642	2.15551	RMSE_6	15.5447	8.45848	8.90926
RMSE_7	4.82204	2.21973	2.31631	RMSE_7	14.0617	7.92791	8.22217
RMSE_8	4.84831	2.02878	2.05589	RMSE_8	15.3238	8.32805	8.32759
RMSE_9	4.69678	2.06416	2.1264	RMSE_9	15.8094	8.43746	8.31814
RMSE_10	4.46085	2.07531	2.14687	RMSE_10	15.6709	8.54586	8.80024
RMSE_All	4.65476	2.09758	2.14197	RMSE_All	15.6029	8.26863	8.51941
MD_1	-1.86052	-0.136475	-0.549683	MD_1	-13.1698	-0.132996	-1.57085
MD_2	-2.14569	-0.0495723	-0.446943	MD_2	-13.015	-0.341421	-1.90636
MD_3	-1.78752	-0.156341	-0.55898	MD_3	-13.3417	-0.902824	-2.12055
MD_4	-2.23248	-0.137975	-0.495847	MD_4	-13.0327	-0.092548	-1.32057

MD_5	-2.22248	0.201438	-0.185525	MD_5	-13.4869	-0.531436	-2.0256
MD_6	-2.17438	-0.112934	-0.501045	MD_6	-12.6152	0.292268	-1.27369
MD_7	-2.28961	-0.420812	-0.798839	MD_7	-11.3592	1.33666	-0.608964
MD_8	-1.98686	0.0807252	-0.323066	MD_8	-12.3813	0.671414	-0.82924
MD_9	-2.33725	-0.0791826	-0.463464	MD_9	-12.7155	0.225884	-1.30138
MD_10	-2.02157	-0.154126	-0.529908	MD_10	-12.6438	0.0280978	-1.58171
MD_All	-2.10584	-0.0965255	-0.48533	MD_All	-12.7761	0.0553093	-1.45389

APPENDIX B

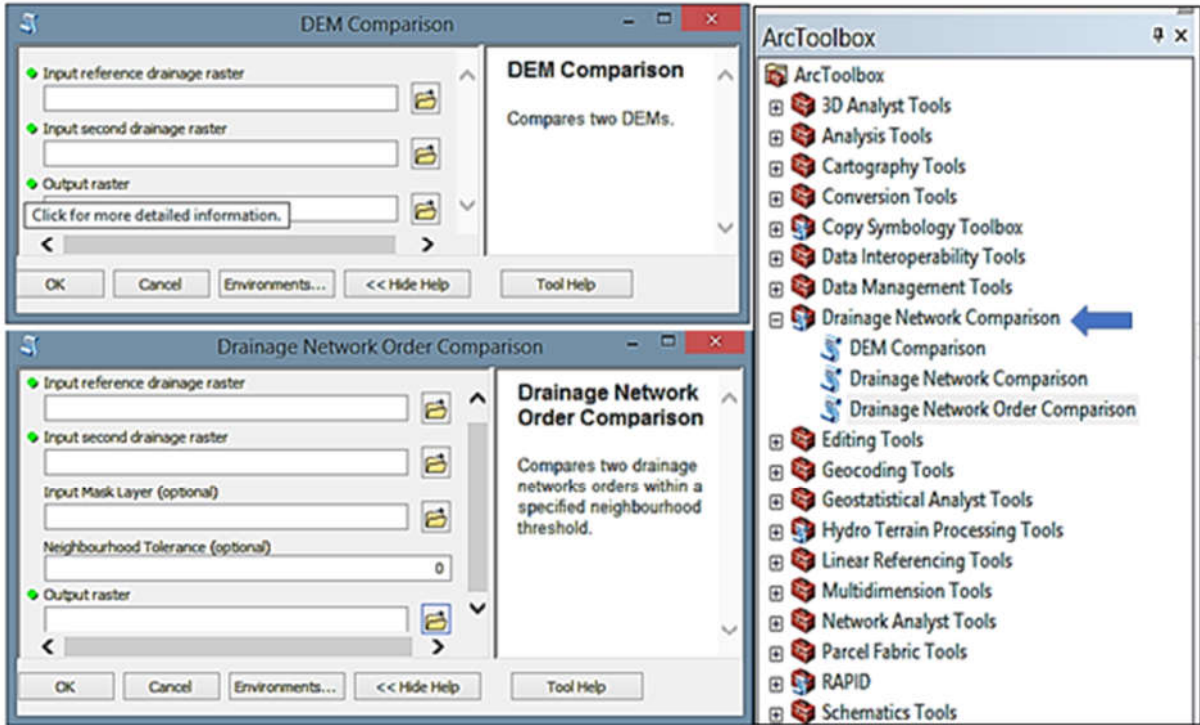


Figure B.1. New developed ArcGIS's Python toolbox for the geometric comparison between drainage networks/orders.

APPENDIX C

COPYRIGHT RELATED INFORMATION

Article

Pixel-Based Geometric Assessment of Channel Networks/Orders Derived from Global Spaceborne Digital Elevation Models

Mohamed Shawky^{1,*}, Adel Moussa^{1,2}, Quazi K. Hassan¹ and Naser El-Sheimy¹

¹ Department of Geomatics Engineering, Schulich School of Engineering, University of Calgary, 2500 University Dr. NW, Calgary, AB T2N 1N4, Canada; [REDACTED]

² Department of Electrical Engineering, School of Engineering, Port Said University, Port Fouad 42523, Egypt

* Correspondence: [REDACTED]

Received: 2 December 2018; Accepted: 21 January 2019; Published: 23 January 2019



Abstract: Digital Elevation Models (DEMs) contribute to geomorphological and hydrological applications. DEMs can be derived using different remote sensing-based datasets, such as Interferometric Synthetic Aperture Radar (InSAR) (e.g., Advanced Land Observing Satellite (ALOS) Phased Array type L-band SAR (PALSAR) and Shuttle Radar Topography Mission (SRTM) DEMs). In addition, there is also the Digital Surface Model (DSM) derived from optical tri-stereo ALOS Panchromatic Remote-sensing Instrument for Stereo Mapping (PRISM) imagery. In this study, we evaluated satellite-based DEMs, SRTM (Global) GL1 DEM V003 28.5 m, ALOS DSM 28.5 m, and PALSAR DEMs 12.5 m and 28.5 m, and their derived channel networks/orders. We carried out these assessments using Light Detection and Ranging (LiDAR) Digital Surface Models (DSMs) and Digital Terrain Models (DTMs) and their derived channel networks and Strahler orders as reference datasets at comparable spatial resolutions. We introduced a pixel-based method for the quantitative horizontal evaluation of the channel networks and Strahler orders derived from global DEMs utilizing confusion matrices at different flow accumulation area thresholds (ATs) and pixel buffer tolerance values (PBTVs) in both $\pm X$ and $\pm Y$ directions. A new Python toolbox for ArcGIS was developed to automate the introduced method. A set of evaluation metrics—(i) producer accuracy (PA), (ii) user accuracy (UA), (iii) F-score (F), and (iv) Cohen's kappa index (KI)—were computed to evaluate the accuracy of the horizontal matching between channel networks/orders extracted from global DEMs and those derived from LiDAR DTMs and DSMs. PALSAR DEM 12.5 m ranked first among the other global DEMs with the lowest root mean square error (RMSE) and mean difference (MD) values of 4.57 m and 0.78 m, respectively, when compared to the LiDAR DTM 12.5 m. The ALOS DSM 28.5 m had the highest vertical accuracy with the lowest recorded RMSE and MD values of 4.01 m and -0.29 m, respectively, when compared to the LiDAR DSM 28.5 m. PALSAR DEM 12.5 m and ALOS DSM 28.5 m-derived channel networks/orders yielded the highest horizontal accuracy when compared to those delineated from LiDAR DTM 12.5 m and LiDAR DSM 28.5 m, respectively. The number of unmatched channels decreased when the PBTV increased from 0 to 3 pixels using different ATs.

Keywords: Vertical accuracy of DEMs; channel networks; LiDAR; confusion matrix; ArcGIS Python toolbox

1. Introduction

Current advances in remote sensing techniques are essential in producing high-quality Digital Elevation Models (DEMs). Because of the general availability of different optical and microwave satellite data-based DEMs, many authors have extensively used these elevation datasets for a

122. Boschetti, M.; Nutini, F.; Manfron, G.; Brivio, P.A.; Nelson, A. Comparative Analysis of Normalised Difference Spectral Indices Derived from MODIS for Detecting Surface Water in Flooded Rice Cropping Systems. *PLoS ONE* **2014**, *9*, e88741. [[CrossRef](#)]
123. Dewitt, J.D.; Warner, T.A.; Conley, J.F. Comparison of DEMs derived from USGS DLG, SRTM, a statewide photogrammetry program, ASTER GDEM and LiDAR: Implications for change detection. *GISci. Remote Sens.* **2015**, *52*, 179–197. [[CrossRef](#)]
124. Acharya, T.D.; Lee, D.; Yang, I.T. Comparative Analysis of Digital Elevation Models between AW3D30, SRTM30 and Airborne LiDAR: A Case of Chunc. *J. Korean Soc. Surv. Geod. Photogramm. Cartogr.* **2018**, *36*, 17–24. [[CrossRef](#)]
125. Liu, J.; Chang, K.; Lin, C.; Chang, L.; Co, L.T.; City, Z.; County, H. Accuracy Evaluation of Alos Dem With Airborne Lidar Data in Southern Taiwan. In Proceedings of the 2015 IEEE International Geoscience and Remote Sensing Symposium (IGARSS), Milan, Italy, 26–31 July 2015.
126. Alganci, U.; Besol, B.; Sertel, E. Accuracy Assessment of Different Digital Surface Models. *ISPRS Int. J. Geo-Inf.* **2018**, *7*, 114. [[CrossRef](#)]
127. Santillan, J.R.; Makinano-Santillan, M. Vertical accuracy assessment of 30-M resolution ALOS, ASTER, and SRTM global DEMs over Northeastern Mindanao, Philippines. *Int. Arch. Photogramm. Remote Sens. Spat. Inf. Sci. ISPRS Arch.* **2016**, *41*, 149–156. [[CrossRef](#)]
128. Hu, Z.; Peng, J.; Hou, Y.; Shan, J. Evaluation of recently released open global digital elevation models of Hubei, China. *Remote Sens.* **2017**, *9*, 262. [[CrossRef](#)]
129. Alaska Satellite Facility (ASF). *ASF Radiometric Terrain Corrected Products—Algorithm Theoretical Basis Document*; ASF: Fairbanks, AK, USA, 2015.
130. Shimada, M. Ortho-Rectification and Slope Correction of SAR Data Using DEM and Its Accuracy Evaluation. *IEEE J. Sel. Top. Appl. Earth Obs. Remote Sens.* **2010**, *3*, 657–671. [[CrossRef](#)]
131. Hofton, M.; Dubayah, R.; Blair, J.B.; Rabine, D. Validation of SRTM elevations over vegetated and non-vegetated terrain using medium footprint lidar. *Photogramm. Eng. Remote Sens.* **2006**, *72*, 279–285. [[CrossRef](#)]
132. Mozas-Calvache, A.T.; Ariza-López, F.J. Adapting 2D positional control methodologies based on linear elements to 3D. *Surv. Rev.* **2015**, *47*, 195–201. [[CrossRef](#)]



© 2019 by the authors. Licensee MDPI, Basel, Switzerland. This article is an open access article distributed under the terms and conditions of the Creative Commons Attribution (CC BY) license (<http://creativecommons.org/licenses/by/4.0/>).

Article

Performance Assessment of Sub-Daily and Daily Precipitation Estimates Derived from GPM and GSMaP Products over an Arid Environment

Mohamed Shawky ^{1,2,*}, Adel Moussa ^{1,3}, Quazi K Hassan ¹ and Naser El-Sheimy ¹

¹ Department of Geomatics Engineering, Schulich School of Engineering, University of Calgary, 2500 University Dr. NW, Calgary, Alberta, AB T2N 1N4, Canada; [REDACTED]

² Department of Geology, Faculty of Science, Mansoura University, Mansoura 35516, Egypt

³ Department of Electrical Engineering, Faculty of Engineering, Port Said University, Port Fouad 42523, Egypt

* Correspondence: [REDACTED]

Received: 3 November 2019; Accepted: 27 November 2019; Published: 29 November 2019



Abstract: Precipitation is a critical variable for comprehending various climate-related research, such as water resources management, flash flood monitoring and forecasting, climatic analyses, and hydrogeological studies, etc. Here, our objective was to evaluate the rainfall estimates obtained from Global Precipitation Mission (GPM), and Global Satellite Mapping of Precipitation (GSMaP) constellation over an arid environment like the Sultanate of Oman that is characterized by a complex topography and extremely variable rainfall patterns. Global Satellite-based Precipitation Estimates (GSPEs) can provide wide coverage and high spatial and temporal resolutions, but evaluating their accuracy is a mandatory step before involving them in different hydrological applications. In this paper, the reliability of the Integrated Multi-satellitE Retrievals for the GPM (IMERG) V04 and GSMaP V06 products were evaluated using the reference in-situ rain gauges at sub-daily (e.g., 6, 12, and 18 h) and daily time scales during the period of March 2014–December 2016. A set of continuous difference statistical indices (e.g., mean absolute difference, root mean square error, mean difference, and unconditional bias), and categorical metrics (e.g., probability of detection, critical success index, false alarm ratio, and frequency bias index) were used to evaluate recorded precipitation occurrences. The results showed that the five GSPEs could generally delineate the spatial and temporal patterns of rainfall while they might have over- and under-estimations of in-situ gauge measurements. The overall quality of the GSMaP runs was superior to the IMERG products; however, it also encountered an exaggeration in case of light rain and an underestimation for heavy rain. The effects of the gauge calibration algorithm (GCA) used in the final IMERG (IMERG-F) were investigated by comparison with early and late runs. The IMERG-F V04 product did not show a significant improvement over the early (i.e., after 4 h of rainfall observations) and late (i.e., after 12 h of rainfall observations) products. The results indicated that GCA could not reduce the missed precipitation records considerably.

Keywords: Dry environment; hydrology; Integrated Multi-satellitE Retrievals for the GPM; rain gauge records; satellite-based precipitation; statistical evaluation; Sultanate of Oman

1. Introduction

Precipitation is one of the key components of the water cycle that is crucial to study the hydrological balance, water resources management, drought monitoring, flood forecasting, as well as critical social and climatological issues [1]. However, quantifying precipitation is complicated because it has a non-normal distribution and high variability, even at a small scale [1,2]. In general, direct surface rain observations from in-situ gauges and indirect measurements through optical and microwave

53. Shu, Y.; Li, H.; Lei, Y. Modelling Groundwater Flow with MIKE SHE Using Conventional Climate Data and Satellite Data as Model Forcing in Haihe Plain, China. *Water* **2018**, *10*, 1295. [[CrossRef](#)]
54. Park, M.; Choi, Y.S.; Shin, H.J.; Song, I.; Yoon, C.G.; Choi, J.D.; Yu, S.J. A Comparison Study of Runoff Characteristics of Non-Point Source Pollution from Three Watersheds in South Korea. *Water* **2019**, *11*, 966. [[CrossRef](#)]
55. Yi, L.; Zhang, W.; Li, X. Assessing Hydrological Modelling Driven by Different Precipitation Datasets via the SMAP Soil Moisture Product and Gauged Streamflow Data. *Remote Sens.* **2018**, *10*, 1872. [[CrossRef](#)]
56. Siddique-E-Akbor, A.H.M.; Hossain, F.; Sikder, S.; Shum, C.K.; Tseng, S.; Yi, Y.; Turk, F.J.; Limaye, A. Satellite Precipitation Data-Driven Hydrological Modeling for Water Resources Management in the Ganges, Brahmaputra, and Meghna Basins. *Earth Interact.* **2014**, *18*, 1–25. [[CrossRef](#)]
57. Sillmann, J.; Thorarinsdottir, T.; Keenlyside, N.; Schaller, N.; Alexander, L.V.; Hegerl, G.; Seneviratne, S.I.; Vautard, R.; Zhang, X.; Zwiers, F.W. Understanding, modeling and predicting weather and climate extremes: Challenges and opportunities. *Weather Clim. Extrem.* **2017**, *18*, 65–74. [[CrossRef](#)]
58. Dewan, A. *Floods in a Megacity: Geospatial Techniques in Assessing Hazards, Risk and Vulnerability*; Springer: Berlin, Germany, 2013.
59. Saber, M.; Yilmaz, K. Evaluation and Bias Correction of Satellite-Based Rainfall Estimates for Modelling Flash Floods over the Mediterranean region: Application to Karpuz River Basin, Turkey. *Water* **2018**, *10*, 657. [[CrossRef](#)]
60. Tuo, Y.; Duan, Z.; Disse, M.; Chiogna, G. Evaluation of precipitation input for SWAT modeling in Alpine catchment: A case study in the Adige river basin (Italy). *Sci. Total Environ.* **2016**, *573*, 66–82. [[CrossRef](#)]



© 2019 by the authors. Licensee MDPI, Basel, Switzerland. This article is an open access article distributed under the terms and conditions of the Creative Commons Attribution (CC BY) license (<http://creativecommons.org/licenses/by/4.0/>).

PUBLISHED WORK

Published Journal Papers:

- **M. Shawky, A. Moussa, Q. Hassan, N. El-Sheimy (2019).** Pixel-Based Geometric Assessment of Channel Networks/Orders Derived from Global Spaceborne Digital Elevation Models. *Remote Sens.* **2019**, *11*, 235.33p.
- **M. Shawky, A. Moussa, Q. Hassan, N. El-Sheimy (2019).** Performance Assessment of Daily and Sub-Daily Scale Precipitation Estimates derived from GPM and GSMaP Products over an Arid Environment. *Remote Sens.* **2019**, *11*, 2840.21p.

Journal Papers (In Preparation):

- Remote Sensing-based An Enhanced Flash Flood Susceptibility Mapping using hybrid Bivariate and Multivariate Statistical Models, A case Study from An Arid Area.
- Flash flood modeling in the arid areas, a review.

Conference Presentations:

- **M. Shawky, Q. Hassan, N. El-Sheimy (2019).** A GIS-based Spatial Bivariate Statistical Model for Flood Susceptibility Mapping. ESRI Canada User Conference. May 15th, Calgary, AB, Canada.
- **M. Shawky, Q. Hassan, N. El-Sheimy (2019).** GIS for Delineating Stream Network. Peer Beyond Graduate Research Symposium. February 22th, Calgary, AB, Canada.
- **M. Shawky, A. Moussa, Q. Hassan, N. El-Sheimy (2018).** Effect of Correcting SRTM Elevation Data on the Geometric Comparison between the Drainage Networks Derived from SRTM DEM and LIDAR DTM. The 39th Canadian Symposium on Remote Sensing. June 19-21, Saskatoon, SK, Canada.
- **M. Shawky, O. Charif, Q. Hassan, N. El-Sheimy (2018).** GPM Mission Over the Middle East; Past Perspectives and Current Advances. Peer Beyond Graduate Research Symposium. February 20th, Calgary, AB, Canada.
- .

- **M. Shawky, N. El-Sheimy (2016).** Is that possible to monitor flash flood in the absence of real-time rainfall data: a review of different case studies from arid regions. The 14th Experimental Chaos and Complexity Conference, Banff, Calgary, Canada.